An Investigation into Methods to Control Breakup and Droplet Formation in Single and Compound Liquid Jets

by

Jamal Uddin

A thesis submitted to
The University of Birmingham
for the degree of
Doctor of Philosophy

School of Mathematics
The University of Birmingham
September 2007

Abstract

The disintegration of a thread of fluid into droplets is ubiquitous in modern engineering applications and research in this area stretches back over two centuries. However, understanding the mechanism, and as a consequence being able to control, the breakup and subsequent droplet formation of a liquid jet remains both an inherently interesting and challenging problem in modern science. Whilst the last few decades have seen a growth in novel techniques for droplet generation, in many such cases, these methods are poorly understood. In this thesis we investigate a number of techniques for controlling rupture of jets, including industrial prilling with non-Newtonian fluids, the use of insoluble surfactants, controlled insonification and thermal modulation. In addition we examine the dynamics of rupture in two-fluid or compound threads as well as the breakup of jets on the microscopic scale using the theory of interface formation. We find that in all these cases, a greater degree of control and ability to manipulate droplet sizes and breakup lengths can be achieved.

Acknowledgements

Firstly and foremost I should like to thank God for indeed all praise and thanks belong to him.

I should also like to take this opportunity to express deep gratitude and heartfelt thanks to my supervisors Prof. Stephen Decent and Dr. Mark Simmons. My progress and development, both academically and personally, throughout my postgraduate studies have received much needed support.

As ever I am indebted to my family, each and everyone of them, including my mother Amina, my brother Altab and my sisters Luftha, Hasina and Mina. This thesis would never have reached completion without their constant support and encouragement. And as such I should like to dedicate this thesis to them.

It would be an injustice on my part not to mention how much I have enjoyed my time spent at Birmingham and not to acknowledge the kindness and generosity which has been forthcoming from staff and fellow students who are too numerous to mention. My thanks and appreciation to them all. I should also like to acknowledge the financial support from EPSRC which made this work possible.

Contents

List of Tables

List of Notation

Symbol	SI unit	Usual Meaning
σ	N m^{-1}	surface tension
k, κ	m^{-1}	wavenumber
ρ	kg m^{-3}	density
ω	s^{-1}	growth rate
δ		initial amplitude of perturbations
t_b	s	time to breakup
Π		total stress tensor
μ	Pa s	dynamic viscosity
Oh	-	Ohnesorge number
$\dot{\gamma}$	s^{-1}	shear rate
λ	m^{-1}	wavelength, growth rate
α	s	flow index number
m	Pa s$^{\alpha}$	flow consistency number
η	Pa s	apparent viscosity
η_{∞}	Pa s	infinite shear viscosity
We	-	Weber number
$\mathcal{R}e_{\alpha}$	-	Generalized Reynolds number
$\mathcal{R}b$	-	Rossby number
ε	N m^{-1}	aspect ratio
k^*	m^{-1}	most unstable wavenumber
τ	s	relaxation time
ϱ_e	kg m^{-3}	equilibrium surface density
σ_e	N m^{-1}	equilibrium surface tension

List of Notation (continued)

Symbol	SI unit	Usual Meaning
δ_θ	-	magnitude of heating
κ_θ	-	frequency of heating
$\mathcal{F}$	-	Froude number
$\mathcal{P}e$	-	Peclet number
$\mathcal{B}i$	-	Biot number
κ_T	$m^2 s^{-1}$	thermal diffusivity
c_p		specific heat capacity
Γ	-	surfactant concentration
∇_s	-	surface gradient operator
T	K	temperature

Chapter 1

Introduction

The disintegration of a thread of fluid into droplets is ubiquitous in modern engineering applications with research in this area stretching back over two centuries. It may therefore come as a surprise that despite such close scrutiny of this classical phenomenon, a good understanding of the mechanisms, along with an ability to control, the breakup and subsequent droplet formation of a liquid jet remains elusive to the scientific community. Whilst the last few decades have seen a growth in novel techniques for the generation of droplets (including variations of existing methods), in many cases, these methods are poorly understood.

The challenge of gaining a greater understanding of the physical mechanisms responsible for the process of rupture in a liquid thread (and consequently droplet formation) is made more difficult for a number of reasons, some of which fundamentally question the foundations of our current understanding of fluid dynamics. Firstly, the process of rupture involves a topological transition of the flow domain, usually from a cylindrical column into a series of spherical droplets. Rupture, by definition, is inherently associated with some length scale, usually the radius of a column of fluid, becoming infinitesimally small whilst at the same time the velocity of a typical fluid element near the point of rupture diverges to infinity. Therefore a singularity is reached in finite time and the fa-

miliar Navier-Stokes equations become inappropriate and no more progress can be made. Secondly, typical length and time scales can change over a number of orders between some initial equilibrium state and rupture. Such obstacles can be classified as 'local' or even 'universal' in the sense that, irrespective of any particular experimental setup, these issues present themselves as the point and time of rupture is approached. The breakup of a liquid thread can also be affected by what may be termed 'global' mechanisms. These include externally imposed vibrations, the use of special chemicals and so forth, and in general, are much more easily manipulated and can effect both the initial steady equilibrium state and the evolution of disturbances towards pinch-off.

In this thesis we seek to explore a number of methods to control droplet formation (and particularly parasitic satellite droplet formation which in many cases is an unavoidable consequence of the generation of droplets) with particular emphasis placed on gaining a deeper mathematical appreciation of rupture in a variety of complex industrial settings. Some of the material within this thesis has already been published (see Uddin *et al.* (2006) and Hawkins *et al.* (2007)) whilst others are under consideration for publication (see Uddin *et al.* (2007*a*) and (2007*b*)) and yet others are under preparation to be submitted (Uddin *et al.* (2007*c*), (2007*d*) and (2007*e*)).

This thesis is arranged in the following manner; the first chapter of this thesis provides a gentle introduction into the world of liquid jets with particular emphasis placed on developments over the last century. An appreciation of linear instability (of disturbances along liquid jets) which forms the backbone of most of the classical literature is followed by more recent non-linear analysis. A review of the most prominent experimental works in this field is then examined highlighting some of the successes of both linear and non-linear theories. We then examine some of the more recent works dealing with similarity solutions to breakup phenomena which become increasingly important as the time and length scales of the flow become very small.

The next chapter introduces the concept of a non-Newtonian fluid. We examine a number of models for the simplest types of non-Newtonian fluids and in particular we consider viscoelastic fluids (which are popular in the literature) as well as some inelastic fluids. We make mention of the Power-Law model which we use as the working fluid for the rest of this thesis.

Chapter Four provides a mathematical introduction to the industrial prilling process. In this process, free surface disturbances (which can be artificially imposed to create desired frequencies) are allowed to travel along a rotating liquid jet to stimulate breakup[1]. Droplets formed upon rupture of the jet are later cooled and solidified in order to produce pellets. This technique is amongst the most favoured method for the preparation of fertilizers. Previous attempts to model this process based on Newtonian liquids are reviewed[2]. A mathematical model is developed to incorporate non-Newtonian flow into the spiralling jet equations. A linear temporal analysis is considered and is shown to produce similar results to spatial instability. The dispersion equation for the growth rate and most unstable wavenumber is derived and solved for certain parameter ranges. A brief summary of the main results is also presented.

In Chapter Five we introduce the reader to numerical methods involving finite difference schemes and we discuss some of the inherent restrictions which apply when using these methods. We solve the spiralling jet equations for fluids with power law rheology (derived in the previous Chapter) using a finite difference scheme based on the two-step Lax-Wendroff scheme. We investigate flows with parameter regimes which apply to in-

[1]Collaborators from the School of Mathematics and the School of Chemical Engineering at the University of Birmingham, with support from EPSRC and *Norsk Hydro*, were the first to present a model for this process. In addition further financial support was provided by Nestle and Prismo (who were mainly interested in developing models for liquid jets made of glue). To date only Newtonian fluids have been considered and since many industrial fluids (including those used for the production of fertilizers) are usually non-Newtonian, a better appreciation of rotating non-Newtonian fluids is needed.

[2]There are a number of commercial and environmental reasons why greater insight into the prilling process is necessary, these include the need to produce droplets with a specific chemical composition (due to regulations regarding fertilizer pellet composition) and a desire to eliminate or reduce wastage through satellite production.

dustrial prilling and our simulations allow us to calculate breakup lengths, droplet sizes and time to breakup. We further explore and discuss the relationship between certain fluid parameters and jet breakup characteristics.

In Chapter Six we re-examine the rotating liquid jet problem with the addition of surfactants to the free surface. Since the presence of surfactants reduce the surface tension of the liquid jet we find that depending upon the initial surfactant concentration and the importance of surfactant activity the dynamics of breakup and droplet formation are qualitatively different. In particular, the effects on satellite formation is noticeable.

We attempt to generalize and incorporate the ideas of the previous chapters in Chapter Seven by considering a surfactant laden jet emerging from a rotating orifice and falling under gravity. The effects of the acceleration due to gravity on the trajectory and linear instability of the jet are investigated further.

The next chapter looks at how insonification can be used at the nozzle to manipulate droplet sizes and breakup lengths. We consider insonification amplitudes which are an order of magnitude larger than the standard perturbation at the nozzle. We also attempt to numerically simulate breakup of non-Newtonian jets to multiple perturbations at the nozzle (thereby attempting to more closely simulate real life breakup dynamics where an infinite number of wave modes are excited at the nozzle).

In Chapter Nine and Ten we eliminate rotation from our investigations and consider the breakup of straight compound jets. Such two-fluid systems have numerous applications in their own right, especially in connection to encapsulated droplets in the fields of pharmaceutics and biotechnology, however, they can also be used to manipulate the dynamics of the inner liquid thread. We consider both an inviscid-inviscid and power law-power law system. In particular, we examine the formation of compound droplets with multiple cores and pay close attention to what factors lead to their formation.

The dynamics of liquid microjets (jets on the micron scale) are considered in more

detail in Chapter Eleven with some references to the latest research and practical applications which exploit such jets. In particular we examine closely the last stages of the topological transition which occurs when a fluid thread ruptures. The creation of *fresh* surface area as the topological transition point is reached allows us to use the theory of interface formation (which allows for a dynamic surface tension and therefore surface tension driven flows) and consider what, if any, differences appear between jets on the macroscopic scale and liquid microjets. We discuss the effects on the most unstable wavenumbers predicted by both theories and make some comparisons to molecular dynamic simulations.

The process of thermally heating a liquid thread at the orifice is examined in detail in Chapter Twelve with special attention paid to the effect on satellite droplet formation. Thermally modulating the free surface of a liquid thread is a technique which is already widely used in ink-jet printing but has particular importance to micro-fabrication in electronics and engineering. We investigate a number of heating 'patterns' at the nozzle including sinusoidal and pulsed heating. The effects of changing the frequency of heating is also considered. We incorporate the changing of viscosity with temperature into our model through an Arrhenius type equation. The effects of changing the thermal properties of the liquid are also examined.

Chapter Thirteen contains a brief summary of all the results we have obtained in the preceding chapters. We attempt to describe the salient features observed for the different techniques considered so far.

Finally, in Chapter Fourteen we look ahead at the future directions of this reserach. We consider a number of different direct extensions of the work presented in previous chapters along with some more novel yet related applications. Particular attention is placed upon techniques for the production of emulsions (or compound drops). We also discuss the technique of creating droplets using a T-shaped junction as well as the creation

of mono-disperse droplets through the process of flow focusing.

Chapter 2

A Brief History of Liquid Jets

2.1 Introduction.

Whether it be the formation of stars or the production of nuclear fuel, or even quite simply the dripping of a kitchen tap, the instability of a liquid jet is a universally recognized phenomenon which finds applications in a wide variety of industrial and scientific processes. Whilst there are many scenarios where the applications of the rupture of a liquid thread can be easily identified, like ink-jet printing for example, there are many more which are not so apparent. Take, for example, the targeted delivery of drugs to the site of a disease (Prausnitz (2001)) or the cooling of microchip components (Wang *et al.* (2004)) which on the surface might not appear to have much in common. However, if we delve a little deeper into the underlying physics we find that such processes are among only a few of the more recent applications which take advantage of the properties of a liquid jet. Although it is true that many traditional applications like ink-jet printing (where nearly 10 patents are registered around the world every day) and industrial prilling (where liquid jets are used to make small pellets) continue to remain popular in industry it is the growing success and maturing of microengineering which has captured the attention of scientists and engineers and has resulted in a number of exciting and innovative uses. Applications like

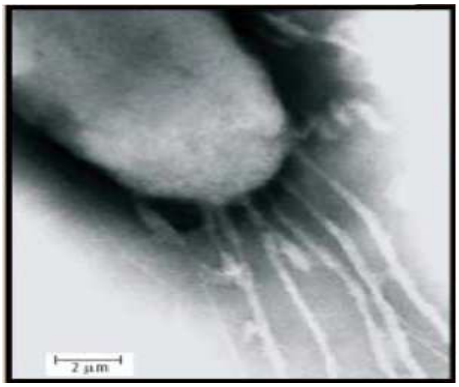

Figure 2.1: Myxobacteria can move at speeds of up to 10 μm a second by squirting out jets of slime from tiny nozzles placed on their bodies. Picture taken from *New Scientist*, April, 2006.

microchip fabrication and modern fuel injection devices are already in common use but more novel and emerging applications in this rapidly growing field include developments in biotechnology, where liquid jets are used to rupture cells, and pharmaceutics where microjets are used to deliver medicine intravenously (see Mortanto (2005) and Fletcher (2002)). Surprisingly, liquid jets are even important to the motion of tiny bacteria which can squirt out slime from tiny nozzles located on their bodies to move at speeds up to 10 μm a second (see Fig. 2.1). All in all, such widespread use of liquid jets, especially in the biochemical sciences where tailor-made fluids are common, provides new and subtle challenges not only in appreciating how different types of fluids behave in such applications but also necessitates a greater understanding of liquid jet dynamics.

The dynamics of liquid jets are a special case of *free surface* flows which elicit huge interest not only for their immense practical applications but also for the fundamental issues they raise about the structure and solutions of the Navier-Stokes equation itself. One such complication is that for a liquid jet to disintegrate it must undergo a topological change at rupture, usually changing from a long cylindrical thread into a series of droplets. This process involves infinitesimally small length scales and singularities of the equations of motion. Furthermore, such flows are made more complicated in comparison with other flow situations due to the presence of a unknown *a priori* boundary (i.e., the

free interface) for which the shape and position must be determined as part of the solution to the flow equations.

Free surfaces (unlike rigid surfaces) can respond to the flow and as such have the tendency to allow for the propagation of free surface waves (or disturbances) and therefore in essentially all such applications an understanding of the stability of a liquid jet to disturbances provides the greatest challenge. This is particularly true in situations where the ultimate aim is the disintegration of the jet and subsequent drop formation. Consequently in a vast majority of such cases the goal is one of two things; the desire for droplets of uniform size and/or the suppression of unwanted satellites. If we take ink-jet printing as an example, then in this case droplets produced from tiny nozzles are deposited onto paper to produce the final image. However the process of breakup near the nozzle may create satellite droplets which can reduce quality. Thus, in this case the complete suppression of satellites is highly desirable. Alternatively, with the advent of increasingly complex printing methods and the need for high quality output the production of uniform or monodisperse droplets can greatly improve image quality.

From everyday observations it is clear that a liquid jet is unable to retain its coherent structure for long periods. Instead the disintegration of a thread of liquid into droplets is a very familiar occurrence with most people observing such a phenomenon every time a kitchen tap is turned on. Nevertheless, this apparent universal behaviour of liquid jets was not recognized until 1849[1] by Plateau who also correctly identified the mechanism driving instability, namely surface tension. Surface tension plays an important role in many free surface flows and particularly so in liquid jets. To gain a better understanding of the tendency for a liquid jet to spontaneously decay into droplets, as well as providing a gentle introduction to the linear stability analysis in the next section, we shall begin by considering the simple interplay between surface tension and the radius of a column of

[1]Although well over a century earlier in 1686 the French scientist E. Mariotte wrote a book, wherein he mentioned the breakup of a liquid thread emerging from the bottom of a container.

fluid.

Firstly, surface tension (also known as interfacial tension) is inherently a physical property of an *interface* separating two bulk phases. Here the interface needs further clarification since despite its intuitive nature it is a term which is rather difficult to describe using continuum mechanics. It is normal in continuum mechanics for length scales of the order of intermolecular forces to be ignored in line with the *continuum hypothesis*. However, since the thickness of the interface is determined by the range of intermolecular forces, it must consequently be modelled as a mathematical surface (i.e.,, a surface of zero thickness). Now the physical properties of the interface must be two dimensional analogues of the physical properties of the bulk fluids and in turn this means that quantities like energy per unit volume become energy per unit area along the interface. Surface tension, which acts along the interface, originates due to asymmetry between intermolecular forces on either side of the *interfacial layer* (see Rowlinson & Widom (1982) and Israelachvili (1995) for discussions of the molecular origins of surface tension). For water, surface tension σ is usually expressed in the units of milli-Newton per meter (mN/m) and takes the value of ~ 70mN/m for a water-air interface. Most oils have a surface tension lower than that of water, typically $\sigma \sim 20$mN/m, however liquid metals like mercury can have surface tensions up to seven times higher than water.

The relationship between the surface tension of a column of liquid and its associated radius is summarized by the Young-Laplace equation which relates the pressure jump across an interface to its curvature. If we consider a cylindrical co-ordinate system (which is invariably the most popular choice when studying liquid jets), there will necessarily be two principle radii of curvature, one along the cross section of the jet and another along its axis. If we assume an initially homogenous column of fluid then the curvature is dominated by variations across the cross section of the jet.

We now imagine an infinitely long horizontal cylindrical thread of fluid having con-

stant radius in a state of rest. At any given time the surface of this liquid column is prone to tiny fluctuations in its surface properties like density, temperature or pressure. These fluctuations may cause the radius of the column to decrease slightly resulting in a small increase in pressure in the locality of the disturbance. Fluid located in the high pressure region of the liquid column has a tendency to migrate to low pressure regions thus further decreasing the radius of the column and ultimately increasing the pressure differential along the thread. This process culminates in breakup (also known as pinch-off) where the radius of the thread goes to zero. Since the coefficient for the curvature term in the Young-Laplace equation is the surface tension, it follows that the magnitude of the surface tension determines the growth of interfacial instability.

Another way of viewing this phenomenon is by considering the linear relationship between surface tension and surface energy. In this case, surface tension can be viewed as a measurement of the direct loss of the energy per unit area caused by molecules losing energy as they move from the bulk phase to the surface (see De Gennes *et al.* (2003)). Thus, surface tension requires the jet to *favour* any distortion which leads to an overall *reduction* in surface area of the liquid column. It is for this reason that any non-axisymmetric disturbances are damped out since they ultimately lead to an increase in the overall surface area (see Rayleigh (1879)).

2.2 Breakup and Linear Instability.

The local analysis of a liquid column considered above can be translated to the global behaviour of a liquid jet (if we ignore any effects due to the presence of a nozzle or orifice[2]). Thus, for a liquid jet the primary source of instability is surface tension and although in

[2]A stress singularity exists at the nozzle-jet interface due to the relaxation of the velocity from Poiseuille flow to laminar or plug flow. Depending upon the material parameters the resulting relaxation of the free surface may lead to a contraction or swelling. At any rate, the effects of the nozzle are only important a few jet diameters away from the nozzle (see Middleman (1993)). A fuller description of the relaxation process of the free surface, generalised to account for non-Newtonian fluids, is presented in Appendix C.

Figure 2.2: A schematic depicting the breakup of a liquid jet under the Rayleigh regime with subsequent main and satellite drop formation. Notice how breakup occurs many jet diameters away from the orifice (far left of picture) and droplet sizes are comparable to the jet radius.

the next section we shall go on to see that the breakup of a liquid jet is strongly non-linear, it turns out that despite this fact, for many situations involving the breakup of liquid jets, the breakup length (and consequently the time to breakup) along with the size of droplets produced can be estimated to a good degree of accuracy using a linear instability analysis about some equilibrium base state. Such an analysis can produce surprisingly accurate estimates for breakup lengths and drop sizes. Before moving on to take a closer look at linear instability we will, for completeness, begin by introducing the different regimes of breakup in the presence of a surrounding fluid (this will become more important when we consider two-fluid systems in Chapters 9 and 10).

The generation of droplets by dispersing one immiscible fluid (known as the dispersed phase) in another immiscible fluid (the continuous phase) through a nozzle, syringe or orifice occurs in many practical applications. Apart from changing the fluid parameters, the flow rate of the dispersed fluid can also be altered. It is found that, depending upon the values of this flow rate, there exist four distinct regimes of breakup. These regimes, in ascending order of flow rate, are known as the *Rayleigh* regime, the *first wind-induced* regime, the *second wind-induced* regime and the *atomization* regime. The first two of these regimes are characterised by breakup occurring many jet diameters away from the orifice (i.e. breakup is determined by long wavelength disturbances) as well as the size of droplets being of the order of the jet diameter[3] (see Fig. 2.2). The *second wind-induced* regime and the *atomization* regime generally tend to breakup very close to the orifice and

[3]The Rayleigh regime usually occurs at lower speeds than the first wind induced regime. Moreover, the Rayleigh regime produces droplets slightly larger than the diameter of the jet.

produce droplets much smaller than the diameter of the orifice. It is not uncommon in these regimes for the jet surface to become disrupted and for drops to emerge laterally.

In addition to taking account of the effects of a quiescent continuous phase, it can be shown that the dynamics of a liquid jet can also be greatly affected if the flow rate of the continuous phase is allowed to vary (so that a liquid jet emerges into a laminar flow field, say). In this case, droplets are formed at the orifice if the flow rate of the dispersed phase is low (droplets are peeled off as they leave the orifice). However, the breakup length is found to correlate with the viscosity and flow rate ratios between dispersed and continuous phases for higher flow rates (see Cramer *et al.* (2002)) in such cases. Modifying the flow of the continuous phase in conjunction with specially patterned surfaces is an interesting area of research which is still very much in its infancy and will provide fertile ground for further research (we will return to this problem in much more detail in Chapter Fourteen).

For most practical applications (especially those considered in this thesis) the flow rate out of the orifice is never high enough to consider any regime other than the *Rayleigh* regime. However, the fluid parameters of both the dispersed and continuous phase do differ in many applications and usually we distinguish three types of liquids; gaseous, low viscosity liquids or high viscosity liquids. A summary of works for different continuous and dispersed liquids is given in Fig. 2.3. The most important case that we will be concerned with is the case of a low viscosity liquid emerging into a gaseous environment so that the effects of the surrounding gas can be ignored. With this in mind, we begin with Rayleigh's classical analysis.

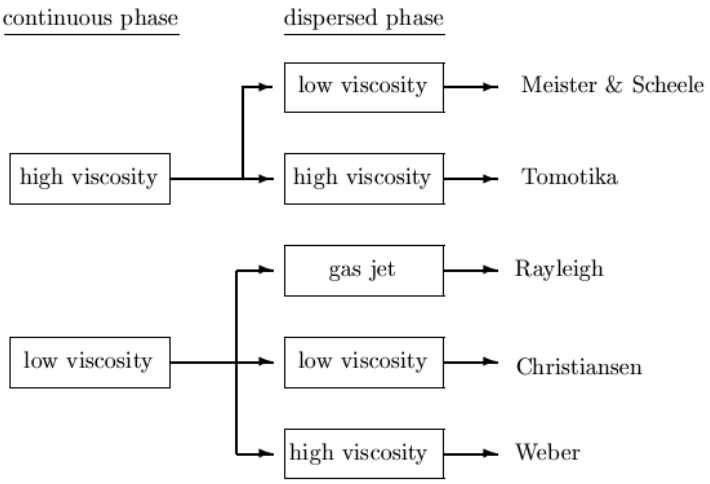

Figure 2.3: Linear stability analysis for liquids with different continuous and dispersed phases. These works constitute the first of their kind and form the foundation of later research.

2.2.1 Classical Inviscid Jets.

It was not until the late nineteenth century that Rayleigh[4](1879) considered the mathematical treatment of disturbances along an infinite *inviscid* column of liquid. Rayleigh was able to show that instability was caused by surface tension and that an optimal wavelength ($\lambda_{opt} \approx 4.5$ jet diameters) at which perturbations grew the fastest existed. Under the assumption that such *optimal* (also known as Rayleigh mode) disturbances effectively determined droplet sizes, Rayleigh was able to confirm and show favorable comparisons to the experimental observations of Savart (1833). Although Rayleigh's analysis has traditionally been the foundation of almost all liquid jet studies we will not attempt to reproduce his work here but instead, in this section, we shall mention some relevant results only. The interested reader is encouraged to refer to Rayleigh (1879) as well as a number of more modern references such as Yarin (1993), Middleman (1995) and Eggers (1997). For an approach which is different but nevertheless produces the same results the

[4]John William Strutt (Lord Rayleigh) (1842-1919) was a prolific contributor in the field of applied mathematics. He was awarded the Nobel Prize in physics for his discovery of the inert gas Argon after which he was made President of the Royal Society for three years between 1905 and 1908. His book the *Theory of Sound* established the field of acoustics and was written on a houseboat on the River Nile.

reader is referred to Anno (1977).

In Rayleigh's analysis a cylindrical jet, in a state of equilibrium, having radius $r = a$ (in cylindrical coordinates) is allowed to be perturbed by an initial disturbance which leads to the radius having the form $r = r_s$ where

$$r_s = a + \delta \cos(kz) \cos(n\theta), \tag{2.1}$$

and δ is a small initial disturbance, k is the wavenumber and n is an integer. Since a cylindrical coordinate system is being considered r, z and θ have their conventional interpretation. Using the standard equations of motion and assuming that disturbances can be written in the form $\exp(\omega t - i(kz - n\theta))$, where t is time, Rayleigh was able to arrive at his famous result. That

$$\omega^2 = \frac{\sigma(ka)}{\rho a^3}(1 - n^2 - (ka)^2)\frac{I_n{}'(ka)}{I_n(ka)}, \tag{2.2}$$

where σ is the surface tension and I_n is the nth modified order Bessel function. If disturbances are axisymmetric then $n = 0$ and we can use the recurrence formulae for Bessel functions,

$$I_{n-1}(x) + I_{n+1}(x) = \frac{2n}{x} I_n(x), \qquad I_n{}'(x) = \frac{1}{2}(I_{n-1}(x) + I_{n+1}(x))$$

to arrive at the dispersion relation for axisymmetric disturbances

$$\omega^2 = \frac{\sigma(ka)}{\rho a^3}(1 - (ka)^2)\frac{I_1(ka)}{I_0(ka)}. \tag{2.3}$$

If ω is plotted against ka for $ka < 1$ we find that the disturbance which grows most rapidly (i.e. has the largest value of ω) occurs for $ka = 0.696$ with a corresponding

growth rate $\omega = 0.34(\sigma/\rho a^3)^{\frac{1}{2}}$. For $ka > 1$, ω is imaginary and the disturbances do not grow with time t. In addition if $n \neq 0$, equation (2) gives that ω^2 is always negative and consequently non-axisymmetric disturbances do not grow with time. Thus for a inviscid (or nearly inviscid) liquid jet, issuing from a nozzle, we would expect that from all the tiny disturbances generated along the interface, the one having a non-dimensional wavenumber of $ka = 0.696$ (with a wavelength of about $9.02a$) to dominate and eventually lead to breakup. The characteristic time taken to breakup t_b can be estimated by inverting the growth rate so that $t_b = 2.94(\rho a^3/\sigma)^{\frac{1}{2}}$. Thus, a jet of water emerging from an orifice of radius 5mm (at modest flow rates so that the Reynolds number is sufficiently large as to consider the fluid as inviscid) will have a characteristic breakup time of about 0.12s.

2.2.2 Classical Viscous Jets.

The above analysis can be repeated with viscosity (Weber (1936)) to arrive at a similar characteristic equation, namely

$$\omega^2 + \frac{3\mu k^2}{\rho}\omega = \frac{\sigma k}{\rho a^2}(1 - (ka)^2)\frac{I_1{}'(ka)}{I_0(ka)}. \tag{2.4}$$

In this case the coefficient in front of ω is positive and will thus contribute in stabilizing or dampening disturbances. The disturbance which dominates and eventually leads to breakup is given by[5]

$$ka = 2^{-\frac{1}{2}}\left(1 + \frac{3\mu}{\sqrt{\rho\sigma a}}\right)^{-\frac{1}{2}},$$

which is better represented by introducing the non-dimensional *Ohnesorge* number $Oh = \mu/\sqrt{\rho\sigma a}$ (which is a measure of the relative importance of viscous forces to surface tension forces) so that we have

$$ka = (2(1 + 3Oh))^{-\frac{1}{2}}.$$

[5]This is really the long wavelength approximation of (2.4). It does however provide a very good approximation.

The observant reader will note that in the limit of $\mu \to 0$ the above equation gives $ka = 1/\sqrt{2} = 0.707$ which slightly overestimates the inviscid limit of $ka = 0.696$ although the growth rate corresponds perfectly. In general, we see that viscosity increases the wavelength of most unstable disturbances (leading to the production of larger droplets) and allows for more viscous jets to have smaller growth rates (and therefore longer breakup times). Both (2.3) and (2.4) provide good qualitative predictions for breakup lengths[6] and droplet sizes.

Tomotika (1935) extended Rayleigh's original analysis to account for the presence of an outside continuous phase and in particular he examined the case of a very viscous fluid encased within another very viscous fluid (i.e., Stokes flow in both fluids). His analysis highlighted the importance of viscosity and density ratios between the two fluids as well as the importance of the ratio of viscous forces to surface tension forces (characterised by the Ohnesorge number) on instability.

So far we have considered what is termed *temporal instability*, that is when considering disturbances, we have assumed they have the form $\exp(\omega t - i(kz - n\theta))$ where the wavenumber k is taken to be real. In this case, the growth rate ω is, in general, complex so that $\omega = \alpha + i\beta$ where α and $-\beta/k$ are known as the *temporal growth rate* and *wave speed* respectively. Normally we find that disturbances grow ($\alpha > 0$) while being convected along the jet ($\beta = kU$, where U is some typical jet velocity).

Keller *et al.* (1983) realised that for liquid jets emerging from a nozzle or orifice disturbances are not just simply created at $t = 0$ and then convected along the jet but instead can occur for later times as well. It therefore follows that disturbances grow spatially as well as temporally and the resulting analysis must now include a complex wavenumber $k = k_r + ik_i$ where k_i represents the spatial growth rate.

[6] An expression for the breakup length of a liquid jet using dimensionless analysis is presented in Appendix B.

2.3 The Non-Linear Dynamics of Breakup.

One may use linear stability analysis to show that a liquid jet should break uniformly along its axis with the size of droplets produced being roughly equal to the wavelength of the initial disturbance. However, the reality of such a result is plainly not true (see Chaudhary & Redekopp (1980*a*)) and instead breakup occurs non uniformly along the jet and a number of 'satellite' droplets are observed which are much smaller then their adjacent parent drops. An attempt to use higher order perturbation theory (Chaudhary & Maxworthy (1980*b* and 1980*c*)) does not replicate unequal droplet sizes. One reason why linear theory fails to predict satellite droplets is the discarding of the non-linear convective term (see Lin (2003)) in any linear analysis. It is this term can induce higher order harmonics despite the imposition of a pure harmonic disturbance at the orifice. More importantly, as breakup is approached the minimum radius goes to zero and the pressure diverges to infinity (i.e. a singularity is reached in finite time) and as such it is no surprise that linear theory breaks down failing even to give a qualitative description of pinch-off.

In order to capture non-linear behaviour near pinch-off, a full analysis of the Navier-Stokes equation with free boundary conditions is needed. Any analytical approach is virtually impossible and even a full numerical analysis of jet breakup is extremely difficult due to high resolutions needed in neck regions near the singularity. For this reason one dimensional models (which are reduced forms of the momentum equations which depend upon just *one* independent spatial variable, normally the variable along the axis of the jet) are popular although some 2D (Abraveneswaren *et al.* (2002)) and 3D (Moseler & Landman (2000)) simulations do exist of liquid jet breakup.

In order to arrive at one dimensional models we start by considering the Navier-Stokes equation in cylindrical coordinates with the assumption of axisymmetric flow. This leads

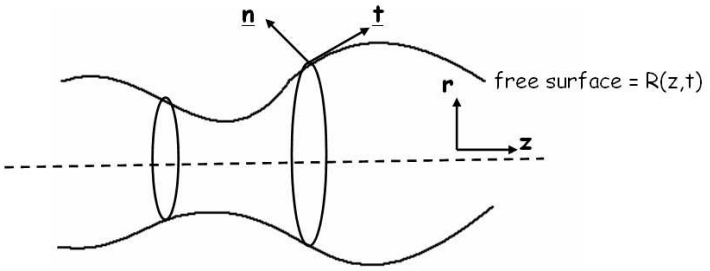

Figure 2.4: A diagram showing the geometry of a free surface in cylindrical co-ordinates. The dashed line represents the axis of symmetry $r = 0$.

to the momentum equation along the radial and axial directions complemented with the continuity equation;

$$\frac{\partial u_r}{\partial t} + u_r\frac{\partial u_r}{\partial r} + u_z\frac{\partial u_r}{\partial z} = -\frac{1}{\rho}\frac{\partial p}{\partial r} + \frac{\mu}{\rho}\left(\frac{\partial^2 u_r}{\partial r^2} + \frac{1}{r}\frac{\partial u_r}{\partial r} - \frac{u_r}{r^2} + \frac{\partial^2 u_r}{\partial z^2}\right), \tag{2.5}$$

$$\frac{\partial u_z}{\partial t} + u_r\frac{\partial u_z}{\partial r} + u_z\frac{\partial u_z}{\partial z} = -\frac{1}{\rho}\frac{\partial p}{\partial z} + \frac{\mu}{\rho}\left(\frac{\partial^2 u_z}{\partial r^2} + \frac{1}{r}\frac{\partial u_z}{\partial r} + \frac{\partial^2 u_z}{\partial z^2}\right), \tag{2.6}$$

$$\frac{\partial u_r}{\partial r} + \frac{\partial u_z}{\partial z} + \frac{u_r}{r} = 0, \tag{2.7}$$

where u_r and u_z are the radial and axial velocities respectively.

The boundary conditions (evaluated at the free surface) express the relationship between the pressure difference (which can be related to the mean curvature) across the free surface with the normal stress

$$\mathbf{n}\cdot\mathbf{\Pi}\cdot\mathbf{n} = \sigma\kappa, \tag{2.8}$$

where $\mathbf{\Pi}$ is the total stress tensor, κ is the mean mean curvature of the free surface (defined as $\boldsymbol{\nabla}\cdot\mathbf{n}$), σ is the isotropic surface tension and $\mathbf{n}$ is the unit normal vector to the free surface (which points from the liquid to the gas) as shown in Fig. 2.4. If the external fluid is a gas then the tangential stresses along the surface of the jet can be equated to zero

$$\mathbf{n}\cdot\mathbf{\Pi}\cdot\mathbf{t} = \mathbf{0}, \tag{2.9}$$

where $\mathbf{t}$ is the tangent vector to the free surface.

Finally, the kinematic condition at the free surface requires that a particle at the free surface to remain there so that

$$\frac{D(r - R(z,t))}{Dt} = 0, \quad \text{i.e. } \frac{\partial R}{\partial t} + u_z \frac{\partial R}{\partial z} = u_r \tag{2.10}$$

The above system of equations can be reduced if suitable asymptotic expansions for both the radial and axial velocity components are chosen. If we follow the example of Eggers (1993) we could expand the axial velocity in powers of r so that

$$u_z(z,r,t) = u_{z0}(z,t) + u_{z2}(z,t)r^2 + ...$$

If a similar expansion is made for the pressure and then substituted into the momentum equations and the continuity equation (this will give an expression for u_r in terms of the components of u_z see Eggers (1993)) together with the boundary conditions we arrive at a closed system of equations for u_{z0} (which we write as u from now on) and R, namely

$$\frac{\partial R^2}{\partial t} + \frac{\partial (R^2 u)}{\partial z} = 0 \tag{2.11}$$

$$\rho\left(\frac{\partial u}{\partial t} + u\frac{\partial u}{\partial z}\right) = -\sigma\frac{\partial}{\partial z}\left(\frac{1}{R_1} + \frac{1}{R_2}\right) + 3\mu\frac{\partial^2 u}{\partial z^2} \tag{2.12}$$

where R_1, R_2 are the principal radii of curvature. If we non-dimensionalize our variables so that

$$\overline{t} = \frac{t}{(\rho a^3/\sigma)^{\frac{1}{2}}}, \quad \overline{z} = \frac{z}{a}, \quad \overline{u} = \frac{u}{(\sigma/\rho a)^{\frac{1}{2}}}, \quad \overline{R} = \frac{R}{a}.$$

where a is the initial radius of the jet and ρ is the density of the liquid, then dropping overbars, the system in non-dimensional form is

$$\frac{\partial R^2}{\partial t} + \frac{\partial (R^2 u)}{\partial z} = 0 \tag{2.13}$$

$$\rho \left(\frac{\partial u}{\partial t} + u \frac{\partial u}{\partial z} \right) = -\frac{\partial}{\partial z} \left(\frac{1}{R_1} + \frac{1}{R_2} \right) + 3Oh \frac{\partial^2 u}{\partial z^2} \tag{2.14}$$

where Oh is the Ohnesorge number (which is a ratio of viscous forces to surface tension forces) given by $Oh = \mu/(\sigma a \rho)^{\frac{1}{2}}$.

The first numerical simulation of (2.13) and (2.14) was that of Lee (1974) who investigated the non uniform breakup of an *inviscid* liquid jet. He was able to calculate the profile of the jet at breakup and thus estimate main and satellite drop sizes. After pinch-off the fate of a satellite droplet can take one of three paths; it can either merge with the downstream or upstream main droplet (known as forward and rear merging respectively) or alternatively it can move along with the same velocity as the main droplets. A systematic analysis of different merging scenarios for satellite droplets is presented by Pimbley & Lee (1977). The analogous one dimensional viscous case has been investigated by Bousfield and Denn (1987) and Bousfield *et al.* (1990).

Eggers and Dupont (1994) investigated the breakup of a viscous liquid jet and the bifurcation of a drop suspended from an orifice using a one dimensional equation of motion. In particular, they were interested in the behaviour of singularities close to the fluid neck in the final stages of pinch-off. Simulations of drops of water suspended from an orifice were compared with the experimental photographs of Peregrine *et al.* (1990) with good agreement.

In order to illustrate and discuss some of the important fluid dynamics close to pinch-off we will use a method similar to Yarin (1993) to solve (2.13) and (2.14) (details of the numerical method are left till Chapter 5). Figure 2.5 shows the profiles of a Newtonian

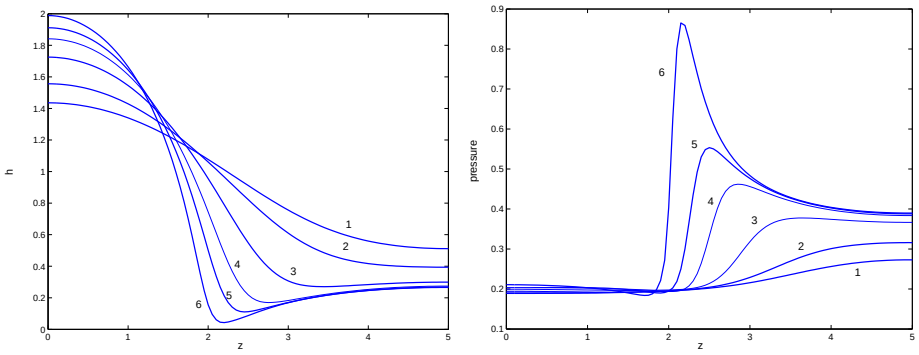

Figure 2.5: The solution of equations (2.13) and (2.14). The profiles of the jet radius close to the pinch off point is shown along with the corresponding pressure. The Ohnesorge number is chosen as 0.62. Profiles are shown for the non-dimensional times corresponding to 1, 2, 3, 4, 5, 6 are 30, 32, 34, 35, 35.5 and 36 respectively.

liquid jet at different times towards the latter stages of pinch-off along with the corresponding pressure. It can be seen that as the surface tension gets to work and causes the jet to contract the curvature increases (since the radius of the jet becomes smaller), this in turn causes the pressure (consistent with the Laplace-Young equation) within the jet to increase. The profiles shown in the figure are taken over half a wavelength and show the radius rapidly decreasing at at point (the pinch-off point) separating a drop on one side with a smaller ligament to the other side. In the locality of the region of pinch-off the pressure can be seen to increase which forces the liquid away from this region into the drop. The rate at which fluid leaves this region is proportional to the magnitude of the pressure and so the drop continues to grow until pinch-off takes place. A closer look at Fig. 2.5 reveals that the ligament connecting the drop stops contracting (while the drop continues to grow), this is in agreement with the experimental results of Goedde and Yuen (1969).

2.4 Experiments.

Experimental studies to investigate the phenomenon of breakup and drop formation in liquid jets generally fall into three categories; those which involve a liquid jet emerging

from a nozzle, a dripping faucet and that of a liquid bridge (where a portion of fluid is held between two moving solid plates). All these experiments have much in common and are essentially the same near the locality of the singularity, where the radius goes to zero and rupture occurs, however there exist certain qualitative differences between them.

The earliest known experimental investigation into liquid jets is that of Bidone (1823), who examined the fluid leaving the holes from the bottom of a container. Savart (1833) was the first to observe that the frequency of disturbances along liquid jets could be controlled by varying the frequency of perturbations applied at the orifice. Bidone's experiments and those of other nineteenth century researchers like Savart are remarkable for the accuracy with which observations were made when due consideration is given to the fact that most observations would inevitably have been confined to the human eye or by crude photographic techniques. In contrast, the success of modern photographic equipment to capture images microseconds apart and with resolutions on the micron scale has made experiments on liquid jets comparatively much easier. As such, there have been a number of modern studies.

Following on from Savart's observations regarding the control of disturbances along a liquid jet by modifying the frequency at the orifice, a number of authors have chosen to investigate the decay of a liquid jet using different methods to induce instability. Crane, Birch and McCormack (1964) studied jet instability by using an electrical vibrator to induce disturbances of different wavelengths. Donelly & Glaberson (1966) used a loudspeaker to do the same. They were also the first to measure the growth of surface waves as a function of time. The presence of non-sinusoidal disturbances in their experiments was attributed to higher order harmonics (as opposed to non-linear effects) induced by vibrations at the nozzle.

Goedde & Yuen (1969) introduced perturbations at the orifice using a number of different methods. Apart from the loudspeaker setup, Donelly & Glaberson also utilized an

electronically driven vibrator. Experiments were carried out using a short vertical nozzle (allowing the velocity profile to remain uniform on exit) and jet speeds were chosen small enough so that surrounding effects could be ignored and a laminar flow field could be assumed yet high enough so that gravity in experiments could be neglected. Measurements of the diameter of both swell regions (the region of onset of droplets) and neck regions were taken as functions of time. As breakup was approached the swell grew and neck diminished as expected but they found that the exponential growth rate for the swell and neck regions were not constant but the difference between them remained constant. Amongst their observations were that pinch-off did not occur at the center of neck regions but instead away towards the swell region. Later stages of breakup were observed to be dominated by non-linear effects and the neck portion of the jet actually stopped contracting while the swell portion became narrower and bigger.

Rutland & Jameson (1970) investigated the decay of a water jet emerging vertically downwards from a tube of length 30cm and diameter 4mm. The typical speed of the jet when leaving the nozzle varied between 2.5-3.5 m/s. To induce perturbations at the nozzle they used a 10W speaker (a similar method had been used by Donelly & Glaberson previously). The authors' main aim was to use non linear theory (they used the non-linear analysis of Yuen (1968)) to calculate the profile of waves on the jet at breakup and to use this to predict the volume (and size) of main and satellite droplets. In essence, the theory of Yuen (1968) allows for a non-sinusoidal wave profile at breakup while also ensuring that the volume of the jet

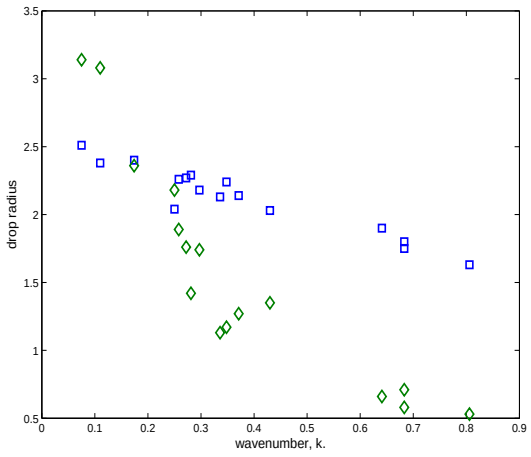

Figure 2.6: Data from Rutland & Jameson (1970) for main (□) and satellite (◊) water droplets. The radius is non-dimensioanlised with respect to the orifice radius

remains constant for higher order terms than the initial perturbation amplitude. Using this theory it is possible to calculate wave profiles at the time when the 'trough' meets the centreline of the jet and thus calculate sizes of main and satellite droplets. Rutland & Jameson (1970) found that in general there was good agreement between their experiments and the theory of Yuen (1968) however their experiments revealed satellite droplets through a range of wavenumbers contrary to the non-linear theory which does not predict satellite formation above wavenumbers of 0.7. Figure 2.6 shows some results from Rutland and Jameson (1970) for main and satellite droplets.

Exploiting high speed photographic techniques, Kowalewski (1996), using an experimental setup resembling that of Becker *et al.* (1991), examined the profile of a thin liquid neck joining droplets. Typical jet diameters were up to eighty times smaller (50-900μm) than those considered by Rutland & Jameson (1970) and typical breakup lengths were between 100-200 jet radii. Micro satellite droplets were observed along the necks. The minimum diameter of the jet before breakup was found to be $\sim$ 1 μm even when the viscosity was varied over several orders. The reasons behind this seemingly constant neck radius before breakup are still unknown, although the molecular simulations of Koplik & Banavar (1993) rule out the influence of molecular effects. Indeed, according to Koplik & Banavar (1993) the Navier-Stokes equations remain valid for length scales down to 100 $\mathring{A}$ (10nm) and time scale 10^{-10}s. The theory of interface formation (see Shikhmurzaev (2005)) attempts to provide one explanation for Kowalewski's experiments by introducing the idea of a *relaxation* time for the free surface. Under this theory, pinch-off is the combined result of capillary pressure (with varying surface tension) and flow-induced Marangoni effects. We will return to this issue, and consider this theory in much more detail, in a later chapter.

Experiments involving liquid bridges or hanging pendant droplets (dripping faucet) allow for a much more controlled investigation of the stability of a thread of liquid. Indeed,

such studies have created a large body of classical literature in the field of fluid mechanics starting from the early pioneering work of Tate (1864), Rayleigh (1899), Harkins and Brown (1919) and much more recently Shi *et al.* (1994). In particular it has been found that gravity can limit the length of a stable liquid bridge and, as such, there is growing interest in investigating the effects of the growth of single-crystal semiconductors in microgravity. As we have mentioned previously, the breakup of a liquid bridge or a hanging pendant droplet is qualitatively similar to the breakup of a liquid jet near the location of pinch-off; as such, we will not delve too deeply into this topic although the interested reader is referred to Middleman (1995) for a more detailed investigation of this topic. We will however mention here some of the most relevant liquid bridge studies which involve shear thinning liquids namely those of Yildirim & Basaran (2000) and Doshi *et al.* (2003).

2.5 Similarity Solutions.

Experiments like those of Haenlein (1931) and Kowalewski (1996) have shown that near the locality of pinch-off, the geometry of a liquid jet exhibits remarkable similarity. In general, we have a thin ligament connected to a (much larger) drop. This configuration at pinch-off remains similar even if certain initial conditions (e.g. the wavelength of disturbances) are varied. However experiments do show a marked difference when the viscosity of the fluid is altered.

These results suggest that while the flow in a liquid jet may be influenced by initial conditions away from breakup, near pinch-off the flow becomes increasingly dependent on internal fluid parameters (this was first recognised by Peregrine *et al.* (1990)). In general there are three fluid parameters which can affect the flow; the kinematic viscosity ν ($\mathrm{cm^2 s^{-1}}$), the surface tension σ ($\mathrm{gm\ s^{-2}}$) and the density ρ ($\mathrm{gm\ cm^{-3}}$). A simple dimensional analysis using these three parameters leads to the so called *natural* length

and time scales given by

$$l_\nu = \frac{\nu^2\rho}{\gamma} \quad \text{and} \quad t_\nu = \frac{\nu^3\rho^2}{\gamma^2}.$$

For water at room temperature (20°C) having viscosity 1.004×10^{-2} cm^{2}s^{-1} and with density 0.998 gm cm^{-3} and surface tension equal to 72.8 gm s^{-2}, we have a *natural* length scale of 1.38×10^{-6}m and time scale 1.91×10^{-10}s. The equivalent length scale for glycerol is 10^6 times greater and the time scale can be up to 10^9 times greater.

Thus, irrespective of whether the experiment involves a liquid jet emerging from an orifice or a dripping faucet, the motion near breakup will become independent of initial and boundary conditions. If the fluid is inviscid and irrotational then Keller and Miksis (1983) have shown that the height of an interface decays like 2/3 of the time remaining to breakup. This has been numerically verified by use of numerical simulations based on the boundary element method (BEM) of Day *et al.* (1998). Similarly, if the fluid under consideration is viscous then Eggers (1993) has shown that the minimum radius h_{min} and maximum velocity v_{max} of a liquid thread depends only upon the time Δt remaining from breakup, that is

$$h_{min} = 0.0304\frac{\gamma}{\mu}\Delta t \quad \text{and} \quad v_{max} = 3.07\left(\frac{\mu}{\rho}\right)^{\frac{1}{2}}(\Delta t)^{-\frac{1}{2}}.$$

Under this theory we would expect a thread of glycerol ($\mu = 0.672$kg m^{-1} s^{-1}, $\sigma = 0.0645$ gm s^{-2} and $\rho = 1248$ kg m^{-3}) at 0.01s before breakup to have a minimum radius h_{min} of 13.1μm and a maximum velocity v_{max} of 1.06m/s (see Eggers (1993)). The experiments of Kowalewski (1996) show good qualitative agreement with Eggers' findings for pre-breakup thinning of a liquid thread on scales down to the order of microns. However, after rupture, Eggers (1993) and Eggers and Dupont (1994) predict that the pressure and the axial velocity diverge to infinity (so that a singularity is reached in finite time) which does not correspond to the experiments of Kowalewski (1996). These unphysical

predictions for the pressure and velocity have been addressed by Shikhmurzaev (2005) with the introduction of the concept of interface formation into the process of thinning. Irrespective of whether the working fluid is viscous or inviscid, Lister and Stone (1998) have shown that the effects due to the dynamics of the surrounding medium (typically air) cannot be neglected once h_{min} reaches some finite minimum value.

Chapter 3

Non-Newtonian Fluids

3.1 Introduction

Fluids like water and air are Newtonian in the sense that the viscosity of such fluids will not change with any applied shear stress. Yet it is clear that there are many fluids which do not fall into this category. Consider for example the difficulty of extracting tomato ketchup from a bottle, yet when a force is applied to the end of the bottle the ketchup flows freely (usually too freely!). Or the behaviour of some fluids (like silly putty) which seem to have the ability to behave like a solid and a liquid. Clearly such fluids motivate models which are different to those that we are familiar with.

The importance of such fluids cannot be overestimated, especially, as is evident from everyday experience, they are increasingly popular in the biological and chemical sciences[1]. Yet unlike Newtonian fluids, it was not until the early twentieth century that non- Newtonian fluids attracted the attention of a number of industrialists who were concerned mainly with finding suitable models to describe the behaviour of fluids like paint solutions, ceramics and lubricants. Initially, the study of such fluids was the preserve of chemical engineers (the first volume of AIChE Journal contained an article by Metzner

[1]just consider the number of new cosmetic and pharmaceutical products which are constantly appearing on the market.

& Reed (1955) on the correlations for turbulent flow of non-Newtonian fluids); it has now grown to include a wide variety of specialists ranging from applied mathematicians, physicists (who will be more familiar with the term complex fluids) and engineers of all fields.

The science of appreciating how different materials respond to the effects of strain and stress is known as *rheology*. Since new materials are being introduced in all areas of industry, the study of rheology is a very important field. As an example, take the manufacture of certain types of honey, even if the product itself tastes great, the texture and consistency might be undesirable and as a result the market potential of this product will suffer. In such cases rheological testing (based on a good rheological model) can be the difference between a successful product and one that is not.

3.2 Rheological Equations of State.

3.2.1 Newtonian Fluids

If we are to understand non-Newtonian fluids we must first appreciate what makes a liquid *Newtonian*. To do this we need to go back to the very basics behind the equations of motion. Let us start with the conservation equations (conservation of mass and linear momentum), so that we end up with the familiar Navier-Stokes equation and the continuity equation,

$$\rho\frac{D\boldsymbol{u}}{Dt} = -\nabla p + \mu\nabla\cdot\boldsymbol{\tau} + \rho\mathbf{g} \tag{3.1}$$

$$\nabla\cdot\boldsymbol{u} = 0. \tag{3.2}$$

where $\boldsymbol{u}$ is the velocity vector, $\boldsymbol{\tau}$ is the stress tensor, $\boldsymbol{g}$ is the external body force, p is the isotropic pressure, ρ is density and μ is the dynamic viscosity. If the flow happens to be isothermal (so that conservation of energy is not important), we will have four equations in ten unknowns (three velocity, one pressure and six independent stress components).

If we desire a mathematically well posed problem we require six extra equations. This is the primary role of the constitutive equation[2], or *rheological equation of state*, which provides information regarding the relationship between the stresses and kinematics that exist within the fluid. For a Newtonian fluid the constitutive equation is given by

$$\boldsymbol{\tau} = \mu(\nabla \boldsymbol{u} + (\nabla \boldsymbol{u})^{\mathrm{T}}) + (\frac{2}{3}\mu - \kappa)(\nabla \cdot \boldsymbol{u})\mathbf{I}, \tag{3.3}$$

where $\mathbf{I}$ is the the identity tensor, $\nabla \boldsymbol{u}$ is the velocity gradient tensor the transpose of which is $(\nabla \boldsymbol{u})^{\mathrm{T}}$. In addition to the dynamic viscosity μ, the above equation also includes the dilatational viscosity κ, which although important in some situations like the fluid mechanics of liquids with gas bubbles, is usually ignored since for incompressible fluids the divergence of the velocity field is zero. Equations (3.1)-(3.3) form a consistent set of equations with which to describe the flow of any *Newtonian* fluid. If the fluid is incompressible then (3.3) simplifies to

$$\boldsymbol{\tau} = \mu(\nabla \boldsymbol{u} + (\nabla \boldsymbol{u})^{\mathrm{T}}) = \mu\boldsymbol{\gamma} \tag{3.4}$$

where $\boldsymbol{\gamma}$ is the rate of strain tensor[3]. The stress tensor is therefore proportional to the rate of strain tensor.

[2]Constitutive equations of state must satisfy a number of conditions in order to be acceptable as an equation relating stress to strain. The first is that the equation be *coordinate invariant*, secondly that it have *material objectivity* (so that the stress be independent of the motion of the observer) and lastly that it have a *fading memory* so that the recent history of the fluid dominates the equation over past history (see also Pozrikidis (1997)). There are a number of other conditions which more complicated non-Newtonian fluids must obey but such conditions are beyond the scope of the present work.

[3]We have chosen here to express the rate of strain tensor as $\boldsymbol{\gamma} = \nabla \boldsymbol{u} + (\nabla \boldsymbol{u})^{\mathrm{T}}$. This is the same form used by a number of authors (see for example Morrison (2001) and Lin (2003)). However in other works (e.g. Batchelor (1967)) it is common to include a factor of $\frac{1}{2}$. In general this does not make much difference since the factor of $\frac{1}{2}$ can be incorporated into the dynamic viscosity μ.

3.2.2 Non-Newtonian Fluids.

We are now in a position to consider a more general class of fluids, namely non-Newtonian fluids. Such fluids can be defined quite simply as fluids which do not obey (3.3).

There are two major differences in the modelling of non-Newtonian liquids in comparison with Newtonian liquids, these are

1. Non-Newtonian fluids in general do not have constant viscosity. This is unlike Newtonian fluids where the dynamic and dilatational viscosities may depend on temperature and pressure but not on velocity gradients.

2. The relaxation times associated with non-Newtonian fluids allows the fluid to respond to the flow with a corresponding time delay. These effects are important for flows which have viscoelastic effects.

In general, non-Newtonian fluids can be divided into two categories; those fluids which are inelastic (sometimes called generalized Newtonian fluids) and those that possess elastic properties, i.e., viscoelastic fluids. Elastic fluids or viscoelastic fluids are time dependent which greatly complicates their behaviour.

As perhaps can be gathered from the introduction to this section, non-Newtonian fluids and the constitutive equations which model them are as diverse as the number of such fluids. Since we will primarily be concerned with inelastic non-Newtonian fluids, especially, those with varying viscosities we will mention in this section a few of the more popular models used to model them. We will however begin by briefly mentioning typical models for viscoelastic liquids due to the growing body of literature on viscoelastic jets as well as the similarity between viscoelastic liquid jets and inelastic liquid jets.

3.2.3 The Maxwell Model.

In order to understand viscoelasticity we must first familiarise ourselves with the concept of elasticity. Most of us are familiar with the basic premise of Hooke's[4] Law which states that the force experienced by an elastic body is proportional to the extension the body experiences. We can write this principle in a similar form to the expression for Newton's law of viscosity as

$$\boldsymbol{\tau} = G(\nabla \boldsymbol{w} + (\nabla \boldsymbol{w})^{\mathrm{T}}) = G\boldsymbol{\gamma} \tag{3.5}$$

where G is the elastic modulus and $\boldsymbol{w}$ represents the displacement vector. The strain tensor here is written as $\boldsymbol{\gamma}$. We should note that Hooke's Law is valid only for very small displacement gradients $\nabla \boldsymbol{w}$.

The Maxwell[5] model is the simplest model (see for example Bird *et al.* (2002), Bird & Armstrong (1987) and Morrison (2001)) which describes a fluid which is both viscous and elastic (hence visco-elastic) through the constitutive equation

$$\boldsymbol{\tau} + \lambda \frac{\partial \boldsymbol{\tau}}{\partial t} = \eta \boldsymbol{\gamma}. \tag{3.6}$$

Here λ is the relaxation time and η is the zero shear viscosity. We see that if $\boldsymbol{\tau}$ is time independent or if λ is very small (for a Newtonian fluid we can consider $\lambda = 0$, i.e. the fluid 'relaxes' instantly) we have the constitutive equation for a Newtonian fluid. The mechanical analogue for a Maxwell fluid in the one dimensional case is shown in Fig. 3.1.

[4]Robert Hooke (1635-1703) was a contemporary of Isaac Newton and Christiaan Huygens. He served as a Laboratory assistant to Robert Boyle (of Boyle's Law). As well as his contributions to science, Hooke helped design a number of prominent buildings with his colleague Christopher Wren after the destruction of most of London in the fire of 1666.

[5]James Clerk Maxwell (1831-1879) is famous for his contributions to the field of electromagnetism and the kinetic theory of gases. Amongst his less well known ideas was that the rings of Saturn were made of small individual particles.

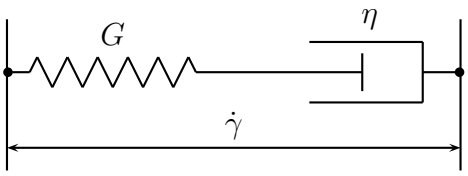

Figure 3.1: Diagram of a mechanical analogy to the Maxwellian fluid model. A dashpot and a spring are connected in series.

3.2.4 Jeffrey's Model.

A better model for viscoelastic fluids is formed by including a time derivative for the shear rate in the Maxwell model. This results in the Jeffrey's Model also known as the Oldroyd[6] fluid model (Bird *et al.* (2002) and Morrison (2001)). This model is similar to the Maxwell model but has another constant λ_r known as the *retardation* constant, which includes the effects of the rate of change in the rate of strain. The constitutive equation for such a fluid is given by

$$\boldsymbol{\tau} + \lambda \frac{\partial \boldsymbol{\tau}}{\partial t} = \eta \left(\boldsymbol{\gamma} + \lambda_r \frac{\partial \boldsymbol{\gamma}}{\partial t} \right). \tag{3.7}$$

3.2.5 Inelastic Fluids: Power-Law Model.

The Power-Law model is the simplest and most common inelastic non-Newtonian fluid. This is probably the most widely used model in most engineering circles due to its simplicity and wide applicability. The Power-Law model is a special case of a generalized Newtonian fluid which has the property that

$$\boldsymbol{\tau} = \eta(\nabla \boldsymbol{u} + (\nabla \boldsymbol{u})^{\mathrm{T}}) = \eta \boldsymbol{\gamma} \tag{3.8}$$

[6]James Gardner Oldroyd (1921-1982) was a professor at the University of Liverpool. He made a number of contributions to the field of continuum mechanics including his method in constructing suitable constitutive equations.

Power Law Fluids	α	$m\ (Pa \cdot s^{\alpha})$
fruit concentrate	0.7	2
molten chocolate	0.5	50
sour milk	0.3	3
tomato paste	0.2	70
grease	0.1	1000
1.0 % polyethylene	0.53	1
2.0 % hydroxyethylcellulose	0.19	94

Table 3.1: A table to show the properties of some common household and industrial fluids which can be considered as non-Newtonian (power law) fluids.

where the apparent (effective) viscosity η now replaces the dynamic viscosity μ for Newtonian liquids and is a function of the shear rate $\dot{\gamma}$ such that

$$\eta = m\dot{\gamma}^{\alpha-1}. \tag{3.9}$$

The shear rate $\dot{\gamma}$ is given by the second invariant of the rate of strain tensor,

$$\dot{\gamma} = \sqrt{\frac{\boldsymbol{\gamma} : \boldsymbol{\gamma}}{2}}. \tag{3.10}$$

In the above expressions the *flow index number* α is dimensionless and the *fluid consistency number* m has dimensions of $Pa \cdot s^{\alpha}$, both of which are found experimentally. Here Pa is Pascals, and s is seconds. Fluids which follow such a model are termed *shear thinning* or *shear thickening* depending on whether α is less than or greater than unity. In the special case where $\alpha = 1$, we have $m = \mu$ and the Newtonian fluid is recovered. Hence m is a measure of the relative viscosity of the fluid, with α measuring how 'non-Newtonian' the fluid is. The Power Law model is unable to describe shear thinning fluids at low shear rates or shear thickening fluids at high shear rates. Since in the first case the Power Law model gives an infinite viscosity for zero shear rates and in the second case zero viscosity for zero shear rates, both such scenarios are clearly unrealistic. However many real fluids

such as liquid fertilizer, paint solution and molten polymers, as well as many household fluids like shampoo and ketchup can be described adequately by a power law model. A few examples of some of the household and industrial fluids which can be considered to be Power Law are shown in Table 3.1.

3.2.6 Carreau Model.

A better model which avoids some of the failings of the Power Law model is the *Carreau Model* (see Carreau *et al.* (1979)). This model takes into account the limiting values of the apparent viscosity. In this case the apparent viscosity is given by

$$\eta = \eta_0[(1-\lambda)(1+(h\dot{\gamma})^2)^{\frac{n-1}{2}} + \lambda],$$

where h is some time constant and $\lambda\eta_0$ is the dimensionless infinite shear viscosity and η_0 is the zero shear rate viscosity. The power law constant here referred to as n is defined to be less than or equal to one and so the Carreau model only takes account of shear thinning properties of a liquid. The limiting values of the viscosity when the shear rate approaches zero and infinity respectively are given by

$$\lim_{\dot{\gamma}\to 0}\eta = \eta_0 \quad \text{and} \quad \lim_{\dot{\gamma}\to\infty}\eta = \lambda\eta_0.$$

3.2.7 Non-Newtonian Liquid Jets.

Linear stability analysis on viscoelastic jets shows that they are less stable than their Newtonian counterparts with the same zero shear viscosity (Middleman (1965)). An increase in the growth of axisymmetric disturbances in viscoelastic jets were shown by Goldin *et al* (1969). In the same paper, the first so called 'beads-on-string' phenomenon was observed. In this case, small droplets are connected by thin cylindrical ligaments several orders in magnitude smaller than the drops. It is found that capillary pressure drives the thinning

process whilst viscous and elastic forces oppose it. The slenderness of the filament means that a one dimensional approximation is sufficient in capturing the main dynamics within the system (see Li & Fontelos (2003) and Fontelos & Li (2004)). Also for highly viscous liquids the effects of inertia may be neglected. Classen *et al.* (2005) and earlier works show that there exists an intermediate region where the filament is being stretched at a constant rate but is thinning exponentially. In this situation, inertial, viscous and gravity forces are negligible and the elastic and capillary forces balance each other. Interestingly Li & Fontelos (2003) have simulated viscoelastic jets to show a number of drop dynamics near pinch-off, including drop migration, drop oscillation and drop merging which are not seen for Newtonian jets.

Power law liquid jets have been numerically investigated by Yarin (1993) to reveal the so called 'sausage' shaped droplets for shear thinning liquids and large spherical droplets resembling the 'beads-on-string' setup for shear thickening liquids. Teng *et al* (1994) considered the size of droplets produced for power law liquids in a Newtonian medium and vice versa.

The stability of non-Newtonian fluids with power law rheology has already been investigated for a diverse range of flows. These include flow down an inclined plane (Hwang *et al.* (1994) and Balmforth *et al.* (2003)), between concentric cylinders (Coronado-Matutti *et al.* (2004)) as well as gravity driven shear flows (Berezin *et al.* (1998)). A simulation of the flow between parallel plates and reentrant flows around corners for a power law fluid using the Lattice Boltzmann method has been investigated by Gabbenelli *et al.* (2005).

Chapter 4

Spiralling Liquid Jets: Linear Case

4.1 Introduction

In chapter 2 we examined the instability of straight liquid jets. Although straight liquid jets are more tractable, due to for instance the ability to use a cylindrical coordinate system to model them, there are many practical situations where jets become curved. A liquid jet may be curved due to a number of reasons including the influence of wind or gravity but more commonly, as is the case in industrial prilling, due to the rotation of the container from which it emerges. There are a number of important works on curved liquid jets and sheets, these include Tuck (1976), Vanden-Broeck & Keller (1982), Entov & Yarin (1984), Dias & Vanden-Broeck (1990), Yarin (1993) and Cummings and Howell (1999).

Curved liquid jets are important to the industrial prilling process which is a quick and relatively cheap technique used for the production of small spherical pellets. In this process, a specially perforated large cylindrical drum rotates about its axis. Molten liquid is pumped into the drum, and long curved jets are produced from the holes in the surface of the drum which break up due to centrifugal and capillary instabilities. Break up leads to the production of droplets, which subsequently solidify, and form pellets. This process

is widely used in industry for the manufacture of fertilizers, magnesium and aluminium pellets (see Andersen & Yttri (1997) and Ornek *et al.* (2000)). In recent times more novel applications of the prilling process, including microencapsulation for drug delivery (Dumas *et al.* (1992), Sakai & Hoshino (1980), Del Gaudio & Colombo (2005)) are becoming increasingly common.

The industrial prilling process is important to many companies, including *Norsk Hydro*, a leading Norwegian manufacturer of fertilizer pellets. For such companies understanding the prilling process is vital in delivering a high quality product and minimizing costs. With support from *Norsk Hydro* the School of Mathematics and the School of Chemical Engineering at the University of Birmingham began, for the first time, to mathematically as well as experimentally investigate the prilling process.

4.1.1 Experiments With Spiralling Jets: Newtonian.

As a first attempt a small can was used to simulate the prilling process and work was carried out in the Applied Mathematics Laboratory. The experimental apparatus used was a cylindrical can of diameter 0.085m and height 0.115m. Two different orifice diameters of 0.001m and 0.003m were considered in experiments. The lost liquid from the can was replenished using a peristaltic pump (Waltson-Mason 505s). The trajectory was captured using a high speed digital camera with time resolution of 100 μs and spatial resolutions of 100 μm were obtained by the use of the digital imaging software Image-Pro Express. Unlike the experiments of Rutland & Jameson (1970), the velocity of the liquid jet emerging from the orifice was not calculated directly and instead the volume of liquid collected over one minute was divided by the cross-sectional area to estimate the jet velocity at the orifice. Photographs from one such experiment using water as the working fluid ($\mu = 0.001$ Pa s at 20°C) and varying the rotation are shown in Fig. 4.1. Both primary droplets (formed by capillary pinch-off) and satellite droplets (formed in-

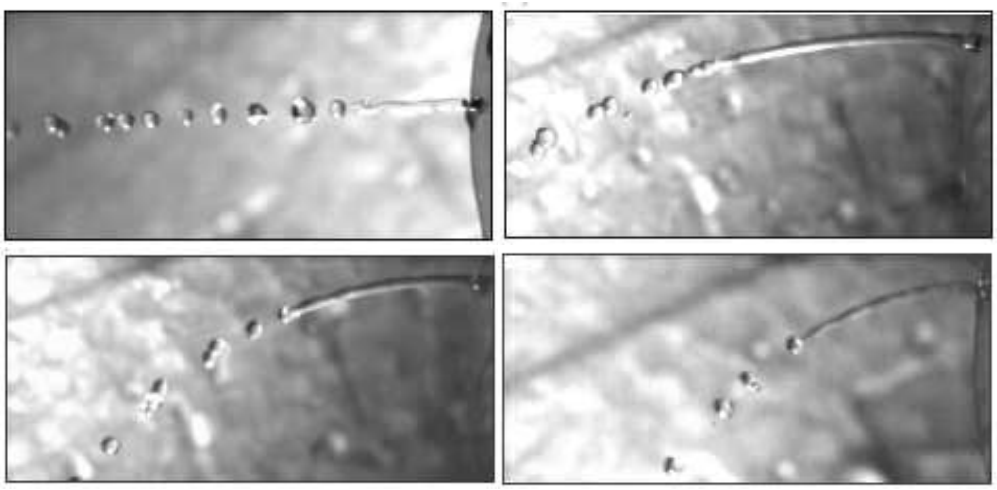

Figure 4.1: Experimental photos of a spiralling liquid jet for different rotation rates. The fluid here is Newtonian and the rotation rates from top to bottom and left to right are 0rpm, 50rpm, 100rpm and 200rpm respectively.

between primary droplets from fragments of fluid created by the break off of the primary drop) are visible. In general, the coherent portion of the jet becomes longer as the rotation rate is increased (this can be observed in the first two frames).

A mathematical formulation of this problem for an inviscid fluid was introduced and investigated by Wallwork *et al.* (2002b). The inclusion of the effects of gravity and Newtonian viscosity were investigated by Decent *et al.* (2002, 2007*a*) who used a temporal and spatial instability analysis to determine breakup lengths and droplet sizes. Nonlinear effects have also been considered by Părău *et al.* (2006, 2007) and Wong *et al* (2004). Experimental studies by Wong *et al.* (2004) show a good agreement with theory and reveal four different modes of break up depending on jet exit conditions (see Table 4.1 and Fig. 4.2). In that paper, it is found that of all the parameters studied, liquid viscosity has the strongest influence on the jet break up length and the dynamics of jet break up. Since many industrial fluids used in prilling are not Newtonian, and therefore likely to have varying viscosities, a better understanding of non-Newtonian effects on break up and droplet formation is needed.

Mode	breakup and droplet characteristics	$\sim$ We	$\sim \mathcal{R}e$
M1	rapid formation of main drops, few or no satellites, surface disturbances convected downstream	$4 < We < 30$	$50 < \mathcal{R}e < 10^4$
M2	short wavelength disturbances observed, satellites are formed in between droplets,	$4 < We < 9$	$1 < \mathcal{R}e < 50$
M3	long wavelength disturbances observed, jet breakup occurs simultaneously along the jet	$9 < We < 30$	$1 < \mathcal{R}e < 50$
M4	nonlinear disintegration, shattering of jet into droplets, bending of centreline	$1 < We < 4$	$1 < \mathcal{R}e < 20$

Table 4.1: A description of the different breakup modes for a spiralling liquid jet along with the approximate range of Reynolds and Weber numbers (which are a measure of the relative importance of inertia and viscosity and inertia and surface tension respectively). Note how Mode 4 (which is quite uncommon in experiments) is produced only for very viscous jets.

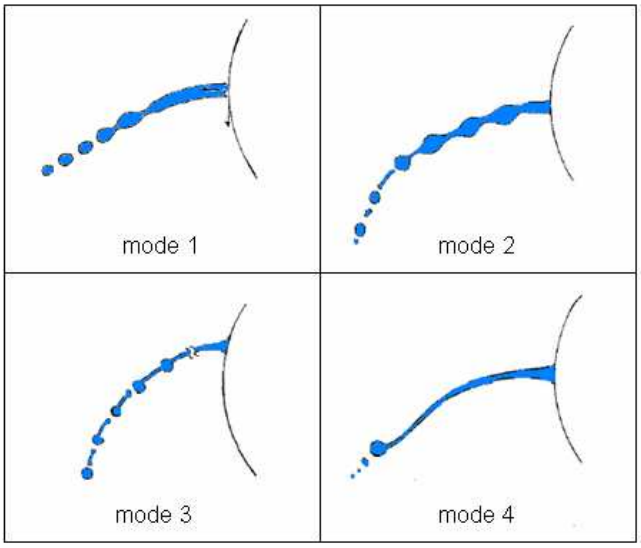

Figure 4.2: Sketches of the different modes of breakup observed for rotating liquid jets. Information about the parameter regimes required to observe such modes are given in Table 4.1

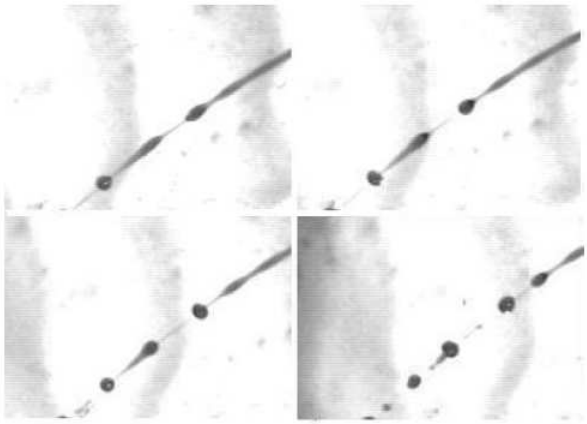

Figure 4.3: Experimental image of pendant drop formation in rotating shear thinning jets. We = 16.06, $\mathcal{R}b$ = 1.9049, Oh = 0.0220, $\mathcal{R}e$ = 181.98, ρ = 1025.05 Kg m^{-}3, k = 0.01197 Pa s, α = 0.920. See Hawkins *et al.* (2007) for more details.

4.1.2 Experiments With Spiralling Jets: non-Newtonian.

An experimental investigation of rotating shear thinning liquid jets is now the subject of current work (see Hawkins *et al.* (2007)). We show drop formation and satellite drop formation for rotating shear thinning liquid jets in Fig. 4.3 and 4.4. Although these experiments are in their early stages a number of interesting features like shattering of ligaments between droplets have already been observed.

4.2 Problem Formulation

To model the prilling process we consider a large cylindrical container having radius s_0 and rotating with angular velocity Ω along its axis of symmetry. A small orifice is placed at the side of the container having radius a which is considered small in relation to the radius of the container.

We examine the problem by considering a coordinate system (x, y, z) which rotates with the container, having an origin on the axis of the container and with the position of the centre of the orifice at $(s_0, 0, y_0)$ (see Fig. 4.5). The effects of gravity on the jet can be neglected if the centripetal acceleration of the jet $s_0\Omega^2$ is much greater than the

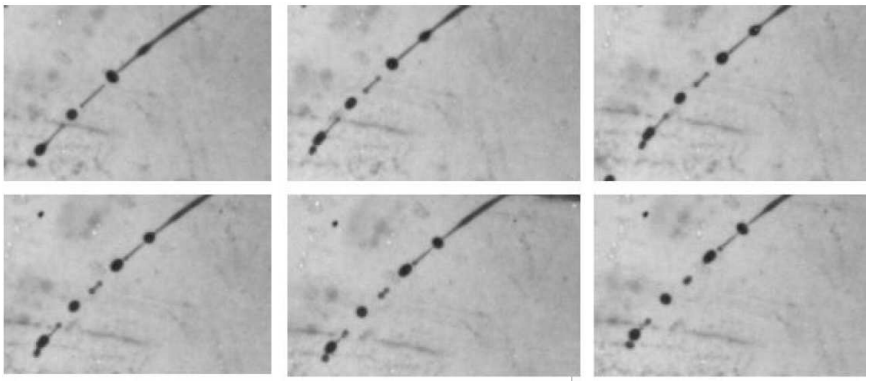

Figure 4.4: Satellite droplets are formed by contraction of the ligands between the primary droplets. There is also an example of rear merging here, where the satellite droplet does not break away from the ligand but instead contracts and merges with the satellite droplet from behind. Here $We = 5.37$, $\mathcal{R}b = 0.552$, $Oh = 0.0229$, $\mathcal{R}e = 101.00$, $\rho = 1025.05$ Kg m-3, k = 0.01197 Pa s, $\alpha = 0.920$. See Hawkins *et al.* (2007) for more details.

acceleration due to gravity g, as is the case with industrial prilling. Then the jet moves solely in the $x-z$-plane and thus we can describe the centreline of the jet by coordinates $(X(s,t), 0, Z(s,t))$, where s is the arclength along the centreline of the jet, measured from the orifice, and t is time.

4.2.1 Spiralling Jet Co-ordinate System

The rotation of the container causes the jet to curve on leaving the orifice and any analysis of the jet in the rotating (x, y, z) coordinate system becomes cumbersome. We therefore introduce a coordinate system previously used by Wallwork (2002a) which is similar to the approach adopted by Ribe (2004) and Entov & Yarin (1984), where we have one coordinate lying along the centreline of the jet corresponding to the arc length s of the jet, with the remaining coordinates as the plane polar coordinates n[1], ϕ (radial and azimuthal) in any cross section of the jet. The associated unit vectors are represented by $\mathbf{e_s}$, $\mathbf{e_n}$ and $\mathbf{e}_\phi$ respectively and their derivation is as follows (see Fig. 4.5). Let us write

[1]We do not use r here since we wish to differentiate between the standard cylindrical coordinate system and the present curved cylindrical system.

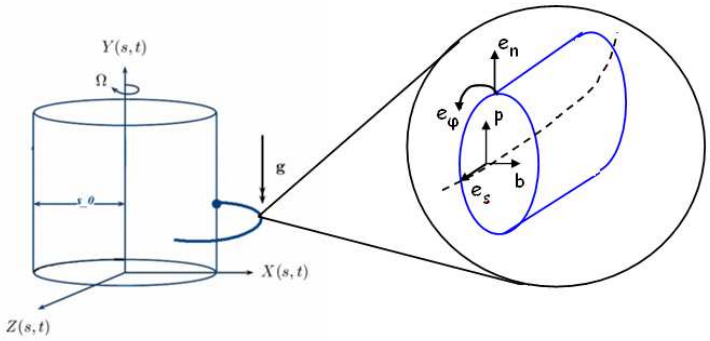

Figure 4.5: A schematic of the prilling system and a segment of the spiralling co-ordinate system showing the orthogonal unit vectors. The jet is assumed to lie in the x-z plane for high rotation rates.

the centreline as

$$\mathbf{r}_c = X_i \boldsymbol{e_i}$$

where

$$\boldsymbol{e_1} = \mathbf{i}, \;\; \boldsymbol{e_2} = \mathbf{j}, \;\; \boldsymbol{e_3} = \mathbf{k},$$

$$X_1 = X, \;\; X_2 = Y \;\text{ and }\; X_3 = Z$$

Now, let $\boldsymbol{e_s}$ be a unit vector along the centreline of the jet. We define a *principal normal* vector $\boldsymbol{p}$ as

$$\boldsymbol{p} = \frac{\partial \boldsymbol{e_s}}{\partial s} \cdot \left| \frac{\partial \boldsymbol{e_s}}{\partial s} \right|^{-1}$$

and another vector $\boldsymbol{b}$ (also lying in a cross section of the jet) by

$$\boldsymbol{b} = \boldsymbol{p} \times \boldsymbol{e_s}.$$

Since $\boldsymbol{e_s} = \frac{\partial X_i}{\partial s} \boldsymbol{e_i}$ ($\boldsymbol{e_s}$ here is a unit vector due to the arc length condition $\left(\frac{\partial X_i}{\partial s}\right)^2 = 1$) we see that

$$\boldsymbol{p} = \frac{\partial^2 X_i}{\partial s^2} \cdot \left| \frac{\partial^2 X_i}{\partial s^2} \right|^{-1} \boldsymbol{e_i}$$

and

$$\boldsymbol{b} = \varepsilon_{ijk} \frac{\partial^2 X_j}{\partial s^2} \cdot \left| \frac{\partial^2 X_j}{\partial s^2} \right|^{-1} \cdot \frac{\partial X_k}{\partial s} \boldsymbol{e_i}.$$

Thus we are able to write our orthogonal set of unit vectors as

$$\boldsymbol{e_s} = \frac{\partial X_i}{\partial s} \boldsymbol{e_i} \tag{4.1}$$

$$\boldsymbol{e_n} = \left| \frac{\partial^2 X_l}{\partial s^2} \right|^{-1} \left(\cos\phi \frac{\partial^2 X_i}{\partial s^2} + \varepsilon_{ijk} \sin\phi \frac{\partial^2 X_j}{\partial s^2} \cdot \frac{\partial X_k}{\partial s} \right) \boldsymbol{e_i} \tag{4.2}$$

$$\boldsymbol{e_\phi} = \left| \frac{\partial^2 X_l}{\partial s^2} \right|^{-1} \left(-\sin\phi \frac{\partial^2 X_i}{\partial s^2} + \varepsilon_{ijk} \cos\phi \frac{\partial^2 X_j}{\partial s^2} \cdot \frac{\partial X_k}{\partial s} \right) \boldsymbol{e_i} \tag{4.3}$$

We note that these vectors do indeed form an orthogonal set of unit vectors since

$$\frac{\partial^2 X_i}{\partial s^2} \cdot \frac{\partial X_i}{\partial s} = 0$$

To describe the flow we use the velocity vector $\boldsymbol{u} = u\boldsymbol{e_s} + v\boldsymbol{e_n} + w\boldsymbol{e_\phi}$ to arrive at the familiar equations of motion (including the continuity equation) given by

$$\rho \left(\frac{\partial \mathbf{u}}{\partial t} + \mathbf{u} \cdot \boldsymbol{\nabla} \mathbf{u} \right) = -\boldsymbol{\nabla} p + \boldsymbol{\nabla} \cdot \boldsymbol{\tau} - 2\boldsymbol{\omega} \times \mathbf{u} - \boldsymbol{\omega} \times (\boldsymbol{\omega} \times \boldsymbol{r}),$$

$$\boldsymbol{\nabla} \cdot \mathbf{u} = 0,$$

where ρ is the constant density of the fluid, p is the pressure within the jet and $\boldsymbol{\omega} = (0, \Omega, 0)$ is the angular velocity vector of the container. Here $\boldsymbol{r}$ denotes the position vector of any particle on the free surface and is given by $\boldsymbol{r} = \int \mathbf{e_s} ds + n\mathbf{e_n}$

The surface of the jet can be described by the equation $n - R(s, t, \phi) = 0$, where

$R(s,t,\phi)$ is a function giving the free surface position, and a normal vector to this surface is given by $\nabla(n - R(s,t,\phi))$. When evaluated this gives the unit normal vector as

$$\mathbf{n} = \frac{1}{E}\left(-\frac{\partial R}{\partial s}\cdot\frac{1}{h_s}\cdot\mathbf{e_s} + \mathbf{e_n} - \frac{\partial R}{\partial \phi}\cdot\frac{1}{R}\cdot\mathbf{e}_\phi\right),$$

where

$$E = \left(1 + \frac{1}{h_s^2}\left(\frac{\partial R}{\partial s}\right)^2 + \frac{1}{R^2}\left(\frac{\partial R}{\partial \phi}\right)^2\right)^{1/2} \quad \text{and} \quad h_s = 1 + n\cos\phi(X_s Z_{ss} - Z_s X_{ss}).$$

The normal stress condition is given by $\mathbf{n}\cdot\mathbf{\Pi}\cdot\mathbf{n} = \sigma\kappa$, where $\mathbf{\Pi}$ is the total stress tensor given by $-p\mathbf{I} + \boldsymbol{\tau}$, σ is the isotropic surface tension and κ is the mean curvature of the free surface

$$\kappa = \frac{1}{nh_s}\left(-\frac{\partial}{\partial s}\left(\frac{n}{Eh_s}\frac{\partial R}{\partial s}\right) + \frac{\partial}{\partial n}\left(\frac{nh_s}{E}\right) - \frac{\partial}{\partial \phi}\left(\frac{h_s}{En}\frac{\partial R}{\partial \phi}\right)\right).$$

Using the two tangent vectors to our free surface, $\mathbf{t}_1 = \partial\mathbf{r}/\partial\mathbf{s}$ and $\mathbf{t}_2 = \partial\mathbf{r}/\partial\phi$, we form our tangential stress conditions $\mathbf{t}_\mathrm{i}\cdot\mathbf{\Pi}\cdot\mathbf{n} = 0$ for $i = 1, 2$. The kinematic condition is given by

$$\frac{D}{Dt}(R(s,t,\phi) - n) = 0 \qquad \text{for } n = R(s,\phi,t).$$

We non-dimensionalise our equations using the transformations

$$\overline{u} = \frac{u}{U}, \quad \overline{v} = \frac{v}{U}, \quad \overline{w} = \frac{w}{U}, \quad \overline{p} = \frac{p}{\rho U^2}, \quad \overline{n} = \frac{n}{a}, \quad \varepsilon = \frac{a}{s_0},$$

$$\overline{R} = \frac{R}{a}, \quad \overline{s} = \frac{s}{s_0}, \quad \overline{t} = \frac{tU}{s_0}, \quad \overline{X} = \frac{X}{s_0}, \quad \overline{Z} = \frac{Z}{s_0},$$

where U is the exit speed of the jet in the rotating frame, s_0 and a are the radius of the

cylindrical drum and radius of the orifice respectively, ε is the aspect ratio of the jet, and u, v and w are the tangential, radial and azimuthal velocity components relative to the centreline of the jet respectively. For power law fluids the viscosity is not constant and we have that

$$\begin{aligned}(\boldsymbol{\nabla}\cdot\boldsymbol{\tau})_j &= (\boldsymbol{\nabla}\cdot(\eta\boldsymbol{\gamma}))_j \\ &= \eta(\boldsymbol{\nabla}\cdot(\boldsymbol{\nabla}\boldsymbol{u}+\boldsymbol{\nabla}\boldsymbol{u}^T))_j + \frac{\gamma_{ij}}{h_i}\partial_i\eta \\ &= (\eta\boldsymbol{\nabla}^2\boldsymbol{u})_j + \frac{\gamma_{ij}}{h_i}\partial_i\eta,\end{aligned}$$

where the free indices go through s, n and ϕ, and h_i are the structure functions given by

$$h_s = 1 + n\cos\phi(X_sZ_{ss} - Z_sX_{ss}),\ \ h_n = 1 \text{ and } h_\phi = n.$$

We should recall here that the apparent viscosity η has the form

$$\eta = m\left(\frac{\boldsymbol{\gamma}:\boldsymbol{\gamma}}{2}\right)^{\frac{\alpha-1}{2}}.$$

Thus our equations of motion will differ from those found in Decent *et al.* (2007) and Părău *et al.* (2007) through the dynamic viscosity being replaced by η and the inclusion of derivatives of η.

If we wish to evaluate the components of $\boldsymbol{\tau}$ we need to determine the gradient of a vector field, i.e., the dyadic product $\nabla\boldsymbol{u}$, this can be written as

$$\nabla\boldsymbol{u} = \left(\sum_i \frac{\boldsymbol{e_i}}{h_i}\frac{\partial}{\partial x_i}\right)\left(\sum_j \frac{\boldsymbol{e_j}}{h_j}u_j\right).$$

The orthogonal set of vectors $\boldsymbol{e_s}, \boldsymbol{e_n}$ and $\boldsymbol{e_\phi}$ are not constant and their derivatives can be

expressed as

$$\frac{\partial \boldsymbol{e_\alpha}}{\partial \beta} = \frac{\boldsymbol{e_\beta}}{h_\alpha}\frac{\partial h_\beta}{\partial \alpha} - \delta_{\alpha\beta}\sum_\gamma \frac{\boldsymbol{e_\gamma}}{h_\gamma}\frac{\partial h_\alpha}{\partial \gamma}.$$

In this case, the variables α, β and γ go through s, n and ϕ. The Kronecker delta symbol has its usual interpretation. Thus our stress components can be written as (recall that $\tau_{ij} = \eta\gamma_{ij}$)

$$\tau_{ss} = \frac{2\eta}{h_s}\left(\frac{\partial u}{\partial s} + (v\cos\phi - w\sin\phi)(X_sZ_{ss} - X_{ss}Z_s)\right) \tag{4.4}$$

$$\tau_{nn} = 2\eta\left(\frac{\partial v}{\partial n}\right) \tag{4.5}$$

$$\tau_{\phi\phi} = \frac{2\eta}{n}\left(\frac{\partial w}{\partial \phi} + v\right) \tag{4.6}$$

$$\tau_{sn} = \tau_{ns} = \eta\left(\frac{1}{h_s}\frac{\partial v}{\partial s} + \frac{\partial u}{\partial n} - \frac{u}{h_s}\cos\phi(X_sZ_{ss} - X_{ss}Z_s)\right) \tag{4.7}$$

$$\tau_{n\phi} = \tau_{\phi n} = \eta\left(\frac{\partial w}{\partial n} - \frac{w}{n} + \frac{1}{n}\frac{\partial v}{\partial \phi}\right) \tag{4.8}$$

$$\tau_{s\phi} = \tau_{\phi s} = \eta\left(\frac{1}{n}\frac{\partial u}{\partial \phi} + \frac{u}{h_s}\sin\phi(X_sZ_{ss} - Z_sX_{ss}) + \frac{1}{h_s}\frac{\partial w}{\partial s}\right) \tag{4.9}$$

An expression for η can be obtained by using the expressions for γ_{ij} such that

$$\eta = m\sum_{ij}\left(\frac{\gamma_{ij}\gamma_{ij}}{2}\right)^{\frac{\alpha-1}{2}}.$$

Moreover, since the expressions for γ_{ij} are lengthy and exhaustive (see the above expressions for τ_{ij}) the resulting expression for η will be rather opaque and is of very little benefit at this stage. For now, it suffices to continue with our analysis using the variable η with the understanding that η is a function of all the variables in (4.4)-(4.9) and most notably the flow index number α. We will eventually go on to consider an asymptotic expansion of the above variables. We shall see that this will greatly simplify the expression for η.

4.2.2 The Equations of Motion

The resulting non-dimensional equations are similar to those found in Părău *et al.* (2007) with some additional terms related to the non-Newtonian effects (i.e., the terms containing derivatives of η are 'novel', see Uddin *et al.* (2006) for more details). The dimensionless parameters in the proceeding equations are the

- Rossby number $\mathcal{R}b = U/(s_0\Omega)$,
- Weber number $We = \rho U^2 a/\sigma$,
- aspect ratio $\varepsilon = a/s_0$
- Generalized Reynolds number[2] based on the radius of the cylinder $\mathcal{R}e_\alpha = (\rho/m)s_0^\alpha U^{2-\alpha}$.

To remain consistent with earlier works (Părău *et al.* (2007)) we have chosen to base the Reynolds number on s_0 rather than the characteristic dimension of the jet flow a. We do however go on to use a Reynolds number based on the jet radius. Although the flow index number α does not explicitly appear in these equations, it is contained in the function η. The equations in their full form are given by

$$\varepsilon n\frac{\partial u}{\partial s} + h_s\left(v + n\frac{\partial v}{\partial n} + \frac{\partial w}{\partial \phi}\right) + \varepsilon n(X_s Z_{ss} - Z_s X_{ss})(v\cos\phi - w\sin\phi) = 0, \tag{4.10}$$

$$\begin{aligned} h_s\left(\varepsilon\frac{\partial u}{\partial t} + \varepsilon(v\cos\phi - w\sin\phi)(Z_{st}X_s - X_{st}Z_s) + v\frac{\partial u}{\partial n} + \frac{w}{n}\frac{\partial u}{\partial \phi}\right) + \varepsilon u\frac{\partial u}{\partial s} \\ +\varepsilon u(v\cos\phi - w\sin\phi)(X_s Z_{ss} - Z_s X_{ss}) = \\ -\varepsilon\frac{\partial p}{\partial s} + \left(\frac{2\varepsilon}{\mathcal{R}b}(v\cos\phi - w\sin\phi) + \frac{\varepsilon}{\mathcal{R}b^2}((X+1)X_s + ZZ_s)\right)h_s \end{aligned} \tag{4.11}$$

[2]The expression for the generalized Reynolds number is indeed dimensionless since the flow consistency number has dimensions $Pa \cdot s^\alpha$ where Pa is Pascals and s is seconds.

$$+\frac{\eta}{\varepsilon\mathcal{R}e_\alpha}\left(\frac{-\varepsilon^3 n\cos\phi S_s}{h_s^2}\left(\frac{\partial u}{\partial s}+v\cos\phi(X_sZ_{ss}-Z_sX_{ss})-w\sin\phi(X_sZ_{ss}-Z_sX_{ss})\right)\right.$$

$$+\frac{\varepsilon^2}{h_s}\left(-u(X_sZ_{ss}-Z_sX_{ss})^2+\frac{\partial^2 u}{\partial s^2}+2\frac{\partial v}{\partial s}\cos\phi(X_sZ_{ss}-Z_sX_{ss})\right.$$

$$\left.+(v\cos\phi-w\sin\phi)(X_sZ_{sss}-Z_sX_{sss})-2\frac{\partial w}{\partial s}\sin\phi(X_sZ_{ss}-Z_sX_{ss})\right)$$

$$\left.+(1+2\varepsilon n\cos\phi(X_sZ_{ss}-Z_sX_{ss}))\frac{1}{n}\frac{\partial u}{\partial n}+h_s\frac{\partial^2 u}{\partial n^2}+\frac{h_s}{n^2}\frac{\partial^2 u}{\partial\phi^2}-\frac{\varepsilon}{n}\frac{\partial u}{\partial\phi}\sin\phi(X_sZ_{ss}-Z_sX_{ss})\right)$$

$$+\frac{1}{\varepsilon\mathcal{R}e_\alpha}\left\{\frac{2\varepsilon^2}{h_s}\frac{\partial\eta}{\partial s}\left(\frac{\partial u}{\partial s}+v\cos\phi(X_sZ_{ss}-Z_sX_{ss})-w\sin\phi(X_sZ_{ss}-Z_sX_{ss})\right)\right.$$

$$+\frac{1}{n}\frac{\partial\eta}{\partial\phi}\left(\varepsilon u\sin\phi(X_sZ_{ss}-Z_sX_{ss})+\frac{h_s}{n}\frac{\partial u}{\partial\phi}+\varepsilon\frac{\partial w}{\partial s}\right)$$

$$\left.\frac{\partial\eta}{\partial n}\left(\varepsilon\frac{\partial v}{\partial s}-\varepsilon u\cos\phi(X_sZ_{ss}-Z_sX_{ss})+h_s\frac{\partial u}{\partial n}\right)\right\},$$

$$h_s\left(\varepsilon\frac{\partial v}{\partial t}+\varepsilon u\cos\phi(X_{st}Z_s-Z_{st}X_s)+v\frac{\partial v}{\partial n}+\frac{w}{n}\frac{\partial v}{\partial\phi}-\frac{w^2}{n}\right)$$

$$+\varepsilon u\frac{\partial v}{\partial s}-\varepsilon\cos\phi(X_sZ_{ss}-Z_sX_{ss})u^2$$

$$= \tag{4.12}$$

$$\left(-\frac{\partial p}{\partial n}-\frac{2\varepsilon}{\mathcal{R}b}u\cos\phi+\frac{\varepsilon\cos\phi}{\mathcal{R}b^2}((X+1)Z_s-ZX_s+\varepsilon n\cos\phi)\right)h_s$$

$$+\frac{1}{\varepsilon\mathcal{R}e_\alpha}\frac{\eta}{n}\left(\frac{-\varepsilon^3 n^2(X_sZ_{sss}-Z_sX_{sss})\cos\phi}{{h_s}^2}\left(\frac{\partial v}{\partial s}-u\cos\phi(X_sZ_{ss}-Z_sX_{ss})\right)\right.$$

$$+\frac{\varepsilon^2 n}{h_s}\left(-v\cos^2\phi(X_sZ_{ss}-Z_sX_{ss})^2+\frac{\partial^2 v}{\partial s^2}-2\cos\phi(X_sZ_{ss}-Z_sX_{ss})\frac{\partial u}{\partial s}\right.$$

$$\left.\left.-u\cos\phi(X_sZ_{sss}-Z_sX_{sss})+w\sin\phi\cos\phi(X_sZ_{ss}-Z_sX_{ss})^2\right)+nh_s\frac{\partial^2 v}{\partial n^2}\right.$$

$$+(1+2\varepsilon n\cos\phi(X_sZ_{ss}-Z_sX_{ss}))\frac{\partial v}{\partial n}-\varepsilon\left(\frac{\partial v}{\partial\phi}-w\right)\sin\phi(X_sZ_{ss}-Z_sX_{ss})$$

$$+\frac{h_s}{n}\left(\frac{\partial^2 v}{\partial\phi^2}-v-2\frac{\partial w}{\partial\phi}\right)\Big)+\frac{1}{\varepsilon\mathcal{R}e_\alpha}\left\{\frac{\varepsilon}{h_s}\frac{\partial\eta}{\partial s}\left(\varepsilon\frac{\partial v}{\partial s}-\varepsilon u\cos\phi(X_sZ_{ss}-Z_sX_{ss})+h_s\frac{\partial u}{\partial n}\right)\right.$$

$$\left.+\frac{\partial\eta}{\partial n}\left(2h_s\frac{\partial v}{\partial n}\right)+\frac{h_s}{n}\frac{\partial\eta}{\partial\phi}\left(\frac{\partial w}{\partial n}-\frac{w}{n}+\frac{1}{n}\frac{\partial v}{\partial\phi}\right)\right\}$$

and

$$h_s\left(\varepsilon\frac{\partial w}{\partial t}+\varepsilon u\sin\phi(Z_{st}X_s-X_{st}Z_s)+w\frac{\partial w}{\partial n}+\frac{w}{n}\frac{\partial w}{\partial\phi}+\frac{vw}{n}\right)$$

$$+\varepsilon u\frac{\partial w}{\partial s}+\varepsilon\sin\phi(X_sZ_{ss}-Z_sX_{ss})u^2= \tag{4.13}$$

$$\left(-\frac{1}{n}\frac{\partial p}{\partial\phi}+\frac{2\varepsilon}{\mathcal{R}b}u\sin\phi+\frac{\varepsilon\sin\phi}{\mathcal{R}b^2}(ZX_s-(X+1)Z_s-\varepsilon n\cos\phi)\right)h_s$$

$$+\frac{1}{\varepsilon\mathcal{R}e_\alpha}\frac{\eta}{n}\left(\frac{-\varepsilon^3\cos\phi}{h_s^2}(X_sZ_{sss}-Z_sX_{sss})\left(\frac{\partial w}{\partial s}+u\sin\phi(X_sZ_{ss}-Z_sX_{ss})\right)\right.$$

$$\frac{\varepsilon^2 n}{h_s}\left(-w\sin^2\phi(X_sZ_{ss}-Z_sX_{ss})^2+\frac{\partial^2 w}{\partial s^2}+2\frac{\partial u}{\partial s}\sin\phi(X_sZ_{ss}-Z_sX_{ss})\right.$$

$$\left.\left.+u\sin\phi(X_sZ_{sss}-Z_sX_{sss})+v\sin\phi\cos\phi(X_sZ_{ss}-Z_sX_{ss})^2\right)+nh_s\frac{\partial^2 w}{\partial n^2}\right.$$

$$+(1+2\varepsilon n\cos\phi(X_sZ_{ss}-Z_sX_{ss}))\frac{\partial w}{\partial n}-\varepsilon\left(\frac{\partial w}{\partial\phi}+v\right)\sin\phi(X_sZ_{ss}-Z_sX_{ss})+\frac{h_s}{n}\left(\frac{\partial^2 w}{\partial\phi^2}-w+2\frac{\partial v}{\partial\phi}\right)$$

$$+\frac{1}{\varepsilon\mathcal{R}e_\alpha}\left\{\frac{\varepsilon}{h_s}\frac{\partial\eta}{\partial s}\left(\varepsilon\frac{\partial w}{\partial s}+\varepsilon u\sin\phi(X_sZ_{ss}-Z_sX_{ss})+\frac{h_s}{n}\cdot\frac{\partial u}{\partial\phi}\right)\right.$$

$$\left.+\frac{h_s}{n}\frac{\partial\eta}{\partial n}\left(\frac{\partial v}{\partial\phi}-w+n\frac{\partial w}{\partial n}\right)+\frac{2h_s}{n^2}\frac{\partial\eta}{\partial\phi}\left(\frac{\partial w}{\partial\phi}+v\right)\right\}.$$

4.2.3 The Boundary Conditions

The normal stress condition which relates the pressure difference across the jet to the curvature is given by

$$p - \frac{2\eta}{\mathcal{R}e_\alpha E^2}\left(\varepsilon^2\left(\frac{\partial R}{\partial s}\right)^2 \cdot \frac{1}{h_s^3}\left(\frac{\partial u}{\partial s} + (v\cos\phi - w\sin\phi)(X_sZ_{ss} - Z_sX_{ss})\right) + \frac{1}{\varepsilon}\frac{\partial v}{\partial n}\right.$$

$$+\frac{1}{\varepsilon R^3}\left(\frac{\partial R}{\partial \phi}\right)^2\left(\frac{\partial w}{\partial \phi} + v\right) - \frac{\varepsilon}{h_s}\frac{\partial R}{\partial s}\left(\frac{1}{h_s}\frac{\partial v}{\partial s} + \frac{1}{\varepsilon}\frac{\partial u}{\partial n} - \frac{u}{h_s}\cos\phi(X_sZ_{ss} - Z_sX_{ss})\right)$$

$$-\frac{1}{R\varepsilon}\frac{\partial R}{\partial \phi}\left(\frac{\partial w}{\partial n} - \frac{w}{R} + \frac{1}{R}\frac{\partial v}{\partial \phi}\right)$$

$$\left.+\frac{\varepsilon}{Rh_s}\frac{\partial R}{\partial s}\frac{\partial R}{\partial \phi}\left(\frac{1}{\varepsilon R}\frac{\partial u}{\partial \phi} + \frac{u}{h_s}\sin\phi(X_sZ_{ss} - Z_sX_{ss}) + \frac{1}{h_s}\frac{\partial u}{\partial s}\right)\right) = \frac{\kappa}{We}, \qquad (4.14)$$

where κ is the mean curvature.

The first tangential stress condition is given by

$$\left(1 - \frac{\varepsilon^2}{{h_s}^2}\left(\frac{\partial R}{\partial s}\right)^2\right)\left(\varepsilon\frac{\partial v}{\partial s} + h_s\frac{\partial u}{\partial n} - \varepsilon u\cos\phi(X_sZ_{ss} - Z_sX_{ss})\right)$$

$$+2\varepsilon\frac{\partial R}{\partial s}\left(\frac{\partial v}{\partial n} - \varepsilon\frac{\partial u}{\partial s}\cdot\frac{1}{h_s} - \frac{\varepsilon}{h_s}(X_sZ_{ss} - Z_sX_{ss})(v\cos\phi - w\sin\phi)\right) = 0, \qquad (4.15)$$

with the second as

$$\left(1 - \frac{1}{R^2}\left(\frac{\partial R}{\partial \phi}\right)^2\right)\left(\frac{\partial w}{\partial n} - \frac{w}{R} + \frac{1}{R}\frac{\partial v}{\partial \phi}\right) + \frac{2}{R}\frac{\partial R}{\partial \phi}\left(\frac{\partial v}{\partial n} - \frac{1}{R}\left(\frac{\partial w}{\partial \phi} + v\right)\right) = 0. \qquad (4.16)$$

We also have the arclength condition ${X_s}^2 + {Z_s}^2 = 1$ as well as the kinematic condition

$$h_s \left(\varepsilon \frac{\partial R}{\partial t} + (\cos\phi + \frac{\partial R}{\partial t}\frac{1}{n}\sin\phi)(X_t Z_s - X_s Z_t) - v + \frac{\partial R}{\partial \phi}\frac{w}{n} \right) + \varepsilon u \frac{\partial R}{\partial s} - \varepsilon \frac{\partial R}{\partial s}(X_t X_s + Z_t Z_s + \varepsilon n \cos\phi (X_s Z_{ss} - Z_s X_{ss})) = 0. \quad (4.17)$$

Boundary conditions (4.14)-(4.17) are applied at the free surface $n = R(s, \phi, t)$.

4.2.4 Asymptotic Analysis

We exploit the fact that the radius of the orifice is small when compared to the radius of the cylinder by expanding u, v, w, p in Taylor series in εn (see Eggers (1997) and Hohman *et al.* (1984)), and R, X, Z in asymptotic series in ε. We assume that the leading order axial component of the velocity is independent of ϕ and that the centreline of the jet is unaffected by small perturbations. Thus we have

$$\begin{aligned}
u(s,n,\phi,t) &= u_0(s,t) + (\varepsilon n)u_1(s,\phi,t) + (\varepsilon n)^2 u_2(s,\phi,t) + \cdots \\
v(s,n,\phi,t) &= (\varepsilon n)v_1(s,\phi,t) + (\varepsilon n)^2 v_2(s,\phi,t) + \cdots \\
w(s,n,\phi,t) &= (\varepsilon n)w_1(s,\phi,t) + (\varepsilon n)^2 w_2(s,\phi,t) + \cdots \\
p(s,n,\phi,t) &= p_0(s,\phi,t) + (\varepsilon n)p_1(s,\phi,t) + \cdots \\
R(s,n,\phi,t) &= R_0(s,t) + \varepsilon R_1(s,\phi,t) + \cdots \\
X(s,n,\phi,t) &= X_0(s) + \varepsilon X_1(s,t) + \cdots \\
Z(s,n,\phi,t) &= Z_0(s) + \varepsilon Z_1(s,t) + \cdots
\end{aligned}$$

From the continuity equation (4.10) we obtain

$$O(\varepsilon n) \quad : \quad u_{0s} + 2v_1 + w_{1\phi} = 0 \tag{4.18}$$

$$O(\varepsilon n)^2 \quad : \quad u_{1s} + 3v_2 + w_{2\phi} + (3v_1 + w_{1\phi})S\cos\phi - w_1 S\sin\phi = 0. \tag{4.19}$$

where $S = (X_s Z_{ss} - Z_s X_{ss})$. From the second tangential stress condition (4.16) we get

$$O(\varepsilon n) \quad : \quad R_0^3 v_{1\phi} = 0 \tag{4.20}$$

$$O(\varepsilon n)^2 \quad : \quad 3R_0^2 R_1 v_{1\phi} + R_0^4(w_2 + v_{2\phi}) - 2R_0^2 R_{1\phi} w_{1\phi} = 0. \tag{4.21}$$

Thus we see that $v_{1\phi} = 0$, and by differentiating (4.18) we see that $w_{1\phi\phi} = 0$. Since w_1 is periodic in ϕ we must have $w_1 = w_1(s,t)$. Then (4.18) implies that $v_1 = -u_{0s}/2$ and from (4.21) we have

$$w_2 + v_{2\phi} = 0. \tag{4.22}$$

From the first tangential stress condition (4.15) we have

$$O(\varepsilon) \quad : \qquad u_1 = u_0 S\cos\phi \tag{4.23}$$

$$O(\varepsilon^2) \quad : \qquad u_2 = \frac{3}{2}u_{0s}\frac{R_{0s}}{R_0} + \frac{u_{0ss}}{4}. \tag{4.24}$$

After differentiating (4.22) with respect to ϕ we obtain

$$w_{2\phi} = -v_{2\phi\phi}. \tag{4.25}$$

Therefore,

$$v_{2\phi\phi} - 3v_2 = u_{1s} + 3v_1 S\cos\phi - w_1 S\sin\phi, \tag{4.26}$$

and using the expressions for u_1 and v_1 we see that

$$v_{2\phi\phi} - 3v_2 = \left(u_0 S_s - \frac{u_{0s}}{2} S\right) \cos\phi - w_1 S \sin\phi. \tag{4.27}$$

Periodic solutions for v_2 and w_2 are

$$v_2 = \frac{1}{4}\left(\frac{u_{0s}}{2} S - u_0 S_s\right) \cos\phi + \frac{w_1}{4} S \sin\phi, \tag{4.28}$$

$$w_2 = \frac{1}{4}\left(\frac{u_{0s}}{2} S - u_0 S_s\right) \sin\phi - \frac{w_1}{4} S \cos\phi. \tag{4.29}$$

The apparent viscosity η (after some lengthy algebra) can be expressed as

$$\eta = m|\sqrt{3}u_{0s}|^{\alpha-1}\left(1 + (\varepsilon n)\frac{(\alpha-1)}{u_{0s}}\left((u_0(X_{0s}Z_{0sss} - Z_{0s}X_{0sss})\right.\right.$$

$$\left.\left. -\frac{u_{0s}}{2}(X_{0s}Z_{0ss} - Z_{0s}X_{0ss})\right)\cos\phi - w_1 \sin\phi (X_{0s}Z_{0ss} - Z_{0s}X_{0ss})\right) + O((\varepsilon n)^2)\Big). \tag{4.30}$$

From the momentum equation in the radial direction, we have at leading order $p_{0n} = 0$. Thus $p_0 = p_0(s, \phi, t)$, i.e., p_0 is independent of n. At order ε we get

$$p_1 = \left({u_0}^2(X_{0s}Z_{0ss} - Z_{0s}X_{0ss}) - \frac{2}{\mathcal{R}b}u_0 + \frac{(X_0+1)Z_{0s} - Z_0 X_{0s}}{\mathcal{R}b^2}\right)\cos\phi$$

$$-\frac{|\sqrt{3}u_{0s}|^{\alpha-1}}{\mathcal{R}e_\alpha}\left(\frac{6-\alpha}{2}u_{0s}(X_{0s}Z_{0ss} - Z_{0s}X_{0ss}) + \alpha u_0(X_{0s}Z_{0sss} - Z_{0s}X_{0sss})\right)\cos\phi \tag{4.31}$$

$$+(\alpha-2)\frac{|\sqrt{3}u_{0s}|^{\alpha-1}}{\mathcal{R}e_\alpha}w_1(X_{0s}Z_{0ss} - Z_{0s}X_{0ss})\sin\phi.$$

For simplicity of notation we will relabel X_0 and Z_0 with X and Z respectively.

The momentum equation in the azimuthal direction gives at leading order $p_{0\phi} = 0$ which is automatically satisfied. At order ε we get the above equation for p_1. From the normal stress condition we obtain at leading order

$$p_0 = -\frac{|\sqrt{3}u_{0s}|^{\alpha-1}u_{0s}}{\mathcal{R}e_\alpha} + \frac{1}{R_0We},$$

and at order ε we have

$$p_1 = \frac{1}{R_0We}\left(-\frac{R_{1\phi\phi}+R_1}{{R_0}^2} + S\cos\phi\right) + \frac{4|\sqrt{3}u_{0s}|^{\alpha-1}}{\mathcal{R}e_\alpha}v_2.$$

If we now substitute the expression for p_1 from (4.31) into the above equation, and note that R is periodic in ϕ, we get

$$\begin{aligned}(X_sZ_{ss} - X_{ss}Z_s)\left(\frac{(7-\alpha)|\sqrt{3}u_{0s}|^{\alpha-1}u_{0s}}{2\mathcal{R}e_\alpha} + \frac{1}{R_0We} - {u_0}^2\right)\cos\phi& \\ + \left(\frac{2}{\mathcal{R}b}u_0 - \frac{(X+1)Z_s - ZX_s}{\mathcal{R}b^2}\right)\cos\phi& \\ -\frac{(\alpha-1)|\sqrt{3}u_{0s}|^{\alpha-1}}{\mathcal{R}e_\alpha}(u_0(X_sZ_{sss} - X_{sss}Z_s)\cos\phi + w_1\sin\phi) = 0.& \qquad (4.32)\end{aligned}$$

The above equation is valid only if the leading order terms in the expansion of X and Z are independent of t. If we had retained leading order translational velocity terms v_0 and w_0 in our expansions for v and w, and had $X_{0t} \neq 0$ and $Z_{0t} \neq 0$, then the right hand side of (4.32) would contain some additional unsteady terms (see Părău *et al.* (2007) in $E = Z_sX_t - Z_tX_s$. However $E \approx 0$ has already been found in Părău *et al.* (2007) to be a very accurate approximation between the orifice and the break up point of the jet (see Appendix D for further details). This is backed up by the experimental observations of Wong *et al.* (2004), which show that the centreline of the jet is steady (in the rotating frame), giving $X_t \approx 0$, $Z_t \approx 0$ and $E \approx 0$ for experimental observations. There seems to be

no reason to suppose this will be different for non-Newtonian jets. (However, experiments are planned to check this using the same apparatus as in Wong *et al.* (2004).)

The Navier-Stokes equation in the axial direction at order ε is

$$u_{0t} + u_0 u_{0s} = -p_{0s} + \frac{(X+1)X_s + ZZ_s}{\mathcal{R}b^2} + \frac{\eta}{\mathcal{R}e_\alpha}(u_{0ss} + 4u_2 + u_{2\phi\phi}) + \frac{2}{\mathcal{R}e_\alpha}\frac{\partial \eta}{\partial s}u_{0s}, \tag{4.33}$$

which after using the expressions for u_2, p_0 and η becomes

$$u_{0t} + uu_{0s} = -\frac{1}{We}\left(\frac{1}{R_0}\right)_s + \frac{(X+1)X_s + ZZ_s}{\mathcal{R}b^2} + \frac{3|\sqrt{3}u_{0s}|^{\alpha-1}}{\mathcal{R}e_\alpha} \cdot \left(\alpha u_{0ss} + 2u_{0s}\frac{R_{0s}}{R}\right). \tag{4.34}$$

From the kinematic condition, we obtain at order ε

$$R_{0t} + \frac{u_{0s}}{2}R_0 + u_0 R_{0s} = 0. \tag{4.35}$$

And finally the last equation to be solved is the arclength equation at leading order

$$X_s{}^2 + Z_s{}^2 = 1. \tag{4.36}$$

We see that we have now four equations (4.32), (4.34), (4.35) and (4.36) for the four unknowns u_0, R_0, X and Z.

4.2.5 Steady State Solution

We now search for steady state solutions to this set of equations. We have the four variables u_0, R_0, X and Z, all of which we can consider as being functions of s only in the steady state. For convenience of notation we replace the leading order velocity and

radius terms by u and R. The resulting steady state equations are

$$uu_s = -\frac{1}{We}\left(\frac{1}{R}\right)_s + \frac{(X+1)X_s + ZZ_s}{\mathcal{R}b^2} + \frac{3|\sqrt{3}u_s|^{\alpha-1}}{\mathcal{R}e_\alpha}\cdot\left(\alpha u_{ss} + 2u_s\frac{R_s}{R}\right), \tag{4.37}$$

$$\frac{u_s}{2}R + uR_s = 0, \tag{4.38}$$

as well as (4.32) and (4.36).

From (4.38) we can see that

$$R^2u = \text{constant}.$$

If we now use the initial conditions

$$R(0) = 1 \qquad \text{and} \qquad u(0) = 1, \tag{4.39}$$

we have that

$$R^2u = 1, \tag{4.40}$$

and using this we get a reduced set of equations

$$uu_s = -\frac{u_s}{2We\sqrt{u}} + \frac{(X+1)X_s + ZZ_s}{\mathcal{R}b^2} + \frac{3|\sqrt{3}u_s|^{\alpha-1}}{\mathcal{R}e_\alpha}\cdot\left(\alpha u_{ss} - \frac{{u_s}^2}{u}\right), \tag{4.41}$$

$$(X_s Z_{ss} - X_{ss} Z_s)\left(\frac{(7-\alpha)|\sqrt{3}u_s|^{\alpha-1}u_s}{2\mathcal{R}e_\alpha} + \frac{\sqrt{u}}{We} - u^2\right)\cos\phi$$

$$+\left(\frac{2}{\mathcal{R}b}u - \frac{(X+1)Z_s - ZX_s}{\mathcal{R}b^2}\right)\cos\phi - \frac{(\alpha-1)|\sqrt{3}u_s|^{\alpha-1}}{\mathcal{R}e_\alpha}u(X_s Z_{sss} - X_{sss}Z_s)\cos\phi$$

$$+\frac{(\alpha-1)|\sqrt{3}u_s|^{\alpha-1}}{\mathcal{R}e_\alpha}w_1\sin\phi = 0. \qquad (4.42)$$

as well as (4.36).

This system of equations can be solved for X and Z (thus giving us a steady trajectory), and for u, using a finite difference scheme (see Părău *et al.* (2006) & (2007)). However, in the next section, in order to obtain a distinguished limit, it will be shown that we require $\mathcal{R}e_\alpha = O(\varepsilon^{-1})$, so that $\mathcal{R}e_\alpha \to \infty$ is the correct limit here. (This was also found in Decent *et al.* (2005) in the Newtonian case.) This inviscid steady state ($\mathcal{R}e_\alpha \to \infty$) is only a valid approximation for the viscous case when the Ohnesorge number $Oh = \sqrt{We}/\mathcal{R}e_\alpha$ is not very large, so we shall therefore confine ourselves to the study of jets where the Ohnesorge number is small or $O(1)$. However Wong *et al.* (2004) showed that jets do not form unless Oh is small, which gives confidence to this approximation.

The inviscid centreline problem is given by (4.41), (4.42) and (4.36) in the limit $\mathcal{R}e_\alpha = \infty$. These equations can be reduced into a set of odes (using five variables) and then integrated using a Runge-Kutta method. We used the ODE45 package in MATLAB for this purpose. The boundary conditions at the nozzle were chosen as $X(0) = Z(0) = Z_s(0) = 0$ and $u(0) = X_s(0) = 1$. Both the trajectory and the jet radius are plotted in Figs. 4.6 - 4.8 for different Rossby and Weber numbers. It can be seen that the jet curves more on leaving the orifice and that the radius along the jet

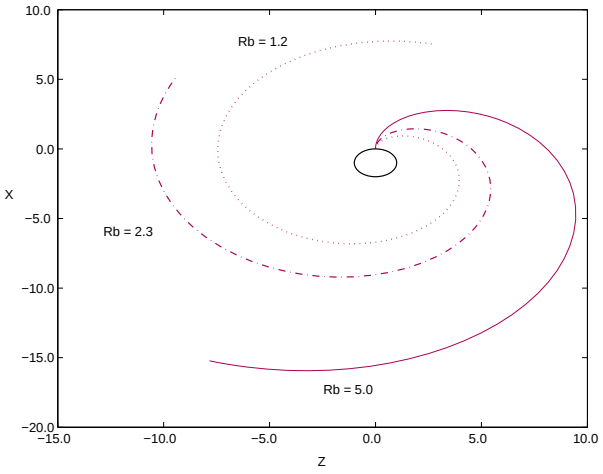

Figure 4.6: The trajectory of an inviscid liquid jet emerging from a rotating orifice placed at the origin (0,0). The cylindrical drum is shown in black. It can be seen that for higher rotation rates (i.e., smaller values of $\mathcal{R}b$) the jet curves more on leaving the orifice. Here $We = 9.4$.

contracts much more rapidly for higher rates of rotation. In the limit of $\mathcal{R}b \to \infty$ (i.e. no rotation) we would expect to have a straight jet emerging from the orifice with the radius remaining constant along the jet. The effects of increasing the Weber number (or decreasing the surface tension) is seen to make the centreline curve less.

4.3 Temporal Instability

The length scale over which the jet curves is $s = O(1)$ but disturbances along the jet are much smaller, typically of the order of the jet radius a. By considering travelling wave modes of the form $\exp(ik\overline{s} + \omega\overline{t})$, where $\overline{s} = s/\varepsilon$ and $\overline{t} = t/\varepsilon$ are small length and time scales, and $k = k(s) = O(1)$ and $\omega = \omega(s) = O(1)$ are the wavenumber and frequency of the disturbances, we have a multiple scales formulation with perturbations along the jet having wavelength of $O(\varepsilon)$, as required. Adding small perturbations to the steady state

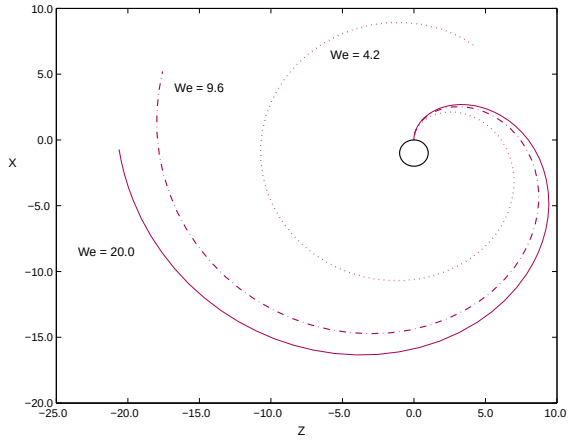

Figure 4.7: The trajectory of an inviscid liquid jet (solved using a Runge-Kutta method) emerging from an orifice placed at (0,0) for Weber numbers. The jet curves more on leaving the orifice when the surface tension is increased (which corresponds to decreasing the Weber number). Here we have $\mathcal{R}b = 4.5$.

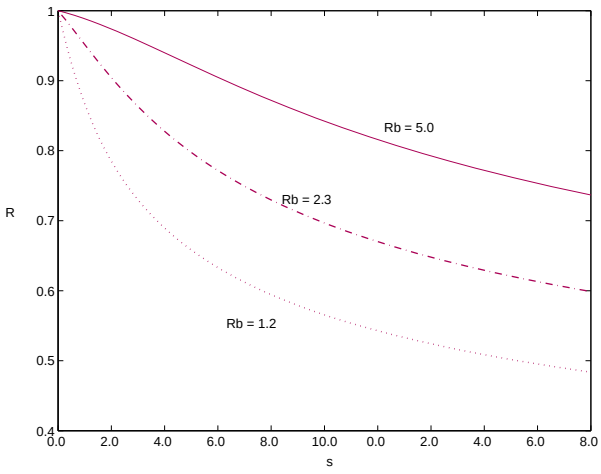

Figure 4.8: The radius of an inviscid liquid jet for different rotations. For high rotation rates the radius of the jet diminishes much more quickly along the jet. Here $We = 20$.

solution found at the end of the previous section, we have

$$u(s,t) = u_0(s) + \delta\widehat{u}\exp(ik\overline{s} + \omega\overline{t}) + O(\delta\varepsilon) + cc., \tag{4.43}$$

$$R(s,t) = R_0(s) + \delta\widehat{R}\exp(ik\overline{s} + \omega\overline{t}) + O(\delta\varepsilon) + cc., \tag{4.44}$$

$$p(s,t) = p_0(s) + \delta\widehat{p}\exp(ik\overline{s} + \omega\overline{t}) + O(\delta\varepsilon) + cc., \tag{4.45}$$

$$X(s,t) = X_0(s) + \delta\varepsilon\widehat{X}(\overline{s}, s, \overline{t}, t) + cc., \tag{4.46}$$

$$Z(s,t) = Z_0(s) + \delta\varepsilon\widehat{Z}(\overline{s}, s, \overline{t}, t) + cc., \tag{4.47}$$

where *cc* denotes complex conjugates. The perturbations above are assumed to leave the centreline of the jet unaffected. The experiments of Wong *et al.* (2004) give support to this assumption since in those experiments four different modes of breakup were observed over a range of experimental parameters (see Table 4.1.1) for which only highly viscous jets were found to have displaced centrelines. In particular it was found in Decent *et al.* (2007) that this simplification did not allow the simulation of "mode 4" breakup which is common for highly viscous fluids where the centreline is sometimes displaced during recoil after droplet detachment. Părău *et al.* (2006) investigated the assumption of time independence of the leading order centreline in further detail.

In the above expansion, the leading order steady state is considered. However, if perturbations of the steady solution are applied to all orders in ε then we require $0 < \delta \ll \varepsilon^2$ for (4.43) - (4.47) to remain valid. We should also note that perturbations are applied implicitly to both the radial and azimuthal velocity components since both depend upon the axial velocity u (see section 4.2, in particular (4.28) and (4.29)). We note that the ε term in the perturbation for X and Z is needed to avoid the trivial solution $\widehat{X} = \widehat{Z} = 0$ in what follows (as is also the case in Wallwork *et al.* (2001)). (We note that this finding backs up the assumption in the previous section that X and Z are time independent at leading order in ε.) Here k is the wavenumber of the travelling wave disturbance, ω is the

frequency and δ is a small constant which gives the amplitude of the wave at the orifice.

A new scaling for the Reynolds number based on the initial jet radius, namely $\tilde{\mathcal{R}e}_\alpha = \varepsilon \mathcal{R}e_\alpha$ is needed to obtain a distinguished limit in the resulting unstable equations. Without this limit no terms from the viscous term can be brought into the resulting equations.

To prevent instability to modes with zero wavelength we must use the full expression for the mean curvature, which is,

$$\frac{1}{We}\left(\frac{1}{R(1+\varepsilon^2 R_s^2)^{\frac{1}{2}}} - \frac{\varepsilon^2 R_{ss}}{(1+\varepsilon^2 R_s^2)^{\frac{3}{2}}}\right).$$

Although to leading order the mean curvature term is $\frac{1}{RWe}$, the complete expression for the mean curvature term is needed (see Eggers (1997)) and has been used previously by a number of authors including Lee (1974) and Garcia & Castellanos (1994). Thus the axial equation of motion becomes

$$u_t + uu_s = -\frac{1}{We}\left(\frac{1}{R(1+\varepsilon^2 R_s^2)^{\frac{1}{2}}} - \frac{\varepsilon^2 R_{ss}}{(1+\varepsilon^2 R_s^2)^{\frac{3}{2}}}\right)_s + \frac{(X+1)X_s + ZZ_s}{\mathcal{R}b^2} + \frac{3|\sqrt{3}u_s|^{\alpha-1}}{\mathcal{R}e_\alpha}\left(\alpha u_{ss} + 2u_s\frac{R_s}{R}\right). \quad (4.48)$$

instead of (4.34). Note that the multiple-length scaling in $\overline{s} = s/\varepsilon$ brings the $O(\varepsilon)$ terms in (4.48) into leading order as required on the short-wavelength modes; this justifies the introduction of the full curvature into the model from a mathematical point of view.

4.3.1 Dispersion Relation

Using $f(s,\alpha) = 3\alpha|\sqrt{3}u_s|^{\alpha-1}$, substituting our perturbed solution (4.43) - (4.47) into (4.32), (4.35), (4.36) and (4.48), we get at leading order the eigenvalue relation

$$(\omega + iku) - \frac{kR}{2We(\omega+iku)}\left(\frac{k}{R^2} - k^3\right) + \frac{k^2 f}{\tilde{\mathcal{R}e}_\alpha} = 0. \quad (4.49)$$

after some algebra. Writing $\omega = \omega_r + i\omega_i$ gives $\omega_i = -ku$ and

$$\omega_r = -(1/2)\frac{k^2 f}{\tilde{\mathcal{R}e}_\alpha} \pm (k/2)\left((kf/\tilde{\mathcal{R}e}_\alpha)^2 + 2(RWe)^{-1}\left(1-(kR)^2\right)\right)^{\frac{1}{2}}. \tag{4.50}$$

For unstable disturbances we require that the growth rate ω_r be positive (otherwise disturbances decay along the jet) which is satisfied when $0 < kR < 1$. This instability range is the same for a straight jet, a result previously found by Lord Rayleigh (1878). We can find the most unstable wavenumber $k = k^*$ for which ω_r is a maximum, and this is

$$k^* = \frac{1}{(2R^3)^{\frac{1}{4}}} \cdot \frac{1}{\sqrt{Ohf + \sqrt{2R}}}. \tag{4.51}$$

Here R and f are found as the solution to the steady equations (4.36) and (4.41)-(4.42). Therefore R and f vary with the arclength s down the jet, and hence the most unstable wavenumber k^* is also a function of arclength s.

We can consider the eigenvalue relationship (4.49) in two ways, either by a temporal instability analysis or by a spatial instability analysis. In a temporal instability analysis we assume that k is real and that perturbations grow or decay in time, over the entire length of the jet. This is the method adopted above. In a spatial instability analysis disturbances are allowed to grow in space along the jet: in this case ω is assumed to be imaginary (so that $\omega = i\omega_i$, where ω_i is a real frequency) and we solve the eigenvalue relationship (4.49) for k, finding k complex. Thus we will have $k = k_r + ik_i$ where k_r describes the wavenumber of the wave and k_i is the spatial growth rate with instability occurring for $k_i < 0$. For viscous Newtonian jets, it was shown by Decent *et al.* (2005) that identical results for the most unstable wavenumber and most unstable frequency were obtained for a one-dimensional model, in the long wavelength limit, for spatial and temporal instability. A similar agreement between temporal instability and spatial insta-

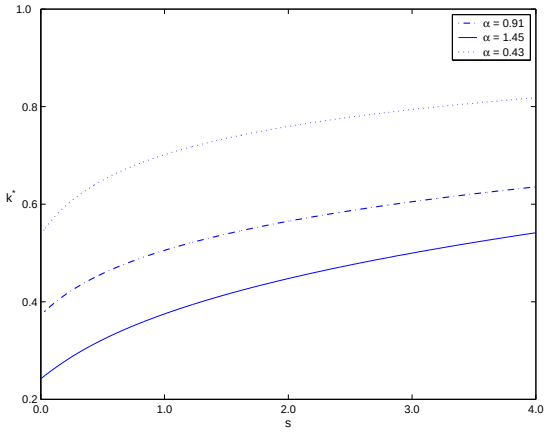

Figure 4.9: Graph showing the wavenumber of the most unstable mode k^* plotted against arc length s of the jet for various values of α. Here $\tilde{\mathcal{R}}e_\alpha = 3.0$, $We = 20.0$ and $\mathcal{R}b = 0.75$.

bility for non-Newtonian liquids also occurs here and we have therefore omitted a spatial instability analysis in this thesis.

The rotation of the container affects both the growth rate and wavenumber of disturbances along the jet. To demonstrate this effect we consider both a moderately high rotation rate ($\mathcal{R}b = 0.75$, which corresponds to a rotation rate of approximately 250rpm if we take $U \approx 1.4ms^{-1}$ and $s_0 \approx 0.14m$) and a low rotation rate ($\mathcal{R}b = 4$, approximately 47rpm) and then compare the wavenumber of the most unstable mode (Figs. 4.9 & 4.10) and the growth rate of disturbances (Figs. 4.11 & 4.12) for different values of α, with the results plotted against the arclength s. Note that shear thinning liquids ($\alpha < 1$) have larger values of k^* and ω_r than shear thickening liquids ($\alpha > 1$) for $\mathcal{R}b = 0.75$, but this comparison is vice-versa for $\mathcal{R}b = 4$.

If we now simplify matters by just considering a typical shear thinning liquid with modest shear thinning properties, say $\alpha = 0.6$, which could be for example some types of fruit juices and if we do a similar thing for shear thickening liquids ($\alpha = 1.4$) we can compare most unstable wavenumbers and growth rates for these liquids. Figures 4.13-4.16 show that for shear thinning liquids both k^* and ω_r increase for increasing rotation rates whereas for shear thickening liquids k^* and ω_r initially increase with $\mathcal{R}b$ but then this

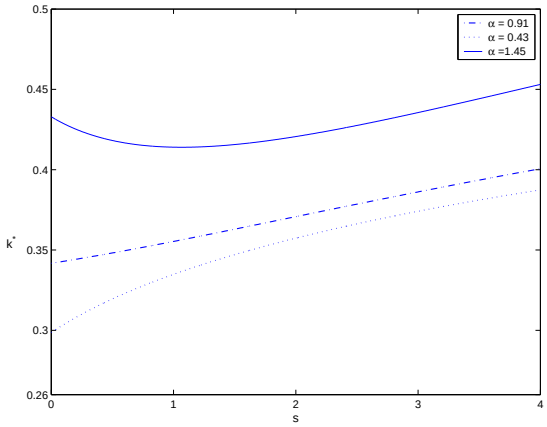

Figure 4.10: Graph showing the wavenumber of the most unstable mode k^* plotted against arc length s of the jet for various values of α. Here $\tilde{\mathcal{R}}e_\alpha = 3.0$, $We = 20$ and $\mathcal{R}b = 4.0$.

trend switches so that jets with high $\mathcal{R}b$ numbers have smaller values of k^* and ω_r than jets with lower $\mathcal{R}b$ numbers. In Figures 4.17 & 4.18 we see that as the surface tension of the liquid is increased k^* and ω_r increase for both shear thinning and thickening liquids. In the case of viscosity (Figs. 4.19 & 4.20) we find that decreasing the viscosity of the liquid results in larger values of k^* and ω_r. For very low viscosities we can compare our results to those of an inviscid spiralling jet considered by Wallwork *et al.* (2002b). In this case Wallwork *et al.* (2002b) has shown that the growth rate of disturbances along the jet can be expressed as

$$\omega_r = \sqrt{\frac{1}{We}\left(\frac{1}{R^2} - k^2\right) k \frac{I_1(kR)}{I_0(kR)}}, \tag{4.52}$$

where I_m is the modified Bessel function of order m and the most unstable mode occurs when $k = k^* = 0.697/R$. Equation (4.52) is obtained without the need to take the long wavelength limit. Taking the inviscid limit of Eq. (4.50) we get

$$\omega_r = \sqrt{\frac{k^2(1-(kR)^2)}{2RWe}}, \tag{4.53}$$

which coincides with (4.52) if an expansion to the lowest order in kR (since $kR < 1$ we can expand the Bessel functions and keep leading order terms) is made, i.e., the long

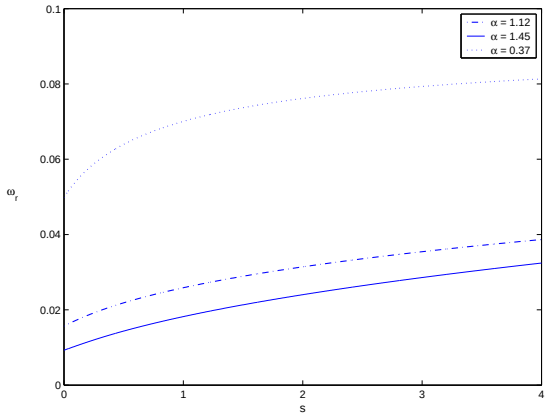

Figure 4.11: Graph showing the growth rate ω_r (of the most unstable mode k^*) plotted against the arclength s for various values of α at a high rotation rate. Here $\tilde{\mathcal{R}}e_\alpha = 3.0$, $We = 20$ and $\mathcal{R}b = 0.75$.

wavelength limit of (4.52) also gives (4.53). By taking a large value of the Reynolds number so that the jet is effectively inviscid, we can plot the growth rate ω_r (as given by (4.50)) against the arc length s for various Weber numbers (Fig. 4.21); reassuringly, this is in agreement with Wallwork *et al.* (2002*b*).

In all the figures 4.9-4.20, it can be seen that k^* and ω_r mainly, but not always increase with arclength (for exceptions see figures 4.9 -4.12, 4.15 and 4.16). Therefore, the wavelength ($= 2\pi/k^*$) of the most unstable mode mainly (but not always) decreases as it travels upstream along the jet (see also Uddin *et al.* (2006)).

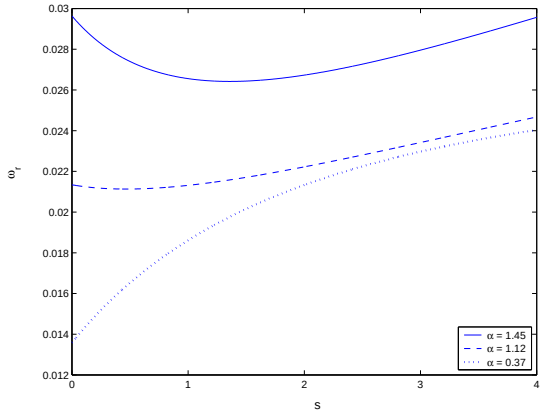

Figure 4.12: Graph showing the growth rate ω_r (of the most unstable mode k^*) plotted against the arclength s for various values of α at a low rotation rate. Here $\tilde{\mathcal{R}e}_\alpha = 3$, $We = 20$ and $\mathcal{R}b = 4.0$.

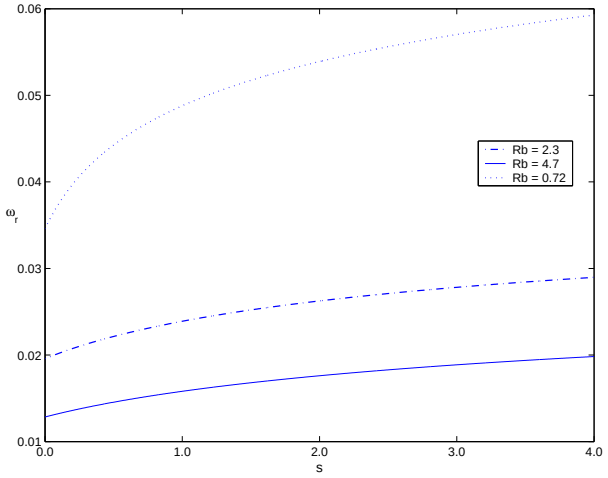

Figure 4.13: Graph showing the growthrate ω_r of the most unstable mode plotted against the arclength s for a shear thinning liquid ($\alpha = 0.63$). Here $\tilde{\mathcal{R}e}_\alpha = 3.0$ and $We = 20$. We see that the growth rate increases as the rotation rate is increased.

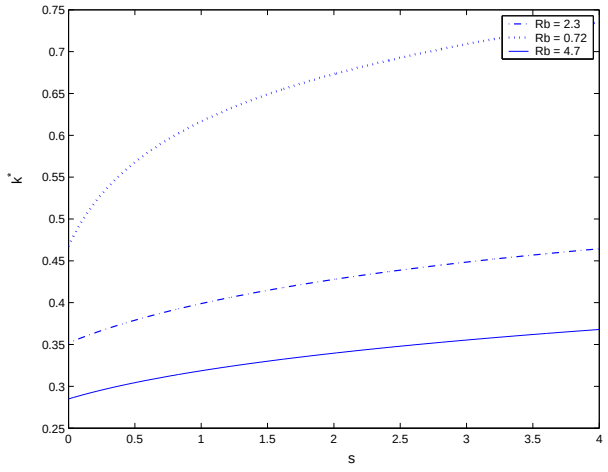

Figure 4.14: Graph showing the wavenumber k^* of the most unstable mode plotted against the arclength s for a shear thinning liquid ($\alpha = 0.63$). Here $\tilde{\mathcal{R}}e_\alpha = 3.0$ and $We = 20$. We see that the most unstable wavenumber, like the growth rate, increases with the rotation rate.

4.4 Discussion

Linear travelling wave disturbances along curved power law non-Newtonian liquid jets were examined. In particular the growth rates and most unstable wavenumbers associated with shear thinning fluids and a shear thickening fluids were investigated and compared to Newtonian fluids.

It is found that the rotation rate of the container can alter the growth rates and wavenumbers of disturbances for shear thinning and shear thickening liquids. Since disturbances are convected along the jet and ω_r is a measure of the growth of these disturbances we expect greater (lesser) instability for larger (smaller) values of ω_r thus leading to shorter (longer) jets. The wavelength of disturbances along the jet is inversely related to the wavenumber k^* so that for larger (smaller) values of k^* we expect smaller (larger) droplets. When the cylindrical container rotates with a high rotation rate we can expect longer jets with larger droplets for shear thickening liquids in comparison with shear thinning liquids. In the case of low rotation rates this trend is reversed. Decent *et al.* (2007) showed that Newtonian jets are generally longer and produce smaller drops as the

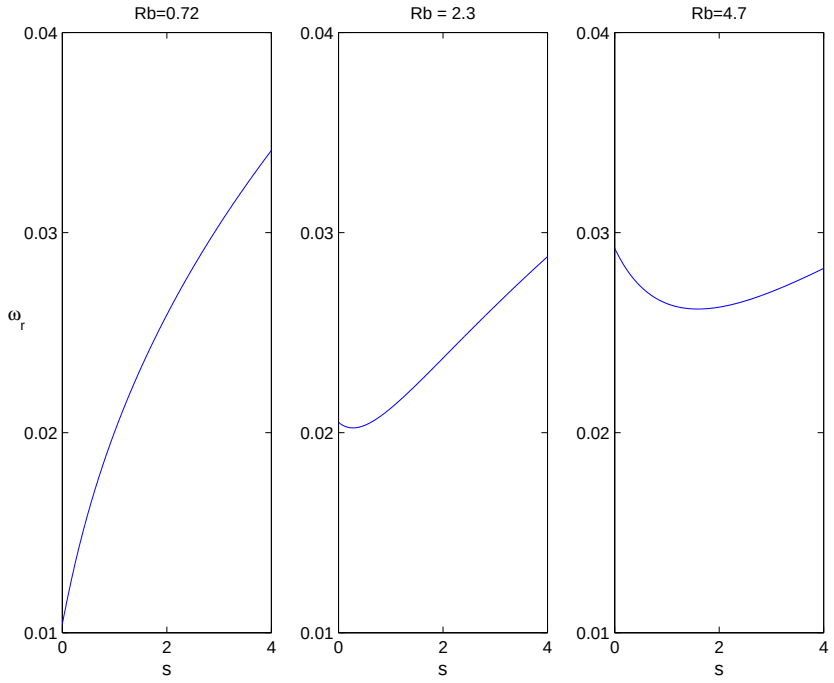

Figure 4.15: Graph showing the growth rate ω_r of the most unstable mode plotted against the arclength s for a shear thickening liquid ($\alpha = 1.36$). Here $\tilde{\mathcal{R}}e_\alpha = 3.0$ and $We = 20$.

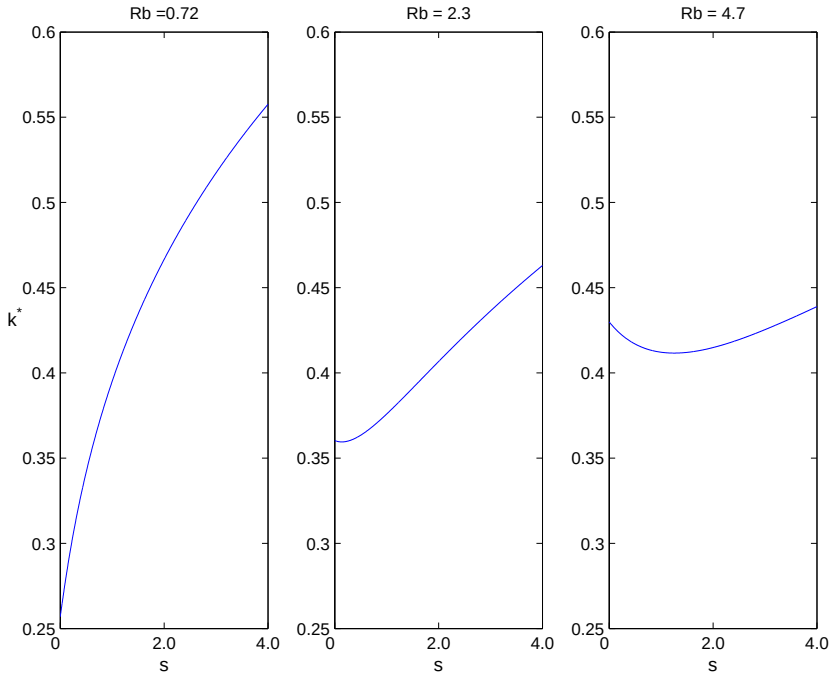

Figure 4.16: Graph showing the wavenumber k^* of the most unstable mode plotted against the arclength s for a shear thickening liquid ($\alpha = 1.36$). Here $\tilde{\mathcal{R}}e_\alpha = 3.0$ and $We = 20$.

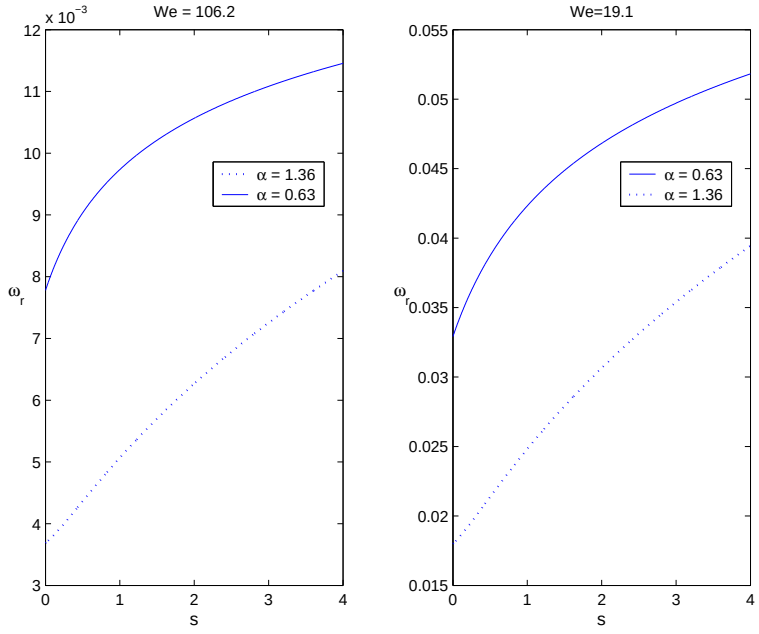

Figure 4.17: Graph showing the effects of surface tension on the growth rate ω_r of the most unstable mode plotted against the arclength s for a shear thickening liquid ($\alpha = 1.36$) and a shear thinning liquid ($\alpha = 0.63$). Here $\mathcal{R}b = 1.21$ and $\tilde{\mathcal{R}}e_\alpha = 3.8$.

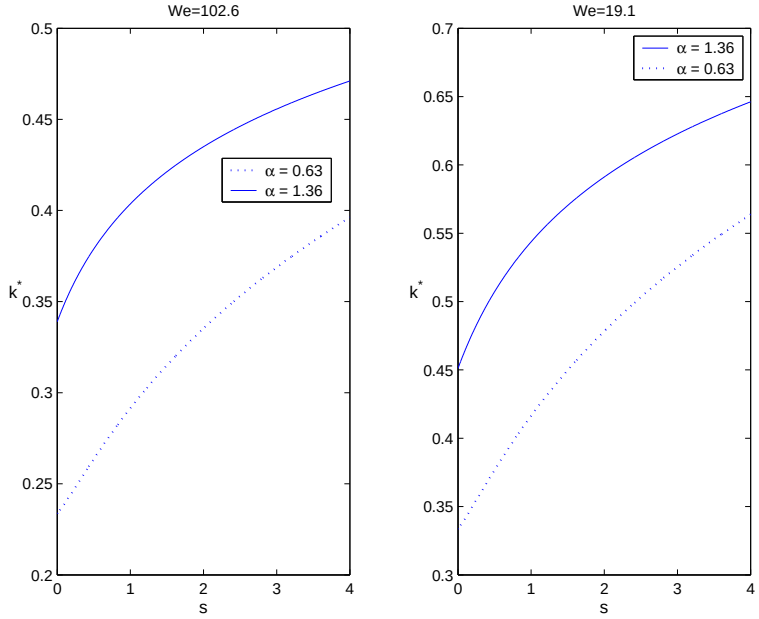

Figure 4.18: Graph showing the effects of surface tension on the wavenumber k^* of the most unstable mode plotted against the arclength s for a shear thickening liquid ($\alpha = 1.36$) and a shear thinning liquid ($\alpha = 0.63$). Here $\mathcal{R}b = 1.21$ and $\tilde{\mathcal{R}}e_\alpha = 3.8$.

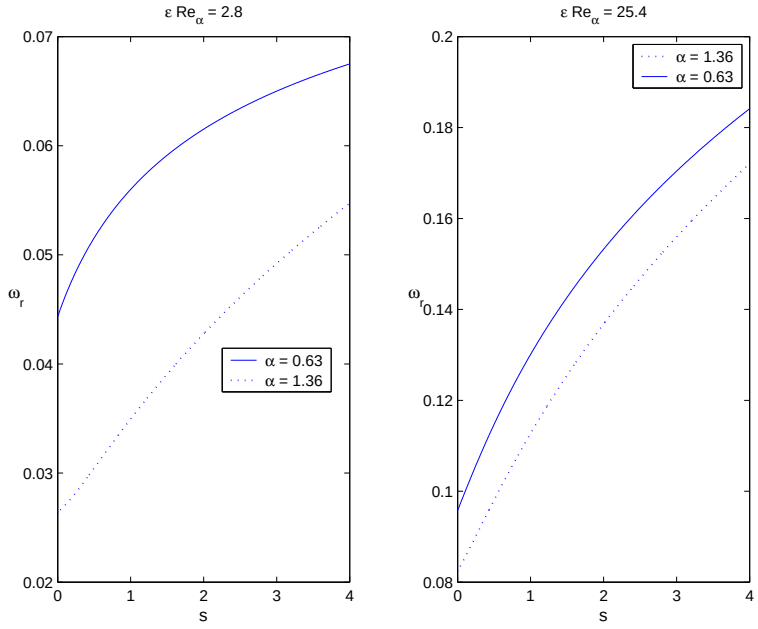

Figure 4.19: Graph showing the effects of viscosity on the growthrate ω_r of the most unstable mode plotted against the arclength s for a shear thickening liquid ($\alpha = 1.36$) and a shear thinning liquid ($\alpha = 0.63$). Here $\mathcal{R}b = 1.3$ and $We = 10.0$.

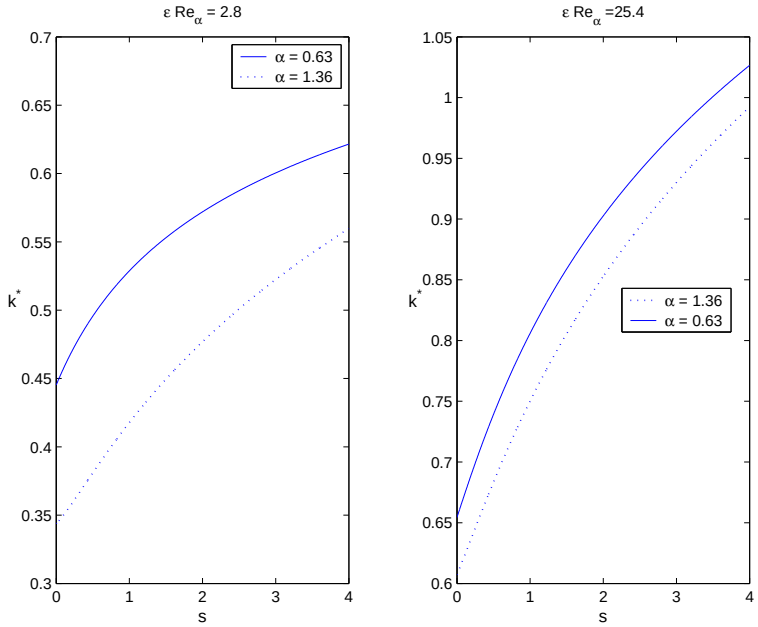

Figure 4.20: Graph showing the effects of viscosity on the wavenumber k^* of the most unstable mode plotted against the arclength s for a shear thickening liquid ($\alpha = 1.36$) and a shear thinning liquid ($\alpha = 0.63$). Here $\mathcal{R}b = 1.3$ and $We = 10.0$.

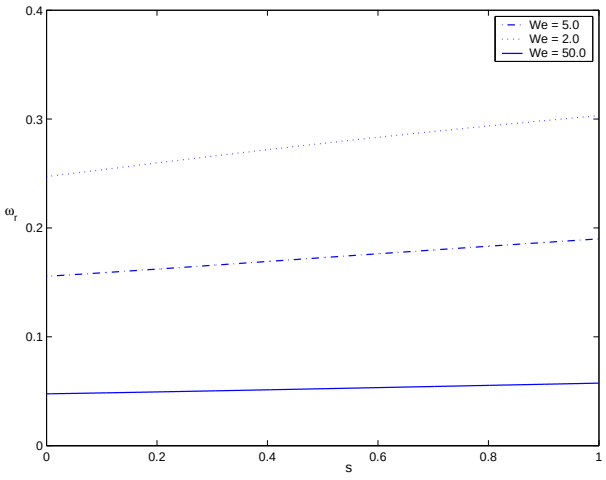

Figure 4.21: Graph showing the arc length s against the growth rate of the most unstable mode for various Weber numbers when the liquid is almost inviscid ($\mathcal{R}b = 2.0$ and $\tilde{\mathcal{R}}e_\alpha = 300$).

rotation rate is increased which corresponds well with the behaviour of shear thinning liquids.

For both shear thinning and shear thickening liquids viscosity is found to impede the growth of disturbances so that more viscous jets are longer and produce larger droplets. This agrees with the Newtonian case considered by Decent *et al.* (2007). Surface tension is found to enhance the growth of disturbances so that jets with high surface tension produce shorter jets and smaller drops. In the case where the Reynolds number is large, we can expect the effects of non-Newtonian viscosity to diminish and our results for the most unstable wavenumbers and growth rates will correspond to those of Wallwork *et al.* (2002*b*)

As we have already remarked, linear theory can be used to give an idea of the instability of power law liquid jets but the actual break up of a liquid jet and subsequent satellite droplet formation is dominated by nonlinear effects. These effects will be considered in the following chapter.

Chapter 5

Spiralling Liquid Jets: Nonlinear

5.1 Nonlinearity of pinch-off

In the previous chapter we used an asymptotic method to derive a set of one dimensional equations for rotating power law liquid jets. A temporal instability analysis was performed to give us a dispersion equation for the growth rate and wavenumber of disturbances along the jet. For straight liquid jets the growth rates and wavenumbers along the jet are constant and do not, in general, depend upon the distance along the jet. This allows an estimation of the breakup length and predicted drop sizes upon breakup. For rotating liquid jets, the growth rate and wavenumber vary along the jet and so little information is available to even provide good estimates of drop sizes or breakup lengths and only a qualitative description is possible. Moreover, linear theory is effective in only describing the evolution of the jet as breakup is approached and is unable to provide an accurate description of the jet near the region of breakup. More importantly, linear theory is unable to predict two experimentally observed processes: the non uniformity in breakup and the formation of satellite droplets. With this in mind, in this chapter, we shall investigate drop formation and breakup using numerical methods.

In the previous chapter, in the asymptotic analysis of the momentum equations, we

started off by using the leading order pressure term given by $\frac{\sigma}{R}$ which is asymptotically valid. We then went on to use the full curvature term in the pressure so that we had

$$p = \kappa/We = 1/We((1+\varepsilon^2 {R_s}^2)^{-\frac{1}{2}} - \varepsilon^2 R_{ss}(1+\varepsilon^2 {R_s}^2)^{-\frac{3}{2}}).$$

Although such a procedure is 'ad hoc', the following argument is used to justify retaining full curvature expressions; away from the breakup point where the effect of disturbances are less important, the mean curvature of the free surface is dominated by variations across the jet and thus using the expression for the pressure to leading order is asymptotically valid for the mean flow. However in the region near breakup, experiments for Newtonian jets reveal the formation of a small spherical drop connected by a slender neck (many magnitudes smaller in the case of highly viscous fluids). The existence of such asymmetrical shapes near breakup gives weight to retaining the expression for the full curvature. Without this expression for the full curvature, the jet is unstable to arbitrarily short wavelengths, which is clearly not true[1]. This approach has been used for Newtonian jets by a number of authors including Lee (1974), Brenner *et al.* (1997) and Papageorgiou (1995) and for viscoelastic jets by Li & Fontelos (2003). Brenner *et al.* (1997) showed that retaining the full curvature terms give correct equilibrium shapes and that growing oscillations caused by short wavelengths in numerical simulations are effectively dissipated without resorting to any artificial means.

In our introduction to liquid jets we showed how tiny disturbances on the surface of a column of liquid can lead to pressure gradients along the axis of the liquid column. This phenomenon is shared by liquid jets and indeed breakup in liquid jets depends very much upon the formation of pressure gradients along the jet. In the case of Newtonian

[1]In addition, in the thin threads all the assumptions of the quasi-one-dimensional asymptotic theory are satisfied. However, in droplets there is practically no liquid motion and internal stresses are small and as a result the flow parameters also vary slowly in the cross section. Thus, assumptions of a quasi-one-dimensional theory are satisfied despite the fact that the region near droplets is not 'slender'. See also Yarin (1993).

jets, Goedde & Yuen (1970) showed that near the breakup point there is a strengthening of the pressure gradient caused by non-linear effects. Thus locally around this point, a divergence of the velocity (i.e., a spatial gradient) is set up along the axis of the jet. Incompressibility of the fluid forces the jet to contract where the divergence is greatest, i.e., at the minimum jet radius. Viscosity is found to have both a dissipating and inhibiting effect on the strengthening of pressure gradients so that breakup takes longer.

Inelastic power law liquid jets behave in very much the same way as Newtonian jets but in this case the apparent viscosity η, namely (4.30) which we rewrite here for convenience,

$$m|\sqrt{3}u_{0s}|^{\alpha-1}\left(1+(\varepsilon n)\frac{(\alpha-1)}{u_{0s}}\left(\left(u_0(X_{0s}Z_{0sss}-Z_{0s}X_{0sss})-\frac{u_{0s}}{2}(X_{0s}Z_{0ss}-Z_{0s}X_{0ss})\right)\cos\phi\right.\right.$$

$$\left.\left.-w_1\sin\phi(X_{0s}Z_{0ss}-Z_{0s}X_{0ss}))+O((\varepsilon n)^2)\right)\right. . \tag{5.1}$$

has a leading order component which is a function of the spatial gradient of the velocity (as is the case with most uniaxial flows). Thus, for power law jets, near the breakup point, as the pressure gradient is strengthened the velocity gradient increases which will either reduce or increase the apparent viscosity depending on the magnitude of u_s and on whether the fluid is shear thinning or shear thickening. This in turn will require a lower or greater pressure gradient to break the jet. This characteristic shear rate dependent viscosity in power law liquids has been a major obstacle to progress in microfluidic devices (see Squires & Quake (2005)).

5.2 The Method of Finite Differences

The advent of microprocessors with their ability to perform large computational tasks in relatively little time has led to a multitude of papers which are primarily concerned with numerical simulations of liquid jets (see for example Lee (1976), Bousfield *et al.* (1990), Eggers and Dupont (1994) and Papageorgiou (1995)). Yet life is far from easy when

modelling free surface flows since it is these types of flows which are vulnerable to the formation of cusp singularities (Joseph *et al.* 1991). The wide range of computational techniques available to the researcher has meant that different flow scenarios are best solved using different methods. For example if the flow is irrotational and inviscid or alternatively very viscous so that the Stokes flow is applicable then a boundary integral method is appropriate. Whereas if the flow domain is irregular then a finite element approach is better (although boundary integral methods are also very efficient for unusual or irregular boundaries). In almost all cases finite difference techniques can be used but like all numerical methods they are prone to instabilities which develop as the flow progresses.

Almost all the numerics in this section, as well as in the following chapter, are based on finite difference schemes and in particular flux conservative initial value problems. Thus in this section, we shall examine some of these schemes which we shall go on to use later.

In many cases when modelling a number of flow situations the PDEs can be recast in the form of a *flux conservative* equation,

$$\frac{\partial \boldsymbol{u}}{\partial t} = -\frac{\partial}{\partial \boldsymbol{x}} \boldsymbol{F}(\boldsymbol{u}),$$

where in general the *flux vector* $\boldsymbol{F}$ can depend upon $\boldsymbol{u}$ as well as upon spatial derivatives of $\boldsymbol{u}$. There are a number of methods which can be used to solve such equations numerically (see Press *et al.* (2001), Hirsch (1990, vol.1 and vol.2) and DuChateau & Zachmann (1989)) but in this section we will limit ourselves to *explicit* schemes and in particular the two step *Lax Wendroff* scheme also known as the *Richtmyer* scheme and a variant of the same scheme known as *McCormack's* scheme.

Before going on to consider the application of such schemes to a PDE let us first mention some of the basics behind finite difference schemes. In general a partial differential

equation will have a domain on which it is applicable. Usually this will involve a time domain and a spatial domain (more spatial domains can be included if required). The aim of finite difference methods is to provide an approximation to the continuous solution on a *finite* number of grid points called *nodes*. These grid points (at which the solutions will be defined) must be chosen in some way, once chosen they form what is called the *mesh*. The choice of how to choose these grid points depends on many factors and this is not the place to go into an in depth discussion of such things. For our purposes it will suffice to choose grid points so that they are uniform, that is the distance between grid points will be fixed. When considering a time domain along with one space domain the mesh may be represented on a 2D diagram (see Fig. 5.1). For a bounded spatial domain say $x \in [a, b]$ we can choose n nodes along this domain by placing them a distance $\Delta x = (b-a)/n$ apart from a, where we call Δx the spatial step size. The ith spatial node is chosen to refer to the grid point located at $a + i\Delta x$ along the spatial axis. In general the time domain is unbounded (say $t > 0$) but this does not prevent us from choosing equally spaced grid points, we simply choose an appropriate time step Δt and place grids Δt apart such that the nth grid line is located a distance $n\Delta t$ from the initial time. We denote by u_i^n the approximate solution of u at the ith (subscript) space node and the nth (superscript) time node. Let us now consider some simple PDEs.

In the scalar case when the flux term $\boldsymbol{F}$ is equal to $f(u, x, t)$, we have the one dimensional convection equation $u_t + f_x = 0$ for which an explicit scheme can be written as

$$u_i^{n+1} - u_i^n = -\frac{C_\sigma}{2}(f_{i+1}^n - f_{i-1}^n),$$

where σ is known as the *Courant* number and is a measure of the ratio between individual time steps and space steps. This method is known to be unstable (see e.g. Hirsch (1990) Vol. 2). A slight modification of the above scheme results in the so called *Lax Friedrichs*

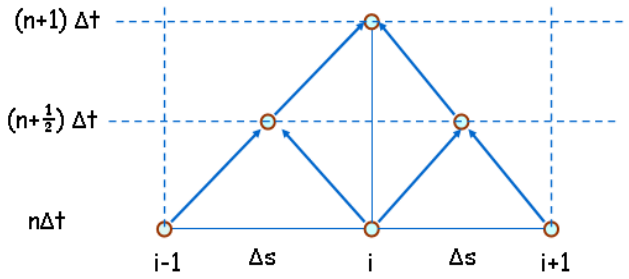

Figure 5.1: A stencil of the Richtmyer Scheme (two-step Lax-Wendroff method) on a uniform grid. Here the spatial dimension is represented by s.

scheme which is given by

$$u_i^{n+1} = \frac{u_{i+1}^n + u_{i-1}^n}{2} - \frac{\sigma}{2}(f_{i+1}^n - f_{i-1}^n).$$

This method is stable but only first order accurate in both time and space.

To cater for nonlinearities and at the same time achieve greater accuracy, second order space centered schemes are used. The *Richtmyer* scheme is the basis of many predictor-corrector schemes which can handle nonlinearities relatively easily. In this scheme an intermediate time step is introduced and the whole solution is moved one time step in two steps (hence this scheme is also known as the two step Lax Wendroff scheme). The scheme can be written as

$$u_{j+\frac{1}{2}}^{n+\frac{1}{2}} = \frac{1}{2}(u_{j+1}^n + u_j^n) - \frac{\Delta t}{2\Delta x}(f_{j+1}^n - f_j^n),$$

$$u_j^{n+1} = u_j^n - \frac{\Delta t}{\Delta x}(\tilde{f}_{j+\frac{1}{2}}^{n+\frac{1}{2}} - \tilde{f}_{j-\frac{1}{2}}^{n+\frac{1}{2}}),$$

where the intermediate fluxes $\tilde{f}_{j+\frac{1}{2}}^{n+\frac{1}{2}}$ are calculated using $u_{j+\frac{1}{2}}^{n+\frac{1}{2}}$ (see also Fig. 5.1).

In some cases the two step predictor-corrector scheme known as *McCormack's* scheme can cope with nonlinearities better. This scheme does not utilize an intermediate step

and the scheme can be written as

$$\tilde{u}_i = u_i^n - \frac{\Delta t}{\Delta x}(f_{i+1}^n - f_i^n),$$

$$u_i^{n+1} = \frac{1}{2}(u_i^n + \tilde{u}) - \frac{\Delta t}{2\Delta x}(\tilde{f}_i - \tilde{f}_{i-1}),$$

where $\tilde{f}_i = f(\tilde{u}_i)$.

We show an example of how to implement the two-step Lax-Wendroff scheme for a rotating shear thinning liquid jet in Appendix G (pages 280-282).

5.3 Newtonian Jet Simulation

We can use the above scheme to simulate the breakup of a Newtonian liquid jet. Our method will follow that of Yarin (1993) and we shall be considering a periodic jet having radius R and velocity u given by the equations

$$\frac{\partial R^2}{\partial t} + \frac{\partial (R^2 u)}{\partial z} = 0, \tag{5.2}$$

$$\rho\left(\frac{\partial u}{\partial t} + u\frac{\partial u}{\partial z}\right) = -\frac{\partial p}{\partial z} + 3Oh\frac{\partial^2 u}{\partial z^2}, \tag{5.3}$$

which we derived earlier in Section 2.3. In this case we shall assume that the pressure can be taken to have the form

$$p = \frac{\kappa}{We} = \frac{1}{We}\left(\frac{1}{(1+\varepsilon^2 {R_z}^2)^{\frac{1}{2}}} - \frac{\varepsilon^2 R_{zz}}{(1+\varepsilon^2 {R_z}^2)^{\frac{3}{2}}}\right)$$

where the aspect ratio ε is used which is the ratio of the typical length scale in the radial direction of the jet to the typical length scale along the jet.

As the initial condition we take a perturbed radius and unperturbed velocity, i.e., we

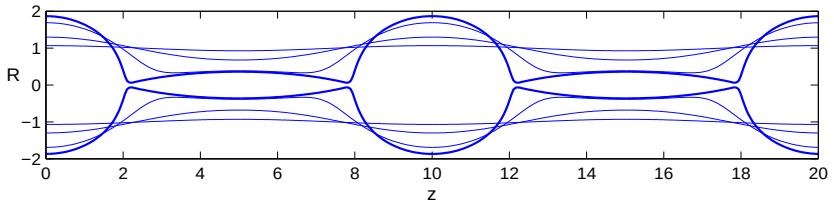

Figure 5.2: The profile of a Newtonian liquid jet at the point of rupture. A two-step Lax-Wendroff scheme is used to solve equations (5.2) and (5.3). The development of a neck (i.e., the ligament between two droplets) and subsequent satellite drop formation can be observed. The Ohnesorge number here is equal to 0.1 and the profiles shown correspond to the non-dimensional times 2.5, 7.5, 10.0 and 10.55 respectively.

have

$$R(z,0) = 1 + 0.05\cos(2\pi z/L) \quad \text{and} \quad u(z,0) = 0.$$

Since we are considering a periodic jet we require the boundary conditions

$$R_z(0,t) \;=\; R_z(L/2,t) \;=\; 0, \qquad\qquad u(0,t) \;=\; u(L/2,t) \;=\; 0.$$

In Fig. 5.2 we use a uniform grid with 200 spatial steps and considering a periodic jet of length $L = 10$ to simulate the evolution of the Newtonian liquid jet until an arbitrary minimum radius. We use a finite difference scheme based on the method of Richtmyer (see preceding section). We stop our numerical scheme when the jet radius has reached 2.5 % of its initial value[2]. Drop formation is characterized by a fluid being forced away from the center towards the ends, which leads to the development of a neck which contracts at either end near the drops. The velocity at these extreme neck regions increases until breakup. Increasing the Ohnesorge number (which is effectively increasing the viscosity of the fluid) leads to smaller satellite formation and for very large Ohnesorge numbers the characteristic neck formation is not observed.

[2]Since the equations to be solved (i.e., (5.2) and (5.3)) contain third order derivatives we found that when the jet radius becomes very small the corresponding pressure becomes very large. Our numerical scheme becomes increasingly unstable as $t \to \infty$ and $R \to 0$. Greater accuracy can however be obtained using more grid points. In any case, there is rapid decay of the jet radius when the jet radius becomes small.

5.4 Non-Newtonian Jet Simulation

We now turn our attention to solving the equations we obtained in the previous chapter which for ease of reference we rewrite here again,

$$u_t + uu_s = -\frac{1}{We}\left(\frac{1}{R(1+\varepsilon^2 R_s^2)^{\frac{1}{2}}} - \frac{\varepsilon^2 R_{ss}}{(1+\varepsilon^2 R_s^2)^{\frac{3}{2}}}\right)_s + \frac{(X+1)X_s + ZZ_s}{\mathcal{R}b^2} + \frac{3|\sqrt{3}u_s|^{\alpha-1}}{\mathcal{R}e_\alpha}\left(\alpha u_{ss} + 2u_s\frac{R_s}{R}\right), \quad (5.4)$$

$$R_t + \frac{u_s}{2}R + uR_s = 0. \quad (5.5)$$

We should note that we have retained the full curvature term in the above expression for the pressure. If we make a slight change of variable so that the position of the free interface is given by $A = A(s,t)$ where we define $A(s,t) = R^2(s,t)$, we can write our equations as

$$\frac{\partial A}{\partial t} = -\frac{\partial}{\partial s}(Au), \quad (5.6)$$

$$u_t + \left(\frac{u^2}{2}\right)_s = -\frac{1}{We}\frac{\partial}{\partial s}\frac{4(2A + (\varepsilon A_s)^2 - \varepsilon^2 AA_{ss})}{(4A + (\varepsilon A_s)^2)^{\frac{3}{2}}} + \frac{(X+1)X_s + ZZ_s}{\mathcal{R}b^2} + \frac{(3|\sqrt{3}u_s|^{\alpha-1}u_s A)_s}{\mathcal{R}e_\alpha}. \quad (5.7)$$

5.4.1 Numerical Method

We solve the above system of equations for s $\in [0, L]$ where L is the (numerical) length of the jet. For rotating liquid jets the jet radius along with the velocity vary down the jet and so we are unable to use the numerical scheme outlined above for a Newtonian jet (since in general we will not have periodic boundaries, see for example Yarin (1993)).

Instead, we shall solve this set of equations using the second order space centered explicit scheme of *Richtmyer* (see Richtmyer and Morton (1967)). The equations are discretized by using a second order method for first derivatives but first order for second derivatives. The initial values of $u(s,t)$ and $A(s,t)$ are taken to be equal to the steady state solution we discussed in the previous chapter (see section 4.2.5). Upstream boundary conditions which correspond to conditions at the nozzle[3] are chosen as

$$A(0,t) = 1, \qquad u(0,t) = 1 + \delta \sin\left(\frac{\kappa t}{\varepsilon}\right), \tag{5.8}$$

where κ is a non-dimensional wavenumber which in our case may also be viewed as a disturbance frequency and δ is the magnitude of the initial disturbance which is non-dimensionalised with respect to the initial jet radius a. In most industrial problems (see Andersen & Yttri (1997)) as well those experiments performed in the lab (see Wong *et al.* (2004)) the aspect ratio $\varepsilon = a/s_0$ (which is the ratio of the radius of the orifice to the radius of the cylindrical tank) was approximately equal to 0.01 (although in some cases when using a smaller orifice the aspect ratio is naturally smaller). We shall, unless otherwise stated, use this value of ε throughout our numerical simulations. We have chosen to perturb the velocity although we could just as easily perturb the initial radius to induce instability. Apart from changing the system parameters we are free to alter both the frequency κ and the amplitude δ of the initial perturbation in our numerical scheme.

The time step must be chosen carefully to ensure convergence of the numerical scheme. Since the equations are nonlinear there is no realistic analytic bound we can put on the

[3]In experiments a whole spectrum of disturbances, with different amplitudes and wavenumbers, are generated at the nozzle. These disturbances interact with each other in a nonlinear way and can affect the breakup of a liquid jet. However in practice, as discussed in preceding chapters, the jet 'favours' the disturbance which leads to the greatest reduction in surface area. This is the so called Rayleigh, or most unstable mode. Thus in these simulations we implicitly assume that this (imposed) disturbance is responsible for the ultimate breakup of the jet. We will go on to investigate jets which have more complicated boundary conditions in connection with insonification of liquid jets (see Chapter 8).

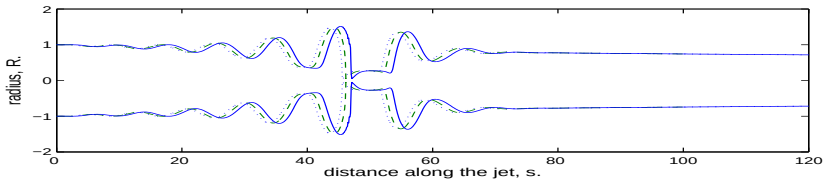

Figure 5.3: A check of the accuracy of the numerical scheme. The solid, dashed and dotted lines represent the spatial step size ds = 1e-3, 5e-4 and 2.5e-4 respectively. The parameters used here are $\mathrm{Re}_\alpha = 30$, We=10, $\mathcal{R}b = 4$, κ=0.89 and $\alpha = 0.6$.

time step, except perhaps to ensure that at the very least, the Courant condition (that the time step be less than half the square of the space step) be observed. In reality we choose a time step much smaller than this, which inevitably leads to relatively longer computational times. One way of reducing long computer times would be to use implicit methods, which do not have such constraints upon the time step and at the same time are capable of better numerical accuracy. Since a number of authors (see Classen *et al.* (2005) and Li & Fontelos (2003)) have found that in the case of viscoelastic straight jets, explicit schemes do not differ significantly to implicit schemes, and in any case for Newtonian spiralling jets Părău *et al.* (2004) showed favourable comparisons between solutions obtained using explicit methods and an implicit Crank-Nicholson method, we shall stick with explicit schemes throughout this chapter[4].

Implementing the numerical boundary condition at the nozzle into the numerical method is rather complex as mentioned in Părău *et al.* (2007) although Sirignano & Mehring (2000) have a more detailed discussion in their work on annular sheets. The downstream boundary condition can be obtained by quadratic extrapolation of the last internal mesh point. Apart from the case when the Weber number is exceptionally small, the boundary condition at the far end of the liquid jet will only influence the jet in a

[4]Explicit schemes were chosen for a number of reasons, firstly, a comparison could be made with previous explicit codes written in FORTRAN for a spiralling Newtonian liquid jets. Secondly, in initial attempts the author found great difficulty in implementing the boundary conditions at the nozzle when using an implicit scheme.

narrow region close to it[5] (see Yarin (1993)). For two-step Lax-Wendroff schemes, and in particular for the Richtmyer scheme, space extrapolation techniques do not destablise these schemes (see Griffin & Anderson (1977) and Gottlieb & Turkel (1978)).

We have chosen breakup to occur when the non-dimensional jet radius has reached a arbitrarily small value which for consistency with earlier works (Părău *et al.* (2006, 2007)) we choose to be five per cent of the initial jet radius. Downstream of the breakup point, where the jet is expected to breakup into droplets, our numerical solution has no real physical meaning, as is also the case in other works.

The accuracy of the numerical scheme is checked by refining the mesh. An example for a shear thinning ($\alpha = 0.6$) liquid jet is shown in Fig. 5.3. Throughout the rest of this thesis, unless otherwise stated, we will use an uniform spatial grid of grid size $ds = 5e-4$.

5.5 Numerical Results

In order to investigate the different effects on breakup dynamics and drop formation in shear thickening and shear thinning spiralling jets we have chosen to consider liquids with flow index numbers $\alpha = 1.4$ and $\alpha = 0.6$ respectively. We will take these flow index numbers to be representative of the two types of liquids under consideration here, although we should note, that such values of the flow index numbers are modest and in reality liquids (particularly shear thinning liquids) with much more extreme values of the flow index number (e.g., grease which has a flow index number of approximately 0.1) do exist. Nevertheless, since our aim here is to identify some of the inherent differences in the structure of breakup for such liquids, the chosen two values of the flow index numbers will suffice. In order to avoid unnecessary repetition we will henceforth refer to these as liquid A ($\alpha = 1.4$) and liquid B ($\alpha = 0.6$) respectively.

In our simulations we found that we were unable to investigate very high viscosity

[5]In addition the numerical 'end' of the jet must be sufficiently chosen far downstream of the breakup point that 'information' is not propagated from the numerical end of the jet.

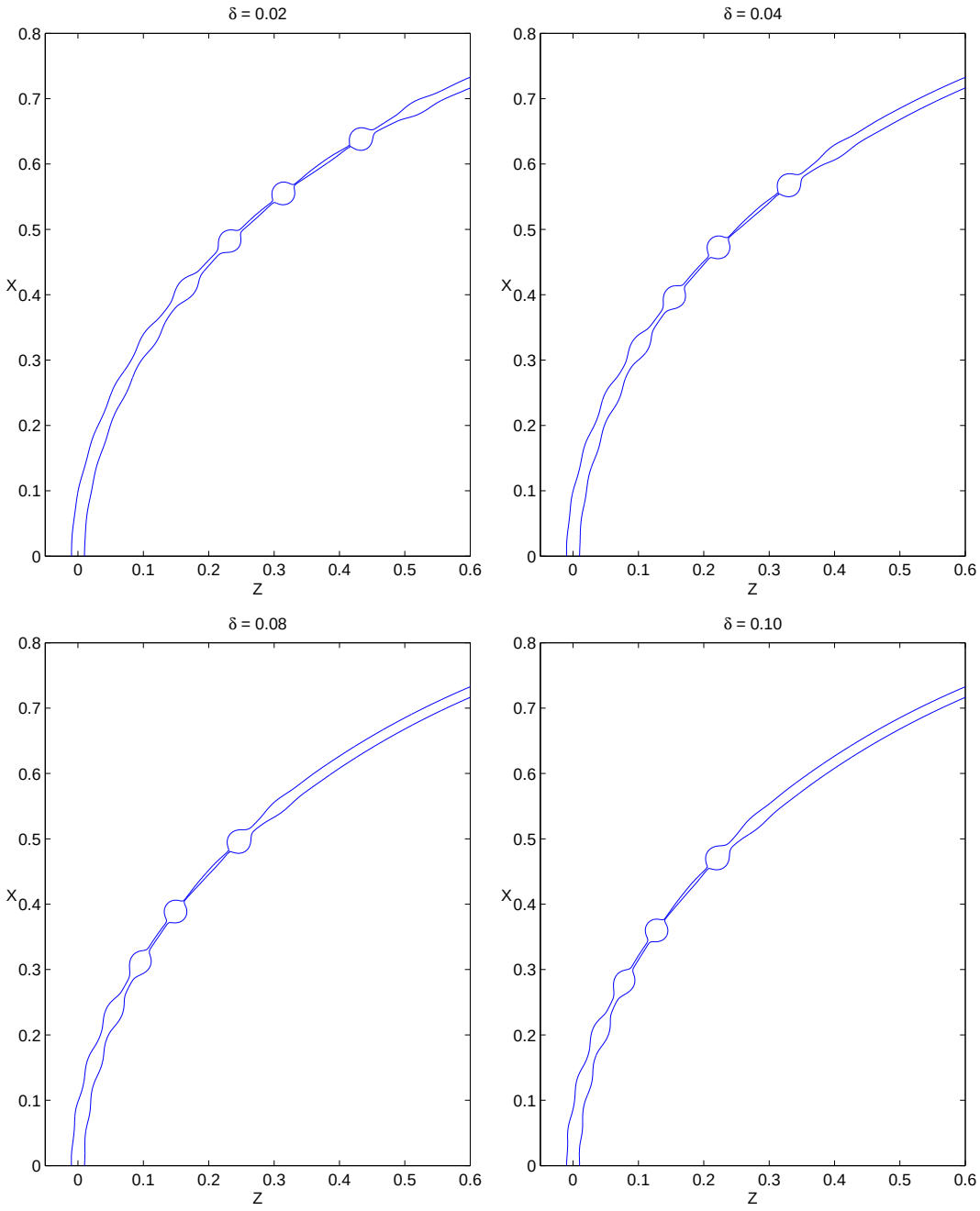

Figure 5.4: The profile at breakup for a rotating shear thickening ($\alpha = 1.4$) liquid jet for different initial perturbation amplitudes $0.02 \leqslant \delta \leqslant 0.1$. We see shorter breakup lengths, as expected, when the initial disturbance amplitude is large. Here $\mathcal{R}e = 30$, $We = 10$, $\mathcal{R}b = 1$, and $\kappa = 0.89$. The numerical length of the jet was taken as 120 jet radii.

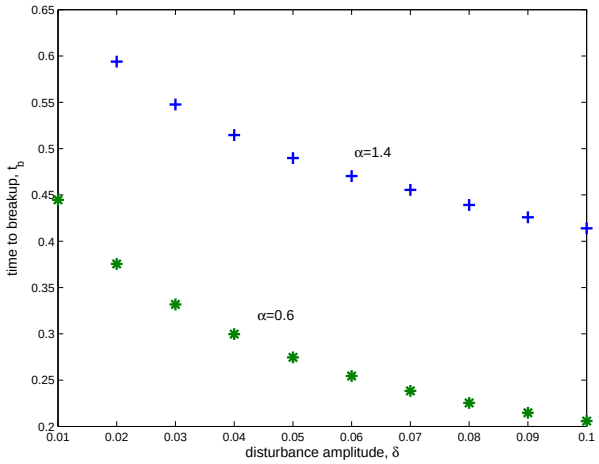

Figure 5.5: The time taken to breakup for liquid A and liquid B against the initial disturbance amplitude δ. Jets are shorter and take less time to break as the δ is increased. Here $\mathcal{R}e = 30$, $We = 10$, $\mathcal{R}b = 1$ and $\kappa = 0.89$.

liquids due to the prohibitively small time step imposed by the Courant condition[6]. Also we stopped our numerical scheme when the minimum radius reached $0.05a$. We took the location of this minimum to be the 'breakup point' of our jet. In most of our simulations the drops were well formed and the ligaments between them were clear (this was especially true for shear thickening liquids). In the case where drops could not be clearly distinguished (usually for low viscosity shear thinning liquids) we evaluated[7] the volume of liquid between the breakup point and the closest adjacent minimum of the jet (this

[6] Although this may appear restrictive in exploring very viscous jet breakup, in reality since the steady centreline solution is only valid when the viscosity of the liquid jet is small, and becomes progressively weaker when the viscosity is increased, using the current method (or any other method for that matter) to investigate highly viscous fluids would be fruitless. At any rate, such highly viscous fluids are not of great industrial relevance to prilling.

[7] The volume of the drop was calculated using a volume of revolution for the jet profile at breakup, so that (this was numerically calculated using the Trapezoidal scheme)

$$V_{drop} = \pi \int R_0^2 ds,$$

whence the drop radius $\widehat{R}$ can be equated to a sphere so that

$$\widehat{R} = \left(\frac{3V_{drop}}{4\pi} \right)^{\frac{1}{3}}.$$

was necessary since in a number of cases we found that upstream of pinch-off the radius was not sufficiently small to convince us that breakup would take place there, and subsequently form a droplet, thus in such cases we assumed that breakup would take place where the profile of the jet assumed a minimum upstream of the pinch-off point).

In our simulations we found that increasing the amplitude of the initial perturbation on liquid A and liquid B both resulted in shorter jets, (we show some profiles for liquid A in Fig. 5.4) we also found that increasing the initial disturbance amplitude resulted in shorter breakup times (which correlates with the breakup length) for both types of liquids (see Fig. 5.5). There is an approximately exponential decay of breakup times with any increase in the initial disturbance amplitude. In addition to the effects upon breakup length, we found that main droplet sizes varied slowly as the disturbance amplitude was increased for both types of liquid (in fact the difference in droplets sizes in the range $0.01 < \delta < 0.1$ was less than 2% and were approximately of the order of 1.7). Satellite droplets for liquid A were found to become smaller as the disturbance amplitude was increased (see Fig. 5.6), where there is an almost exponential like decay in the size of satellite droplets against the disturbance amplitude (the equivalent analysis for liquid B could not be performed since for these parameter ranges no satellite droplets were observed). We should note here that for Newtonian liquid jets, Părău *et al.* (2007) has shown that main (satellite) droplet sizes increase (decrease) as the disturbance amplitude is increased until some critical δ is reached when this behaviour switches. This behaviour in the growth and decay of main and satellite droplet sizes with respect to the initial disturbance amplitude can be compared to similar solutions of Hilbing & Heister (1996), obtained using the boundary integral method. However in these simulations the Weber number is significantly higher than those considered in the present work. Our results here correspond well with those of Ashgriz & Mashayek (1996) who found that at a fixed wavelength, satellite droplets became smaller as δ was increased.

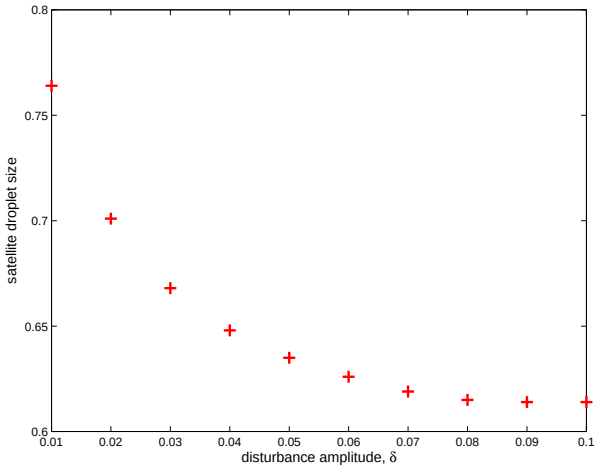

Figure 5.6: The size of satellite droplets for liquid A against the initial disturbance amplitude δ. It can be seen that there is an exponential decay in the size of satellite droplets as δ is increased. Here $\mathcal{R}e = 30$, $We = 10$, $\mathcal{R}b = 1$ and $\kappa = 0.89$. Main droplets are roughly the same size ≈ 1.7 for $0.01 < \delta < 0.1$.

Increasing the flow index number α produced longer jets in our simulations (Fig. 5.7). For the lowest value of the flow index number (namely $\alpha = 0.2$) we found that drops were not well formed (by this we mean that upstream of the pinch-off point the radius of the jet was not small enough to give a good impression of where breakup would take place) although the ligaments between two drops could be clearly distinguished. The appearance of further drops with adjoining ligaments appears as the flow index number is increased. For small α the difference in breakup lengths for jets with a Reynolds number of 10 and jets with a Reynolds number of 30 is relatively much smaller than the difference as α is increased (Fig. 5.8). Indeed, increasing the viscosity of the jet by a factor of three will almost double the breakup length for a Newtonian fluid ($\alpha = 1.0$) whereas for liquid B ($\alpha = 0.2$) the increase in breakup length is less than ten per cent. Additionally, satellite droplets become successively smaller as α is decreased whereas main droplets are relatively stable to changes in the flow index number (see Fig. 5.9).

We know from our earlier linear instability analysis that viscosity tends to stabilize disturbances so that droplets are larger and breakup lengths increase as the viscosity is

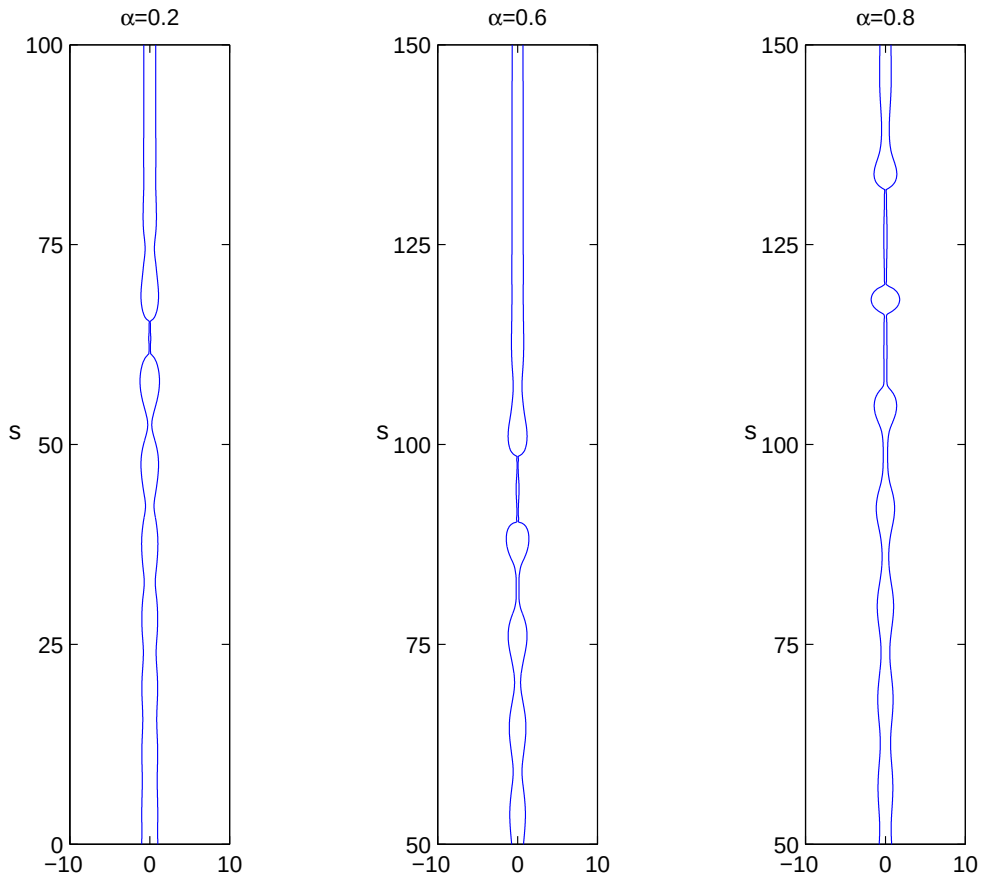

Figure 5.7: The profile at breakup for rotating shear thinning liquid jets for different flow index numbers ($\alpha = 0.2$ (Left), $\alpha = 0.6$ (Middle) and $\alpha = 0.8$ (Right)). The vertical axis represents the arclength distance s along the rotating jet. Here $\mathcal{R}e = 10$, $We = 20$, $\mathcal{R}b = 1$, $\delta = 0.01$ and $\kappa = 0.89$. It is important to note that the vertical axes for $\alpha = 0.6$ and $\alpha = 0.8$ begin at $s = 50.0$.

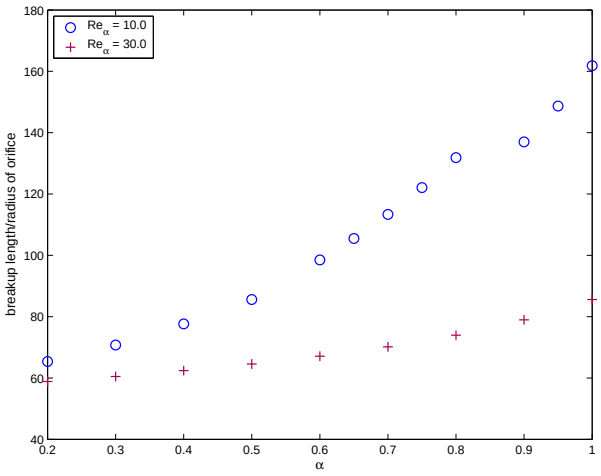

Figure 5.8: The breakup length of a rotating liquid jet for increasing values of the flow index number α. Here $\mathcal{R}b = 1$, $We = 20$ and $\kappa = 0.89$. As the flow index number is increased we see a significant increase in the difference between breakup lengths as the Reynolds number is varied between $\mathcal{R}e_\alpha = 10$ and $\mathcal{R}e_\alpha = 30$.

increased. In addition we know from our one dimensional evolution equations that for large Reynolds number we can effectively ignore the effects of non-Newtonian viscosity and consider the jet to behave as a Newtonian jet with low viscosity. The response of liquid A ($\alpha = 1.4$) to changes in the Reynolds number demonstrates this feature well (Fig. 5.10), where we see a reduction in the number of droplets produced combined with much shorter breakup lengths as the Reynolds number is increased. For low Reynolds number ($\mathcal{R}e_\alpha = 10$) we notice an increase in breakup lengths along with the appearance of many more droplets. There is also a dramatic elongation of the ligament between two main droplets, although these are now much more thinner than the ligaments found in the case of $\mathcal{R}e_\alpha = 300$.

In Fig. 5.11 we show how rotation rates affect breakup lengths and size of droplets (main and satellite) for liquids A and B. It was found that breakup lengths for liquid A decrease with decreasing rotation rate however the breakup length for liquid B is fairly stable to changes to rotation (in fact there is a non-monotonic relationship between breakup length and rotation rate with breakup lengths decreasing as the rotation rate is decreased

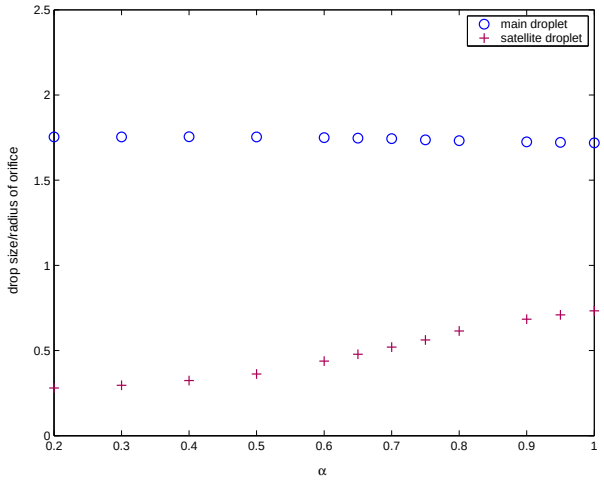

Figure 5.9: The size of droplets produced by a rotating liquid jet as the flow index number α is changed. Here $\mathcal{R}e_\alpha = 10$, $We = 20$, $\mathcal{R}b = 1.0$ and $\kappa = 0.89$. Satellite droplets become successively smaller as α is decreased whereas main droplets are relatively stable to changes in the flow index number.

from $\mathcal{R}b = 0.75$ to $\mathcal{R}b \approx 1.25$ after which it increases again as $\mathcal{R}b$ is increased). Both liquid A and B produce similar size droplets as the rotation rate is decreased (the size of droplets increasing with decreasing rotation rate in agreement with results for Newtonian spiralling jets). Satellite droplets for liquid A decrease in size with the rotation rate however no satellites were observed for liquid B. The profiles at breakup for different rotation rates in the case of liquid B is shown in Fig. 5.12. It can be seen that the breakup length increases as the rotation rate is increased with the ligaments connecting droplets being stretched so that they are longer (albeit much thinner) when compared to low rotation rates. In Fig. 5.13 we plot the profile of shear thickening liquid jets for low and high rotation rates. Droplet sizes can be seen to be larger and the ligaments between droplets are longer and bigger for high rotation rates.

In Figure 5.14 we show how changing the wavenumber (or alternatively the frequency) of perturbations at the orifice affects the breakup lengths for liquid A in the case of a low rotation rate ($\mathcal{R}b = 4$) and a high rotation rate ($\mathcal{R}b = 1$). The most unstable wavenumber is the wavenumber at which the breakup length is the smallest and as can be seen from

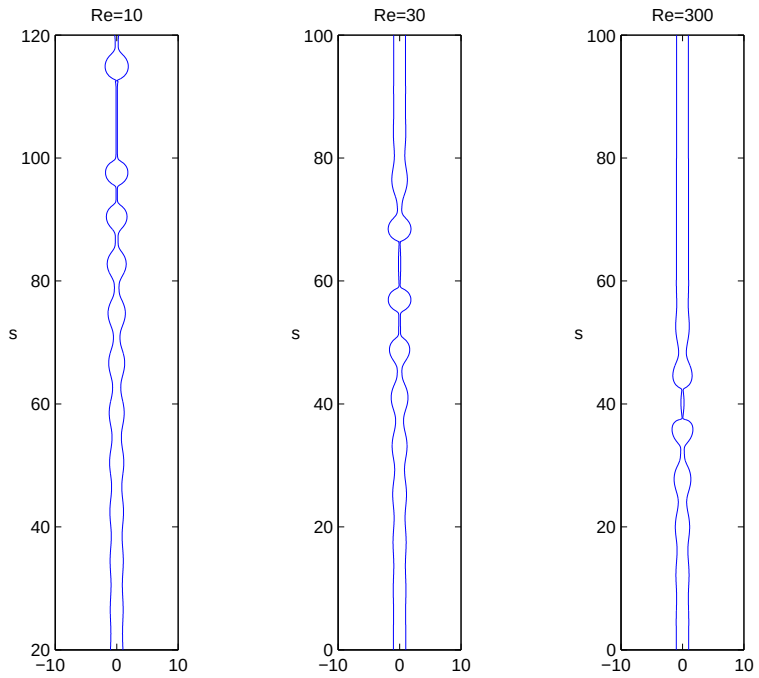

Figure 5.10: The profile at breakup for rotating shear thickening liquid jets for different Reynolds numbers ($\mathcal{R}e = 10$ (Left), $\mathcal{R}e = 30$ (Middle) and $\mathcal{R}e = 300$ (Right)). The vertical axis represents the arclength distance s along the rotating jet. Here $We = 10$, $\mathcal{R}b = 4.0$, $\delta = 0.01$ and $\kappa = 0.80$.

Fig. 5.14 for $\mathcal{R}b = 1$ this is close to $\kappa = 0.89$ whereas for $\mathcal{R}b = 4$ it is about $\kappa = 0.74$. Here it is probably appropriate to remind ourselves that for straight inviscid jets, the most unstable wavenumber (as calculated using linear theory) is $\kappa = 0.697$ with viscous jets having a corresponding wavenumber smaller than this value. The size of main droplets are plotted in Fig. 5.15 where it is seen that there is a general trend for smaller droplets (irrespective of the rotation rate) as the disturbance wavenumber (frequency) is increased. We also notice that high rotation rates always produce smaller drops and that for large disturbance frequencies the size of droplets begins to increase. Following on from Fig. 5.14 and 5.15 we show some corresponding profiles of liquid A at the point of breakup for low rotation rates in Fig. 5.16. In these cases the form of breakup has the same qualitative structure in terms of location along the jet, i.e. moving downstream from the nozzle we have a droplet, then a ligament and then pinch-off.

We do a similar thing with liquid B in Fig. 5.17 where we plot the breakup lengths against the disturbance wavenumber. In this case the most unstable wavenumber at high rotation rates ($\mathcal{R}b = 1$) is again close to $\kappa = 0.89$ and for lower rotation rates ($\mathcal{R}b = 4$) it is about $\kappa = 0.69$ which is slightly smaller than for liquid A. The discontinuity in breakup lengths for intermediate values of the disturbance wavenumber occurs as a result of changes in the location of breakup as the disturbance wavenumber (frequency) is varied. This phenomena of 'switching' is demonstrated more clearly in Fig. 5.18 where the location of breakup for low and high disturbance wavenumbers (frequencies) is different to that found in Fig. 5.16 (here instead we have the form moving downstream of the nozzle as a drop and then breakup, without the ligament). However for intermediate values of the wavenumber the jet has the same structure seen in Fig. 5.16.

The effects of changing the Weber number on the profile of liquid A is shown in Fig. 5.19. We see that for low values of the Weber number (which corresponds to large surface tension forces), liquid A produces a short jet (as expected, since breakup is driven by

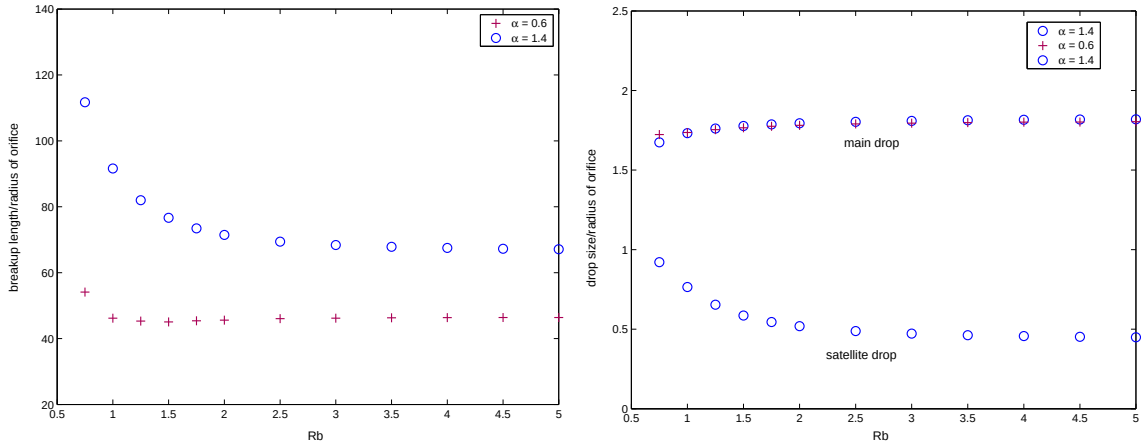

Figure 5.11: The break up lengths (top) and size of main/satellite droplets (bottom) of a shear thickening ($\alpha = 1.4$,) and shear thinning jet ($\alpha = 0.6$) plotted against $\mathcal{R}b$. In this case $\mathcal{R}e_\alpha = 30$, $We = 10$ and $\kappa = 0.89$. In general breakup lengths decrease with lower rotation rates although for shear thinning liquids there is a non-monotonic relationship between breakup lengths and rotation rates. In addition we see a general trend for larger main droplets and smaller satellite droplets as $\mathcal{R}b$ is increased which is similar to the behaviour of Newtonian liquids.

capillary instability) with longer jets produced as the Weber number is increased.

To illustrate the most striking difference in breakup between liquid A and liquid B we examine the evolution of the jet radius over one wavelength (Fig. 5.20). We see that for early times the evolution of the radius is similar for both liquids but as the radius shrinks shear thinning jets experience a rapid decay in the radius (since the viscosity becomes progressively smaller). However shear thickening jets take significantly longer (as the apparent viscosity begins to increase) to breakup and at the same time produce larger droplets once breakup is reached.

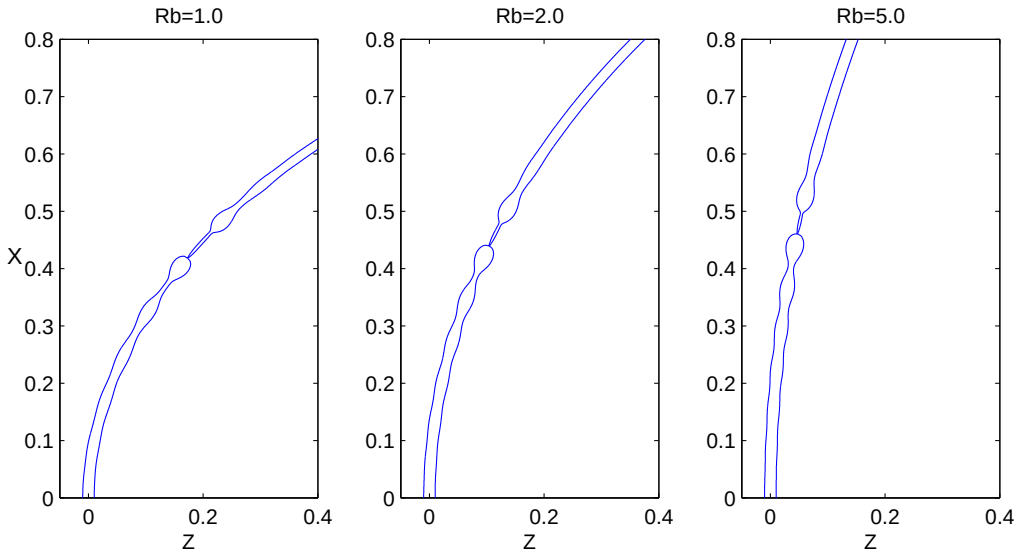

Figure 5.12: The profile of a shear thinning liquid jet for different *Rossby* numbers. Here $\mathcal{R}e_\alpha = 30$ and $We = 10$. The breakup length increases as the rotation rate is increased with the ligaments connecting droplets being stretched so that they are longer (albeit thinner) as compared to low rotation rates.

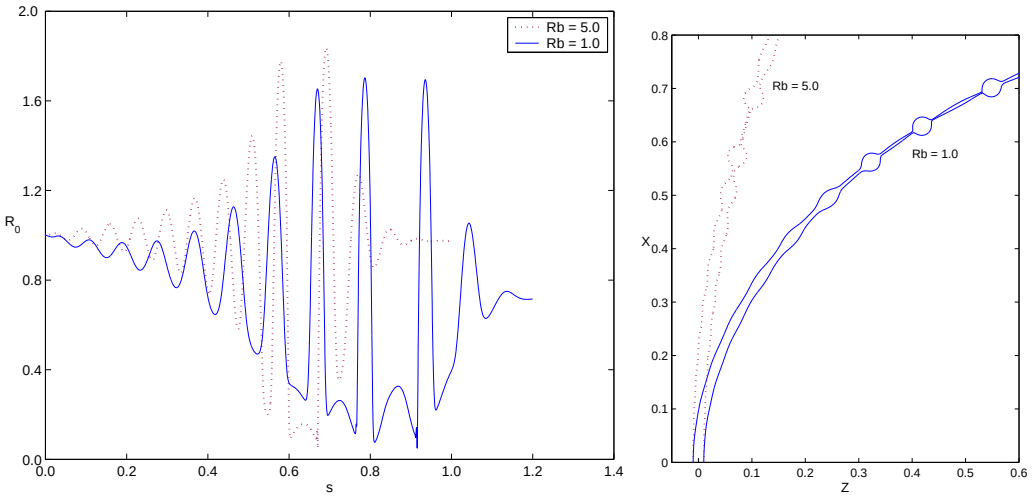

Figure 5.13: The profile of a shear thickening liquid jet for different *Rossby* numbers. Here $\mathcal{R}e_\alpha = 30.0$ and $We = 10.0$. The breakup length increases as the rotation rate is increased, however, droplet sizes can be seen to be smaller and the ligaments connecting droplets are longer and bigger when compared to low rotation rates. The 'kink' seen near the profile of the liquid jet for Rb =1.0 is due to the numerics (i.e., the inability to accurately capture rapid changes in values of pressure and jet radii) and does not represent a physical phenomenon. Higher resolution of mesh sizes or stopping the algorithm earlier will eliminate such 'kinks'.

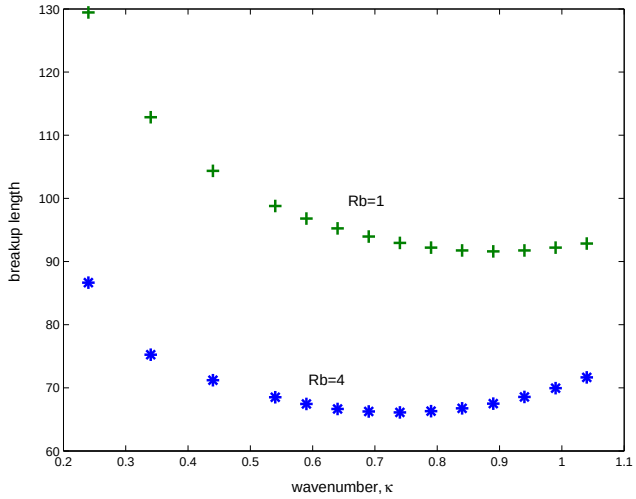

Figure 5.14: The breakup length of a shear thickening jet plotted against the frequency at the nozzle. In this case $\mathcal{R}e_\alpha = 30$, $We = 10$ and $\mathcal{R}b = 1, 4$. Higher rotation rates produce longer jets but are unstable to disturbances with larger wavenumbers (i.e., short wavelength disturbances).

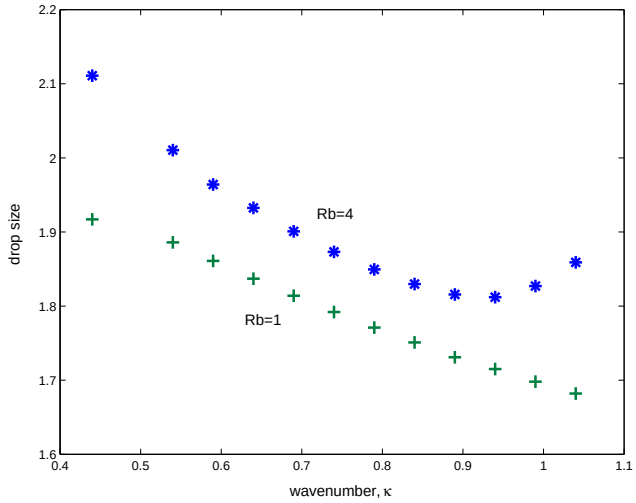

Figure 5.15: The size of droplets produced by a shear thickening jet plotted against the frequency at the nozzle. In this case $\mathcal{R}e_\alpha = 30$, $We = 10$ and $\mathcal{R}b = 1, 4$. Increasing the rate of rotation produces smaller droplets and in general droplets become smaller as the disturbance frequency is increased. In addition for large disturbance frequencies (i.e., short wavelength disturbances) the size of droplets for low rotation rates begins to increase.

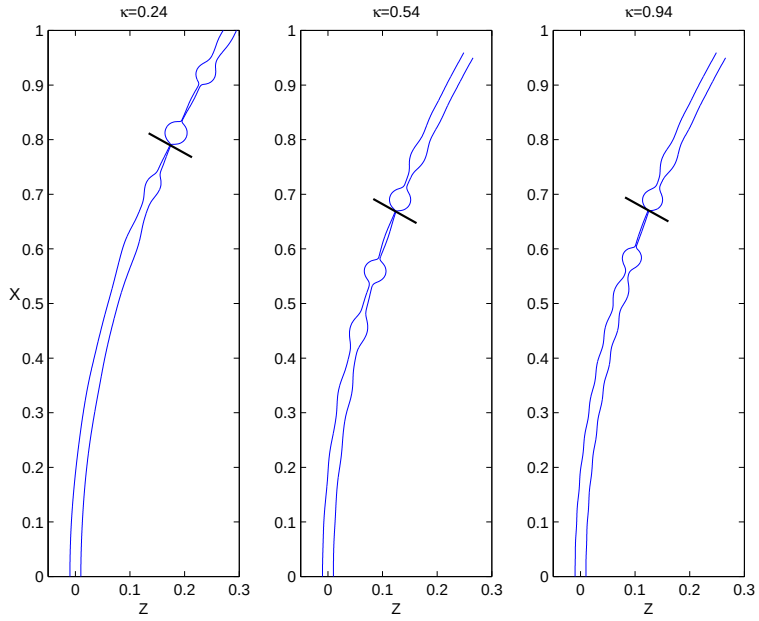

Figure 5.16: The effect of the wavenumber on the jet for liquid A. Here $\mathcal{R}e_\alpha = 30$, $\mathcal{R}b = 4$ and $We = 10$. From left to right we have the wavenumbers κ equal to 0.24, 0.54 and 0.94 respectively also note that pinch-off always takes place upstream of droplets. A small line segment is included to indicate the region of breakup.

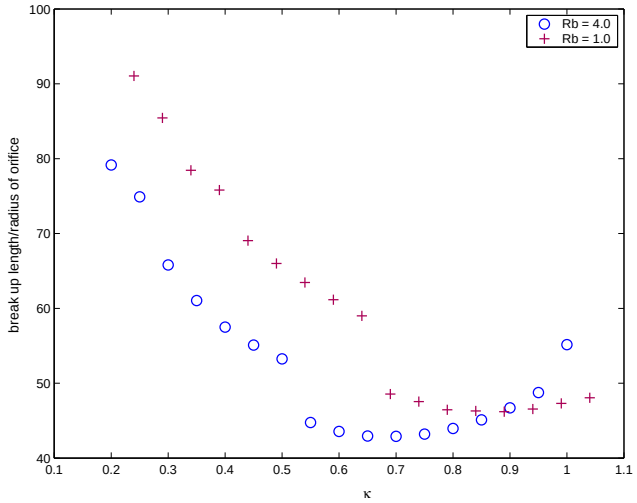

Figure 5.17: The breakup length plotted against wavenumber for a shear thinning liquid jet. Here $\mathcal{R}e_\alpha = 30$ and $We = 10$. Like the corresponding plot for shear thickening liquids we see that shear thinning jets are more unstable to short wavelength disturbances.

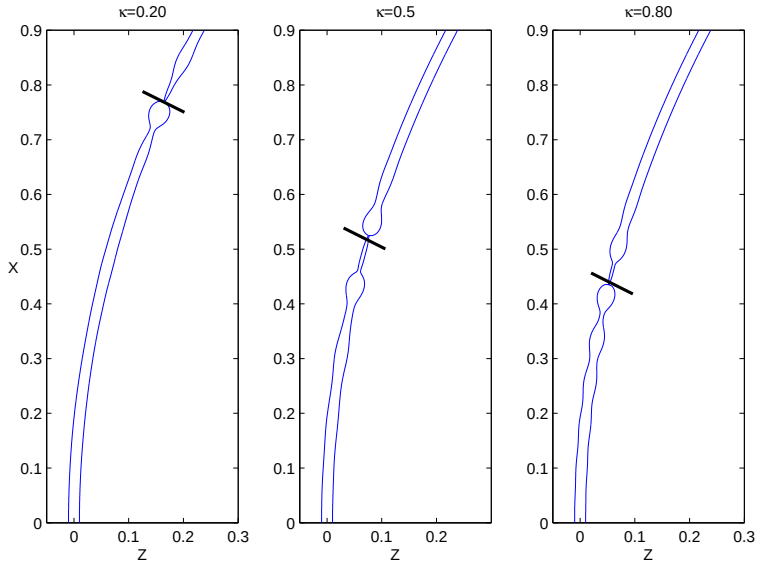

Figure 5.18: The effect of changing the wavenumber κ on a rotating shear thinning liquid jet. Here $\mathcal{R}e_\alpha = 30$, $\mathcal{R}b = 4$ and $We = 10$. In this figure we have the wavenumbers κ equal to 0.20, 0.50 and 0.80 from left to right. For small and large values of κ the location of breakup is downstream of the drop but for intermediate values of κ the region of pinch-off is upstream of droplets. A small line segment is included to indicate the region of breakup.

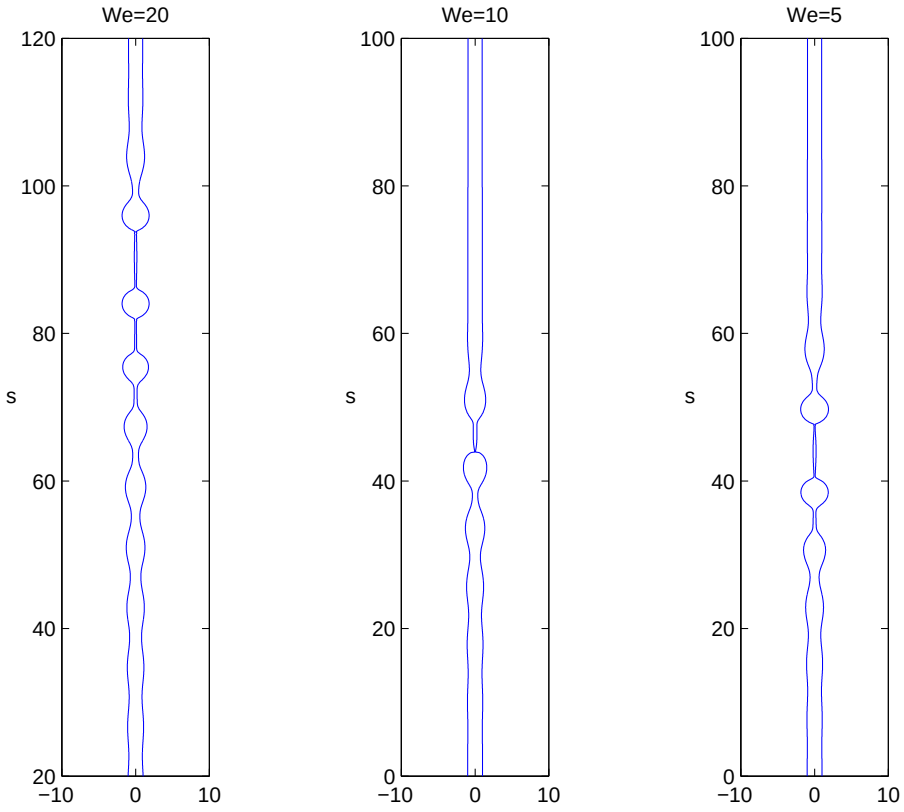

Figure 5.19: The profile at breakup for rotating shear thickening liquid jets for different Weber numbers ($We = 20$ (Left), $We = 10$ (Middle) and $We = 5$ (Right)). The horizontal axis represents the arclength distance s along the rotating jet. Here $\mathcal{R}e = 30$, $\mathcal{R}b = 4$, $\delta = 0.01$ and $\kappa = 0.80$.

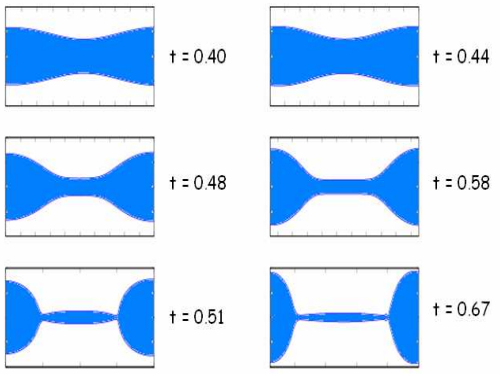

Figure 5.20: The evolution of disturbances along shear thinning (left column) and shear thickening (right column) liquid jets over approximately one period. The non-dimensional times are given and it can be seen that shear thickening liquids take significantly longer times to reach 'pinch-off'.

5.6 Discussion and Analysis

For most standard applications involving the breakup of a liquid jet emerging from a nozzle or orifice, like ink-jet printing, the centreline of the jet can be considered straight. This assumption is relatively robust for most practical applications, especially if the flow rate is such that the emerging liquid jet breaks up on a time scale small enough to ignore the effects of gravity or any other imposed force field. In such cases it is normal for the velocity and radius to take uniform values in the initial steady state (i.e, the mean flow is just a constant radius and constant velocity). It follows therefore that there is no velocity gradient along the jet and consequently for power law fluids there is an initially zero shear rate along the jet. This is problematic when considering non-Newtonian jets which obey a power law model since zero shear rates lead to infinite viscosities when the fluid is shear thinning. For Newtonian jets in a similar situation there is no such problem and breakup lengths and droplet sizes will effectively be determined by the effects of surface tension and viscosity on disturbances.

In many applications where liquid jets *are* required to be curved, like industrial prilling for example, the assumption of a straight centreline is clearly not applicable. In such cases the aim is to fully understand how the curved centreline affects stability to disturbances. The curvature of the centreline also allows us to use the power law model since in general the steady state for the velocity and radius vary along the jet, thus avoiding any problems with infinite viscosities.

With regards to the prilling process, it is primarily the rotation of the cylindrical drum which determines the trajectory of the emerging liquid jet. Thus, the rotating drum not only imparts momentum to the liquid jet but can also affect the curvature of the centreline of the jet. For this reason the rate of rotation provides a controllable parameter which can be used to influence breakup lengths and drop sizes.

We have seen that viscosity is found to have a negligible influence on the trajectory of a liquid jet emerging from a rotating orifice (see Section 4.2 and also Decent *et al.* (2005)) so that the centreline of a power law liquid jet (which can have varying viscosity along the jet) is closely approximated by an inviscid liquid jet. Under this assumption the trajectory and radius of a jet of liquid emerging from a nozzle placed on a rotating can is independent of the flow index number α and as such depends purely upon the Weber number We and the Rossby number $\mathcal{R}b$. Changes in the Rossby number which cause the rotation rate to increase, cause the jet trajectory to curve more but also lead to a quicker contraction of the jet radius along the jet (see Figs. 4.6 & 4.8). Thus on the one hand we should expect breakup lengths to increase due to the added momentum transferred from the rotating container to the jet (centrifugal forces) but at the same time initial steady state has a rapidly decreasing radius (thus downstream of the nozzle the radius is smaller, and so needs less time to reach breakup) and thus we would expect breakup lengths to decrease.

In our simulations it was found that higher rotation rates produce longer jets irrespective of the power law properties of the fluid (see Fig. 5.11). In particular, it is found that shear thickening fluids produce longer jets in comparison to shear thinning for any chosen value of $\mathcal{R}b$. This is similar to the results obtained for viscous Newtonian jets in Decent *et al.* (2005) where breakup lengths are much longer for increasingly more viscous jets. Drop sizes remain fairly stable over different rotation rates although there is is a tendency for larger main drops as the rotation rate is reduced. The effect on satellite drop sizes is more visible with satellite droplets sizes decreasing by a factor of two for rotation rates in the range $0.75 < \mathcal{R}b < 2.5$.

Interfacial instability is driven by surface tension so we expect surface tension to play a integral part for both shear thinning and shear thickening liquid jets. From our linear theory we see that both types of liquids have decreasing breakup lengths as the surface

tension is increased and this corresponds well with our numerical simulations (see Fig. 5.19). In addition it is expected from linear theory that the droplet sizes will also increase with increasing surface tension.

The evolution of a shear thickening and shear thinning liquid jet can be seen in Fig. 5.20 where the profile over approximately one wavelength is shown for different times. It is clear that shear thickening liquids take significantly longer times to reach 'pinch-off'. However closer examination of Fig. 5.20 shows that shear thinning jets decay rapidly once some critical minimum radius is reached whereas in the same situation shear thickening jets tend to take much longer.

Chapter 6

Rotating Liquid Jets with Surfactants

In this chapter we investigate the effects of special chemicals, known a surfactants,[1] which have a tendency to accumulate at the interface between two fluids and lower the surface tension. Since surface tension is the primary source of instability in liquid jets, we present here a short discussion on the role of surface tension which supplements our earlier analysis (see also introduction p. 7-9). We then take a closer look at the chemical properties of surfactants before we consider the instability of rotating liquid jets with surfactants.

Surface tension can be defined as the macroscopic characterization of the molecular interactions that occur at the interface between two immiscible fluids. In a liquid the surface tension can be thought of as an internal pressure caused by the attraction of molecules below the surface to those on the surface. Since a molecule on the surface of a liquid experiences intermolecular forces from below the surface and not from above[2], there is a disparity in potential energy between molecules in the bulk and on the free surface, with the potential energy of a molecule on the surface *exceeding* those in the bulk. This disparity between potential energies generates an inward 'pull', or internal pressure,

[1] originating from the term surface active agents.

[2] this is only true providing that the effects of the molecules from the surrounding fluid are negligible.

which inhibits the tendency of the liquid to flow or form large interfaces.

Surfactants reduce the ability of molecules to interact with each other, and thus lower the difference in potential energies between them, leading to lower surface tension. A molecule of a surfactant will usually consist of two distinct parts, each having its own properties[3], known as the polar 'head' and non-polar 'tail'. The polar 'head' is hydrophillic (or water loving) with the non-polar 'tail' being hydrophobic (water hating). A surfactant molecule in a liquid with a free surface will thus position itself *on* the free surface (thereby satisfying both the attractive and repulsive forces on it) so that the head points towards the liquid and the tail points away from the liquid into the free surface. Surfactants can also arrange themselves into tiny 'micelles', which are specially formed 'balls' of surfactants, with the heads forming the surface of the 'ball' and the tails aggregating in the center.

In this chapter we re-examine the analysis of Chapter Four and incorporate the effects of surfactants on the free surface of a rotating liquid jet. Our aim shall be, in line with the goals of this thesis, to investigate whether surfactants, along with the effects of rotation, can be used to control and manipulate the dynamics of breakup and drop formation in liquid jets. Since it is well known that, in many cases, the addition of even small amounts of surfactants can markedly reduce surface tension, this work will have relevance to industrial prilling, where surfactants may be used without drastically altering the chemical constitution of the material to be prilled.

Surfactants tend to have a stabilizing effect on the breakup of liquid jets. The reasons for this are as follows; as the capillary pressure 'squeezes' the thread of fluid, it sweeps away surfactants from the region of pinch-off. Since surface tension varies with the surfactant concentration, the pinch-off region has high surface tension and local regions on either side of the pinch-off region have low surface tension (due to the accumulation of sur-

[3]this type of chemical property of molecules, of having two characteristics, is known as amphipathic.

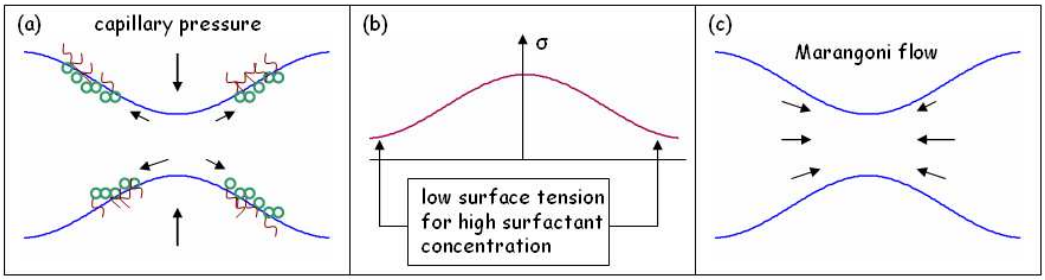

Figure 6.1: Capillary pressure 'squeezes' the liquid thread forcing liquid away from the pinch-off region (a), this also leads to surfactants being swept away from the region of pinch-off. The accumulation of surfactants in certain regions lead to gradients in surface tension (b). Marangoni flows are generated and are directed towards regions high in surface tension (i.e., the pinch-off region) which thus opposes capillary pressure thinning (c).

factants there). Spatial gradients in surface tension along the jet lead to Marangoni-type flows which are directed from regions low in surface tension to regions of higher surface tension. Thus flow is generated towards the pinch-off region opposing the effects of the capillary pressure (which attempts to displace fluid away from the pinch-off region) and thus stabilizing instabilities which lead to rupture. This process is shown pictorially in Fig. 6.1.

Previous studies on the effect of surfactants along straight liquid threads or bridges have been carried out by Whitaker (1976), who considered the instability of a liquid thread encased in an inviscid environment and Hansen *et al.* (1999) who investigated the linear instability of a liquid thread (containing soluble surfactants) with a viscous surrounding fluid. They found, as expected, that surfactants slow the growth of disturbances and that as the importance of surfactant activity increases, the dominant, or most unstable, wavenumber decreases. Timmermans and Lister (2002) have considered nonlinear approximations to the governing equations of a surfactant laden thread in an inviscid surrounding. They formulated a one-dimensional nonlinear model to investigate instability of the thread to changes in surface tension gradients. Using a scaling argument they showed that surfactants are swept away from pinching regions and thus have little effect

on any dynamics in those regions. An extension of these situations involving coaxial jets have been considered by Kwak and Pozrikidis (2001), core-annular flows with insoluble surfactants by Blyth *et al.* (2006) and a fully non linear one dimensional approximation to the governing equations for liquid bridges has been performed by Abravaneswaran and Basaran (1999). The effects of surfactants on the deformation of droplets has also been extensively studied (see Stone & Leal (1990)). The stability of two-layer channel flow and flow down an inclined plane with insoluble surfactants has been investigated by Blyth & Pozrikidis (2004*b* & 2004*c*). A review of the surfactant transport equation for an elongating thread and a stretched interface is provided by Blyth & Pozrikidis (2004*a*).

6.1 Formulation of Problem

The prilling process is modelled in the same way as before (see section 4.2 for more details). We again assume that a liquid jet emerges from a rotating cylindrical drum and is curved by the action of centripetal forces. We further assume that the jet, upon leaving the orifice, has a layer of insoluble[4] surfactant (having a fixed concentration) deposited on its free surface. We consider the problem in the rotating coordinate system developed earlier. We omit repeating the derivation of the coordinate system and simply rely on the reader to refer back to earlier chapters for their derivation and explanation[5].

We begin here with the standard Navier-Stokes equation and continuity equation to describe the flow. We have a convection-diffusion equation which relates the surfactant concentration along the surface to deformations of the fluid interface. These can be written as

$$\nabla \cdot \boldsymbol{u} = 0, \tag{6.1}$$

[4]One such example of an insoluble surfactant is N-octadecanol $C_{18}OH$. The properties of this type of surfactant have been extensively discussed in Liao *et al.* (2006), and in addition the Szyskowsky equation relating surface tension to surfactant concentration was also used to describe such surfactants.

[5]We shall also adopt the convention that symbols which are not defined retain their previous meanings. In most cases this will be self explanatory.

$$\boldsymbol{u}_t + \boldsymbol{u}\cdot\nabla\boldsymbol{u} = -\frac{1}{\rho}\nabla p + \nu\nabla^2\boldsymbol{u} - 2\boldsymbol{\omega}\times\boldsymbol{u} - \boldsymbol{\omega}\times(\boldsymbol{\omega}\times\boldsymbol{r}), \tag{6.2}$$

where ρ, ν and p are the density, kinematic viscosity and pressure of the liquid respectively. The angular velocity vector $\boldsymbol{\omega}$ and the displacement vector $\boldsymbol{r}$ are described on page 44. The concentration of surfactant along the free surface of the jet is governed by (see Stone and Leal (1990) and Blyth and Pozrikidis (2004*a*))

$$\Gamma_t + \boldsymbol{\nabla}_s\cdot(\Gamma\boldsymbol{u}_s) + \Gamma(\boldsymbol{\nabla}_s\cdot\mathbf{n})(\boldsymbol{u}\cdot\mathbf{n}) = S(\Gamma, B_s) + D_s\boldsymbol{\nabla}_s^2\Gamma, \tag{6.3}$$

where $\boldsymbol{\nabla}_s = (\mathbf{I}-\mathbf{nn})\cdot\boldsymbol{\nabla}$ is the surface gradient operator, D_s is the surface diffusivity of surfactant, $\boldsymbol{u}_s = (\mathbf{I}-\mathbf{nn})\cdot\boldsymbol{u}$ is the surface or tangential velocity and $\boldsymbol{\nabla}_s\cdot\mathbf{n} = 2\kappa$ where κ is the mean curvature of the free surface. S is the surfactant source term which takes into account absorption from the free surface and is a function of the surfactant concentration on the surface Γ and surfactant concentration in the bulk B_s. The third term on the left of (6.3) expresses the dilatation by expansion due to normal forces (see Blyth and Pozrikidis (2004*a*)). In the present study we consider insoluble surfactants (so S is taken as zero) and assume that the diffusivity of surfactant is small[6] and negligible (i.e., $D_s = 0$). Under these assumptions, and after using the properties of the surface gradient operator[7], we have

$$\Gamma_t + \boldsymbol{u}\cdot\boldsymbol{\nabla}\Gamma - \Gamma\mathbf{n}\cdot((\mathbf{n}\cdot\boldsymbol{\nabla})\boldsymbol{u}) = 0. \tag{6.4}$$

[6]This was also the approach adopted by Timmermans & Lister (2002) in their work on the instability of a liquid thread. In addition Liao *et al.* (2006) report that the limiting length of a stretched liquid bridge covered with insoluble surfactants increases slightly with increasing the Peclet number (which is a non-dimensional constant inversely proportional to diffusivity) until a plateau is reached at $Pe = 10^3$ whence the Peclet number is effectively infinite (i.e., surface diffusvity is zero).

[7]Where $\nabla_s\cdot\boldsymbol{u}_s = \text{Trace}[(\boldsymbol{I}-\boldsymbol{nn})\cdot(\nabla\boldsymbol{u})\cdot(\boldsymbol{I}-\boldsymbol{nn})] = \nabla_s\cdot\boldsymbol{u}_s + 2\kappa\boldsymbol{u}\cdot\boldsymbol{n}$

The boundary conditions are, by now, the familiar kinematic equation

$$\frac{\partial R}{\partial t} + \mathbf{u} \cdot \nabla R = 0, \tag{6.5}$$

normal and tangential stress conditions

$$p + \mathbf{n} \cdot \mathbf{P} \cdot \mathbf{n} = \sigma \nabla \cdot \mathbf{n}, \tag{6.6}$$

and

$$\mathbf{t_i} \cdot \mathbf{P} \cdot \mathbf{n} = \mathbf{t_i} \cdot \nabla \sigma, \tag{6.7}$$

where $\mathbf{P} = -p\mathbf{I} + \mu[\nabla \mathbf{u} + (\nabla \mathbf{u})^T]$ and the arc length condition

$$X_s^2 + Z_s^2 = 1. \tag{6.8}$$

In addition the equation of state relating the surfactant concentration Γ to the surface tension of the liquid-gas interface is given by the nonlinear Szyskowsky[8] equation

$$\sigma = \tilde{\sigma} + \Gamma_\infty R_g T \log\left[\frac{\Gamma_\infty - \Gamma}{\Gamma_\infty}\right], \tag{6.9}$$

where $\tilde{\sigma}$ is the surface tension of the liquid in the absence ($\Gamma = 0$) of any surfactant, Γ_∞ is the maximum packing concentration of surfactant, R_g is the universal gas constant and T is the temperature.

[8]This equation is a special case of the so called Frumkin equation of state $\sigma = \tilde{\sigma} + \Gamma_\infty R_g T(\log(1 - \frac{\Gamma_\infty}{\Gamma}) + \frac{A\Gamma_\infty^2}{2\Gamma^2})$ where A is the molecular interaction parameter. We could have easily used other equations of state (of which there are many) but for consistency with previous works (like [1] for example) we chose this particular equation.

We non-dimensionalise this set of equations using the following transformations

$$(\overline{u},\overline{v},\overline{w}) = \frac{1}{U}(u,v,w), \quad \overline{p} = \frac{p}{\rho U^2}, \quad (\overline{n},\overline{R}) = \frac{1}{a}(n,R) \quad \varepsilon = \frac{a}{s_0},$$
$$(\overline{s},\overline{X},\overline{Z}) = \frac{1}{s_0}(R,X,Z), \quad \overline{t} = \frac{tU}{s_0}, \quad \overline{\sigma} = \frac{\sigma}{\tilde{\sigma}}, \quad \text{and} \quad \overline{\Gamma} = \frac{\Gamma}{\Gamma_\infty}, \tag{6.10}$$

where U the exit speed of the jet in the rotating frame, ρ is the liquid's density, s_0 is the radius of the cylindrical drum, a is the radius of the orifice, ε is the aspect ratio, p is the pressure and R is the jet radius. The surface tension is made dimensionless with respect to the surface tension, $\tilde{\sigma}$, of the pure liquid in the absence of surfactants, and Γ is non-dimensionalised with respect to Γ_∞ the maximum packing concentration of surfactant.

In this system the continuity equation reduces to

$$\varepsilon n\frac{\partial u}{\partial s} + h_s\left(v + n\frac{\partial v}{\partial n} + \frac{\partial w}{\partial \phi}\right) + \varepsilon n(X_s Z_{ss} - Z_s X_{ss})(v\cos\phi - w\sin\phi) = 0. \tag{6.11}$$

The equations of motion are almost identical to those found in Chapter Four, namely (4.11), (4.12) and (4.13). However in this case we do not require a variable viscosity (i.e., we will use the above mentioned equations with a constant viscosity) and the non-dimensional constants are given by $\mathcal{R}e = \rho U s_0/\mu$ and $We = \rho U^2 a/\tilde{\sigma}$ where $\tilde{\sigma}$ is defined above. The surfactant concentration equation, after some algebra, becomes

$$\begin{aligned}
\varepsilon\Gamma_t &= -\frac{\varepsilon u}{h_s}\frac{\partial \Gamma}{\partial s} - v\frac{\partial \Gamma}{\partial n} - \frac{w}{n}\frac{\partial \Gamma}{\partial \phi} \\
&+ \frac{\Gamma}{E}\left(\frac{\varepsilon^3}{h_s^2}\left(\frac{\partial R}{\partial s}\right)^2\frac{\partial u}{\partial s} - \frac{\varepsilon}{h_s}\left(\frac{\partial R}{\partial s}\right)\frac{\partial u}{\partial n} + \frac{\varepsilon}{nRh_s}\frac{\partial R}{\partial \phi}\frac{\partial R}{\partial s}\frac{\partial u}{\partial \phi} - \frac{\varepsilon^2}{h_s^2}\left(\frac{\partial R}{\partial s}\right)\frac{\partial v}{\partial s}\right. \\
&+ \left.\frac{\partial v}{\partial n} - \frac{1}{nR}\frac{\partial R}{\partial \phi}\frac{\partial v}{\partial \phi} + \frac{\varepsilon^2}{Rh_s^2}\frac{\partial R}{\partial \phi}\frac{\partial R}{\partial s}\frac{\partial w}{\partial s} - \frac{1}{R}\frac{\partial R}{\partial \phi}\frac{\partial w}{\partial n} + \frac{1}{nR^2}\left(\frac{\partial R}{\partial \phi}\right)^2\frac{\partial w}{\partial \phi}\right),
\end{aligned} \tag{6.12}$$

$$\text{where} \quad E = \left(1 + \frac{\varepsilon^2}{h_s^2}\left(\frac{\partial R}{\partial s}\right)^2 + \frac{1}{n^2}\left(\frac{\partial R}{\partial \phi}\right)^2\right)^{\frac{1}{2}}.$$

These equations are supplemented by boundary conditions. The kinematic boundary condition, which requires a particle on the interface to remain there, can be written as

$$h_s\left(\varepsilon\frac{\partial R}{\partial t}+\cos\phi(X_tZ_s-X_sZ_t)-v+\frac{w}{n}\frac{\partial R}{\partial\phi}\right)+\varepsilon u\frac{\partial R}{\partial s}=0\quad\text{on}\quad n=R(s,t). \tag{6.13}$$

At the free surface we have the normal vector $\boldsymbol{n}$ given by

$$\boldsymbol{n}=\frac{1}{E}\left(-\frac{\partial R}{\partial s}\frac{1}{h_s}\,\boldsymbol{e_s}+\boldsymbol{e_n}-\frac{\partial R}{\partial\phi}\frac{1}{R}\boldsymbol{e_\phi}\right),$$

and two tangential vectors

$$\boldsymbol{t}_1=\boldsymbol{e_s}+\frac{1}{h_s}\frac{\partial R}{\partial s}\boldsymbol{e_n}\quad\text{and}\quad\boldsymbol{t}_2=\frac{1}{R}\frac{\partial R}{\partial\phi}\boldsymbol{e_n}+\boldsymbol{e_\phi}.$$

The normal stress condition relates the pressure difference across the liquid jet interface to the mean curvature of the interface, this is given by

$$\begin{aligned}p-\frac{2}{\mathcal{R}e}\frac{1}{E^2}\Bigg(&\varepsilon^2\left(\frac{\partial R}{\partial s}\right)^2\frac{1}{h_s^3}\left(\frac{\partial u}{\partial s}+(v\cos\phi-w\sin\phi)(X_sZ_{ss}-Z_sX_{ss})\right)+\frac{1}{\varepsilon}\frac{\partial v}{\partial n}\\&+\frac{1}{\varepsilon R^3}\left(\frac{\partial R}{\partial\phi}\right)^2\left(\frac{\partial w}{\partial\phi}+v\right)-\frac{\varepsilon}{h_s}\frac{\partial R}{\partial s}\left(\frac{1}{h_s}\frac{\partial v}{\partial s}+\frac{1}{\varepsilon}\frac{\partial u}{\partial n}-\frac{u}{h_s}\cos\phi(X_sZ_{ss}-Z_sX_{ss})\right)\\&+\frac{\varepsilon}{Rh_s}\frac{\partial R}{\partial s}\frac{\partial R}{\partial\phi}\left(\frac{1}{\varepsilon R}\frac{\partial u}{\partial\phi}+\frac{u}{h_s}\sin\phi(X_sZ_{ss}-Z_sX_{ss})+\frac{1}{h_s}\frac{\partial u}{\partial s}\right)\Bigg)\\&-\frac{1}{R\varepsilon}\frac{\partial R}{\partial\phi}\left(\frac{\partial w}{\partial n}-\frac{w}{R}+\frac{1}{R}\frac{\partial v}{\partial\phi}\right)=\frac{\sigma\kappa}{We}\quad\text{on}\quad n=R(s,t),\end{aligned} \tag{6.14}$$

where

$$\kappa=\frac{1}{nh_s}\left(-\frac{\partial}{\partial s}\left(\frac{n}{h_sE}\frac{\partial R}{\partial s}\right)+\frac{\partial}{\partial n}\left(\frac{nh_s}{E}\right)-\frac{\partial}{\partial\phi}\left(\frac{h_s}{nE}\frac{\partial R}{\partial\phi}\right)\right), \tag{6.15}$$

The tangential stress conditions are written as

$$\left(1-\frac{\varepsilon^2}{h_s^2}\left(\frac{\partial R}{\partial s}\right)^2\right)\left(\varepsilon\frac{\partial v}{\partial s}+h_s\frac{\partial u}{\partial n}-\varepsilon u\cos\phi(X_sZ_{ss}-X_{ss}Z_s)\right)$$
$$+2\varepsilon\frac{\partial R}{\partial s}\left(\frac{\partial v}{\partial n}-\frac{\varepsilon}{h_s}\frac{\partial u}{\partial s}-\frac{\varepsilon(X_sZ_{ss}-X_{ss}Z_s)}{h_s}(v\cos\phi-w\sin\phi)\right)$$
$$=\frac{\varepsilon\mathcal{R}e}{We}\left(\frac{\varepsilon}{h_s}\frac{\partial\sigma}{\partial s}+\frac{1}{h_s}\frac{\partial R}{\partial s}\frac{\partial\sigma}{\partial n}\right), \tag{6.16}$$

and

$$\left(1-\frac{1}{R^2}\left(\frac{\partial R}{\partial\phi}\right)^2\right)\left(\frac{\partial w}{\partial n}-\frac{w}{R}+\frac{1}{R}\frac{\partial v}{\partial\phi}\right)+\frac{2}{R}\frac{\partial R}{\partial\phi}\left(\frac{\partial v}{\partial n}-\frac{1}{R}\left(\frac{\partial w}{\partial\phi}+v\right)\right)$$
$$=\frac{\varepsilon\mathcal{R}e}{We}\left(\frac{1}{R}\frac{\partial R}{\partial\phi}\frac{\partial\sigma}{\partial n}+\frac{1}{n}\frac{\partial\sigma}{\partial\phi}\right). \tag{6.17}$$

In addition we have the arclength condition which is

$$X_s^2+Z_s^2=1. \tag{6.18}$$

6.2 Asymptotic Analysis

We exploit the fact that the radius of the orifice is small when compared to the radius of the cylinder by expanding u, v, w, p in Taylor series in εn (see Eggers (1997) and Hohman *et al.* (1984)), and R, X, Z in asymptotic series in ε. We assume that the leading order axial component of the velocity is independent of ϕ and that the centreline of the jet is

unaffected by small perturbations. Thus we have

$$\begin{aligned} u &= u_0(s,t) + (\varepsilon n)u_1(s,\phi,t) + (\varepsilon n)^2 u_2(s,\phi,t) + \cdots \\ v &= (\varepsilon n)v_1(s,\phi,t) + (\varepsilon n)^2 v_2(s,n,\phi,t) + \cdots \\ w &= (\varepsilon n)w_1(s,\phi,t) + (\varepsilon n)^2 w_2(s,\phi,t) + \cdots \\ p &= p_0(s,\phi,t) + (\varepsilon n)p_1(s,\phi,t) + \cdots \\ R &= R_0(s,t) + \varepsilon R_1(s,\phi,t) + \cdots \end{aligned}$$

$$X = X_0(s) + \varepsilon X_1(s,t) + \cdots \qquad Z = Z_0(s) + \varepsilon Z_1(s,t) + \cdots \tag{6.19}$$

In addition we have the following expansions for the surfactant concentration Γ and variable surface tension σ as

$$\begin{aligned} \Gamma &= \Gamma_0(s,t) + \varepsilon^2 \Gamma_1(s,t) + O(\varepsilon^4), \\ \sigma &= \sigma_0(s,t) + \varepsilon^2 \sigma_1(s,t) + O(\varepsilon^4). \end{aligned} \tag{6.20}$$

Both these quantities are assumed to vary on the free surface of the jet and only along the jet.

For completeness we have, in the above expansion for the leading order pressure term p_0 assumed a dependence upon n. We shall eventually go on to see that the following analysis will suggest that p_0 is independent of n (as is to be expected under the slender jet assumption).

From the continuity equation we obtain

$$O(\varepsilon n) \quad : \quad u_{0s} + 2v_1 + w_{1\phi} = 0 \tag{6.21}$$

$$O(\varepsilon n)^2 \quad : \quad u_{1s} + 3v_2 + w_{2\phi} + (3v_1 + w_{1\phi})\cos\phi S - w_1 \sin\phi S = 0. \tag{6.22}$$

From the second tangential stress condition we get

$$O(\varepsilon) \quad : \quad R_0^3 v_{1\phi} = 0 \tag{6.23}$$

$$O(\varepsilon^2) \quad : \quad 3R_0^2 R_1 v_{1\phi} + R_0^4(w_2 + v_{2\phi}) - 2R_0^2 R_{1\phi} w_{1\phi} = 0. \tag{6.24}$$

Thus we see that $v_{1\phi} = 0$, and by differentiating (6.21) we see that $w_{1\phi\phi} = 0$. Since w_1 is periodic in ϕ we must have $w_1 = w_1(s,t)$. Then (6.21) implies that $v_1 = -u_{0s}/2$ and from (6.24) we have

$$w_2 + v_{2\phi} = 0. \tag{6.25}$$

From the first tangential stress condition we have

$$O(\varepsilon) \quad : \qquad u_1 = u_0 S \cos\phi \tag{6.26}$$

$$O(\varepsilon^2) \quad : \qquad u_2 = \frac{3}{2} u_{0s} \frac{R_{0s}}{R_0} + \frac{u_{0ss}}{4} + \left(\frac{\mathcal{R}e}{We}\right) \frac{\sigma_{0s}}{2R_0}. \tag{6.27}$$

After differentiating (6.25) with respect to ϕ (and noting that v_2 is periodic in ϕ) we obtain

$$w_{2\phi} = -v_{2\phi\phi}. \tag{6.28}$$

Therefore,

$$v_{2\phi\phi} - 3v_2 = u_{1s} + 3v_1 S\cos\phi - w_1 S\sin\phi, \tag{6.29}$$

and using the expressions for u_1 and v_1 we see that

$$v_{2\phi\phi} - 3v_2 = \left(u_0 S_s - \frac{u_{0s}}{2} S\right)\cos\phi - w_1 S\sin\phi. \tag{6.30}$$

Periodic solutions for v_2 and w_2 are

$$v_2 = \frac{1}{4}\left(\frac{u_{0s}}{2} S - u_0 S_s\right)\cos\phi + \frac{w_1}{4} S\sin\phi, \tag{6.31}$$

$$w_2 = \frac{1}{4}\left(\frac{u_{0s}}{2}S - u_0 S_s\right)\sin\phi - \frac{w_1}{4}S\cos\phi \tag{6.32}$$

From the momentum equation in the radial direction, we have at leading order $p_{0n} = 0$. Thus $p_0 = p_0(s, \phi, t)$, i.e., p_0 is independent of n. At order ε we get

$$\begin{aligned} p_1 = &\left({u_0}^2 S - \frac{2}{\mathcal{R}b}u_0 + \frac{(X_0+1)Z_{0s} - Z_0 X_{0s}}{\mathcal{R}b^2}\right)\cos\phi \\ &-\frac{1}{\mathcal{R}e}\left(\frac{5}{2}u_{0s}S + u_0 S_s\right)\cos\phi - \frac{1}{\mathcal{R}e}w_1 S\sin\phi. \end{aligned} \tag{6.33}$$

For simplicity of notation we will relabel X_0 and Z_0 with X and Z respectively.

The momentum equation in the azimuthal direction gives at leading order $p_{0\phi} = 0$ which is automatically satisfied. At order ε we get the above equation for p_1 (with every term being differentiated by ϕ). From the normal stress condition we obtain at leading order

$$p_0 = -\frac{u_{0s}}{\mathcal{R}e} + \frac{\sigma_0}{R_0 We},$$

and at order ε we have

$$p_1 = \frac{\sigma_0}{R_0 We}\left(-\frac{R_{1\phi\phi} + R_1}{{R_0}^2} + S\cos\phi\right) + \frac{4v_2}{\mathcal{R}e}.$$

If we now substitute the expression for p_1 from (6.33) into the above equation, and note that R is periodic in ϕ, we get

$$S\left(u_0^2 - \frac{3u_{0s}}{\mathcal{R}e} - \frac{1}{R_0 We}\right) = \frac{2u_0}{\mathcal{R}b} - \frac{(X+1)Z_s - ZX_s}{\mathcal{R}b^2}. \tag{6.34}$$

This equation is valid only if the leading order terms in the expansion of X and Z are independent of t. If we had retained leading order translational velocity terms v_0 and w_0 in our expansions for v and w, and had $X_{0t} \neq 0$ and $Z_{0t} \neq 0$, then the right hand

side of (6.34) would contain some additional unsteady terms (see Părău *et al.* (2006)) in $E = Z_s X_t - Z_t X_s$ (see also Appendix D for further details). However $E \approx 0$ has already been found in Părău *et al.* (2006) to be a very accurate approximation between the orifice and the break up point of the jet. This is backed up by the experimental observations of Wong *et al.* (2004), which show that the centreline of the jet is steady (in the rotating frame), giving $X_t \approx 0$, $Z_t \approx 0$ and $E \approx 0$ for experimental observations.

The Navier-Stokes equation in the axial direction at order ε is given by

$$u_{0t} + u_0 u_{0s} = -p_{0s} + \frac{(X+1)X_s + ZZ_s}{\mathcal{R}b^2} + \frac{1}{\mathcal{R}e}(u_{0ss} + 4u_2 + u_{2\phi\phi}), \tag{6.35}$$

which after using the expressions for u_2 and p_0 becomes

$$\begin{aligned} u_{0t} + uu_{0s} = &-\frac{1}{We}\left(\frac{\sigma_0}{R_0}\right)_s + \frac{(X+1)X_s + ZZ_s}{\mathcal{R}b^2} \\ &+\frac{3}{\mathcal{R}e}\left(u_{0ss} + 2u_{0s}\frac{R_{0s}}{R}\right) + \frac{2\sigma_{0s}}{WeR_0}. \end{aligned} \tag{6.36}$$

From the kinematic condition, we obtain at order ε

$$R_{0t} + \frac{u_{0s}}{2}R_0 + u_0 R_{0s} = 0. \tag{6.37}$$

The arclength equation at leading order gives

$$X_s{}^2 + Z_s{}^2 = 1. \tag{6.38}$$

And finally the last equation to be found is the surfactant transport equation which at leading order is

$$\Gamma_{0t} + u_0\Gamma_{0s} + \frac{u_{0s}}{2}\Gamma_0 = 0. \tag{6.39}$$

We see that we have now five equations (6.34), (6.36), (6.37), (6.38) and (6.39) for the six unknowns u_0, R_0, σ_0, Γ_0, X and Z. To complete this system of equations we have the dimensionless equation of state relating the surfactant concentration Γ to the surface tension of the liquid-gas interface, which is given by the nonlinear Szyskowsky equation[9]

$$\sigma = 1 + \beta \log(1 - \Gamma), \tag{6.40}$$

where the parameter $\beta = \Gamma_\infty R_g T/\tilde{\sigma}$ determines how 'effective' or important surfactants are.

6.3 Steady State Solutions

From (6.37) and (6.39) we observe that $R_0^2 u_0$ and $\Gamma_0^2 u_0$ are both constants. By using the initial conditions at the orifice $R_0(0) = 1 = u_0(0)$ and $\Gamma_0(0) = \zeta$, where ζ is the initial concentration of surfactant ($0 \leqslant \zeta \leqslant 1$), we have

$$R_0^2 u_0 = 1 \qquad \text{and} \qquad \Gamma_0^2 u_0 = \zeta^2, \tag{6.41}$$

which we can use in the previous equations to obtain

$$\begin{aligned} u_0 u_{0s} = &-\frac{(1 + \beta \log(1 - \zeta u_0^{-\frac{1}{2}}))}{We} \frac{u_{0s}}{2\sqrt{u_0}} + \frac{\beta\zeta}{2u_0 We} \frac{u_{0s}}{(1 - \zeta u_0^{-\frac{1}{2}})} \\ &+ \frac{(X+1)X_s + ZZ_s}{\mathcal{R}b^2} + \frac{3}{\mathcal{R}e}\left(u_{0ss} - \frac{u_{0s}^2}{u_0}\right), \end{aligned} \tag{6.42}$$

[9]For this equation we have that the derivative of the surface tension with respect to the surfactant concentration is given by $(\partial\sigma/\partial\Gamma) = -\beta/(1-\Gamma)$, which diverges as Γ approaches unity. The Marangoni stress, which can be written as $-\boldsymbol{\nabla}_s\sigma = -(\partial\sigma/\partial\Gamma)\boldsymbol{\nabla}_s\Gamma$ will therefore also diverge. In practice the mechanical properties of the system will prevent Γ from approaching unity (i.e., the maximum packing concentration Γ_∞) (see Eggleton *et al.* (1999) for more details).

$$(X_s Z_{ss} - X_{ss} Z_s)\left(u_0^2 - \frac{3u_{0s}}{\mathcal{R}e} - \frac{1}{We}(1+\beta\log(1-\zeta u_0^{-\frac{1}{2}}))\sqrt{u_0}\right) = \frac{2u_0}{\mathcal{R}b} - \frac{(X+1)Z_s - ZX_s}{\mathcal{R}b^2}, \tag{6.43}$$

$$X_s^2 + Z_s^2 = 1. \tag{6.44}$$

The unknowns in (6.42)-(6.44) are X, Z and u_0. We will now show that the solution to this leading order problem is identical to the solution of (6.42)-(6.44) in the inviscid limit (i.e., as $\mathcal{R}e \to \infty$). A similar analysis, for jets without surfactants, has already been performed for Newtonian spiralling liquid jets by Decent *et al.* (2007). However in the proceeding analysis we find a few extra terms not found in Decent *et al.* (2007*b*). In addition, as mentioned earlier, this set of equations, for $\zeta = 0$ can be solved numerically using a Runge-Kutta method for the inviscid case $\mathcal{R}e = \infty$. When viscosity is included (i.e., $\mathcal{R}e \neq \infty$) this method fails (the system of equations becomes extremely stiff due to the presence of a small term $(1/\mathcal{R}e)$ in front of the largest derivative in u_0). To overcome this problem, Părău *et al.* (2007) put this set of equations for a Newtonian fluid without surfactants into the form of a second-order centred finite difference discretization. The resulting equations were solved using Newton's method or a modified Newton's method (the Jacobian was only calculated for the first iteration). It was found, in that paper, that the viscous centreline (using Newton's method) was almost identical to the inviscid centreline found using the Runge-Kutta method (see Părău *et al.* (2007), p.167 for more details) except in the case of highly viscous fluids (which we do not consider in this thesis). Thus Părău *et al.* (2007) showed numerically that viscosity is unimportant in determining the steady state solutions.

We present here a modified version of the analysis of Decent *et al.* (2007) and show that the centreline is independent of viscosity to leading order. In order to do this we rewrite our equations of motion using $\mathcal{O}h/\sqrt{We}$ as the non-dimensional term in front

of the viscous terms (instead of the usual Reynolds number $\mathcal{R}e$). Here $\mathcal{O}h$ is taken as $\mathcal{O}h = \mu/\sqrt{\sigma a \rho}$ and rather than expanding in the small parameter (εn) we consider expansions of the form $u = u_0(s) + \varepsilon u_1(s,n,\phi) + O(\varepsilon^2)$, $R = R_0(s) + \varepsilon R_1(s,n,\phi) + O(\varepsilon^2)$, $v = \varepsilon v_1(s,\phi) + O(\varepsilon^2)$, $p = p_0(s) + \varepsilon p_1(s,n,\phi) + O(\varepsilon^2)$, $\sigma = \sigma_0(s) + \varepsilon\sigma_1(s,n,\phi) + O(\varepsilon^2)$, $\Gamma = \Gamma_0(s) + \varepsilon\Gamma_1(s,n,\phi) + O(\varepsilon^2)$ and set $w = 0$ so that we have no azimuthal velocity. After substitution into the governing equations, we obtain, to leading order,

$$v_1 = -\frac{n}{2}\frac{du_0}{ds}, \tag{6.45}$$

$$\begin{aligned}\frac{\partial u_0}{\partial t} + u_0\frac{\partial u_0}{\partial s} = &-\frac{\partial p_0}{\partial s} + \frac{1}{\mathcal{R}b^2}((X+1)X_s + ZZ_s) \\ &+\frac{\mathcal{O}h}{\sqrt{We}}\left(\frac{1}{n}\frac{\partial u_1}{\partial n} + \frac{\partial^2 u_1}{\partial n^2} + \frac{1}{n^2}\frac{\partial^2 u_1}{\partial \phi^2}\right),\end{aligned} \tag{6.46}$$

$$\frac{\partial p_0}{\partial n} = 0, \quad \text{and} \quad \frac{\partial p_0}{\partial \phi} = 0, \tag{6.47}$$

$$-\cos\phi(X_sZ_{ss} - X_{ss}Z_s)u_0^2 = -\frac{\partial p_1}{\partial n} - \frac{2u_0\cos\phi}{\mathcal{R}b} + \frac{\cos\phi}{\mathcal{R}b^2}((X+1)Z_s - ZX_s), \tag{6.48}$$

$$\sin\phi(X_sZ_{ss} - X_{ss}Z_s)u_0^2 = -\frac{1}{n}\frac{\partial p_1}{\partial \phi} + \frac{2u_0\sin\phi}{\mathcal{R}b} - \frac{\sin\phi}{\mathcal{R}b^2}((X+1)Z_s - ZX_s), \tag{6.49}$$

$$u_0\frac{\partial R_0}{\partial s} = v_1 \quad \text{on} \quad n = R_0, \tag{6.50}$$

$$p_1 - \frac{2\mathcal{O}h}{\sqrt{We}}\frac{\partial v}{\partial n} = \frac{\sigma_0}{We}\left(-\frac{1}{R_0^2}\left(R_1 + \frac{\partial^2 R_1}{\partial \phi^2}\right) + \cos\phi(X_sZ_{ss} - X_{ss}Z_s)\right) \quad \text{on} \quad n = R_0, \tag{6.51}$$

$$\frac{\partial u_1}{\partial n} = u_0\cos\phi(X_sZ_{ss} - X_{ss}Z_s) + \frac{\mathcal{O}h^{-1}}{We^{\frac{1}{2}}}\frac{\partial \sigma_0}{\partial s} \tag{6.52}$$

Now we have

$$u_0\frac{\partial u_0}{\partial s}+\frac{\partial p_0}{\partial s}++\frac{(X+1)X_s+ZZ_s}{\mathcal{R}b^2}=\frac{\mathcal{O}h}{\sqrt{We}}(\nabla^2_{n,\phi}u_1), \tag{6.53}$$

where

$$\nabla^2_{n,\phi}=\frac{1}{n}\frac{\partial}{\partial n}+\frac{\partial^2}{\partial n^2}+\frac{1}{n^2}\frac{\partial^2}{\partial\phi^2},$$

Let us assume that

$$f(s)=\frac{\sqrt{We}}{\mathcal{O}h}\left(u_0\frac{\partial u_0}{\partial s}+\frac{\partial p_0}{\partial s}-((X+1)X_s+ZZ_s)/\mathcal{R}b^2\right).$$

We then have a Neumann problem on a circular domain, where s is a parameter. To determine a solvability condition we multiply the above by $\widehat{u}(s,n,\phi)$ and integrate over the domain of interest S $(0\leqslant n\leqslant R_0, 0\leqslant\phi\leqslant 2\pi)$ so that

$$\int\int_S \widehat{u}\nabla^2_{n,\phi}u_1 dS=\int\int_S \widehat{u}f(s)dS$$

where $\widehat{u}$ satisfies the homogeneous Neumann problem such that

$$\nabla^2_{n,\phi}\widehat{u}=0 \quad \text{with} \quad \frac{\partial\widehat{u}}{\partial n}=0 \quad \text{on} \quad n=R_0.$$

Green's identity gives

$$\int\int_S \widehat{u}\nabla^2_{n,\phi}u_1 dS=\int_B \widehat{u}\frac{\partial u_1}{\partial n}d\Omega_S$$

where Ω_S is the boundary of S. Then we have

$$\int_0^{2\pi}\int_0^{R_0} \widehat{u} n f(s) \mathrm{d}n\mathrm{d}\phi = \int_0^{2\pi} \left[\widehat{u}\frac{\partial u_1}{\partial n}\right]_{n=R_0} R_0 \mathrm{d}\phi$$
$$= \int_0^{2\pi} [\widehat{u}]_{n=R_0} \left(u_0 \cos\phi (X_s Z_{ss} - X_{ss} Z_s) + \frac{Oh^{-1}}{\sqrt{We}} \frac{\partial \sigma_0}{\partial s} \right) R_0 \mathrm{d}\phi$$
$$= \int_0^{2\phi} [\widehat{u}]_{n=R_0} (g(s)\cos\phi + h(s)) R_0 \mathrm{d}\phi$$

where $g(s) = u_0(X_s Z_{ss} - X_{ss} Z_s)$ and $h(s) = (\mathcal{O}h^{-1}/We^{\frac{1}{2}})\partial\sigma/\partial s$.

The general solution to the homogeneous Neumann problem which is bounded in $0 \leqslant n \leqslant R_0$ and is periodic in ϕ with period 2π is $\widehat{u} = \gamma(s)$[10]. Thus we have

$$\gamma(s) R_0 g(s) [\sin\phi]_0^{2\pi} + \gamma(s) R_0 h(s) [\phi]_0^{2\pi} = \gamma(s) f(s) \left[\frac{n^2}{2}\right]_0^{R_0} [\phi]_0^{2\pi}$$

since $R_0 \neq 0$ we must have $f(s) = 2h(s)/R_0$ so that

$$f(s) = \frac{1}{\mathcal{O}h\sqrt{We}} \frac{2}{R_0} \frac{\partial \sigma_0}{\partial s}.$$

We therefore have

$$\frac{\partial u_0}{\partial t} + u_0 \frac{\partial u_0}{\partial s} + \frac{(X+1)X_s + Z Z_s}{\mathcal{R} b^2} = -\frac{\partial p_0}{\partial s} + \frac{2}{R_0 We} \frac{\partial \sigma_0}{\partial s}. \tag{6.54}$$

Solving (6.48), (6.49) and (6.51) for p_1 we obtain

$$p_1 = \frac{\sigma n}{R_0 We} \cos\phi (X_s Z_{ss} - X_{ss} Z_s) - \frac{Oh}{\sqrt{We}} \frac{\partial u_0}{\partial s} + h_1(s), \tag{6.55}$$

where $h_1(s)$ is an arbitrary function of s which could be found at higher order. We note that we have made use of the fact that R_1 is a periodic function, of period 2π, with respect

[10]This is due to the fact that the solution to the homogeneous Neumann problem on a circular domain is a constant, i.e., it cannot be a function of the radial or azimuthal direction.

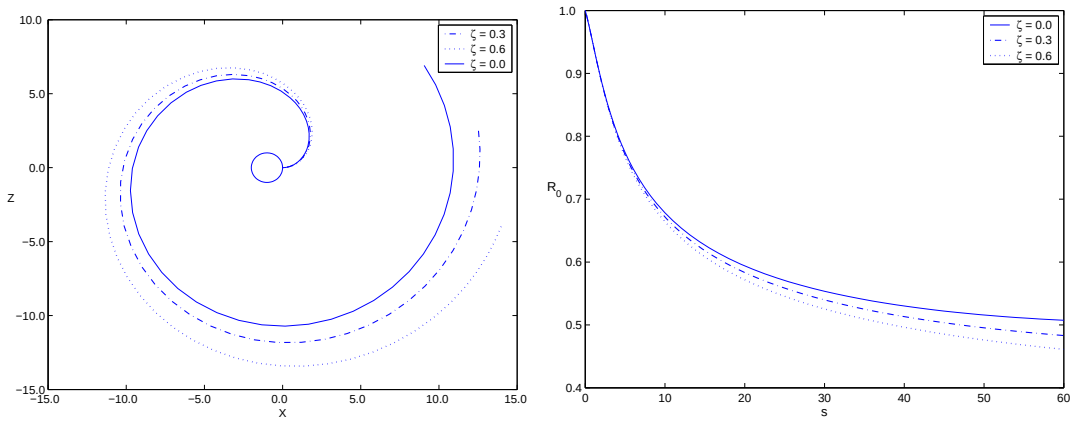

Figure 6.2: The effect of changing the initial surfactant concentration ζ on the steady centreline and radius of a rotating liquid jet obtained using a Runge-Kutta method. Here we have $\mathcal{R}b = 3.2$, $We = 5.4$ and $\beta = 0.5$. Clearly a greater initial surfactant concentration leads to the jet curving less and radius decaying more quickly.

to ϕ in order to obtain the above equation. Since the contribution of viscosity (denoted by $\mathcal{O}h$) to p_1 in the above equation is a function of s only, it does not affect the leading order trajectory of the liquid jet.

It is sufficient, therefore, to solve the equations (where we have dropped the subscript zero from all variables for convenience)

$$uu_s = -\frac{(1+\beta\log(1-\zeta u^{-\frac{1}{2}}))}{We}\frac{u_s}{2\sqrt{u}} + \frac{\beta\zeta}{2uWe}\frac{u_s}{(1-\zeta u^{-\frac{1}{2}})} + \frac{(X+1)X_s + ZZ_s}{\mathcal{R}b^2}, \quad (6.56)$$

$$(X_sZ_{ss} - X_{ss}Z_s)\left(u^2 - \frac{1}{We}(1+\beta\log(1-\zeta u^{-\frac{1}{2}}))\sqrt{u}\right) = \frac{2u}{\mathcal{R}b} - \frac{(X+1)Z_s - ZX_s}{\mathcal{R}b^2}, \quad (6.57)$$

$$X_s^2 + Z_s^2 = 1. \quad (6.58)$$

We solve this system of nonlinear ordinary differential equations using a Runge-Kutta method. We use as our initial conditions $u = X_s = 1$ and $X = Z = Z_s = 0$ at $s = 0$.

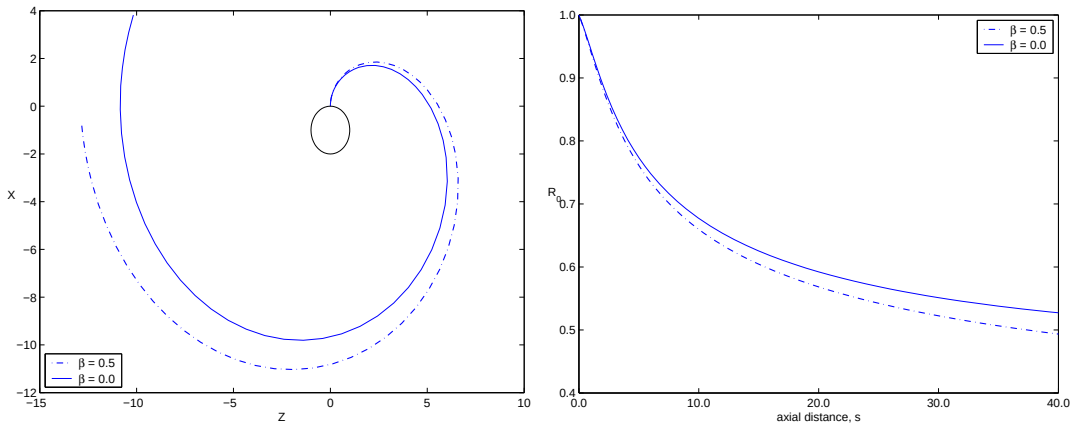

Figure 6.3: The effect of changing β on the steady centreline and radius of a rotating liquid jet obtained using the Runge-Kutta method. Here we have $\mathcal{R}b = 3.2$, $We = 5.5$ and the initial surfactant concentration as $\zeta = 0.5$. Clearly when surfactants are present we have a reduced surface tension leading to the jet curving less and the radius decaying more quickly.

We show the effect of changing the initial surfactant concentration ζ on the trajectory of a rotating liquid jet in Fig. 6.2. A greater initial surfactant concentration leads to the jet curving less and radius decaying more quickly along the jet. In Fig. 6.3 we show the effect of changing the parameter β on trajectories. Larger values of β, which correspond to a greater effectiveness of surfactants and thus a lower surface tension, lead to the jet curving less and jet radius decaying more. The effects of changing the rotation rate ($\mathcal{R}b$ number) or the Weber number We on the steady state solution for the surface tension (which depends upon the surfactant concentration) along the jet is shown in Fig. 6.4 and Fig. 6.5. We see that high rotation rates and high Weber numbers lead to greater differences in surface tension along the jet.

6.4 Linear Instability

In this section we consider the linear stability of disturbances about our leading order steady state solution obtained in the previous section. In this linear analysis it is sufficient to consider a linearized version of the surface tension equation of state. By expanding

(6.40) in a Taylor series about the initial surfactant concentration ζ we have

$$\begin{aligned}\sigma &= (1+\beta\log(1-\zeta)) + \sigma'(\zeta)(\Gamma-\zeta) \\ &= (1+\beta\log(1-\zeta)) - \frac{\beta}{(1-\zeta)}(\Gamma-\zeta) \\ &= \sigma_e - E\Gamma \end{aligned} \tag{6.59}$$

where $\sigma_e = (1+\beta\log(1-\zeta)) + \frac{\beta\zeta}{(1-\zeta)}$ is the surface tension of the undisturbed liquid jet corresponding to a uniform surfactant concentration ζ and $E = \beta/(1-\zeta)$ is the Gibbs elasticity.

If the centreline of the rotating jet is assumed to curve over a lengthscale of $s = O(1)$ and perturbations along the jet are of order a (which is comparable to ε when $s = O(1)$) then travelling wave modes of the form $\exp(ik\overline{s} + \lambda\overline{t})$ must be considered, where $\overline{s} = s/\varepsilon$ and $\overline{t} = t/\varepsilon$, in order to have $k = k(s) = O(1)$ and $\lambda = \lambda(s) = O(1)$. We begin by expressing our disturbances about our steady state as

$$(u, R, \Gamma) = (u_0, R_0, \Gamma_0) + \delta(\widehat{u}, \widehat{R}, \widehat{\Gamma})\exp(ik\overline{s} + \lambda\overline{t}), \tag{6.60}$$

where δ is some dimensionless small constant. In this case u_0, R_0 and Γ_0 denote the steady state solutions found in the preceding section and k is a real wavenumber with λ being complex, so that $\lambda = \lambda_r + i\lambda_i$ where λ_r is the growth rate of disturbances and λ_i is the wavenumber of disturbances along the jet. In order to prevent instability to wavemodes with zero wavelength we replace the leading order pressure term in (6.36) with the full curvature expression. We thus have

$$\begin{aligned} u_{0t} + uu_{0s} = -\frac{1}{We}\left(\sigma_0\left(\frac{1}{R(1+\varepsilon^2R_{0s}^2)^{\frac{1}{2}}} - \frac{\varepsilon^2R_{0ss}}{(1+\varepsilon^2R_{0s}^2)^{\frac{3}{2}}}\right)\right)_s + \frac{(X+1)X_s + ZZ_s}{\mathcal{R}b^2} \\ + \frac{3}{\mathcal{R}e}\left(u_{0ss} + 2u_{0s}\frac{R_{0s}}{R}\right) + \frac{2\sigma_{0s}}{WeR_0}. \end{aligned} \tag{6.61}$$

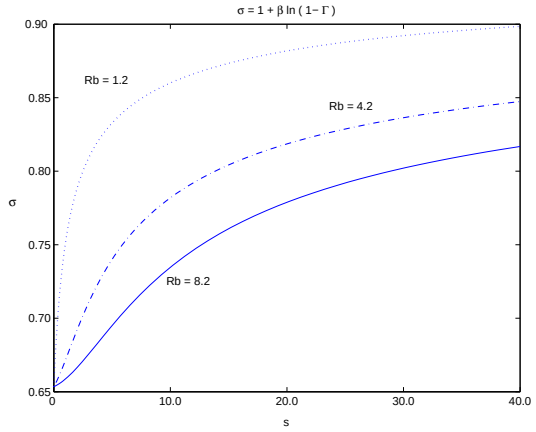

Figure 6.4: The dynamic surface tension as the rotation rate of the cylindrical drum in changed. Here we have $We = 5.5$, $\beta = 0.5$ and the initial surfactant concentration as $\zeta = 0.5$. As the rotation rate is increased (corresponding to smaller values of $\mathcal{R}b$) we see that the surface tension changes more along the jet.

We substitute (6.60) into our governing equations (6.61), (6.37), (6.39), and drop overbars from our variables. Taking $\varepsilon \to 0$ gives that λ and k are related by the equation obtained by setting the determinant of the matrix to zero

$$\begin{pmatrix} 3k^2/\overline{\mathcal{R}e} + \xi & -ik\sigma_0\chi/We & ikE/R_0We \\ ikR_0/2 & \xi & 0 \\ ik\Gamma_0/2 & 0 & \xi \end{pmatrix}$$

where

$$\chi = \left(\frac{1}{R_0^2} - k^2\right) \quad \text{and} \quad \xi = (\lambda + iku_0).$$

We have rescaled the Reynolds number (and based it on the orifice radius a) so that $\overline{\mathcal{R}e} = \varepsilon\mathcal{R}e$ to bring in viscous terms. Non trivial solutions exist if this system has determinant zero, whence we get

$$\left(\frac{3}{\overline{\mathcal{R}e}}k^2 + (\lambda + iku_0)\right)(\lambda + iku_0)^2 - \frac{k^2\sigma_0 R_0}{2We}\left(\frac{1}{R_0^2} - k^2\right)(\lambda + iku_0) + \frac{Ek^2\Gamma_0}{2R_0We}(\lambda + iku_0) = 0 \tag{6.62}$$

choosing $\lambda_i = -ku_0$ so that disturbances are convected along the jet we find that

$$\lambda_r^2 + \frac{3}{\overline{\mathcal{R}e}}k^2\lambda_r - \frac{k^2}{2We}\left(\sigma_0 R_0\left(\frac{1}{R_0^2} - k^2\right) - \frac{E\Gamma_0}{R_0}\right) = 0, \tag{6.63}$$

which has solution

$$\lambda_r = -\frac{3}{2\overline{\mathcal{R}e}}k^2 + \frac{k}{2}\sqrt{\left(\frac{3k}{\overline{\mathcal{R}e}}\right)^2 + \frac{2}{We}\left(\frac{1}{R_0^2} - k^2\right)\sigma_0 R_0 - \frac{2E\Gamma_0}{RWe}}. \tag{6.64}$$

Differentiating the above equation to find the wavenumber for which λ_r is a maximum (which we shall henceforth refer to as k^*) we find

$$k^* = \frac{1}{(2R_0^3)^{\frac{1}{4}}}\left(\frac{(\sigma_0 - \Gamma_0 E)}{\sigma_0\sqrt{2R_0} + 3Oh\sqrt{\sigma_0}}\right)^{\frac{1}{2}} \tag{6.65}$$

where $Oh = \sqrt{We}/\overline{\mathcal{R}e}$ is the Ohnesorge number. When there is no surfactant present (i.e., $\Gamma_0 = 0$) we have $\sigma = 1$ and the above expression reduces to the most unstable wavnenumber of a viscous jet

$$k^* = \frac{1}{(2R_0^3)^{\frac{1}{4}}}\frac{1}{\sqrt{3Oh + \sqrt{2R_0}}}. \tag{6.66}$$

The effects on the most unstable wavenumber k^* in changing the parameter β (which is a measure of the importance of surfactant activity) is shown in Fig. 6.6. Irrespective of the value of β we see that the most unstable wavenumber increases along the jet. A larger value of β leads to smaller values of the most unstable wavenumber. It can be seen that the growth rate of the most unstable mode also decreases as β is increased (Fig. 6.7) so that jets with greater surfactant 'activity' are expected to be longer. In Fig. 6.8 we plot the wavenumber of the most unstable mode against arc length along the jet for different Rossby numbers. It can be observed that jets with higher rotation rates (or

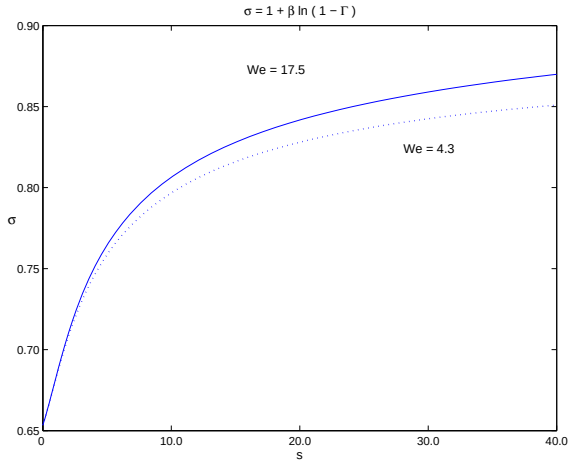

Figure 6.5: The dynamic surface tension against distance along the jet as the Weber number is changed. Here we have $\mathcal{R}b = 3.2$, $\beta = 0.5$ and the initial surfactant concentration as $\zeta = 0.5$. As the Weber number is increased the surface tension increases more quickly along the jet.

smaller Rossby numbers) lead to larger wavenumbers.

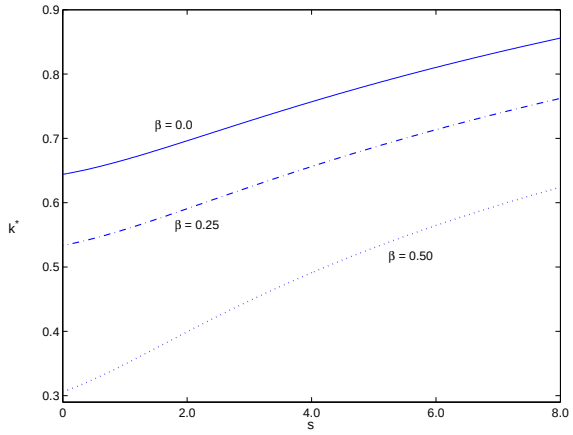

Figure 6.6: The wavenumber of the most unstable mode k^* plotted against the distance along the jet s for different β. Here we have $We = 8.4$, $\zeta = 0.5$, $Oh = 0.097$ and $\mathcal{R}b = 4.2$. It can be observed that k^* increases along the jet and is smaller for smaller values of β (i.e., as the 'effectiveness' of surfactants increases the wavenumber of the most unstable mode decreases)

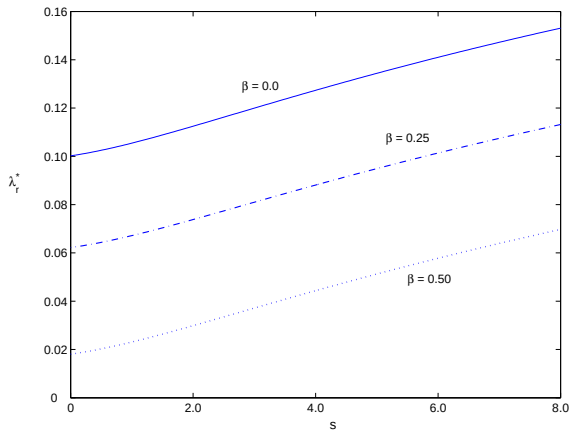

Figure 6.7: The growth rate λ_r^* of the most unstable mode plotted against the distance along the jet s for different β. Here we have $We = 8.4$, $\zeta = 0.5$, $Oh = 0.097$ and $\mathcal{R}b = 4.2$. As the 'effectiveness' of surfactants increases (i.e., β increases) the growth rate of the most unstable mode decreases so that longer jets are expected when surfactants are important.)

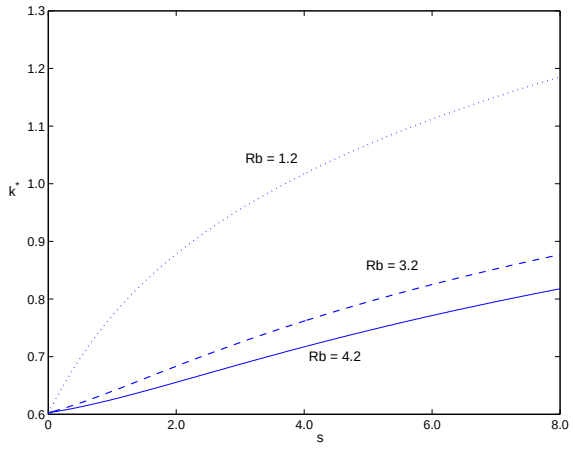

Figure 6.8: The wavenumber of the most unstable mode k^* plotted against the distance along the jet s for different Rossby number $\mathcal{R}b$. Here we have $We = 8.4$, $\zeta = 0.35$, $Oh = 0.097$ and $\beta = 0.2$. The most unstable wavenumber can be seen to increase for decreasing Rossby numbers.

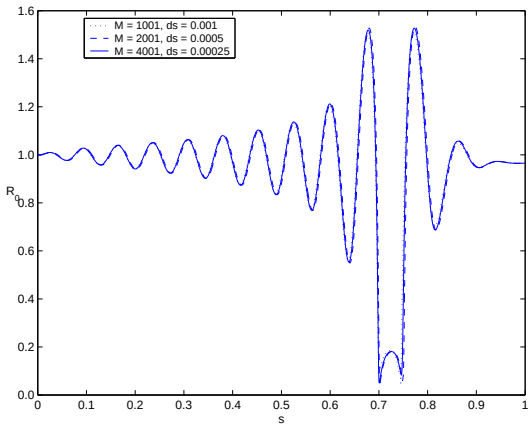

Figure 6.9: Accuracy check for various ds and various number of mesh points M. The other parameters are $We = 14.5$, $\mathcal{R}b = 4.3$, $\beta = 0.2$, $\zeta = 0.33$, $\mathcal{R}e = 2250$, $\kappa = 0.88$, $\delta = 0.01$, $dt = 5 \times 10^{-6}$ and the final time $t_f = 0.7386$.

6.5 Nonlinear Temporal Solutions

We next consider nonlinear temporal simulations of rotating surfactant laden liquid jets. To remain consistent with our previous chapters, and for similar reasons presented therein, we replace the leading order pressure term $p_0 = \frac{1}{We}\frac{1}{R_0}$ by the expression for the full curvature term which contains only R_0 and is not ϕ-dependent, namely

$$p = \frac{\kappa}{We} = \frac{1}{We}\left[\frac{1}{(1+\varepsilon^2 R_{0s}^2)^{\frac{1}{2}}} - \frac{\varepsilon^2 R_{0ss}}{(1+\varepsilon^2 R_{0s}^2)^{\frac{3}{2}}}\right]. \tag{6.67}$$

We denote $A = R_0^2$ and $G = \Gamma_0^2$ so that we have the nonlinear system to be solved as

$$\frac{\partial A}{\partial t} = -\frac{\partial}{\partial s}(Au), \tag{6.68}$$

$$\begin{aligned} u_t + \left(\frac{u^2}{2}\right)_s &= -\frac{1}{We}\frac{\partial}{\partial s}\left(\sigma\frac{4(2A+(\varepsilon A_s)^2 - \varepsilon^2 A A_{ss})}{(4A+(\varepsilon A_s)^2)^{\frac{3}{2}}}\right) + \frac{2\sigma_s}{A^{\frac{1}{2}}We} \\ &+ \frac{(X+1)X_s + ZZ_s}{\mathcal{R}b^2} + \frac{3}{\mathcal{R}e}\cdot\frac{(u_s A)_s}{A}, \end{aligned} \tag{6.69}$$

$$\frac{\partial G}{\partial t} = -\frac{\partial}{\partial s}(Gu). \tag{6.70}$$

The initial conditions at $t = 0$ are given by the steady solutions calculated using the method described in section 6.3, so that

$$A(s,0) = R_0^2(s), \quad u(s,0) = u_0(s) \quad \text{and} \quad G(s,0) = \Gamma_0^2(s). \tag{6.71}$$

The conditions at the nozzle are given by

$$u(0,t) = 1 + \delta \sin\left(\frac{\kappa t}{\varepsilon}\right), \quad R(0,t) = 1 \quad \text{and} \quad \Gamma(0,t) = \zeta,$$

where once again we have δ as an initial disturbance amplitude and κ is the wavenumber of disturbances.

We again use an explicit finite difference scheme to solve the above set of equations. The spatial grid is fixed and uniform. The time integration method is based on an explicit scheme, using the Lax-Wendroff method. The accuracy of this numerical scheme for this set of equations is shown in Fig. 6.9 by changing the spatial grid size and/or the time step.

In Figs. 6.10 and 6.11 we show the effect of changing the initial surfactant concentration on the breakup of a rotating liquid jet. It can be seen that as the initial surfactant concentration is increased we have longer jets and fewer droplets. The effects of surfactants in reducing the magnitude (or the growth rate) of interfacial disturbances as well as delaying the onset of pinch-off can be seen in Fig. 6.11. This figure also clearly shows the reduction in the size of satellite droplets when surfactants are added.

Main droplet sizes with and without surfactants are shown to be very similar for large disturbance wavenumbers. However for low disturbance wavenumbers (frequencies) we see that rotating surfactant laden jets produce slightly larger droplets (see Fig. 6.12).

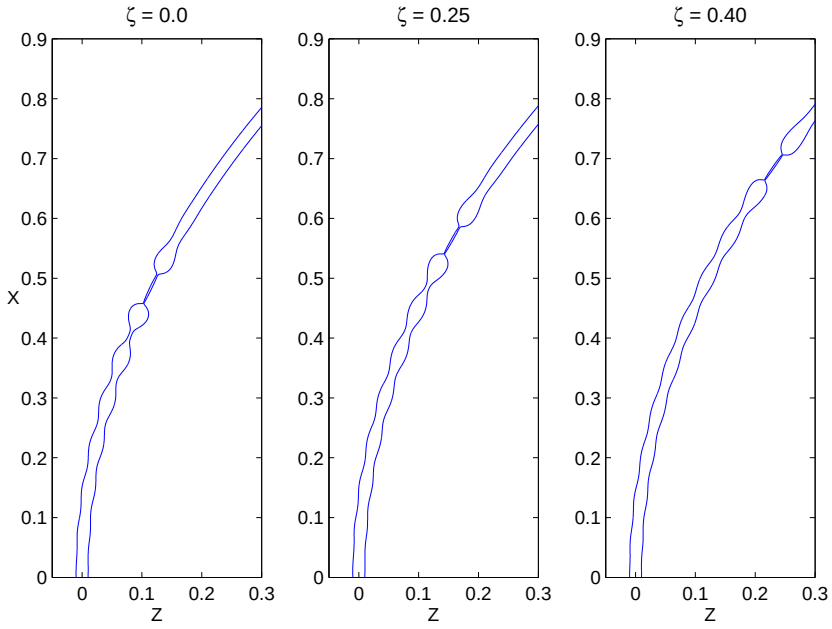

Figure 6.10: Rotating liquid jets with surfactants when the initial surfactant concentration ζ is changed. Here we have $We = 18.4$, $\beta = 0.4$, $\mathcal{R}e = 2250$, $\delta = 0.04$, $\kappa = 0.88$ and $\mathcal{R}b = 2.1$. As the surfactant concentration is increased we see longer jets and fewer droplets.

In Fig. 6.13 we see a similar comparison for satellite droplets. In this case we see that the presence of surfactants always lead to smaller satellites irrespective of the wavenumber of disturbances, although it can be seen that the difference between sizes attains a maximum when $\kappa \approx 0.8$. The use of surfactants impedes the growth of disturbances and leads to larger breakup lengths. In Fig. 6.14 we see that differences in breakup lengths remain fairly consistent for a range of rotation rates although differences are largest for low Rossby numbers (i.e., high rotation rates). This suggests that the effects of rotation slightly enhance the role of surfactants on breakup. In Fig. 6.15 satellite droplet sizes are shown for different rotation rates. Decreasing the rotation of the cylindrical drum leads to smaller satellite droplets (which agrees with the findings of Părău *et al.* (2007) for surfactant free spiralling jets). It can be observed that satellite droplets are smaller for all rotation rates when surfactants are present. In particular the relative difference in sizes between satellite droplets for surfactant laden rotating jets and surfactant-free

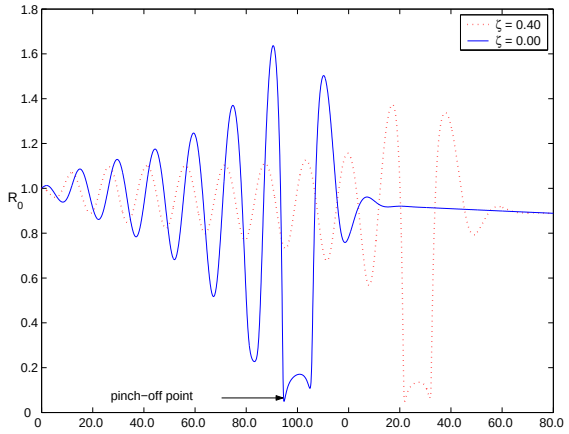

Figure 6.11: The radius R_0 against the distance along the jet s for a surfactant free jet and a jet with surfactants ($\zeta = 0.4$). Here we have $We = 18.4$, $\beta = 0.4$, $\delta = 0.04$, $\kappa = 0.88$, $\mathcal{R}e = 2250$ and $\mathcal{R}b = 2.1$. Clearly disturbances are damped (owing to the reduced surface tension) when the free surface has a layer of surfactants.

jets are smaller for small Rossby numbers. Thus we see that the effect of rotation is to diminish the role played by surfactants in reducing the size of satellites and that in the limit $\mathcal{R}b \to \infty$, or no rotation, we expect the most dramatic difference in satellite droplet sizes. We should also note here that the size of main droplets are difficult to determine when sufficiently large amounts of surfactants are present, since in these cases the jet is stable for long periods and produces a long coherent thread which snaps some distance away from the orifice.

The breakup lengths for different values of β are shown in Fig. 6.16. A high ($\mathcal{R}b = 1.2$) and low ($\mathcal{R}b = 4.3$) rotation rate is considered. We find, as anticipated, that breakup lengths increase with β and that large rotation rates lead to longer jets. Droplets sizes for both main droplets and satellite droplets are shown in Fig. 6.17 where we see that main droplets for high rotation rates are slightly smaller than their low rotation rate counterparts. However for satellites droplets the reverse is true with the difference much more noticeable (the relative sizes of main and satellite droplets at the different rotation rates agrees perfectly with the findings of Părău *et al.* (2007) for rotating jets without surfactants). The profile and surfactant distribution along the jet is shown for the case

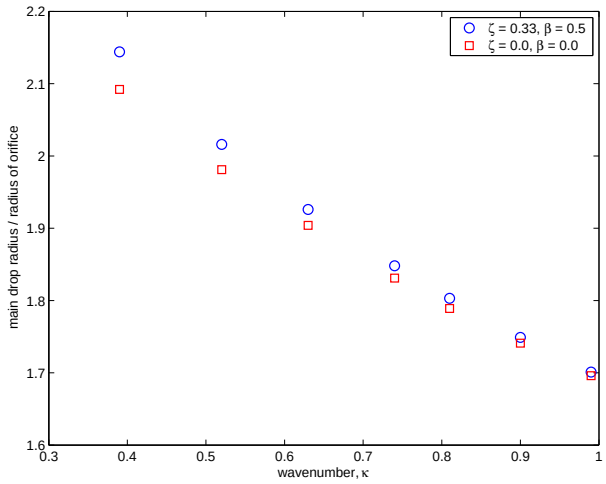

Figure 6.12: Main droplet sizes versus the wavenumber of disturbances κ for $\delta = 0.1$, $We = 20.4$, $\mathcal{R}e = 2750$ and $\mathcal{R}b = 2.1$. Two sets of data are shown which include jets with surfactants and jets without. Droplet sizes are very similar except for low wavenumbers where the use of surfactants produce larger droplets.)

$\beta = 0.2$ in Fig. 6.18. In this case we see the familiar elongation of the ligament between droplets for high rotation rates and large gradients in surfactant concentration for high rotation rates. Finally in Fig. 6.19 we show the radius plotted against arc length for a rotating surfactant laden jet at the non dimensional time $t = 0.4$ for three different initial surfactant concentrations ζ. This figure demonstrates that it is only the final stages, near to pinch-off, which significantly influence breakup lengths and size of droplets.

The linear instability of a rotating non-Newtonian liquid jet with surfactants is presented in Appendix G.

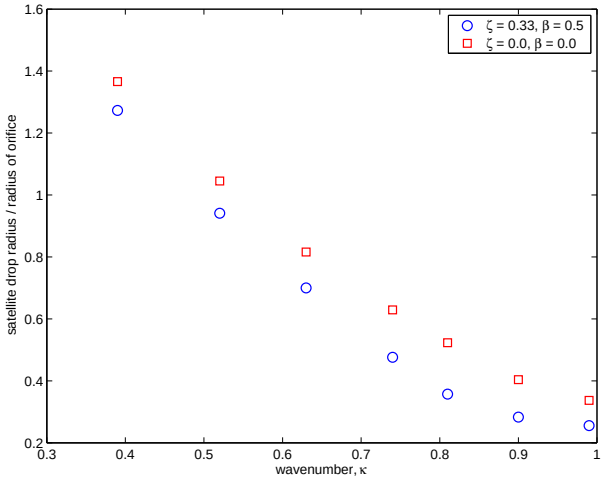

Figure 6.13: Satellite droplet sizes versus the wavenumber of disturbances κ for $\delta = 0.1$, $We = 20.4$, $\mathcal{R}e = 2750$ and $\mathcal{R}b = 2.1$. We see that surfactants produce smaller satellite droplets irrespective of the wavenumber.

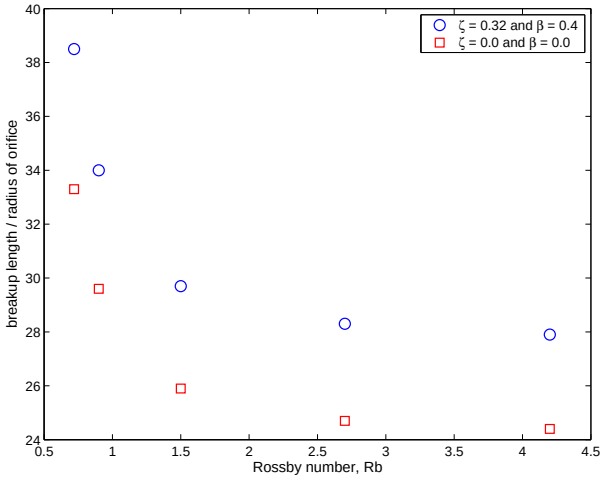

Figure 6.14: Breakup lengths for different rotation rates in the case of rotating liquid jet with surfactants (circle) and without surfactants (square). The parameters here are $\mathcal{R}e = 2600$, $We = 14.5$, $\delta = 0.1$ and $\kappa = 0.8$. Breakup lengths decrease with decreasing rotation rate (larger $\mathcal{R}b$) and the presence of surfactants leads to longer jets.

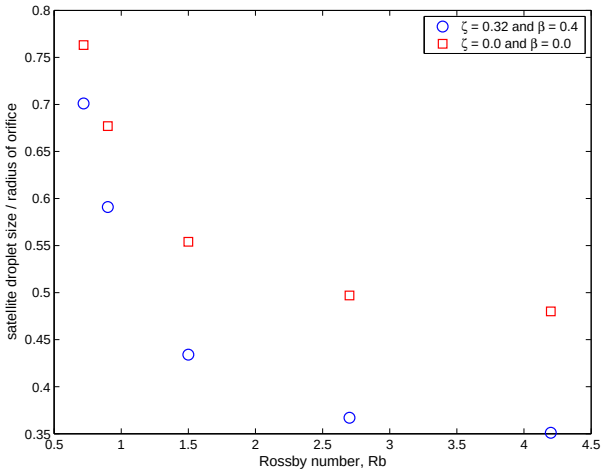

Figure 6.15: Satellite droplet sizes for different rotation rates in the case of rotating liquid jet with surfactants (circle) and without surfactants (square). The parameters here are $\mathcal{R}e = 2600$, $We = 14.5$, $\delta = 0.1$ and $\kappa = 0.8$. Clearly the satellite droplets decrease in size as the rotation rate is decreased but the difference between satellite droplet sizes for a surfactant laden jet increases with decreasing rotation rate.

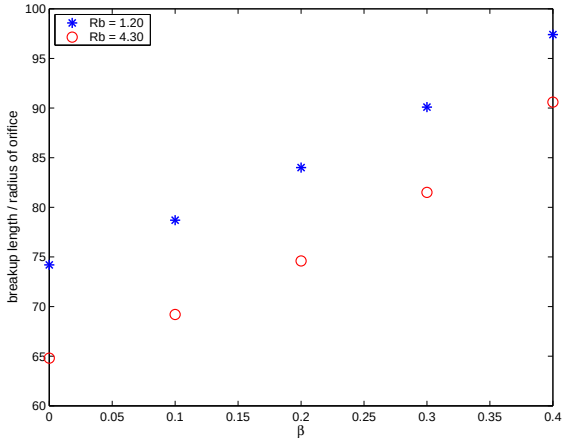

Figure 6.16: The breakup length of a rotating surfactant laden liquid jet for different values of β at high ($\mathcal{R}b = 1.2$) and low ($\mathcal{R}b = 4.3$) rotation rates. Here we have $We = 14.5$, $\zeta = 0.33$, $\delta = 0.01$, $\kappa = 0.88$ and $\mathcal{R}e = 2900$.

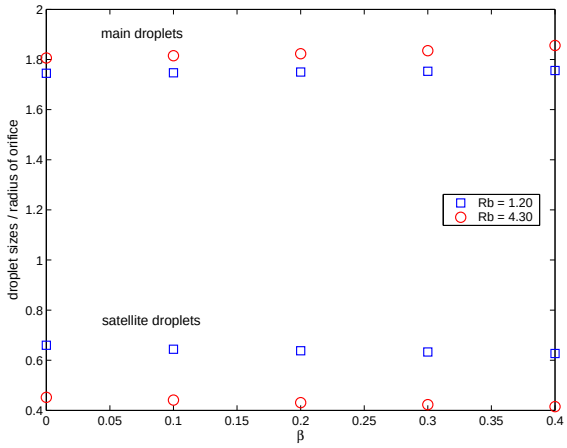

Figure 6.17: Droplet sizes (including satellite droplets) for a rotating surfactant laden liquid jet for different values of β at high ($\mathcal{R}b = 1.2$) and low ($\mathcal{R}b = 4.3$) rotation rates. Here we have $We = 14.5$, $\zeta = 0.33$, $\delta = 0.01$, $\kappa = 0.88$ and $\mathcal{R}e = 2900$.

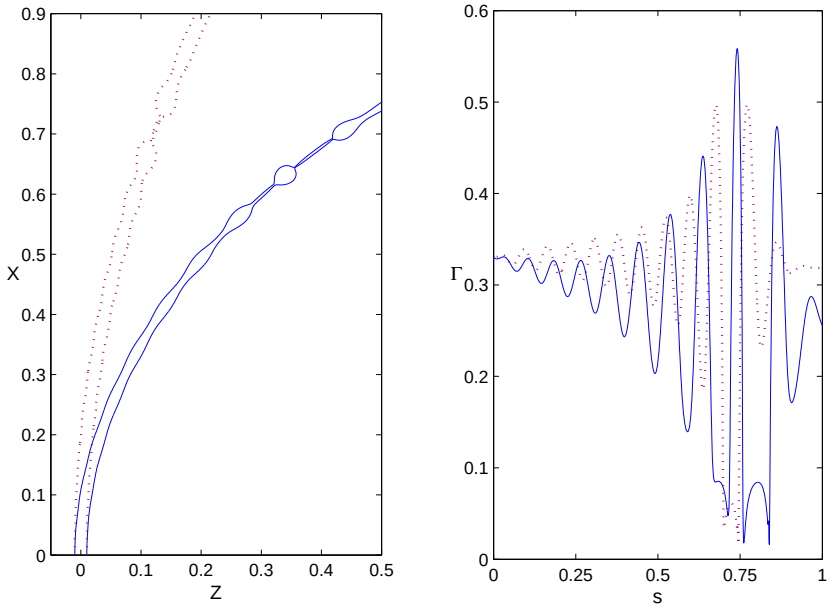

Figure 6.18: The profile and surfactant concentration along a rotating liquid jet for high ($\mathcal{R}b = 1.2$, dotted line) and low ($\mathcal{R}b = 4.3$, solid line) rotation rates. Here we have $We = 14.5$, $\zeta = 0.33$, $\delta = 0.01$, $\kappa = 0.88$ and $\mathcal{R}e = 2900$.

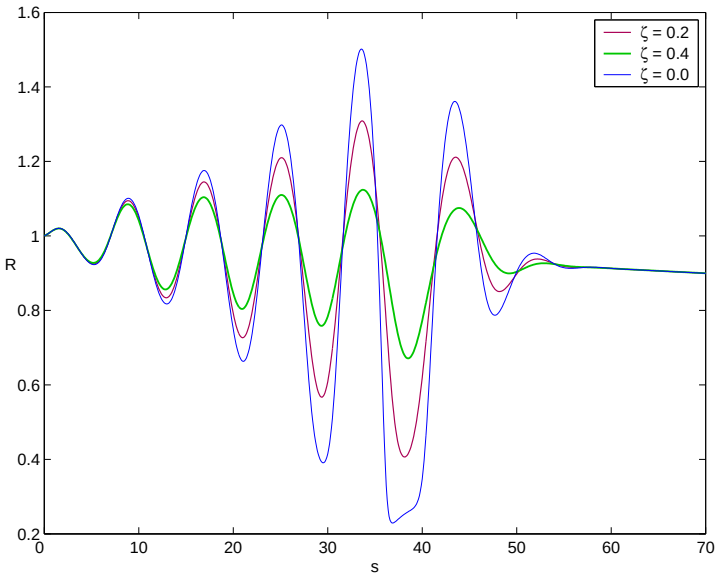

Figure 6.19: The radius plotted against distance along a rotating liquid jet for different values of ζ at the non-dimensional time $t = 0.4$. Here we have $We = 14.5$, $\beta = 0.5$, $\mathcal{R}e = 2600$, $\mathcal{R}b = 1.8$, $\delta = 0.04$ and $\kappa = 0.81$.

Chapter 7

Liquid Jets curved by Gravity

7.1 Introduction

In the preceding chapters we have considered the linear and nonlinear instability of curved liquid jets emerging from a rotating orifice. The motivating application was that of industrial prilling where the rotation rate introduces a controllable parameter with which to manipulate breakup lengths and drop sizes. The effects of changing the rheology of the fluid, so as to include the effects of a shear rate dependent viscosity were considered as was the effects of adding surfactants to the free surface. In both these cases we assumed that the effects of gravity were negligible[1] so that the jet was constrained to move in a plane parallel to the initial direction of motion of the jet.

In this chapter we generalize the results we have obtained hitherto (although we shall not consider non-Newtonian fluids here) and incorporate all the ideas we have considered so far by examining the case of a liquid jet emerging from a rotating orifice and falling under gravity. Here, the primary mechanisms leading to a curved centreline are the forces of gravity *and* the centripetal acceleration of the jet caused by the rotating cylinder. We

[1]We assumed that the effects of gravity on the jet were negligible if the centripetal acceleration of the jet, $s_0\Omega^2$, was much greater than the acceleration due to gravity, g. Such an assumption is therefore strong for high rotation rates (which correspond well with the rotation rates used in industrial prilling) and becomes increasingly weaker as the rotation rate is decreased.

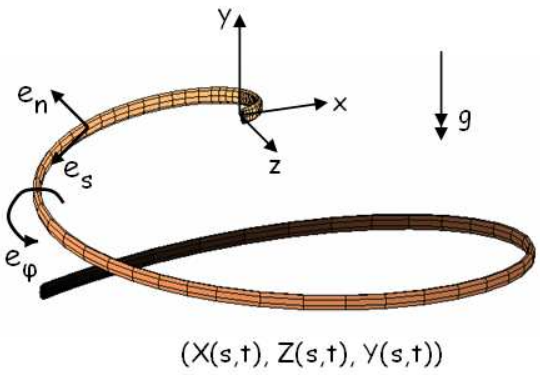

Figure 7.1: A liquid jet emerging from a rotating orifice and falling under the influence of gravity. The location of the orifice is at (0,0,0) on the Cartesian axes shown. The centreline of the jet is described by $(X(s,t), Z(s,t), Y(s,t))$.

will assume, as we did in the previous chapter, that the jet is coated with a layer of insoluble surfactant upon leaving the orifice. Since this problem is similar and utilizes much of the analysis we have considered so far, we shall present our results here with a lot less rigour than we would do otherwise. Furthermore, since the non-dimensional equations of motion and boundary conditions are extremely tedious and can be found elsewhere (for a rotating liquid jet falling under gravity without surfactants see Decent *et al.* (2001), Wallwork (2001) and Partridge (2006)) we will omit much of the details and, where necessary, refer the reader to other works. The reader may wish to re-familiarise themselves with Chapter Four and in particular section 4.2 before proceeding.

Let us begin by considering a liquid jet emerging from a rotating orifice (see Fig. 7.1) and falling under the influence of gravity. We choose the Cartesian x-axis as the direction of the initial motion of the jet, the negative y-axis is chosen as the direction of the acceleration due to gravity and the z-axis is chosen so as to form a triad of coordinate vectors. In this case the centreline of the jet can be described by $x = X(s,t)$, $z = Z(s,t)$ and $y = Y(s,t)$ where s is the arc length along the jet and t is time. Our orthogonal curvilinear coordinate are the same as those presented in Chapter Four. The equations of motion, the continuity equation and the boundary conditions are similar to those

presented hitherto (except here we must include Y and derivatives of Y) and are given by

$$\boldsymbol{\nabla} \cdot \boldsymbol{u} = 0, \tag{7.1}$$

$$\rho \left(\frac{\partial \mathbf{u}}{\partial t} + \mathbf{u} \cdot \boldsymbol{\nabla} \mathbf{u} \right) = -\boldsymbol{\nabla} p + \boldsymbol{g} + \boldsymbol{\nabla} \cdot \mathbf{T} - 2\boldsymbol{\omega} \times \mathbf{u} - \boldsymbol{\omega} \times (\boldsymbol{\omega} \times \boldsymbol{r}), \tag{7.2}$$

$$\Gamma_t + \boldsymbol{u} \cdot \boldsymbol{\nabla} \Gamma - \Gamma \mathbf{n} (\mathbf{n} \cdot \boldsymbol{\nabla}) \boldsymbol{u} = 0, \tag{7.3}$$

$$\frac{\partial R}{\partial t} + \boldsymbol{u} \cdot \boldsymbol{\nabla} R = 0 \quad \text{on} \quad n = R(s, \phi, t) \tag{7.4}$$

$$\boldsymbol{n} \cdot \mathbf{P} \cdot \boldsymbol{n} = \sigma \kappa \quad \text{and} \quad \boldsymbol{t_i} \cdot \mathbf{P} \cdot \boldsymbol{n} = \boldsymbol{t_i} \cdot \boldsymbol{\nabla} \sigma \tag{7.5}$$

and

$$X_s^2 + Y_s^2 + Z_s^2 = 1, \tag{7.6}$$

where $\mathbf{P} = p\boldsymbol{I} + \mathbf{T}$. These equations are similar to those found in Decent *et al.* (2001) and Partridge (2006) except here we include (7.3) to describe the transport of surfactants along the free surface and (7.5) has been modified so as to incorporate non-zero tangential stresses.

Posing the same asymptotic expansion of 4.2.4 (along with an asymptotic expansion for Y akin to those of X and Z) we have at leading order the equations (see also Partridge (2006) and Wallwork (2001) for similar equations without surfactants)

$$R_{0t} + u_0 R_{0s} + \frac{R_0}{2} u_{0s} = 0, \tag{7.7}$$

$$u_{0t} + u_0 u_{0s} = -\frac{Y_s}{\mathcal{F}^2} - \frac{1}{We} \left(\frac{\sigma_0}{R_0} \right)_s + \frac{(X+1)X_s + ZZ_s}{\mathcal{R}b^2} + \frac{3(R_0^2 u_{0s})}{\mathcal{R}eR_0^2} + \frac{2\sigma_{0s}}{R_0 We}, \tag{7.8}$$

$$\Gamma_{0t} + u_0 \Gamma_{0s} + \frac{u_{0s}}{2} \Gamma = 0, \tag{7.9}$$

$$\frac{Z_s X_{ss} - Z_{ss} X_s}{\mathcal{F}^2} - \frac{2Y_{ss} u_0}{\mathcal{R}b} + \frac{(X+1)(Y_{ss} Z_s - Y_s Z_{ss})}{\mathcal{R}b^2} + \frac{Z(Y_s X_{ss} - Y_{ss} X_s)}{\mathcal{R}b^2} = 0, \tag{7.10}$$

$$\left(u_0^2 - \frac{3u_{0s}}{\mathcal{R}e} - \frac{\sigma_0}{R_0 We}\right)(X_{ss}^2 + Y_{ss}^2 + Z_{ss}^2) = -\frac{Y_{ss}}{\mathcal{F}^2} + \frac{2u_0}{\mathcal{R}b}(X_s Z_{ss} - Z_s X_{ss}) + \frac{1}{\mathcal{R}b^2}((X+1)X_{ss} + ZZ_{ss}), \tag{7.11}$$

where $\sigma_0 = 1 + \beta \log(1 - \Gamma_0)$ and the arc length condition (7.6). The Reynolds number $\mathcal{R}e$ and Weber number We are given in section 4.2.3, however here we have an additional non-dimensional number known as the Froude[2] number $\mathcal{F} = U/\sqrt{gs_0}$ where g is the acceleration due to gravity. This is a set of seven equations in the seven unknowns u_0, R_0, σ_0, Γ_0, X, Y and Z. In the next section we will solve this set of equations, in the steady state, using a Runge-Kutta method with the initial conditions as $u_0 = R_0 = X_s = 1$, $\Gamma_0 = \zeta$ and $Z = Z_s = Y = Y_s = 0$ where $0 < \zeta < 1$ is the initial surfactant concentration.

7.2 Steady State Solutions

By considering the steady state solutions of (7.7) and (7.9) we find, after some algebra, that the steady state of this system is governed by the equations[3]

$$u_0 u_{0s} = -\frac{(1 + \beta \log(1 - \zeta u_0^{-\frac{1}{2}}))}{We}\frac{u_{0s}}{2\sqrt{u_0}} + \frac{\beta\zeta}{2u_0 We}\frac{u_{0s}}{(1 - \zeta u_0^{-\frac{1}{2}})} \frac{(X+1)X_s + ZZ_s}{\mathcal{R}b^2} - \frac{Y_s}{\mathcal{F}^2} + \frac{3}{\mathcal{R}e}\left(u_{0ss} - \frac{u_{0s}^2}{u_0}\right), \tag{7.12}$$

$$\left(u_0^2 - \frac{3u_{0s}}{\mathcal{R}e} - \frac{1}{We}(1 + \beta \log(1 - \zeta u_0^{-\frac{1}{2}}))\sqrt{u_0}\right)(X_{ss}^2 + Y_{ss}^2 + Z_{ss}^2) = -\frac{Y_{ss}}{\mathcal{F}^2} + \frac{2u_0}{\mathcal{R}b}(X_s Z_{ss} - Z_s X_{ss}) + \frac{1}{\mathcal{R}b^2}((X+1)X_{ss} + ZZ_{ss}), \tag{7.13}$$

[2]William Froude (1810 - 1879) was an English mathematician and engineer. He was commissioned by Brunel to help construct the Bristol and Exeter Railway. He is famous for his work on the design of ships and in particular for the derivation of formulae to determine the resistance that water has on ships.

[3]The kinematic and surfactant transport equations reduce to $R_0^2 u_0 = C_1$ and $\Gamma_0^2 u_0 = C_2$ where after using the initial conditions we have $C_1 = 1$ and $C_2 = \zeta^2$. Thus R_0 and Γ_0 can be expressed as functions of u_0

$$\frac{Z_s X_{ss} - Z_{ss} X_s}{\mathcal{F}^2} - \frac{2Y_{ss}u_0}{\mathcal{R}b} + \frac{(X+1)(Y_{ss}Z_s - Y_s Z_{ss})}{\mathcal{R}b^2} + \frac{Z(Y_s X_{ss} - Y_{ss}X_s)}{\mathcal{R}b^2} = 0, \quad (7.14)$$

and

$$X_s^2 + Y_s^2 + Z_s^2 = 1. \quad (7.15)$$

The above set of equations contains only four variables, namely u_0, X, Y and Z.

For similar reasons to those described in Chapter Four we assume that the centreline of the jet is independent of viscosity to leading order (this is also shown analytically by Decent *et al.* (2007*a*) for viscous liquid jets curved by gravity without rotation i.e., $\mathcal{R}b \to \infty$ and can be modified for the case under consideration here). Solving (7.12 - 7.15) in the inviscid limit with the initial conditions $R_0(0) = u_0(0) = X_s(0) = 1$ and $Y(0) = X(0) = Z(0) = Z_s(0) = Y_s(0) = 0$ we obtain the trajectory of the jet. In Fig 7.2 we show how surfactants affect the trajectory of the jet. It can be seen that the surfactant laden jet tends to curve less and fall more quickly under gravity. In Fig. 7.3 and Fig. 7.4 we show the effects of changing the Froude number and Rossby number on the trajectory of the liquid jet. Increasing the Froude number (which corresponds to decreasing the effects of gravity) leads to jets which fall in the negative y axis less. It can also be observed that for small Rossby numbers (i.e., high rotation rates) the jet curves more but falls less under gravity. If we eliminate rotation from the problem so that we have a liquid jet emerging from an orifice and falling under gravity (see Fig. 7.5) lying solely in the $x - y$ plane (see also Decent *et al.* (2007)) then the steady state is given by (7.12 - 7.15) subject[4] to $\mathcal{R}b \to \infty$ and $Z = 0$. In this case we show the trajectory of the liquid jet in 7.6.

[4]In this case all derivatives of Z will also be zero and (7.14) will be identically equal to zero. Alternatively, when taking the limit $\mathcal{F} \to \infty$ and $Y = 0$ we obtain the spiralling jet equation with surfactants (see previous chapter).

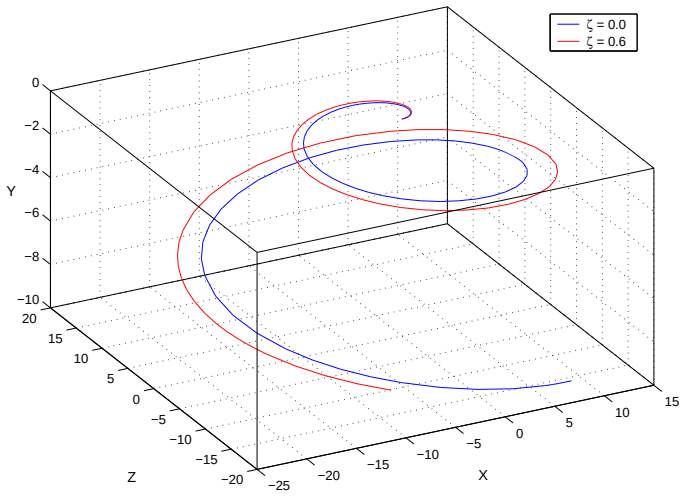

Figure 7.2: A rotating liquid jet when both gravity and rotation are included in the model with $\mathcal{F} = 8.0$, $We = 6.0$ and $\mathcal{R}b = 3.0$. Here we show the different trajectories with surfactants ($\zeta = 0.6$ and $\beta = 0.6$, red line in colour) and without (blue line in colour). The addition of surfactants leads to a centreline which is less curved.

7.3 Linear Analysis

When we considered the linear stability analysis of the governing equations for a rotating liquid jet with surfactants, we did not find an explicit relationship between rotation rate and most unstable wavenumber and maximum growth rates. Instead we found that the rotation of the cylindrical drum only affects the most unstable wavenumber and growth rate implicitly through changing the initial steady state solutions for u_0, R_0 and Γ_0. The case of a liquid jet falling under gravity is similar in that respect so that the most unstable wavenumber is given by

$$k^* = \frac{1}{(2R_0^3)^{\frac{1}{4}}} \left(\frac{(\sigma_0 - \Gamma_0 E)}{\sigma_0 \sqrt{2R_0} + 3Oh\sqrt{\sigma_0}} \right)^{\frac{1}{2}} \tag{7.16}$$

where $Oh = \sqrt{We}/\mathcal{R}e$ is the Ohnesorge number. The effects of gravity, now characterized by the Froude number, enters only through the steady state solutions. In Fig. 7.7 we show the effects of changing $\mathcal{F}$ on the wavenumber of the most unstable mode for a surfactant

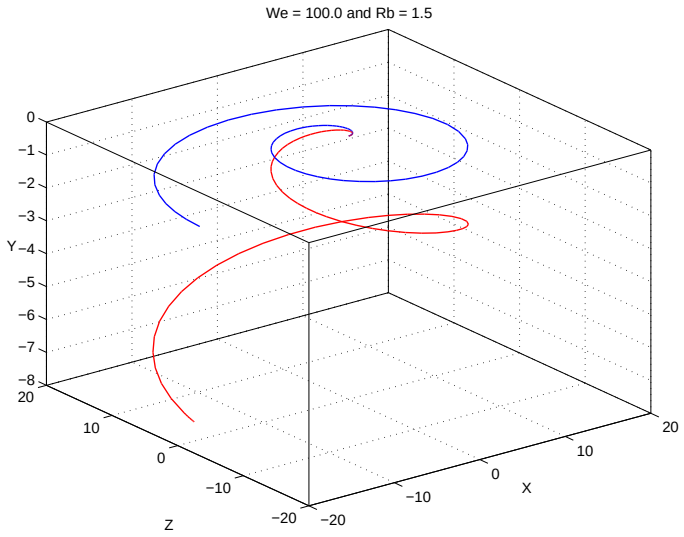

Figure 7.3: A rotating liquid jet when both gravity and rotation are included in the model. Here we show the different trajectories when the Froude number is changed from $\mathcal{F} = 4.0$ (red line) to $\mathcal{F} = 10.0$ (blue line).

laden jet with rotation. The growth rate of disturbances is given by (see also (6.64))

$$\lambda_r = -\frac{3}{2\mathcal{R}e}k^2 + \frac{k}{2}\sqrt{\left(\frac{3k}{\mathcal{R}e}\right)^2 + \frac{2}{We}\left(\frac{1}{R_0^2} - k^2\right)\sigma_0 R_0 - \frac{2E\Gamma_0}{RWe}}. \tag{7.17}$$

Growth rates of disturbances for the most unstable mode with the same parameters as in Fig. 7.7 are shown in Fig. 7.8. It can be observed that the relative importance of gravity is proportional to the growth rates of disturbances. In Fig. 7.9 and 7.10 we show the wavenumber of the most unstable mode along with its associated growth rate for different values of β. Since β is a measure of the 'effectiveness' or importance of surfactants we see that k^* decreases (corresponding to larger droplets) and the growth rate of the most unstable mode λ_r^* also decreases (corresponding to longer jets) as the importance of surfactants increases. This is in agreement with the findings of Hansen *et al.* (1999).

In the limit of no rotation ($\mathcal{R}b \to \infty$), where we have a jet simply falling under the influence of gravity, we see that here too the most unstable wavenumber and growth rate

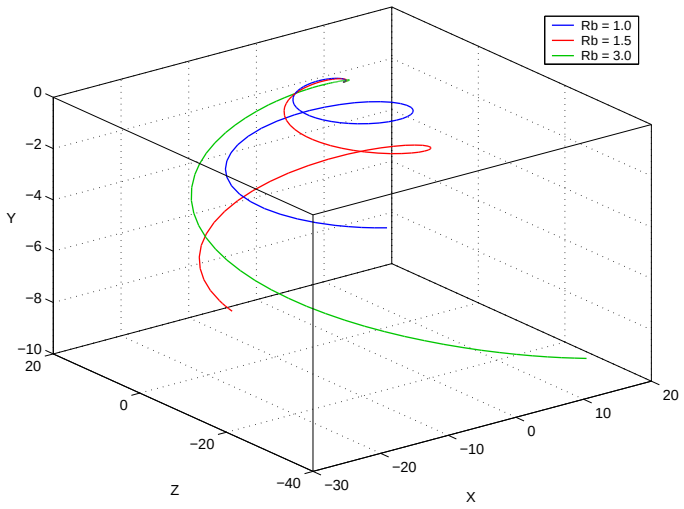

Figure 7.4: A surfactant covered liquid jet when both gravity and rotation are included in the model. Here we show the different trajectories for different Rossby numbers. The parameters are given by $We = 20$, $\mathcal{F} = 4.0$, $\beta = 0.5$ and $\zeta = 0.5$.

of disturbances decrease as the initial surfactant concentration is increased (see Figs. 7.11 and 7.12).

Experimental pictures showing the breakup of surfactant laden rotating liquid jets falling under gravity are shown in Fig. 7.13 and Fig. 7.14. These pictures were taken using the experimental rig in Chemical Engineering by Victoria Hawkins[5]. All images are of 0.1 % Sodium Dodecyl Sulphate mixture with distilled water with the SDS having 95 % purity. A close up of one such case is shown in Fig. 7.15 with the outline near rupture reinforced by a solid line (which appears as red in colour). The profile somewhat resembles the pinch-off region in our numerical simulations in Fig. 6.10, where two similarly sized ligaments are connected by a much thinner ligament.

[5]These images were taken in the last few days before submission of this thesis at the request of the author. It is hoped that a more thorough analysis (including breakup lengths and droplet sizes) will be available in due course.

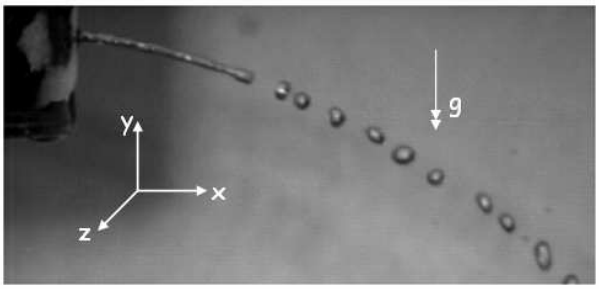

Figure 7.5: A liquid jet falling under the influence of gravity. In this case there is no rotation of the cylindrical drum (i.e., $\mathcal{R}b = \infty$) so the jet moves solely in the $x - y$ plane with no motion taking place along the z-axis. The centreline can be described by $(X(s,t), 0, Y(s,t)$. Photo taken from Decent *et al.* (2007*a*).

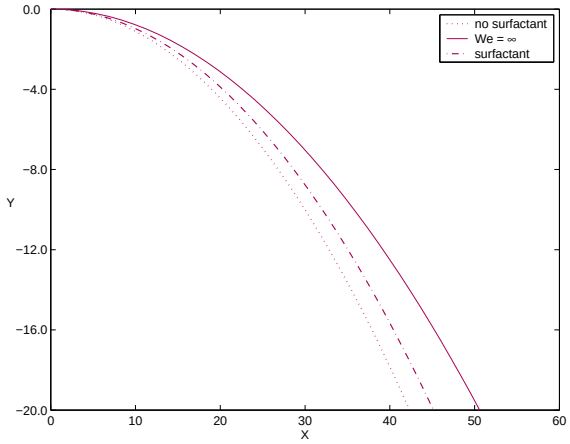

Figure 7.6: The trajectory of a liquid jet falling under gravity without surfactants (solid line) and with surfactants (dashed line, $\beta = 0.5$ and $\zeta = 0.5$). The jet follows a ballistic trajectory of particle when there is no surface tension (i.e., $We = \infty$). For these trajectories there is no rotation so that $\mathcal{R}b \to \infty$, $We = 3.4$ and $\mathcal{F} = 8.0$.

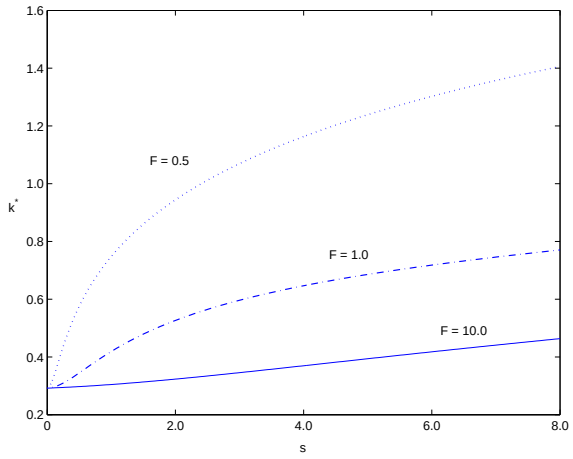

Figure 7.7: The wavenumber of the most unstable mode against arc length s for a liquid jet falling under gravity with surfactants ($\beta = 0.5$ and $\zeta = 0.5$). The most unstable wavenumber increases as the Froude number is decreased (i.e., the relative importance of gravity is increased). Here $We = 40.0$, $\mathcal{R}b = 8.0$ and $\mathcal{O}h = 0.143$.

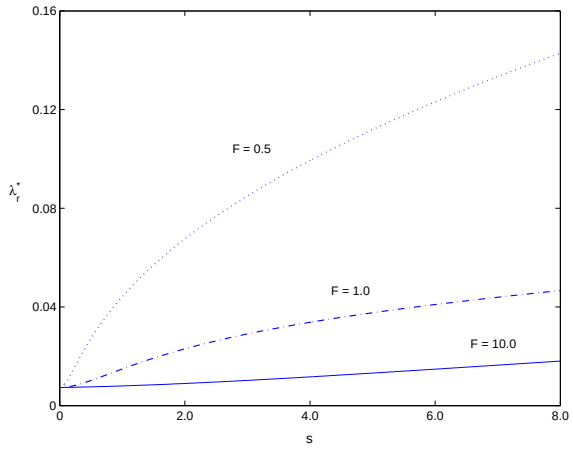

Figure 7.8: The growth rate λ_r^* of the most unstable mode against arc length s for a liquid jet falling under gravity with surfactants ($\beta = 0.5$ and $\zeta = 0.5$). The most unstable wavenumber increases as the Froude number is decreased (i.e., the relative importance of gravity is increased). Here $We = 40.0$, $\mathcal{R}b = 8.0$ and $\mathcal{O}h = 0.143$.

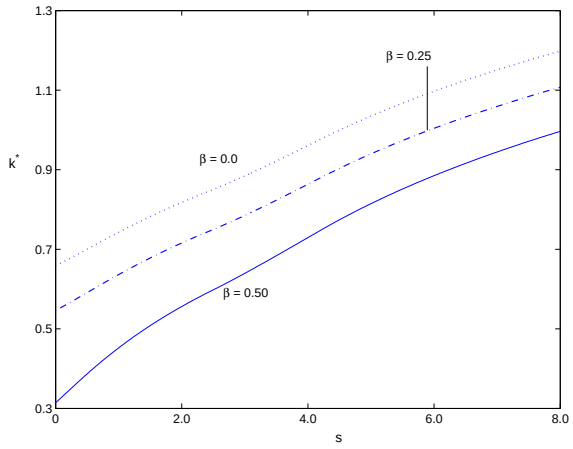

Figure 7.9: The wavenumber k^* of the most unstable mode against arc length s for a rotating liquid jet falling under gravity for different values of β. The most unstable wavenumber is smaller for larger values of β (i.e., when the 'effectiveness' of surfactants is greater) however the difference between k^* becomes smaller along the jet. Here $We = 10.0$, $\mathcal{R}b = 2.0$, $\mathcal{F} = 4.0$, $\zeta = 0.5$ and $Oh = 0.072$.

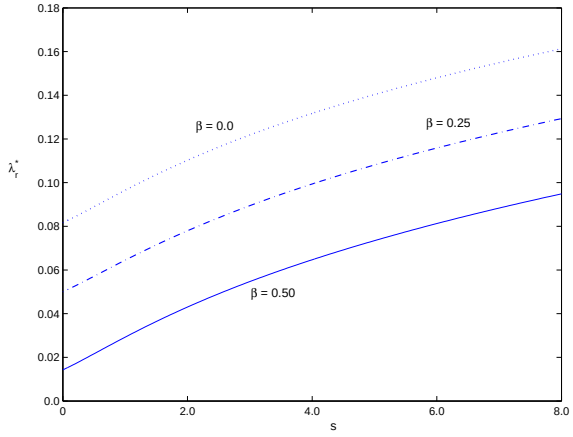

Figure 7.10: The growth rate λ_r^* of the most unstable mode against arc length s for a rotating liquid jet falling under gravity for different values of β. The growth rate also decreases as β is increased (i.e., when the 'effectiveness' of surfactants is greater) but the difference in λ_r^* is largest for small s values and decreases along the jet. Here $We = 10.0$, $\mathcal{R}b = 2.0$, $\mathcal{F} = 4.0$, $\zeta = 0.5$ and $Oh = 0.072$.

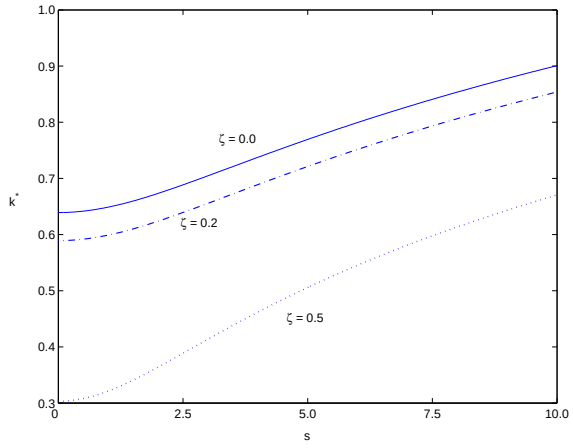

Figure 7.11: The wavenumber k^* of the most unstable mode against arc length s for a liquid jet falling under gravity without rotation (i.e., $\mathcal{R}b \to \infty$) for different values of ζ. The most unstable wavenumber is smaller for larger values of ζ (i.e., when the initial concentration of surfactants is greater). Here $We = 10.0$, $\mathcal{F} = 2.0$, $\beta = 0.5$ and $Oh = 0.105$.

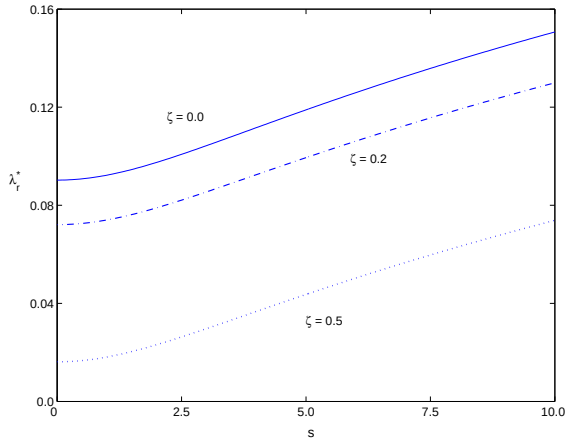

Figure 7.12: The growth rate λ_r^* of the most unstable mode against arc length s for a liquid jet falling under gravity without rotation (i.e., $\mathcal{R}b \to \infty$) for different values of ζ. The growth rate also decreases as ζ is increased. Here $We = 10.0$, $\mathcal{F} = 2.0$, $\beta = 0.5$ and $Oh = 0.105$.

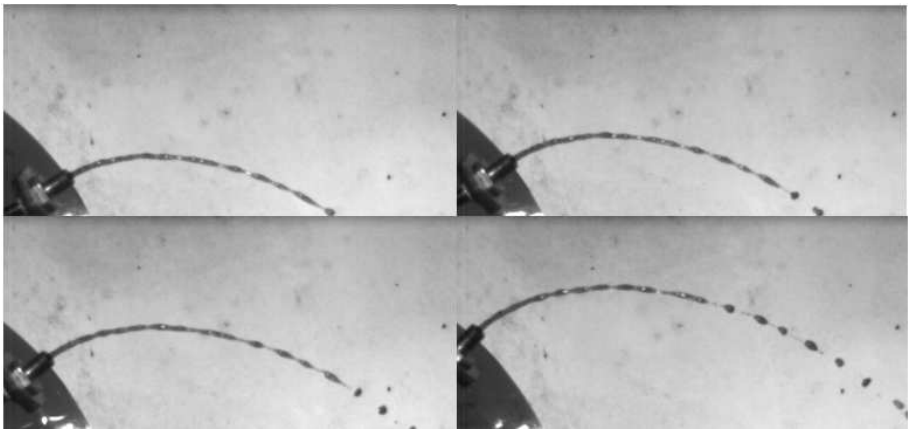

Figure 7.13: Experimental images of a rotating liquid jet with surfactants falling under gravity (the picture is taken from above the jet so the drop in height cannot be observed). Here we have $\kappa = 0.705$, $We = 26.76$, $\mathcal{R}e = 1.63 \times 10^5$, $\mathcal{R}b = 0.626$ and $\mathcal{F} = 1.33$. Pictures courtesy of Victoria Hawkins from Chemical Engineering.

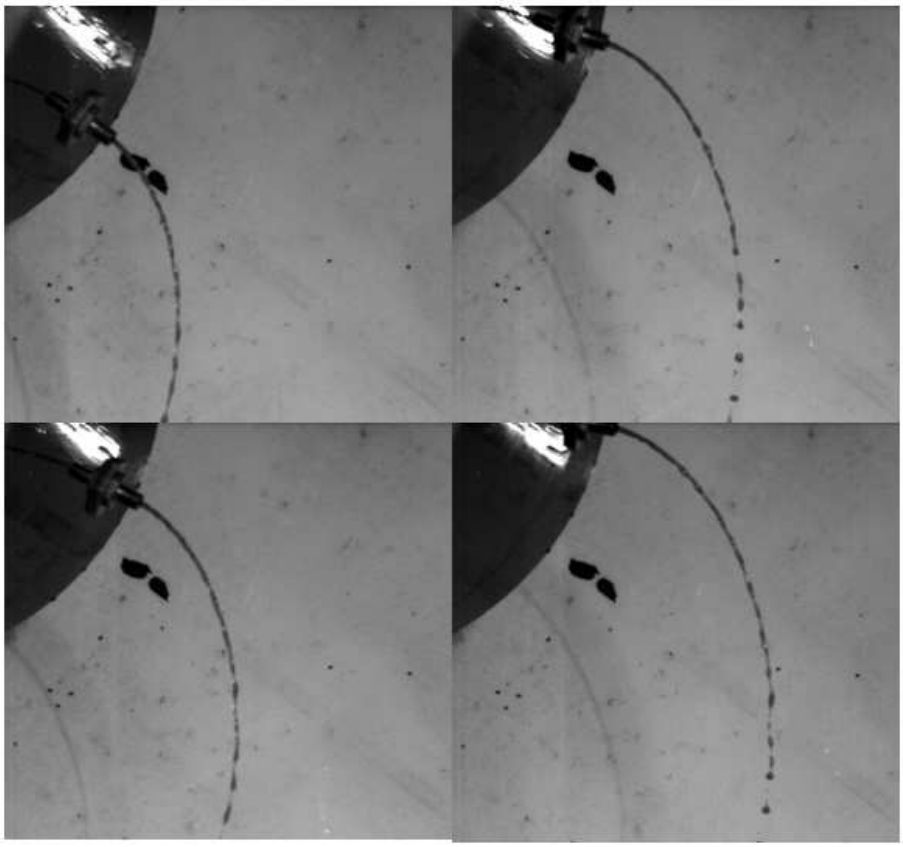

Figure 7.14: Experimental images of a rotating liquid jet with surfactants falling under gravity (the picture is taken from above the jet so the drop in height cannot be observed). Here we have $\kappa = 0.705$, $We = 93.75$, $\mathcal{R}e = 2.32 \times 10^5$, $\mathcal{R}b = 0.596$ and $\mathcal{F} = 1.33$. Pictures courtesy of Victoria Hawkins from Chemical Engineering.

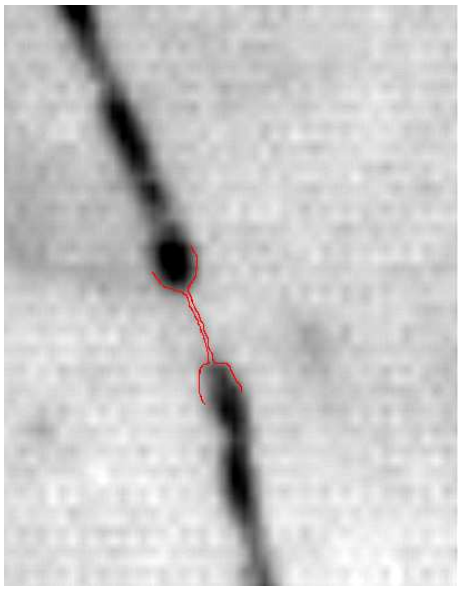

Figure 7.15: A close of an experimental picture of a rotating Newtonian liquid jet with surfactants. The outline of the pinch-off region is reinforced to show a qualitative picture. Note how rupture of the jet corresponds to ligaments of approximately equal size joining an extremely thin ligament as in the numerical simulations of Fig. 6.10. The experimental parameters here are $\kappa = 0.705$, $We = 135.01$, $\mathcal{R}e = 3.65 \times 10^5$, $\mathcal{R}b = 0.56$ and $\mathcal{F} = 1.33$. Pictures courtesy of Victoria Hawkins from Chemical Engineering.

Chapter 8

Controlling Breakup: Insonification

8.1 Experiments to eliminate satellite drops.

The ability to control drop formation is an issue of great importance to industry. Successful methods which allow for the production of droplets with desired sizes, or a predetermined breakup regime, can lead to greater product quality and less wastage through the reduction of satellites. All this leads to greater efficiency and lower costs and as such accurate techniques for such control are highly sought after.

In previous chapters we have examined a number techniques, like rotation and the addition of surfactants, which may be employed in order to control the breakup and subsequent droplet formation in liquid jets. Insonification is, however, the most traditional method used to control droplet sizes. We will therefore, in this chapter, begin with a description of the process of insonification. Our aim here, is not to produce a thorough analysis, but instead we wish to briefly demonstrate some of the features observed for insonificated power law liquid jets as well as to provide the foundations for a more detailed analysis in the future.

Savart (1833) was the first experimentalist to investigate the decay of a liquid jet by disturbing the jet periodically at the nozzle. He was able to produce disturbances

along the jet with the same frequencies as that of the orifice. Crane *et al.* (1964) used an electrical vibrator to do the same thing. Donelley and Glaberson (1966) investigated the disintegration of a liquid jet falling vertically under gravity using a loudpseaker to induce perturbations at the nozzle (Rutland and Jameson (1970) used a similar set-up with a 10W loudspeaker). They found that capillary forces caused the jet to breakup into main and satellite droplets. However for more viscous fluids they found that the loudspeaker alone had no effect on the jets. The sound waves could not overcome the viscous forces. Control was achieved by introducing a vibrating pin into the jet. This pin was attached to the loudspeaker so that the pin vibrated with the loudspeaker. Goedde and Yuen (1970) also investigated vertically falling liquid jets. They used electrical forces to generate perturbations on the surface of the jet. For more viscous jets however they had to use a pin attached to an electronic vibrator which was brought into contact with the jet, in a similar way to Donelley and Glaberson (1966). Again the electronic forces alone were unable to counteract the viscous forces. In Becker *et al.* (1991) a much more sophisticated method to control droplets was used. A piezoceramic transducer was used to produce pressure oscillations, which effectively translate as sinusoidal disturbances of the jet speed at the nozzle. The resulting breakup of the liquid jet could be controlled to produce periodic drops with a high degree of accuracy.

In Partridge (2006) the breakup of insonificated Newtonian liquid jets were experimentally studied using a pilot scale rig (see Fig. 8.1). A fully waterproof sub-aqua speaker was placed within the can. The speaker was connected to a personal computer and a sound wave, with a particular frequency and amplitude, was generated using signal generator software.

By using a dimensional version of the frequency of the most unstable wave (calculated using linear theory) the natural frequency of breakup for a low viscous fluid ($Oh \approx 0.003$)

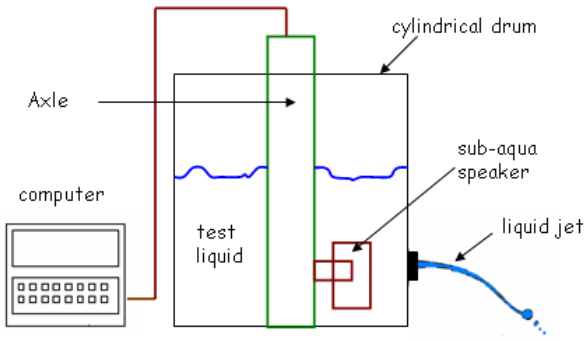

Figure 8.1: A sketch of the pilot rig with a sub-aqua speaker used to produce insonificated liquid jets. Picture adapted from Partridge (2006).

was found to be approximately 7.1 Hz[1]. The lowest frequency obtainable from the speakers was 10Hz and this was used to simulate 'natural' mode breakup. It was found that insonification with a sound wave at 10Hz had little effect on drop size distributions for all Rossby numbers (see Partridge (2006)). A possible explanation, propounded by the author, for this outcome was that the amplitude of the sound wave was not large enough to affect the jet. However, even when higher frequency sound waves of 100Hz were used, it was found that insonification produced negligible effects on droplets sizes for low Rossby numbers ($\mathcal{R}b = 1.12 - 1.67$) whilst for larger Rossby numbers (lower rotation rates) the effects were more conspicuous with satellite droplets completely eliminated in the limit $\mathcal{R}b = \infty$. In Fig. 8.2 we show experimental images taken from Partridge (2006) depicting the effects of changing the frequency of the sound wave at the orifice. The reduction in satellite droplets at high sound wave frequencies is clearly evident, although there appears to be a greater tendency for droplets to coalesce.

[1]recall that the most unstable wavenumber for a straight viscous liquid jet is given by (see also p.15)

$$k^* = \frac{1}{2^{1/4}\sqrt{\sqrt{2} + 3\mathcal{O}h}},$$

which is related to the dimensional frequency at the orifice $f^* = (U/s_0)k^*$ (see Wallwork (2002)). Thus when $\mathcal{O}h \approx 0.003$ we have $k^* = 0.705$ and for $s_0 \sim 0.136m$ and $U \sim 1.37ms^{-1}$ we have $f^* \sim 7.1$Hz.

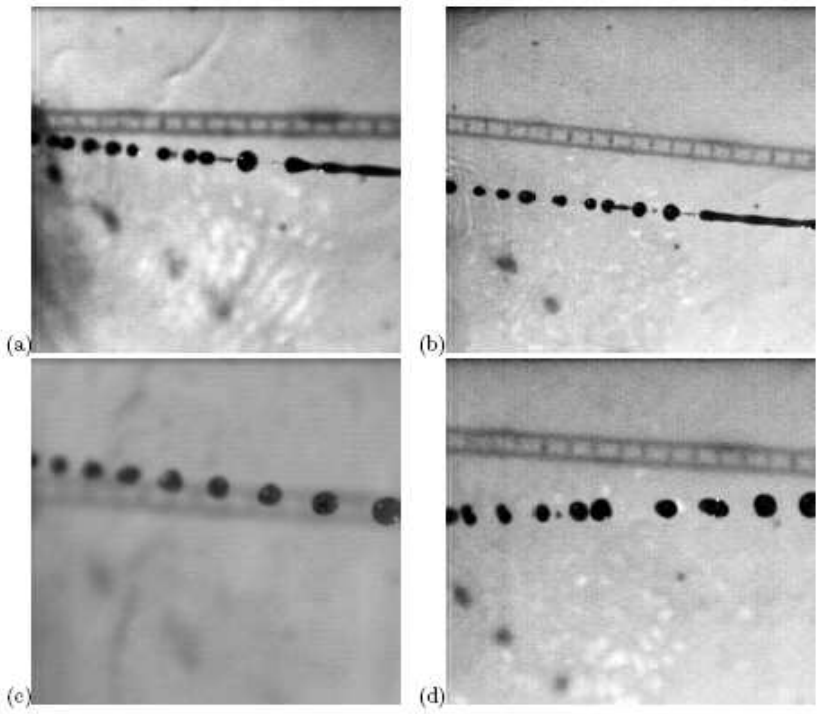

Figure 8.2: Experimental images of straight Newtonian liquid jets ($\mathcal{R}b = \infty$) undergoing insonification. Here $We = 30.4$ and $\mathcal{R}e = 1800$. Pictures (a) and (b) represent insonification with a frequency of 10 Hz with (c) and (d) representing insonification frequencies of 100Hz. Higher frequency insonification is more effective in eliminating satellite droplets. Picture taken from Partridge (2006) p.175.

8.2 Insonificated non-Newtonian jets.

The effects of insonification on Newtonian liquid jets with and without rotation were investigated in Partridge (2006). However, we have seen in previous chapters that the types of liquids used in the industrial prilling process are, in general, non-Newtonian. In addition, non-Newtonian liquid jets exhibit a number of intricate dynamics near the location of pinch-off,[2]which may, depending upon the particular parameters, enhance or inhibit the formation of satellite droplets.

In order to investigate the effects of introducing a sound wave at the orifice it is sufficient to simply change the initial conditions at the orifice for our simulations of rotating non-Newtonian liquid jets. We reproduce here, for convenience, the non-Newtonian spiralling jet equation we solved in Chapter Five (see eq. (5.5) and (5.6))

$$u_t + uu_s = -\frac{1}{We}\left(\frac{1}{R(1+\varepsilon^2 R_s^2)^{\frac{1}{2}}} - \frac{\varepsilon^2 R_{ss}}{(1+\varepsilon^2 R_s^2)^{\frac{3}{2}}}\right)_s + \frac{(X+1)X_s + ZZ_s}{\mathcal{R}b^2} \tag{8.1}$$

$$+\frac{3|\sqrt{3}u_s|^{\alpha-1}}{\mathcal{R}e_\alpha}\left(\alpha u_{ss} + 2u_s\frac{R_s}{R}\right), \tag{8.2}$$

$$R_t + \frac{u_s}{2}R + uR_s = 0, \tag{8.3}$$

where the symbols have their familiar meanings and once again α is the flow index number. Our aim will be to solve this set of equations with the upstream boundary conditions (at the nozzle) given by (5.6), except that here we shall attempt to incorporate a sound wave

[2]We have already seen how shear thinning jets have a tendency to 'snap' at a point, leading to the formation of long coherent portions of the jet. Also shear thickening jets can sometimes resemble the 'beads-on-strings' phenomena where the jet assumes the geometry of spherical droplets connected by long slender ligaments.

at the nozzle by having

$$u(0,t) = 1 + \delta \sin\left(\frac{\kappa t}{\varepsilon}\right) + \delta_{sw} \cos\left(\frac{\kappa_{sw} t}{\varepsilon}\right), \tag{8.4}$$

where δ_{sw} is the sound wave amplitude and κ_{sw} is the wavenumber of the sound wave. The numerical method remains the same as that presented in section 5.4.

In Fig. 8.3 we show the profiles of a shear thinning and shear thickening straight liquid jet with the amplitude of insonification twice that of the initial disturbance amplitude. For the shear thinning case we see no satellite droplet formation although for the shear thickening case we a number of ligaments connected to drops of variable sizes. In Fig. 8.4 straight shear thickening liquid jets undergoing insonification with different sound wavenumbers are shown. Increasing κ_{sw} leads to longer ligaments between droplets and larger droplets upstream of the pinch-off point.

The profile of rotating shear thinning jets ($\alpha = 0.8$) when the frequency of the sound wave is altered is shown in Fig. 8.5. Clearly increasing the frequency of the sound wave leads to shorter jets. In Fig. 8.6 we show droplet sizes when the frequency of the sound wave is altered. There is approximately a 8% drop in droplet sizes for $0 < \kappa_{sw} < 0.25$.

A more detailed analysis of how the amplitude and wavenumber of sound waves affects rotating liquid jets for different Rossby numbers and flow index numbers is the focus of current work. Experimental investigations along the same lines are also in the pipeline. Despite the lack of numerical simulations, we hope that the reader is convinced that insonification of straight and rotating liquid jets provides a viable option in controlling droplet sizes.

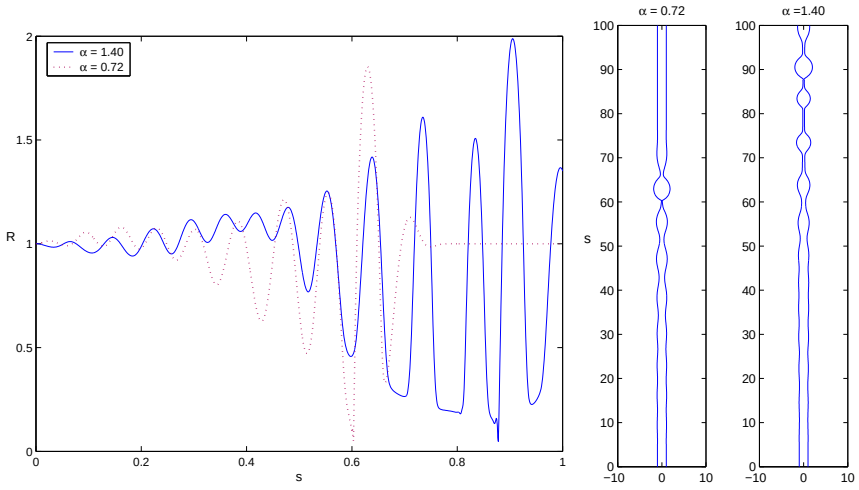

Figure 8.3: Simulation of straight power law liquid jets experiencing isonification. Here we have $We = 20.4$, $\mathcal{R}e = 2750$, $\mathcal{R}b = \infty$, $\kappa_{sw} = 0.009$, $\kappa = 0.84$, $\delta = 0.01$ and $\delta_{sw} = 0.02$.

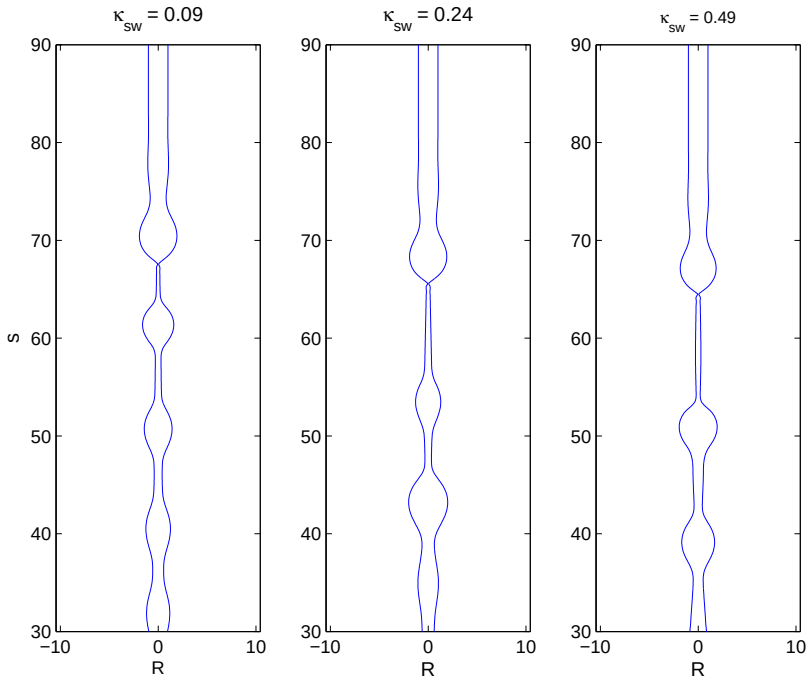

Figure 8.4: Profiles of straight shear thickening liquid jets experiencing isonification at the nozzle with different insonification frequencies κ_{sw}. Here we have $We = 24.4$, $\mathcal{R}e = 2750$, $\alpha = 1.5$ $\kappa = 0.84$, $\delta = 0.05$ and $\delta_{sw} = 0.1$. Notice how the value of κ_{sw} affects the ligaments between droplets as well as droplet formation upstream of pinch-off.

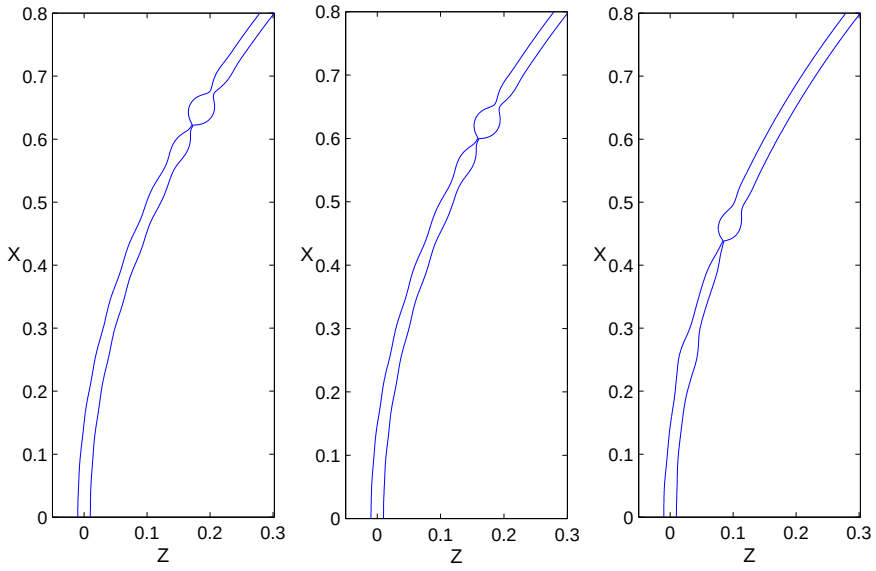

Figure 8.5: Simulation of curved power law liquid jets experiencing isonification with different insonification frequencies. Here we have $We = 29.4$, $\mathcal{R}e = 2250$, $\mathcal{R}b = 2.3$, $\alpha = 0.8$ $\kappa = 0.84$, $\delta = 0.01$ and $\delta_{sw} = 0.1$. From left to right we have $\kappa_{sw} = 0.009$, $\kappa_{sw} = 0.04$ and $\kappa_{sw} = 0.25$ respectively.

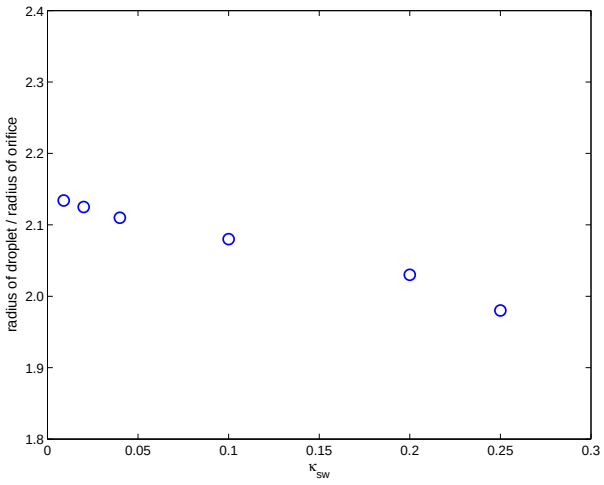

Figure 8.6: Droplet sizes for curved power law liquid jets experiencing isonification with different insonification frequencies κ_{sw}. Here we have $We = 29.4$, $\mathcal{R}e = 2250$, $\mathcal{R}b = 2.3$, $\alpha = 0.8$ $\kappa = 0.84$, $\delta = 0.01$ and $\delta_{sw} = 0.1$. Droplet sizes are seen to decrease with increasing the sound wave frequency.

Chapter 9

Compound Liquid Jets: Inviscid

A simple extension of single liquid jets are compound liquid jets, often referred to as a two-fluid jet, which consists of an inner thread of fluid which is totally encased within an outer immiscible liquid thread. Whilst the dynamics of such two fluid systems are more complicated than say their single fluid counterparts, the mechanisms which cause the jet to break up into droplets is the same, namely capillarity. When rupture of the inner and outer fluids coincide (or if the inner fluid breaks first), liquid droplets which are completely surrounded by another fluid (the outer fluid) are produced. Applications of such compound liquid jets are far reaching, and the need for encapsulated liquid droplets has relevance to pharmaceutics and food manufacturing (see Hardas *et al.* (2000) and Jung *et al.* (2000)). The inclusion of the outer shell fluid introduces another free surface and in addition requires the flow equations in the shell fluid to be solved subject to boundary conditions at two interfaces (one of which is shared with the core fluid). Surprisingly compound jets have received much less attention than their single counterparts and it is only recently (compared to the early nineteenth century works on single jets) that Hertz & Hermanrud (1983) described an experimental setup to produce compound droplets through the disintegration of a compound jet, with applications to ink-jet printing. Kendall (1987) showed the viability of producing compound jets where the inner fluid

is a gas so that droplets formed upon breakup are hollow spheres. Sanz and Meseguer (1985) performed a linear temporal stability analysis for compound liquid jets with both fluids as inviscid. Radev and Tchavdarov (1985) and Shkadov and Sisoev (1996) included the effects of viscosity in compound jets. Ramos (1999) has examined compound jets and annular jets at low Reynolds numbers. Recent contributions extending these works include those of Chauhan *et al.* (2003). Craster *et al.* (2005) have considered the instability of compound threads with large viscosity and density contrasts. Suryo *et al.* (2006) have numerically investigated the breakup of compound jets. The inclusion of surfactants on the instability of compound threads has been considered by a number of authors (see for example Kwak & Pozrikidis (2001)).

An important feature of compound jets is the ability to fully encapsulate one substance by another substance which necessarily has many applications in science and technology. It is estimated that the market potential of coating and encapsulation was worth in excess of 100 billion dollars at the turn of this century.[1] Some of the applications of encapsulation include the development of food additives (see Yosi *et al.* (2001) and Bousfield *et al.* (1990)) and the improvement of insecticides (Perrin (2004)). The most exciting uses of encapsulation techniques however are taking place in the field of pharmaceutics. Here uses include protective coatings for cell and tissue encapsulation as well as targeted drug delivery. In modern medicine the need for a sustained release of a medication requires the use of encapsulation. Taking aspirin as an example; it provides effective relief for fever and inflammation but direct doses can cause peptic ulcers and bleeding. If the aspirin is encapsulated by a substance which allows the drug to diffuse slowly, its release in the human body can be properly controlled. To date a range of core materials have successfully been encapsulated. They include adhesives, agrochemical catalysts, pharmaceutical and vitamins. Currently the most popular choice of the shell material are liposomes, these

[1]Particle Coating for Food and Nutraceuticals, Glatt Technology Training System, Oct 1999

are uni or multi- lamellar lipid/water structures which have a great ability to encapsulate chemical and bioactive reagents (see Maguire *et al.* (2003)).

The are a number of benefits in using encapsulation techniques. Among the most important of these are the ability to handle liquids as solids (i.e., having a solid shell covering a liquid core) and the ability to subdue or completely remove odour or taste from food products. Also the protection of the core substance from an unstable environment can also be achieved through an appropriate choice of the shell substance.

One method employed in order to create compound drops (or emulsions) at the forefront of modern research is the *co-extrusion* process. In this process a liquid core and shell materials are pumped through concentric orifices, with the core material flowing in the central orifice and the shell material flowing through the annulus . A jet is formed where we have a core fluid encased by the shell fluid. Disturbances on the jet surface cause the jet to break up, leading to encapsulated droplets. This process is quite complex, with the size of capsules produced, as well as the quantity of core material contained within each capsule depending upon a number of physical properties of the two fluids, namely density, viscosity, interfacial tension as well as a number of processing conditions including flow rate and temperature.

Disturbances can be imparted to the jet mechanically, but forced break up of a compound jet is complex. The geometry of the compound drops being dependent upon imposed frequency. There are a number of problems that are yet to be understood fully in the fluid mechanics of compound jets; they include

1. suppression of satellite droplets caused by pinch-off of jet necks at both ends,

2. differences in growth rate of disturbances at the shell/air interface and the core/shell interface,

3. formation of satellite droplets in the shell fluid resulting in multiple core capsules.

Micro and Nano capsules have been created with the aid of electrified liquid jets (see Loscertales *et al.* (2002)). Here capsules with typical diameters ranging from 10 to 0.15 micrometers were produced. The initial stages of the co-extrusion process will possibly require an understanding of channel flow of co-extruded liquids. Wilson & Rallison (1997) investigated the stability of co-extruded elastic liquids using the Oldroyd-B fluids and Lister & Stone (1998) have considered the capillary breakup of a viscous thread surrounded by another viscous thread.

9.1 Inviscid Compound Jets

We begin by considering the simplest case of an inviscid[2] compound liquid jet. Let us assume that a liquid jet emerges from a concentric tube, so that we have a jet consisting of an inner thread of liquid which is completely surrounded by another liquid. We consider the dynamics, of such a compound jet, sufficiently far away from the tube exit so that exit effects are negligible. We assume that both the inner and outer fluids are incompressible and immiscible and that the surrounding air is quiescent and thus can be ignored. We consider the problem in a cylindrical coordinate system where x lies along the axis of the jet and r and θ are the usual radial and azimuthal directions respectively (see Fig. 9.1). The resulting dynamics are assumed to be axis-symmetric. Let the inner fluid interface be described by the equation $r = R(x,t)$ with the outer fluid/air interface given by $r = S(x,t)$. The density and surface tension of each fluid is denoted by the symbols $\rho^{[i]}$ and $\sigma^{[i]}$ with superscripts 1 and 2 referring to the inner fluid and outer fluids respectively.

The continuity and momentum equations within the inner and outer jets are given by

$$\frac{\partial v^{[i]}}{\partial r} + \frac{\partial u^{[i]}}{\partial x} + \frac{v^{[i]}}{r} = 0, \tag{9.1}$$

[2]As mentioned in Sanz & Meseguer (1985) the effects of viscosity within this one dimensional model could be accommodated for through an unsteady boundary layer at the interface between the two liquids. This would then take account of the velocity and tangential stress difference in both fluids.

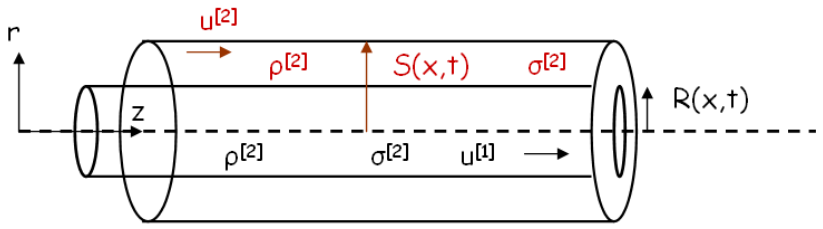

Figure 9.1: The geometry of a compound liquid jet. Both fluids here are taken to be inviscid. The dotted line is the axis of symmetry of the jet.

$$\left(\frac{\partial u^{[i]}}{\partial t} + u^{[i]}\frac{\partial u^{[i]}}{\partial x} + v^{[i]}\frac{\partial u^{[i]}}{\partial r}\right) = -\frac{1}{\rho^{[i]}}\frac{\partial p^{[i]}}{\partial x}, \tag{9.2}$$

and

$$\left(\frac{\partial v^{[i]}}{\partial t} + u^{[i]}\frac{\partial v^{[i]}}{\partial x} + v^{[i]}\frac{\partial v^{[i]}}{\partial r}\right) = -\frac{1}{\rho^{[i]}}\frac{\partial p^{[i]}}{\partial r}. \tag{9.3}$$

The kinematic condition applied at the two jet interfaces $r = R(t,x)$ and $r = S(t,x)$ are given by

$$v^{[1]}(R,x,t) = \frac{\partial R}{\partial t} + u^{[1]}(R,x,t)\frac{\partial R}{\partial x} \quad \text{and} \quad v^{[2]}(R,x,t) = \frac{\partial R}{\partial t} + u^{[2]}(R,x,t)\frac{\partial R}{\partial x}, \tag{9.4}$$

$$v^{[2]}(S,x,t) = \frac{\partial S}{\partial t} + u^{[2]}(S,x,t)\frac{\partial S}{\partial x}. \tag{9.5}$$

Also we have the normal stress condition relates the pressure difference across the outer interface to the mean curvature of the interface, this has the form

$$p^{[2]} = \sigma^{[2]}\kappa_2 \quad \text{on} \quad n = S(s,t), \quad \text{where} \quad \kappa_2 = \frac{\left(1+\left(\frac{\partial S}{\partial x}\right)^2\right)^{-\frac{1}{2}}}{S} - \frac{\frac{\partial^2 S}{\partial x^2}}{\left(1+\left(\frac{\partial S}{\partial x}\right)^2\right)^{\frac{3}{2}}}, \tag{9.6}$$

and similarly at the inner interface ($n = R(x,t)$) where the two fluids meet, we have

$$p^{[1]} - p^{[2]} = \sigma^{[1]}\kappa_1, \quad \text{where} \quad \kappa_1 = \frac{\left(1 + \left(\frac{\partial R}{\partial x}\right)^2\right)^{-\frac{1}{2}}}{R} - \frac{\frac{\partial^2 R}{\partial x^2}}{\left(1 + \left(\frac{\partial R}{\partial x}\right)^2\right)^{\frac{3}{2}}}. \tag{9.7}$$

We assume that the jet is slender and non-dimensionalize the above equations by scaling our axial and radial velocity components with U, the exit speed of the compound jet, radial lengths with a, the initial radius of the outer jet, and axial lengths with l_0 such that $a/l_0 = \varepsilon << 1$, time by U/l_0 and pressure by $\rho^{[2]}U^2$. The resulting dimensionless equations are given by

$$\frac{\partial v^{[i]}}{\partial r} + \varepsilon\frac{\partial u^{[i]}}{\partial x} + \frac{v^{[i]}}{r} = 0, \tag{9.8}$$

$$\left(\frac{\partial u^{[i]}}{\partial t} + u^{[i]}\frac{\partial u^{[i]}}{\partial x} + \frac{v^{[i]}}{\varepsilon}\frac{\partial u^{[i]}}{\partial r}\right) = -\frac{\rho^{[2]}}{\rho^{[i]}}\frac{\partial p^{[i]}}{\partial x}, \tag{9.9}$$

and

$$\left(\frac{\partial v^{[i]}}{\partial t} + u^{[i]}\frac{\partial v^{[i]}}{\partial x} + \frac{v^{[i]}}{\varepsilon}\frac{\partial v^{[i]}}{\partial r}\right) = -\frac{\rho^{[2]}}{\rho^{[i]}}\frac{1}{\varepsilon}\frac{\partial p^{[i]}}{\partial r}. \tag{9.10}$$

The kinematic conditions remain the same and the normal stress condition is given by

$$p^{[2]} = \frac{\kappa_2}{We} \quad \text{on} \quad r = S(x,t), \quad \text{where} \quad \kappa_2 = \frac{\left(1 + \varepsilon^2\left(\frac{\partial S}{\partial x}\right)^2\right)^{-\frac{1}{2}}}{S} - \varepsilon^2\frac{\frac{\partial^2 S}{\partial x^2}}{\left(1 + \varepsilon^2\left(\frac{\partial S}{\partial x}\right)^2\right)^{\frac{3}{2}}}, \tag{9.11}$$

and similarly at the inner interface ($r = R(x,t)$) where the two fluids meet, we have

$$p^{[1]} - p^{[2]} = \frac{\sigma^{[1]}}{\sigma^{[2]}} \frac{\kappa_1}{We}, \quad \text{where} \quad \kappa_1 = \frac{\left(1 + \varepsilon^2 \left(\frac{\partial R}{\partial x}\right)^2\right)^{-\frac{1}{2}}}{R} - \varepsilon^2 \frac{\frac{\partial^2 R}{\partial x^2}}{\left(1 + \varepsilon^2 \left(\frac{\partial R}{\partial x}\right)^2\right)^{\frac{3}{2}}}, \tag{9.12}$$

where the Weber number We is given by $We = \rho^{[2]} U^2 a / \sigma^{[2]}$.

9.1.1 Leading order solution

We expand our variables $u^{[i]}, v^{[i]}$ and $p^{[i]}$ in a Taylor series in (εr) (see Eggers (1997) and Hohman *et al.* (1984)), and R, S in asymptotic series in ε. We assume, in line with the slender jet assumption, that radial velocities are much smaller than axial velocities so that we then have

$$u^{[i]} = u_0^{[i]}(x,t) + (\varepsilon r) u_1^{[i]}(x,t) + O((\varepsilon r)^2),$$

$$v^{[i]} = (\varepsilon r) v_1^{[i]}(x,t) + (\varepsilon r)^2 v_2^{[i]}(x,t) + O((\varepsilon r)^3), \quad p^{[i]} = p_0^{[i]}(x,r,t) + (\varepsilon r) p_1^{[i]}(x,t) + O((\varepsilon r)^2),$$

$$R = R_0(x,t) + \varepsilon R_1(x,t) + O(\varepsilon^2), \quad S = S_0(x,t) + \varepsilon S_1(x,t) + O(\varepsilon^2), \tag{9.13}$$

After substitution into the governing equations, we obtain, to leading order, from the continuity equation

$$v_1^{[1]} = -\frac{1}{2} \frac{\partial u_0^{[1]}}{\partial x}, \quad v_1^{[2]} = -\frac{1}{2} \frac{\partial u_0^{[2]}}{\partial x}. \tag{9.14}$$

The normal stress condition gives at leading order

$$p_0^{[2]} = \frac{1}{S_0 We} \quad \text{and} \quad p_0^{[1]} = \frac{1}{We} \left(\frac{\sigma}{R_0} + \frac{1}{S_0} \right), \tag{9.15}$$

where we have replaced $\sigma^{[1]}/\sigma^{[2]}$ with σ. Using these expressions for the leading order pressure in the axial momentum equations, for both the inner and outer fluids, at leading

order gives

$$\frac{\partial u_0^{[1]}}{\partial t} + u_0^{[1]}\frac{\partial u_0^{[1]}}{\partial x} = -\frac{1}{\rho We}\frac{\partial}{\partial x}\left(\frac{\sigma}{R_0} + \frac{1}{S_0}\right), \tag{9.16}$$

and

$$\frac{\partial u_0^{[2]}}{\partial t} + u_0^{[2]}\frac{\partial u_0^{[2]}}{\partial x} = -\frac{1}{We}\frac{\partial}{\partial x}\left(\frac{1}{S_0}\right), \tag{9.17}$$

where $\rho = \rho^{[1]}/\rho^{[2]}$. The momentum equation in the radial direction gives at leading order

$$\frac{\partial p_0^{[1]}}{\partial r} = 0 \quad \text{and} \quad \frac{\partial p_0^{[2]}}{\partial r} = 0, \tag{9.18}$$

which is what we expect for slender liquid jets.

The leading order kinematic condition at the inner interface $r = R(x,t)$ is

$$\frac{\partial R_0}{\partial t} - v_1^{[1]} + u_0^{[1]}\frac{\partial R_0}{\partial x} = 0, \quad \text{and} \quad \frac{\partial R_0}{\partial t} - v_1^{[2]} + u_0^{[2]}\frac{\partial R_0}{\partial x} = 0, \tag{9.19}$$

and at the outer interface $r = S(x,t)$ we have

$$\frac{\partial S_0}{\partial t} - v_1^{[2]} + u_0^{[2]}\frac{\partial S_0}{\partial x} = 0. \tag{9.20}$$

By using (9.14)[3] the kinematic conditions (9.19) and (9.20) can be written as a set of two equations, namely

$$\frac{\partial R_0^2}{\partial t} + \frac{\partial}{\partial x}u_0^{[1]}R_0^2 = 0 \tag{9.21}$$

$$\frac{\partial}{\partial t}(S_0^2 - R_0^2) + \frac{\partial}{\partial x}(u_0^{[2]}(S_0^2 - R_0^2)) = 0. \tag{9.22}$$

We thus have four nonlinear differential equations (9.16), (9.17), (9.21) and (9.22) for the leading order terms $u_0^{[1]}$, $u_0^{[2]}$, R_0 and S_0. These are identical to the equation obtained

[3]The continuity equation in both fluids are multiplied by r and integrated between 0 and R for the inner fluid and R and S for the outer fluid (see also Ramos (1998)). Alternatively (9.21) and (9.22) can be seen as conservation of mass equations for the inner and outer fluids.

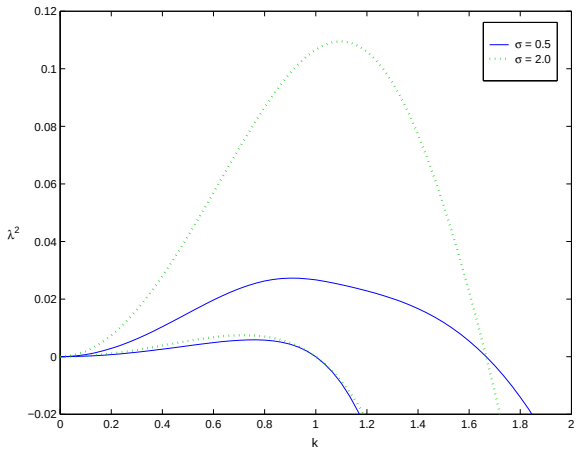

Figure 9.2: The influence of changing the surface tension ratio σ on the growth rate of instabilities. Here we have $We = 10.0$ and $\chi = 0.6$. It is readily observed that as σ is increased the growth rate increases and that there are critical values of the wavenumber above which λ^2 is negative so that disturbances no longer grow but oscillate.

by Sanz & Meseguer (1985). A steady state solution of the above set of equations is $u^{[1]} = u^{[2]} = 1, S = 1$ and $R = \chi$ (where $0 < \chi < 1$ is the radius of the inner nozzle). By considering small traveling disturbances to this steady state of the form $\exp(ikz + \lambda t)$, where k is the wavenumber and λ is the growth rate of disturbances, we arrive at the dispersion relation (after choosing $\lambda = \lambda + i$, i.e., we have that disturbances are simply convected with the base velocity)

$$\lambda^4 - \frac{\lambda^2}{2}\left(\frac{k^2}{We}(1-k^2) + \frac{\sigma\chi k^2}{We}\left(\frac{1}{\chi^2} - k^2\right)\right) + \frac{\sigma\chi k^4}{4We^2}(1-\chi^2)(1-k^2)\left(\frac{1}{\chi^2} - k^2\right) = 0, \tag{9.23}$$

where for simplicity we have assumed $\rho = 1$. This dispersion relation was obtained by Sanz & Meseguer (1985) who showed that this dispersion relation is a quadratic in λ^2 having a non-negative determinant thus giving two real solutions for λ^2. In Fig. 9.2 we show the effects of changing the interfacial surface tension ratio σ on the growth rates of instabilities. It can be seen that as the σ is increased we have larger growth rates and that

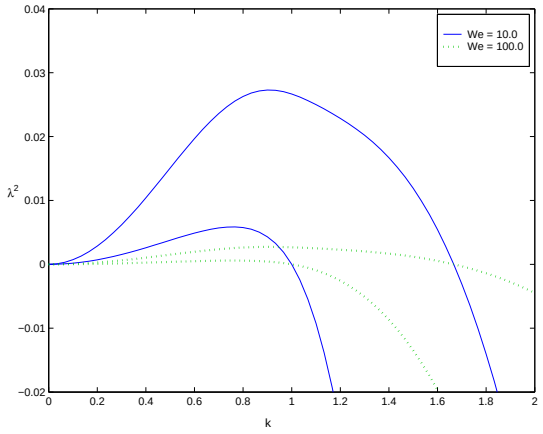

Figure 9.3: The influence of changing the Weber number on the growth rate of instabilities. Here we have $\sigma = 0.5$ and $\chi = 0.6$. It is readily observed that as the Weber number is increased the growth rate decreases.

there are critical values of the wavenumber k above which the growth rate λ^2 is negative so that disturbances no longer grow but oscillate. We show a similar thing in Fig. 9.3 for changes in the Weber number. Larger Weber numbers corresponding to lower surface tension lead to smaller growth rates. In both these cases we see that the wavenumber of the most unstable mode (i.e., the wavenumber for which λ^2 is a maximum) increases with both the surface tension ratio and the Weber number. Sanz and Meseguer (1985) have a more detailed account of the linear instability of inviscid compound jets with a discussion on the case where the outer radius decays faster than the inner fluid so that the outer interface touches the inner interface before breakup occurs (i.e., a dry spot occurs on the inner surface).

9.2 Nonlinear Temporal Analysis

In this section we numerically solve, using the method of finite differences, the equations derived in the previous section thereby extending the work of Sanz and Meseguer (1985) who did not consider an non-linear analysis of the governing equations.

In numerical simulations it is convenient to retain the full curvature terms from (9.16)

and (9.17) for the leading order pressure. This technique, although not asymptotically correct, is necessary in order to produce correct equilibrium shapes at breakup. In addition without this expression for the full curvature, the jet is unstable to arbitrarily short wavelengths, which is clearly not true. This approach has been used for Newtonian jets by a number of authors including Brenner et al. (1997) and Papageorgiou (1995) and for viscoelastic jets by Li & Fontelos (2003). Brenner et al. (1997) showed that retaining the full curvature terms give correct equilibrium shapes and that growing oscillations caused by short wavelengths in numerical simulations are effectively dissipated without resorting to any artificial means.

We solve this system of equations using the same finite difference scheme of previous chapter (see Chapter Four for more details). We make a change of variables so that we can write our nonlinear equations in conservative form, we choose $A(x,t) = R^2$ and $B(x,t) = S^2$. Then we have

$$u_t^{[2]} = -\left(\frac{(u^{[2]})^2}{2} + \frac{1}{We} \frac{4(2B + (\varepsilon B_x)^2 - \varepsilon^2 B B_{xx})}{(4B + (\varepsilon B_x)^2)^{\frac{3}{2}}} \right)_x, \tag{9.24}$$

$$\begin{aligned} u_t^{[1]} = -\frac{(u^{[1]})^2}{2} &- \frac{1}{\rho}\left(\frac{1}{We} \frac{4(2B + (\varepsilon B_x)^2 - \varepsilon^2 B B_{xx})}{(4B + (\varepsilon B_x)^2)^{\frac{3}{2}}} \right)_x \\ &- \frac{1}{\rho}\left(\frac{\sigma}{We} \frac{4(2A + (\varepsilon A_x)^2 - \varepsilon^2 A A_{xx})}{(4A + (\varepsilon A_x)^2)^{\frac{3}{2}}} \right)_x, \end{aligned} \tag{9.25}$$

$$A_t = (A u^{[1]})_x, \tag{9.26}$$

$$(B - A)_t = ((B - A) u^{[2]})_x, \tag{9.27}$$

The initial conditions are chosen so that

$$u^{[1]}(x,0) = u^{[2]}(x,0) = S(x,0) = 1 \quad \text{and} \quad R(x,0) = \chi, \tag{9.28}$$

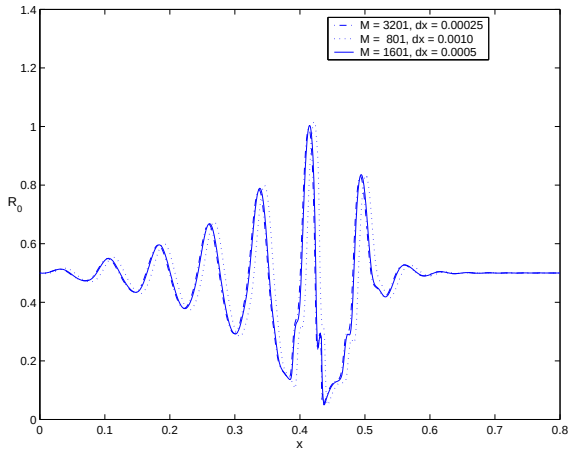

Figure 9.4: Accuracy check for various spatial step sizes dx and various number of mesh points M. The other parameters are $We = 48.4$, $\sigma = 0.22$, $\rho = 1.2$, $\kappa = 0.81$, $\chi = 0.5$, $dt = 10^{-6}$ and the final time $t_f = 0.493$

where $\chi \in (0, 1)$ is the initial radius of the inner liquid jet. We further impose the upstream boundary conditions at the nozzle as

$$u^{[1]}(0,t) = u^{[2]}(0,t) = 1 + \delta \cos\left(\frac{\kappa t}{\varepsilon}\right), \quad R(0,t) = \chi \quad \text{and} \quad S(0,t) = 1, \tag{9.29}$$

where δ and κ are the disturbance amplitude and wavenumber respectively. We are therefore only considering the case where both the inner and outer velocities are perturbed with the same frequency. These parameters can be chosen (along with the aspect ratio ε, which is typically 0.01 in experiments) to obtain the desired break up length.

Unlike previous sections where we have assumed that breakup occurs when the thread radius reaches a predetermined non-dimensional size, usually 5% of the initial thread radius, here we apply this principle to our numerical method for the inner jet only. Thus in some cases we stop our numerical simulations when the outer fluid thread radius may not be relatively small and implicitly assume that the compound thread will break at this point. In any case we usually find that the 'pinch-off' point for the inner thread corresponds with the global minimum for the outer thread.

The accuracy of the numerical scheme is checked by refining the mesh and changing the time step. An example is shown in Fig. 9.4. In this figure we plot only the inner radius at the point of breakup, for the outer fluid a similar graph can be shown.

We consider the breakup of an inviscid compound jet with a small interfacial surface tension ratio (i.e., $\sigma^{[1]} < \sigma^{[2]}$) for different disturbance wavenumbers κ in Fig. 9.5. The formation of compound droplets with multiple cores (i.e., when two or more core droplets are seen to be encased in the outer fluid drop) can be observed for both cases, for low and high wavenumbers. However it can be seen that for low wavenumbers, multiple core formation is most conspicuous. At a significantly higher Weber number, we show the profiles and size of the compound droplets (including the size of the inner core droplet) for different κ (see Fig. 9.6 and Fig. 9.7). We notice immediately the familiar decay in breakup lengths as the disturbance wavenumber is decreased (consistent with the single jet case). In addition it is clear that both the sizes of the compound drop and the inner core drop decrease with increasing wavenumber.

The evolution of an inviscid compound jet is shown in Fig. 9.8. The inner interface becomes qualitatively more different as the breakup time is approached. Increasing the Weber number leads to longer jets but the 'structure' of breakup remains the same (see Fig. 9.9).

The profiles, at breakup, of the inner and outer interface for two different initial disturbance amplitudes are shown in Fig. 9.10. Satellite formation is more visible and the inner and outer interface resemble each other more when the disturbance amplitude is large. The size of the whole compound droplet and the inner core droplet is shown in Fig. 9.11. There is a general trend for droplet sizes to decrease with increasing disturbance amplitude.

We investigate droplet formation in inviscid compound jets for changes in the interfacial surface tension ratio in Fig. 9.12. We notice that multiple core formation occurs when

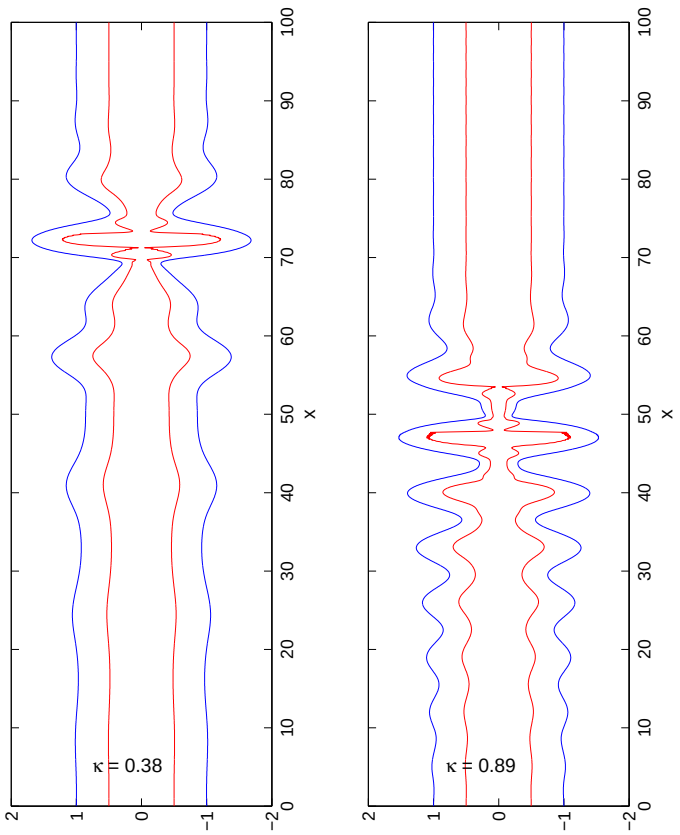

Figure 9.5: Profiles of an inviscid-inviscid compound liquid jet at the point of breakup for different disturbance wavenumbers $\kappa = 0.38$ and $\kappa = 0.89$. The formation of a compound drop with multiple cores can be seen in both cases but is more pronounced when $\kappa = 0.38$. The other parameters here are $We = 31.2$, $\sigma = 0.22$, $\rho = 1.2$, $\delta = 0.01$ and $\chi = 0.5$.

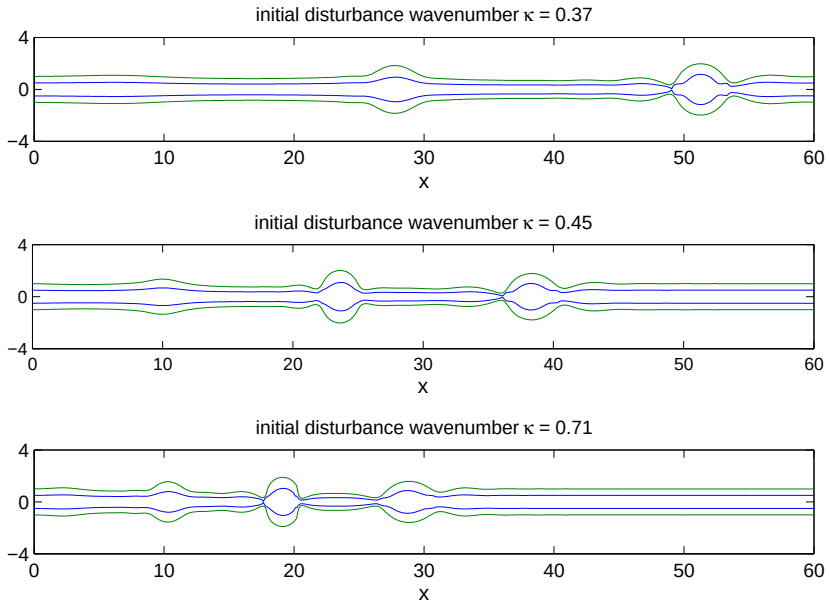

Figure 9.6: The breakup of inviscid compound liquid jets for different disturbance wavenumbers κ at high Weber numbers. Here we have $We = 103.2$, $\sigma = 0.22$, $\rho = 1.2$, $\delta = 0.1$ and $\chi = 0.5$. It can be observed that the breakup lengths decrease as κ is increased.

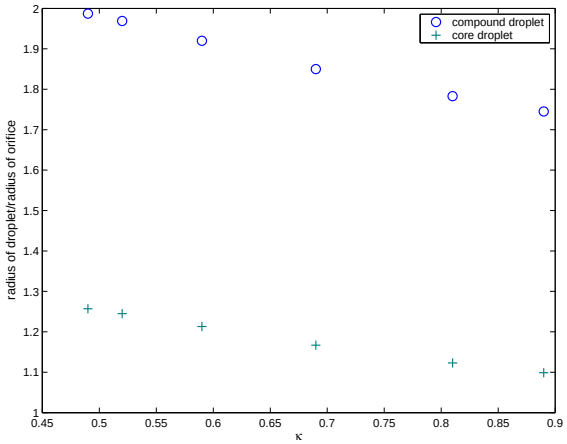

Figure 9.7: The size of compound droplets when the initial frequency is varied. Here we have $We = 42.6$, $\sigma = 0.102$, $\delta = 0.025$ and $\chi = 0.5$. As the frequency is increased we see smaller droplets sizes for both the whole compound drop and the inner drop size.

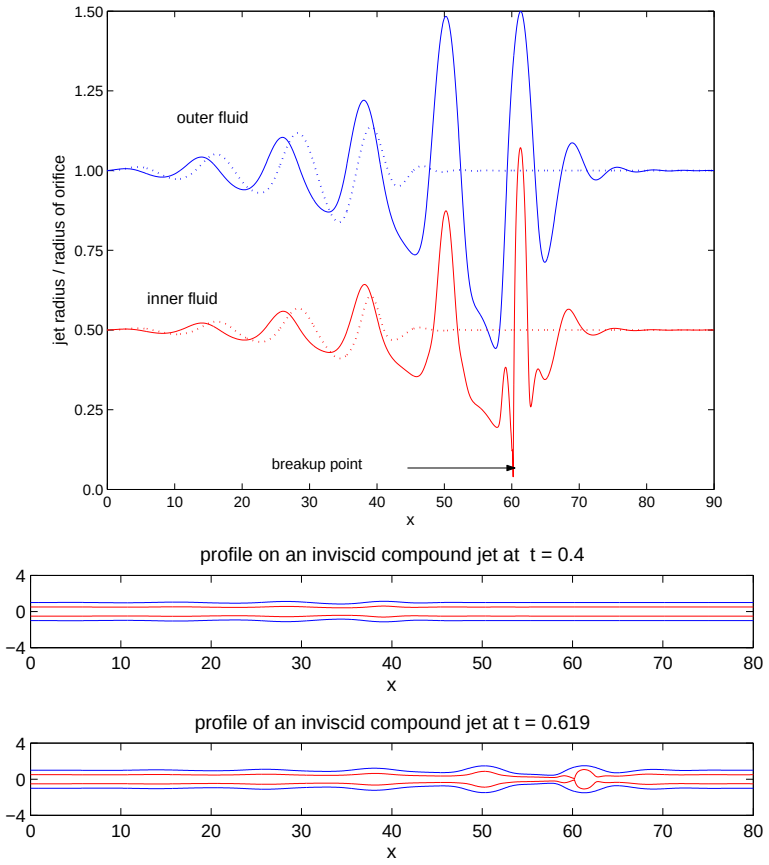

Figure 9.8: The evolution of the jet radius in time of a compound jet consisting of two inviscid fluids. The profile of the jet at the different times is also shown. In this case we have $We = 32.2$, $\chi = 0.5$, $\kappa = 0.52$, $\sigma = 0.28$, $\rho = 1.2$ and $\delta = 0.01$.

$\sigma \approx 0.22$ (the inset shows a close up profile at breakup). For values of σ greater than this value we see a qualitative change in the structure near breakup with the inner liquid jet rupturing in a more familiar manner (i.e., without many drops aggregating together). We also notice that as $\sigma \to 1$ the difference in lengths between the outer jet radius and the inner jet radius at the point of rupture is greatly increased.

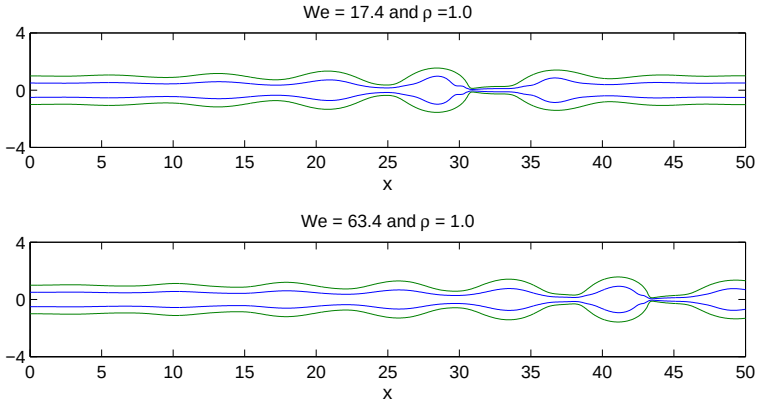

Figure 9.9: The breakup of inviscid compound liquid jets for different Weber numbers. Here $\sigma = 0.102$, $\rho = 1.0$, $\delta = 0.025$ and $\chi = 0.5$. As expected we see shorter breakup lengths when the Weber number is small (i.e., large surface tension). In addition we see that the qualitative structure of droplets are the same.

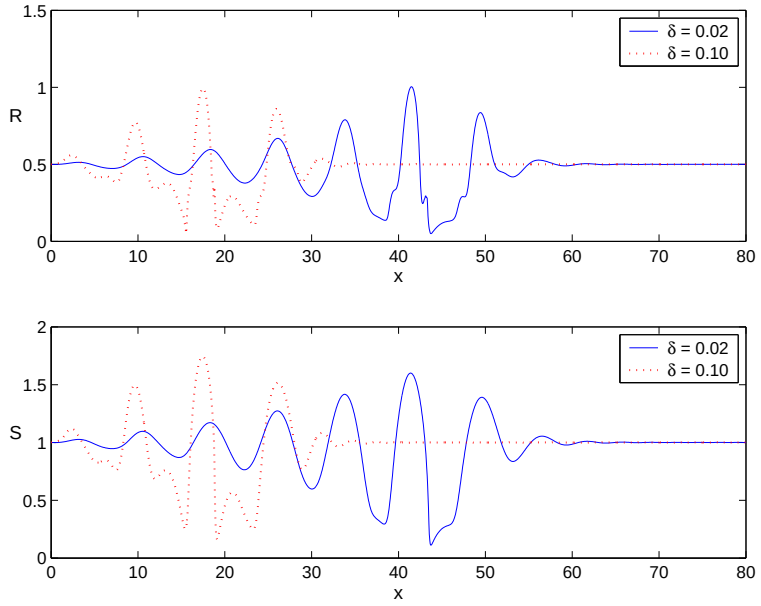

Figure 9.10: The inner and outer radii of inviscid compound liquid jets for different disturbance amplitudes δ. Here we have $We = 48.4$, $\sigma = 0.22$, $\rho = 1.2$, $\kappa = 0.81$ and $\chi = 0.5$. Near the drop regions, it can be observed that the outer radii for $\delta = 0.1$ is larger than the corresponding radii for $\delta = 0.02$.

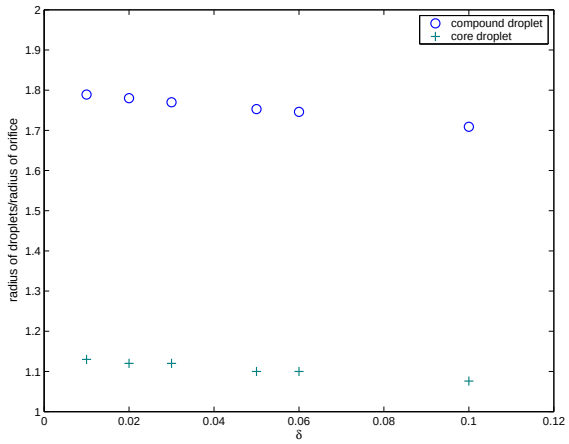

Figure 9.11: The size of compound droplets (including the size of the inner, or core, droplet) when the initial amplitude δ is varied. Here we have $We = 48.4$, $\sigma = 0.22$, $\rho = 1.2$, $\kappa = 0.81$ and $\chi = 0.5$. There is a general trend for the droplet sizes to decrease with the disturbance amplitude.

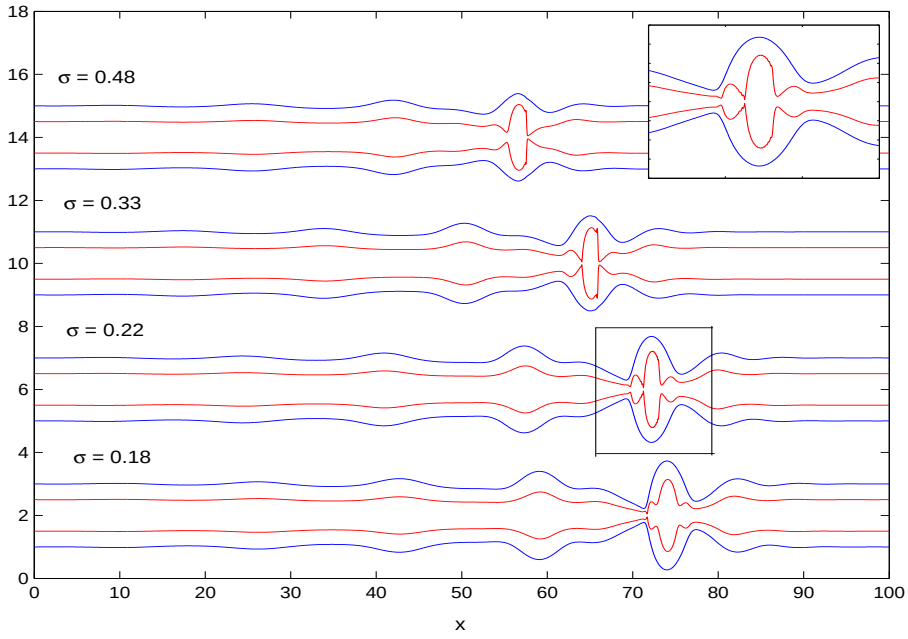

Figure 9.12: Profiles at breakup of an inviscid-inviscid compound liquid jet for different surface tension ratios σ. The formation of a compound drop with multiple cores can be seen when $\sigma \approx 0.22$. The other parameters here are $We = 31.2$, $\kappa = 0.38$, $\rho = 1.2$, $\delta = 0.01$ and $\chi = 0.5$. An enlarged inset showing a close up profile of the compound drop is shown in the top right hand corner.

Chapter 10

Compound Liquid Jets: non-Newtonian

In this chapter we examine the instability of a viscous compound thread with both the inner and outer fluids having non-Newtonian viscosity thereby extending the analysis of the previous chapter. In keeping with the formulation of inviscid compound threads we assume that two immiscible fluids emerge from two co-axial cylinders and that the resulting flow is axisymmetric and incompressible. The governing equations consist of the continuity equation and the Navier-Stokes equations (generalized to include a variable viscosity) within each fluid

$$\nabla \cdot \boldsymbol{u}^{[i]} = 0, \tag{10.1}$$

$$\rho_i \frac{D\boldsymbol{u}^{[i]}}{Dt} = -\nabla p^{[i]} + \nabla \cdot (\eta_i \boldsymbol{E}^{[i]}) = -\nabla p + \eta_i \nabla^2 \boldsymbol{u}^{[i]} + \nabla \eta_i \cdot \boldsymbol{E}^{[i]} \tag{10.2}$$

where $\boldsymbol{u}^{[i]} = (u^{[i]}, 0, v^{[i]})$ is the velocity vector in cylindrical coordinates with u and v as the axial and radial velocities respectively (we assume there is no azimuthal velocity), $\mathbf{E}^{[i]} = \nabla \mathbf{u}^{[i]} + (\nabla \mathbf{u}^{[i]})^T$ is the deformation tensor, t is time, ρ is the density of the liquids, η is the variable viscosity and p is pressure. The superscript $[i]$ denotes variables in the core fluid when $i = 1$ and in the outer fluid when $i = 2$. Moreover, whenever the subscript

i is used, it is to be understood that $i = 1$ or 2 except where reference is made otherwise (we adopt the convention of generally having material parameters to have subscripts). Writing out these equations in cylindrical coordinates we have,

$$\rho_i u_t^{[i]} + u^{[i]}u_x^{[i]} + v^{[i]}u_r^{[i]} = -p_x^{[i]} + \eta_i u_{xx}^{[i]} + \frac{1}{r}(ru_r^{[i]})_r + 2\eta_{ix}u_x^{[i]} + \eta_{ir}\left(v_x^{[i]} + u_r^{[i]}\right), \quad (10.3)$$

$$\rho_i v_t^{[i]} + u^{[i]}v_x^{[i]} + v^{[i]}v_r^{[i]} = -p_r^{[i]} + \eta_i v_{xx}^{[i]} + ((rv_r^{[i]})_r/r)_r + 2\eta_{ir}v_r^{[i]} + \eta_{ix}\left(v_x^{[i]} + u_r^{[i]}\right), \quad (10.4)$$

and

$$v_r^{[i]} + u_x^{[i]} + v^{[i]}/r = 0, \quad (10.5)$$

where subscripts which are variables represent differentiation with respect to that variable. These equations are supplemented by boundary conditions but before we evaluate them we define the 'apparent viscosity' η_i. This is given by

$$\eta_i = \tilde{\eta}_0^{[i]}[(1-\lambda_i)(1+(h\dot{\gamma}_{[i]})^2)^{\frac{n_i-1}{2}} + \lambda_i], \quad (10.6)$$

which is commonly known as the Carreau model (see Carreau *et al.* (1979) for more details). In this case, η is the shear rate dependent viscosity, $\dot{\gamma} = \sqrt{\boldsymbol{E} : \boldsymbol{E}/2}$ is the second invariant of the deformation tensor, $\tilde{\eta}_0$ is the zero-shear rate viscosity, h is a time constant, $\lambda\tilde{\eta}_0$ is the viscosity in the limit of infinite shear and finally n_i is the flow index number within each fluid.

Evaluating $\dot{\gamma}$ we have

$$\dot{\gamma}_{[i]} = \left(2\left(v_r^{[i]}\right)^2 + 2\left(v^{[i]}/r\right)^2 + \left(v_x^{[i]} + u_r^{[i]}\right)^2 + 2\left(u_x^{[i]}\right)^2\right)^{\frac{1}{2}}. \quad (10.7)$$

10.1 Boundary conditions

If we denote the inner-outer fluid interface by $R(x,t)$ and the outer fluid interface by $S(x,t)$ then the inner fluid is constrained to move within $0 \leqslant r \leqslant R(t,x)$ with the outer fluid occupying $R(t,x) \leqslant r \leqslant S(t,x)$ where x and r are the axial and radial coordinates respectively. The kinematic boundary condition, which states that a fluid particle on the free surface remains there is applied at the two interfaces $r = R(t,x)$ and $r = S(t,x)$, so that

$$v^{[1]}(R,x,t) = R_t + u^{[1]}(R,x,t)R_x \quad \text{and} \quad v^{[2]}(R,x,t) = R_t + u^{[2]}(R,x,t)R_x, \tag{10.8}$$

$$v^{[2]}(S,x,t) = S_t + u^{[2]}(S,x,t)S_x. \tag{10.9}$$

In addition we require tangential and normal stress conditions on these two interfaces, these can be written as

$$\begin{aligned} &2\eta_2 R_x \left(v_r^{[2]} - u_x^{[2]}\right) + \eta_2 \left(1 - (R_x)^2\right)\left(u_r^{[2]} + v_x^{[2]}\right) \\ &= 2\eta_1 R_x \left(v_r^{[1]} - u_x^{[1]}\right) + \eta_1 \left(1 - (R_x)^2\right)\left(u_r^{[1]} + v_x^{[1]}\right) \qquad \text{at} \quad r = R(x,t), \end{aligned} \tag{10.10}$$

$$2\eta_2 S_x \left(v_r^{[2]} - u_x^{[2]}\right) + \eta_2 \left(1 - (S_x)^2\right)\left(u_r^{[2]} + v_x^{[2]}\right) = 0 \qquad \text{at} \quad r = S(x,t), \tag{10.11}$$

and

$$\begin{aligned} &2\eta_2 u_x^{[2]} (S_x)^2 + 2\eta_2 v_r^{[2]} - 2\eta_2 \left(u_r^{[2]} + v_x^{[2]}\right) S_x + (p^e - p^{[2]})\left(1 + (S_x)^2\right) \\ &\qquad = -\sigma_2 \kappa_2 \left(1 + (S_x)^2\right) \qquad \text{at} \quad r = S(x,t), \end{aligned} \tag{10.12}$$

$$2\eta_2 u_x^{[2]}\left(R_x\right)^2+2\eta_2 v_r^{[2]}-2\eta_2\left(u_r^{[2]}+v_x^{[2]}\right)R_x+\left(p^{[1]}-p^{[2]}\right)\left(1+\left(R_x\right)^2\right)-2\eta_1 u_x^{[1]}\left(R_x\right)^2$$
$$-2\eta_1 v_r^{[1]}+2\eta_1\left(u_r^{[1]}+v_x^{[1]}\right)R_x=\sigma\kappa_1\left(1+\left(R_x\right)^2\right)\qquad\text{at}\quad r=R(x,t),\tag{10.13}$$

where σ_1 and σ_2 represent the surface tension of the inner and outer interfaces, p^e and $p^{[i]}$ represent the ambient pressure of the surrounding fluid and the pressures within each fluid respectively[1]. In addition the radii of curvature at the inner and outer fluid interfaces are given by

$$\kappa_1=\frac{\Lambda_R^{-1}}{R}-\frac{R_{xx}}{\Lambda_R^3},\tag{10.14}$$

and

$$\kappa_2=\frac{\Lambda_S^{-1}}{S}-\frac{S_{xx}}{\Lambda_S^3},\tag{10.15}$$

where $\Lambda_R=\left(1+\left(R_x\right)^2\right)^{\frac{1}{2}}$ and $\Lambda_S=\left(1+\left(S_x\right)^2\right)^{\frac{1}{2}}$. No slip requires that the velocities at the shared interface $r=R(x,t)$ are continuous so that

$$\boldsymbol{u}^{[1]}\cdot\boldsymbol{n}=\boldsymbol{u}^{[2]}\cdot\boldsymbol{n}\quad\text{ and }\quad\boldsymbol{u}^{[1]}\cdot\boldsymbol{t}=\boldsymbol{u}^{[2]}\cdot\boldsymbol{t},\tag{10.16}$$

where $\boldsymbol{n}$ and $\boldsymbol{t}$ are the unit normal and tangent vectors to the interface $r=R(x,t)$.

10.1.1 The Dimensionless Equations.

Since we are considering slender liquid jets we non-dimensionalise our variables such that radial and axial distances have characteristic lengths $\mathcal{R}_0$ and $\mathcal{L}_0$ respectively, where $\mathcal{R}_0/\mathcal{L}_0=\varepsilon\ll 1$ (as is usual in slender jets). In addition, we assume that the jet has a dominant velocity along the axis of the jet so that if U_0 is a typical velocity along the jet, the velocity in the radial direction is made dimensionless with $v_0=U_0\mathcal{R}_0/\mathcal{L}_0=\varepsilon U_0$. Time t and pressure p are non-dimensionalized with respect to $\mathcal{L}_0/U_0$ and $\rho_i U_0^2$ respectively.

[1]The surrounding gas is considered to be passive which is a reasonable assumption since usually it will have a much smaller density and dynamic viscosity.

This is similar to the scalings used by Ramos (1999), except here we use a different scaling for the pressure. This allows us to consider compound jets at higher Reynolds numbers than those considered by Ramos (1999). The variable viscosities within each fluid are made dimensionless with respect to their zero shear rate viscosities $\tilde{\eta}_0^{[i]}$. We choose $\mathcal{R}_0$ to be the radius of the outer nozzle so that $S(0,t) = 1$ follows immediately and let U_0 be the exit velocity at the nozzle. The resulting dimensionless equations for the continuity equation and equation of motion are given by

$$v_r^{[i]} + u_x^{[i]} + v^{[i]}/r = 0. \tag{10.17}$$

$$\begin{aligned}(\rho_i/\rho_2)\left(u_t^{[i]} + u^{[i]}u_x^{[i]} + v^{[i]}u_r^{[i]}\right) = -(\rho_i/\rho_2)p_x^{[i]} + \frac{\tilde{\eta}_0^{[i]}}{\tilde{\eta}_0^{2]}}\frac{\eta_i}{\mathcal{R}e}\left(u_{xx}^{[i]} + \varepsilon^{-2}\frac{1}{r}\left(ru_r^{[i]}\right)_r\right) \\ + \frac{\tilde{\eta}_0^{[i]}}{\tilde{\eta}_0^{2]}}\left(\frac{2}{\mathcal{R}e}\eta_{ix}u_x^{[i]} + \frac{1}{\mathcal{R}e}\eta_{ir}\left(v_x^{[i]} + \varepsilon^{-2}u_r^{[i]}\right)\right),\end{aligned} \tag{10.18}$$

and

$$\begin{aligned}(\rho_i/\rho_2)\left(v_t^{[i]} + u^{[i]}v_x^{[i]} + v^{[i]}v_r^{[i]}\right) = -(\rho_i/\rho_2)\varepsilon^{-2}p_r^{[i]} + \varepsilon^{-2}\frac{\tilde{\eta}_0^{[i]}}{\tilde{\eta}_0^{2]}}\frac{2\eta_{ir}}{\mathcal{R}e}v_r^{[i]} \\ \frac{\tilde{\eta}_0^{[i]}}{\tilde{\eta}_0^{2]}}\frac{\eta_i}{\mathcal{R}e}\left(v_{xx}^{[i]} + \varepsilon^{-2}\left((v_r^{[i]}/r) - (v^{[i]}/r^2) + v_{rr}^{[i]}\right)\right) + \frac{\eta_{ix}}{\mathcal{R}e}\frac{\tilde{\eta}_0^{[i]}}{\tilde{\eta}_0^{2]}}\left(v_x^{[i]} + \varepsilon^{-2}u_r^{[i]}\right),\end{aligned} \tag{10.19}$$

where $\mathcal{R}e = \rho_2 L_0 U_0/\tilde{\eta}_0^{[2]}$ is the generalized Reynolds number and the dimensionless viscosities within each fluid is given by $\eta_i = (1-\lambda_i)(1+(h\dot{\gamma}_{[i]})^2)^{\frac{n_i-1}{2}} + \lambda_i$.

The kinematic condition applied at the two jet interfaces $r = R(t,x)$ and $r = S(t,x)$ are given by

$$v^{[1]}(R,x,t) = R_t + u^{[1]}(R,x,t)R_x \quad \text{and} \quad v^{[2]}(R,x,t) = R_t + u^{[2]}(R,x,t)R_x, \tag{10.20}$$

$$v^{[2]}(S,x,t) = S_t + u^{[2]}(S,x,t)S_x. \tag{10.21}$$

The dimensionless expression for the shear rate $\dot{\gamma}$ has the form

$$\dot{\gamma}_{[i]} = \left(2\left(v_r^{[i]}\right)^2 + 2\left(v^{[i]}/r\right)^2 + \left(\varepsilon v_x^{[i]} + \varepsilon^{-1}u_r^{[i]}\right)^2 + 2\left(u_x^{[i]}\right)^2\right)^{\frac{1}{2}}. \tag{10.22}$$

The tangential stress conditions are given by

$$\begin{aligned}\frac{1}{\psi}\frac{\eta_2}{\eta_1}\left(2\varepsilon^2 R_x\left(v_r^{[2]} - u_x^{[2]}\right) + \left(1-\varepsilon^2\left(R_x\right)^2\right)\left(u_r^{[2]} + \varepsilon^2 v_x^{[2]}\right)\right) &= 2\varepsilon^2 R_x\left(v_r^{[1]} - u_x^{[1]}\right) \\ &+ \left(1-\varepsilon^2\left(R_x\right)^2\right)\left(u_r^{[1]} + \varepsilon^2 v_x^{[1]}\right) \quad \text{at} \quad r = R(x,t), \end{aligned} \tag{10.23}$$

$$2\varepsilon^2 S_x\left(v_r^{[2]} - u_x^{[2]}\right) + \left(1-\varepsilon^2\left(S_x\right)^2\right)\left(u_r^{[2]} + \varepsilon^2 v_x^{[2]}\right) = 0 \quad \text{at} \quad r = S(x,t), \tag{10.24}$$

with the normal stress conditions on each interface given by

$$\begin{aligned}\frac{2\eta_2}{\mathcal{R}e}\frac{1}{\left(1+\varepsilon^2\left(S_x\right)^2\right)}\left(\varepsilon^2 u_x^{[2]}\left(S_x\right)^2 + v_r^{[2]} - \left(u_r^{[2]} + \varepsilon^2 v_x^{[2]}\right)S_x\right) + \left(p_e - p^{[2]}\right) \\ = -\frac{1}{We}\left(\frac{\Lambda_S^{-1}}{S} - \frac{\varepsilon^2 S_{xx}}{\Lambda_S^3}\right) = -\frac{1}{We}\kappa_2 \quad \text{at} \quad r = S(x,t), \end{aligned} \tag{10.25}$$

$$\begin{aligned}\frac{2}{\mathcal{R}e}\frac{1}{\left(1+\varepsilon^2\left(R_x\right)^2\right)}\left[\eta_2\left(\varepsilon^2 u_x^{[2]}\left(R_x\right)^2 + v_r^{[2]} - \left(u_r^{[2]} + \varepsilon^2 v_x^{[2]}\right)R_x\right) - \psi\eta_1\left(\varepsilon^2 u_x^{[1]}\left(R_x\right)^2\right. \right. \\ \left. \left. + v_r^{[1]} - \left(u_r^{[1]} + \varepsilon^2 v_x^{[1]}\right)R_x\right)\right] = \left(p^{[2]} - \rho p^{[1]}\right) + \frac{\sigma}{We}\left(\frac{\Lambda_R^{-1}}{R} - \frac{\varepsilon^2 R_{xx}}{\Lambda_R^3}\right), \end{aligned} \tag{10.26}$$

where $\Lambda_R = \left(1+\varepsilon^2\left(R_x\right)^2\right)^{\frac{1}{2}}$ and $\Lambda_S = \left(1+\varepsilon^2\left(S_x\right)^2\right)^{\frac{1}{2}}$, $\psi = \tilde{\eta}_0^{[1]}/\tilde{\eta}_0^{2]}$ is the zero shear rate viscosity ratio, $\rho = \rho_1/\rho_2$ is the density ratio, $\sigma = \sigma_1/\sigma_2$ is the interfacial surface tension ratio and $We = \rho_2 U_0^2 R_0/\sigma_2$ is the Weber number. We now expand all our variables in

the form (see Ramos (1999))

$$\chi = \chi_0 + \varepsilon^2 \chi_2 + O(\varepsilon^4),$$

and make the assumption that to leading order the axial velocity components in both fluids is independent of the radial direction (this is a reasonable assumption for slender liquid jets). After substituting into our dimensionless equations we get some leading order equations.

10.2 Leading Order Equations

At leading order the shear rate $\dot{\gamma}$ is given by

$$\dot{\gamma}_{[i]} = \sqrt{2}\left(\left(v_{0r}^{[i]}\right)^2 + \left(v_0^{[i]}/r\right)^2 + \left(u_{0x}^{[i]}\right)^2\right)^{\frac{1}{2}}. \tag{10.27}$$

The continuity equation at leading order is given by

$$u_{0x}^{[i]} + \frac{1}{r}(r v_0^{[i]})_r = 0, \tag{10.28}$$

which implies, after writing $u_0^{[i]} = \mathcal{U}_i(x,t)$, that $v_0^{[i]} = C_i/r - r\mathcal{U}_{ix}/2$ where $C_i = C_i(x,t)$. By making use of (10.27), we can formulate the leading order expression for the apparent viscosity in both the inner and outer fluids, so that we have the dimensionless viscosities given by

$$\eta_i = \left[(1-\lambda_i)\left(\sqrt{1 + h^2\left(\frac{4C_i^2}{r^2} + 3\mathcal{U}_{ix}^2\right)}\right)^{n_i - 1} + \lambda_i\right] + O(\varepsilon^2). \tag{10.29}$$

Since disturbances are axisymmetric we require a condition on the radial velocity such that $v^{[1]} = 0$ at $r = 0$ so that we require that $C_1(x,t) = 0$.

At leading order the kinematic conditions give

$$v_0^{[1]}(R,x,t) = -\frac{R}{2}\mathcal{U}_{1x} = R_t + \mathcal{U}_1 R_x, \quad v_0^{[2]}(R,x,t) = R_t + \mathcal{U}_2 R_x, \tag{10.30}$$

$$\text{and} \quad v_0^{[2]}(S,x,t) = S_t + \mathcal{U}_2 S_x. \tag{10.31}$$

These can be written in a more concise form so that we have

$$(R^2)_t + (R^2\mathcal{U}_1)_x = 0, \tag{10.32}$$

and

$$4C_2 = (S^2 - R^2)_t + ((S^2 - R^2)\mathcal{U}_2)_x. \tag{10.33}$$

If the fluids are viscous then we must have continuity of velocities at the interface $r = R(x,t)$, this requires

$$u_0^{[1]}(R,x,t) = u_0^{[2]}(R,x,t) \quad \text{and} \quad u_2^{[1]}(R,x,t) = u_2^{[2]}(R,x,t). \tag{10.34}$$

Since at leading order the axial velocities are independent of r, this implies that $\mathcal{U}_1(x,t) = \mathcal{U}_2(x,t) = \mathcal{U}(x,t)$. In addition by using (10.30) we that $C_1(x,t) = C_2(x,t) = 0$.

At leading order, from the normal stress at $r = S(x,t)$, we get[2]

$$(p_e - p_0^{[2]}) + \frac{2\eta_2}{\mathcal{R}e} v_{0r}^{[2]} = -\frac{1}{We}\kappa_2, \tag{10.35}$$

[2]We have retained the symbol for the full curvature here. In this context we require the leading order term only, which in this case is $1/S_0$, however we shall go on to use the full expression for the mean curvature. This is an ad-hoc approach which has been used by a number of previous authors and is essential for the correct reproduction of equilibrium shapes in numerical simulation. A fuller explanation is provided in Chapter 4 and in Yarin (1993).

which can be written, after substitution of $v_0^{[2]}$, as

$$(p_e - p_0^{[2]}) - \frac{\eta_2}{\mathcal{R}e}\mathcal{U}_x = -\frac{1}{We}\kappa_2. \tag{10.36}$$

Similarly from the normal stress condition at $r = R(x,t)$ we have

$$\begin{aligned}&\left(\rho p^{[1]} - p^{[2]}\right) + \frac{2}{\mathcal{R}e}\left(\eta_2 v_{0r}^{[2]} - \psi\eta_1 v_{0r}^{[1]}\right)\\ &= \left(\rho p^{[1]} - p^{[2]}\right) - \frac{1}{\mathcal{R}e}\mathcal{U}_x\left(\eta_2 - \psi\eta_1\right) = \frac{\sigma}{We}\kappa_1,\end{aligned} \tag{10.37}$$

both these conditions imply that

$$p_0^{[2]} = \frac{\kappa_2}{We} - \frac{\eta_2}{\mathcal{R}e}\mathcal{U}_x \quad \text{and} \quad p_0^{[1]} = \frac{1}{\rho We}\left(\kappa_2 + \sigma\kappa_1\right) - \psi\frac{\eta_1}{\rho\mathcal{R}e}\mathcal{U}_x, \tag{10.38}$$

where we have taken the ambient air pressure of the surrounding p_e to be equal to 0.

The tangential stress equations at leading order give

$$u_{0r}^{[2]} = 0 \quad \text{and} \quad u_{0r}^{[1]} = 0, \tag{10.39}$$

respectively, which are both satisfied.

The axial equation of motion for the inner and outer fluids, that is equation (10.18) at $O(1)$ give

$$\frac{\mathcal{R}e}{\eta_1}\frac{\rho}{\psi}\left(\mathcal{U}_t + \mathcal{U}\mathcal{U}_x + p_{0x}^{[i]}\right) - \left(\eta_i\mathcal{U}_{xx} + 2\mathcal{U}_x\eta_{ix}\right) = \frac{1}{r}\left(r u_{2r}^{[i]}\right)_r, \tag{10.40}$$

which have general solutions for $u_2^{[1]}$ and $u_2^{[2]}$ in the form of,

$$u_2^{[i]} = Q_i(x,t)\frac{r^2}{4} + M_i(x,t)\log r + N_i(x,t), \tag{10.41}$$

where

$$Q_i(x,t) = \frac{\mathcal{R}e}{\eta_1}\frac{\rho}{\psi}\left(\mathcal{U}_t + \mathcal{U}\mathcal{U}_x + p_{0x}^{[i]}\right) - \left(\eta_i \mathcal{U}_{xx} + 2\mathcal{U}_x\eta_{ix}\right). \tag{10.42}$$

Within the inner fluid we must have the conditions

$$u_r^{[1]}(0,x,t) = 0 \quad \text{and} \quad v^{[1]}(0,x,t) = 0, \tag{10.43}$$

and thus in order to avoid having a singular solution for $u_2^{[1]}$ as $r \to 0$ we must have $M_1 = 0$.

The tangential stress condition at $r = S(x,t)$, gives at $O(\varepsilon^2)$

$$2S_{0x}\left(v_{0r}^{[2]} - \mathcal{U}_x\right) + \left(u_{2r}^{[2]} + v_{0x}^{[2]}\right) = 0, \tag{10.44}$$

which, after substitution and using (10.41), gives an expression for M_2 as,

$$M_2 = 3S_0S_{0x}\mathcal{U}_x + \frac{S_0^2}{2}\mathcal{U}_{xx} - \frac{1}{2}S_0^2Q_2. \tag{10.45}$$

Similarly the tangential stress condition at $r = R(x,t)$ gives

$$\begin{aligned}\frac{\eta_2}{\psi\eta_1}\left(3R_0R_{0x}\mathcal{U}_x + \frac{R_0^2}{2}\mathcal{U}_{xx} - \frac{R_0^2}{2}Q_2 - M_2\right)& \\ = 3R_0R_{0x}\mathcal{U}_x + \frac{R_0^2}{2}\mathcal{U}_{xx} - \frac{R_0^2}{2}Q_1.&\end{aligned} \tag{10.46}$$

We now substitute the expressions for Q_1, Q_2 and M_2 into the above equation to yield

$$\begin{aligned}\left(S_0^2 + (\rho-1)R_0^2\right)\left(\mathcal{U}_t + \mathcal{U}\mathcal{U}_x\right) = -\frac{1}{We}\left(S_0^2\kappa_{2x} + \sigma R_0^2\kappa_{1x}\right)& \\ + \frac{3}{\mathcal{R}e}\left[\psi R_0^2\mathcal{U}_x\eta_1 + (S_0^2 - R_0^2)\mathcal{U}_x\eta_2\right]_x.&\end{aligned} \tag{10.47}$$

Therefore (10.32), (10.33) and (10.47) give a closed set of equations for R_0, S_0 and $\mathcal{U}$. We see that if we have $n_1 = n_2 = 1$ than the equations reduce to those found in Ramos (1999) for a Newtonian compound liquid jet. Also when $n_1 = n_2 = 1$ and $\psi = \rho = 1$ and $\sigma = 0$ we have the equation for a single Newtonian liquid jet.

10.3 Nonlinear Temporal Analysis

Removing the zero subscripts from our variables we have the nonlinear system to be solved as

$$\begin{aligned}\left(S^2 + (\rho - 1)R^2\right)\left(\mathcal{U}_t + \mathcal{U}\mathcal{U}_x\right) = &-\frac{1}{We}\left(S^2\kappa_{2x} + \sigma R^2\kappa_{1x}\right) \\ &+\frac{3}{\mathcal{R}e}\left[\psi R^2\mathcal{U}_x\eta_1 + (S^2 - R^2)\mathcal{U}_x\eta_2\right]_x, \end{aligned} \tag{10.48}$$

$$(R^2)_t + (R^2\mathcal{U})_x = 0, \tag{10.49}$$

and

$$(S^2 - R^2)_t + [(S^2 - R^2)\mathcal{U}]_x = 0, \tag{10.50}$$

where it is understood that the full expression for the mean curvature term is included by retaining the symbols κ_i. We solve this set of equations using a finite difference scheme based on the Lax-Wendroff method of previous sections. The initial conditions, at the nozzle exit $x = 0$, for the three variables are chosen so that we have

$$\mathcal{U}(0,t) = 1 + \delta \sin\left(\frac{\kappa}{\varepsilon}t\right) \tag{10.51}$$

where δ is the initial disturbance amplitude and κ (no subscript) is the frequency of the disturbance. The initial conditions for R and S are chosen so that

$$R(0,t) = \chi \quad \text{and} \quad S(0,t) = 1 \tag{10.52}$$

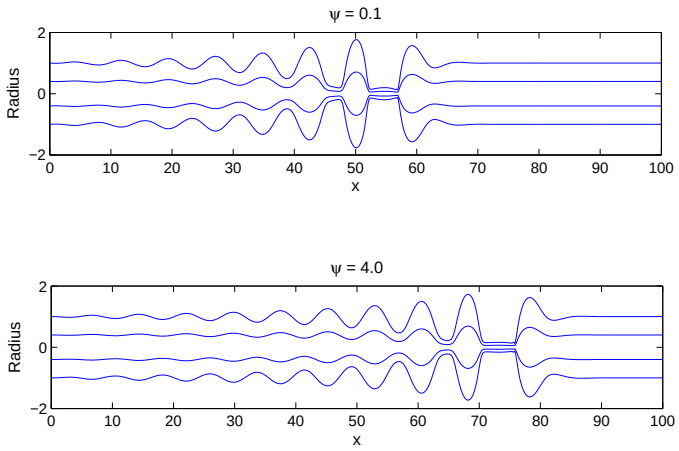

Figure 10.1: The breakup of a compound Newtonian liquid jet for different values of the viscosity ratio ψ. The effect of increasing ψ is to reduce the 'effective' Reynolds number of the flow and lead to longer jets and thinner ligaments between droplets. The other parameters are $\mathcal{R}e = 2100$, $We = 32.4$, $\delta = 0.025$, $\kappa = 0.81$, $\rho = 1.0$, $\sigma = 1.0$, $n_1 = 1.0$, $n_2 = 1.0$ and $\chi = 0.4$.

where χ is some constant chosen to be smaller than 1 which denotes the initial radius of the inner thread of fluid. The initial steady state of the system is chosen so that $\mathcal{U}(x,0) = S(x,0) = 1$ and $R(x,0) = \chi$.

In Fig. 10.1 we show the profile of a compound Newtonian liquid jet at the point of breakup for different values of the viscosity ratio ψ. It can be observed that the effect of increasing ψ is to reduce the 'effective' Reynolds number of the flow and thus lead to longer jets and thinner ligaments between droplets. The almost linear relationship between breakup lengths and changes in ψ are shown in Fig. 10.2.

In Fig. 10.3 we plot the profile of a viscous compound liquid jet with a shear thinning core fluid surrounded by a Newtonian outer fluid and vice versa. It this case we see that the flow index number of the outer fluid dominates the overall dynamics of the jet structure at breakup. In particular notice the difference in breakup lengths and the slightly longer ligaments connecting droplets. The breakup lengths and size of satellite droplets for viscous compound liquid jets when the wavenumber of disturbances κ is changed is shown in Fig. 10.4 and Fig. 10.5. From this figure it is clear that when the

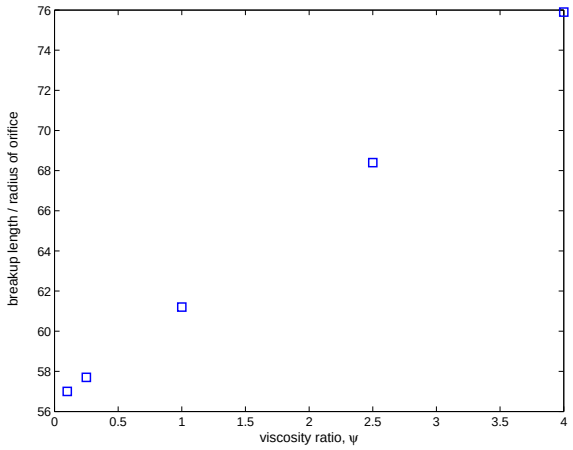

Figure 10.2: The breakup length of a compound liquid jet plotted against the viscosity ratio ψ. There is an almost linear relationship between breakup lengths and changes in ψ. The other parameters are $\mathcal{R}e = 2100$, $We = 32.4$, $\delta = 0.025$, $\kappa = 0.81$, $\rho = 1.0$, $\sigma = 1.0$, $n_1 = 1.0$, $n_2 = 1.0$ and $\chi = 0.4$.

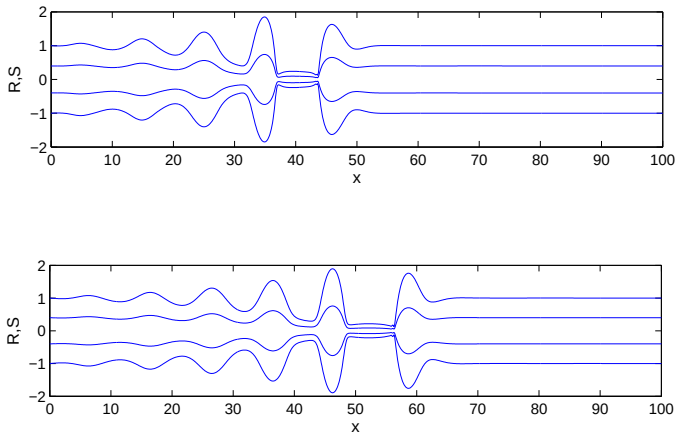

Figure 10.3: The breakup of a compound liquid jet with a shear thinning core (flow index number 0.4) surrounded by a Newtonian shell (Top) and vice versa (Bottom). The core fluid is seen to have a big effect on the resulting dynamics - both breakup lengths and satellite drops are bigger when the core is shear thinning. The other parameters are $\mathcal{R}e = 950$, $We = 19.5$, $\delta = 0.05$, $\kappa = 0.62$, $\rho = 1.0$, $\sigma = 1.0$, $\psi = 1.0$, $\lambda = 0.2$, $h = 1$ and $\chi = 0.4$.

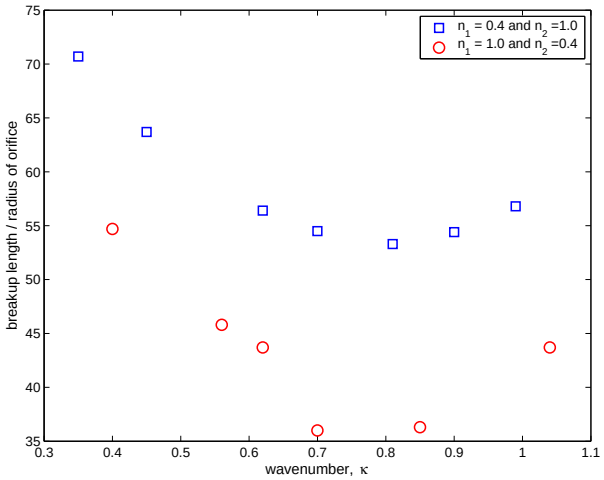

Figure 10.4: The breakup lengths for a viscous compound jet with a Newtonian fluid for the outer fluid and a shear thinning fluid for the core and vice versa for different disturbance wavenumbers. The other parameters are $\mathcal{R}e = 950$, $We = 19.4$, $\delta = 0.05$, $\psi = 1.0$, $\rho = 1.0$, $\sigma = 1.0$, $\lambda = 0.2$, $h = 1$ and $\chi = 0.4$.

outer fluid is Newtonian, as opposed to shear thinning, the jet always has larger breakup lengths. The difference in breakup lengths remains fairly consistent throughout the range of wavenumbers shown[3]. Satellite droplet sizes decrease with increasing κ (which is the case for single jets) but show very little variation for the two cases considered here.

We next plot the breakup lengths for a viscous compound liquid jet with a Newtonian shell and shear thinning core and vice versa for different surface tension ratios σ in Fig. 10.6. Evidently there is an exponential decay in breakup lengths as the surface tension ratio is increased. In addition note how the difference in breakup lengths increases when $\sigma \to 0$.

In Figs. 10.7 and 10.8 we show the breakup lengths and satellite droplet sizes for compound liquid jets with a Newtonian and shear thinning ($n_1 = 0.2$) core respectively when the flow index number of the outer fluid, n_2, is changed. We have chosen to consider the case when the density, surface tension and viscosity of the outer fluid is twice that of the inner fluid (i.e., $\rho = \sigma = \psi = 0.5$). We find that breakup lengths decrease as

[3]The discrepancy when $\kappa \approx 0.7$ is accounted for by the change in the location of breakup, i.e., the inner liquid jet ruptures upstream of the ligaments as opposed to downstream of ligaments.

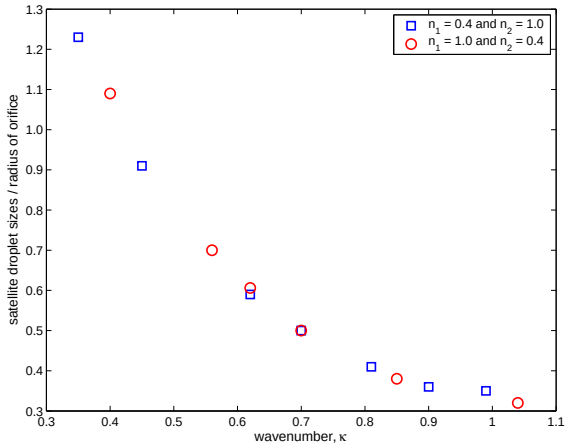

Figure 10.5: The breakup lengths for a viscous compound jet with a Newtonian fluid for the outer fluid and a shear thinning fluid for the core and vice versa for different disturbance wavenumbers. The other parameters are $\mathcal{R}e = 950$, $We = 19.4$, $\delta = 0.05$, $\psi = 1.0$, $\rho = 1.0$, $\sigma = 1.0$, $\lambda = 0.2$, $h = 1$ and $\chi = 0.4$.

the outer fluid is made more shear thinning (i.e., as n_2 is decreased). We also observe longer breakup lengths when the inner fluid is Newtonian as compared to the case when the inner fluid is shear thinning ($n_1 < 1$). Satellite droplet sizes exhibit a non monotonic relationship with the flow index number of the outer fluid (see Fig. 10.8). A compound jet with a Newtonian core produces larger satellite droplet sizes when compared to a shear thinning inner fluid. Furthermore, satellite sizes are seen to increase when the flow index number of the outer fluid is increased or decreased from $n_2 = 0.7$. The size of main droplets increases very slightly as $n_2 \to 1$ for both a shear thinning and Newtonian core (the non-dimensional size of main droplets is about 1.77).

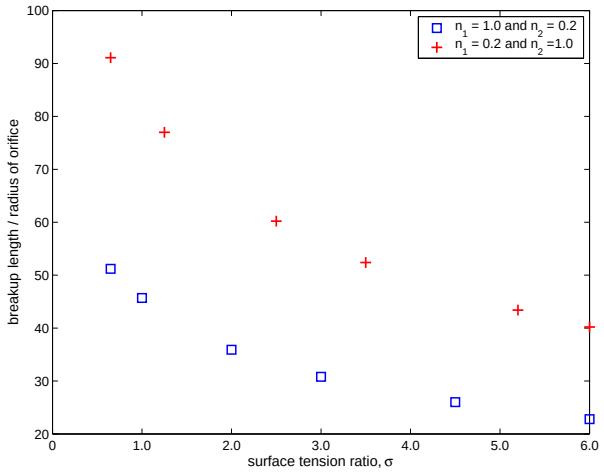

Figure 10.6: Breakup lengths for a compound viscous liquid jet with different flow index numbers for the inner and outer fluids. We only vary the flow index number of the shell fluid whilst keeping the flow index number of the inner fluid constant. The other parameters are $\mathcal{R}e = 500$, $We = 19.4$, $\delta = 0.05$, $\kappa = 0.86$, $\psi = 0.5$, $\rho = 0.5$, $\lambda = 0.1$, $h = 1$ and $\chi = 0.4$.

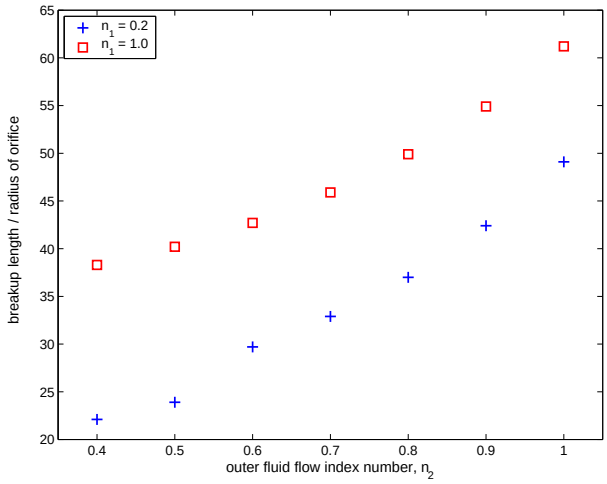

Figure 10.7: Breakup lengths for a compound viscous liquid jet with a shear thinning core surrounded by a Newtonian shell and vice versa for different interfacial surface tension ratios. The other parameters are $\mathcal{R}e = 480$, $We = 16.4$, $\delta = 0.1$, $\kappa = 0.88$, $\psi = 0.5$, $\rho = 0.5$, $\sigma = 0.5$, $\lambda = 0.1$, $h = 1$ and $\chi = 0.7$.

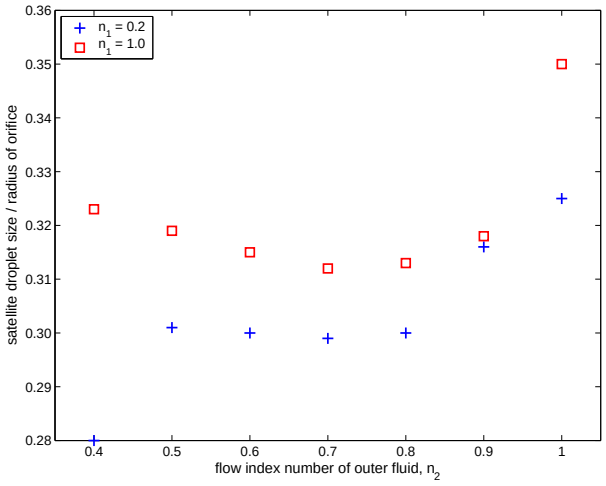

Figure 10.8: Satellite droplet sizes for a compound viscous liquid jet with a shear thinning core surrounded by a Newtonian shell and vice versa for different interfacial surface tension ratios. The other parameters are $\mathcal{R}e = 480$, $We = 16.4$, $\delta = 0.1$, $\kappa = 0.88$, $\psi = 0.5$, $\rho = 0.5$, $\sigma = 0.5$, $\lambda = 0.1$, $h = 1$ and $\chi = 0.7$.

Chapter 11

Drop formation and Breakup in Microjets

We live in a world which is increasingly reliant on ever smaller and fragile technology. Many people will be familiar with the term nanotechnology but many more will already be using some form of this technology. At such small scales the behaviour of fluids can be markedly different to what might be expected on an everyday macroscopic scale and a whole new field of interest exists devoted to understanding such behaviour; this is the world of micro-fluidics. In this field the key concern lies with finding suitable devices to contain and manipulate fluids at the micrometer scale. In most general cases the fluid is confined to move within a tube or some other bounding surface but even then the use of multiple fluids may create an interface between two fluids and therefore jet like phenomena. In other cases (like modern ink-jet printing or the development of micro-needles) the creation of a liquid thread through a micrometer sized nozzle or syringe produces a liquid jet in the normal manner. In both cases an understanding of liquid jet dynamics at the microscopic scale is required.

In this Chapter we shall examine liquid jets where the typical length scale is of the order of micrometers or even nanometers. At the extreme end of such scales the Navier-

Stokes equation will become inappropriate as will the continuum hypothesis itself. It is unclear whether the dynamics of liquid jets on such small scales will even qualitatively resemble the standard macroscopic theory of liquid jets.

In the previous chapters we have looked at a number of models for liquid jets but have not really said anything much about the relative dimensions involved. Clearly there must be a limit to the applicability of such models, as we would not expect the linear theories of Rayleigh (1879) or Weber (1936) to apply when the typical jet diameter consists of say tens of molecules. In addition it is important to note that the fluid under consideration will have a big effect upon the length scales where we would expect standard models to breakdown. For instance, the smallest molecule by size is helium which has a typical diameter of 0.52 nm whereas molecules of some polymeric fluids may have diameters ten thousand times larger, typically at 50 μm .

If the typical length scale of a liquid jet is of the order of nanometers then molecular dynamics simulations are required to make progress (since the Navier-Stokes equation is valid for length scales as small as 10nm (see Koplik and Banavar (1993))). This was the approach adopted by Moseler and Landman (2000) who simulated the emergence of liquid jet of propane from a gold nozzle of diameter 6nm. At larger length scales, say tens or hundreds of micrometers, we might expect the Navier-Stokes equation to remain valid but the small scales and the large surface area to volume ratio allow us to introduce effects which might not so easily be incorporated into the classical continuum approach.

Since the early pioneering work of Rayleigh there has accumulated a large body of literature on liquid jets (see Eggers (1997) for an excellent review). Almost all of these works are concerned with jets on a macroscopic length scale with relatively little literature available for jets where the typical length scale is of the order of microns. It therefore remains unclear how the standard jet model will fare for microjets.

Since the ratio of surface area to volume is relatively large at such small scales it is

to be expected that surface and interfacial effects (which are the primary mechanisms leading to breakup in the standard model) are likely to be enhanced for the evolution of a liquid micro-thread to breakup. In particular the role played by the interface *itself* upon the dynamics of the liquid thread as the topological transition is reached is likely to produce noticeable effects. For this reason we shall attempt to use the theory of interface formation developed by Shikhmurzaev (1993) to explore the dynamics of liquid microjets.

The theory of interface formation (which allows for dynamic surface tension and consequently flow induced Marangoni effects) was first presented by Shikhmurzaev (1993) in relation to the problem of moving contact lines. It has since been used to explore a number of different free surface flow phenomena, including dynamic wetting, rupture of films and jets and the effects of droplet coalescence. The theory concerns itself primarily with the small but finite time required for interfaces to acquire their surface properties. This is termed the *relaxation time*. The main ideas within this theory are as follows. Firstly, for processes involving pinch-off and related phenomena there will be circumstances (like capillary thinning (see Shikhmurzaev (2005))) where the rate of stretching of the free surface is high enough so that the free surface can no longer be said to be in thermodynamic equilibrium. A consequence of this is that the capillary pressure becomes a function of the variable surface tension (whereas before it was simply proportional to the product of surface tension and mean curvature). In this case the free surface boundary conditions need to be re-evaluated. For instance, the normal stress condition now contains a variable surface tension which must be determined as part of the flow. The tangential stress on the free surface can no longer be equated with zero (since the gradient of the surface tension will, in general, be non-zero), in this case the tangential stress condition will express a balance between the tangential stress and the surface tension gradient. Thus the rupture of a thread of liquid under this theory will be a consequence of capillary pressure *and* the flow-induced Marangoni effect.

Shikhmuzaev (2005) presented work which demonstrated the effects of surface relaxation on the local region around pinch-off and in particular showed that surface relaxation can avoid the inherent singularities present within the standard lubrication type equation for slender jets (see Appendix F). However, Shikhmurzaev (2005) did not include the full term for the mean curvature in his one dimensional equations which therefore did not allow him to simulate accurately the profile at breakup[1] and thereby determine droplet sizes or location of rupture. The inclusion of the full curvature term along with a linear stability analysis exploring the effects of liquids with different relaxation times and initial jet radii was developed by Decent (2006). Since the equations, and their derivations in Decent (2006), are similar to those which we have presented hitherto we begin along the same lines as Decent (2006) and attempt to incorporate the theory of interface formation within the framework of the standard slender jet equations. We shall attempt to provide numerical simulations of a liquid thread at the point of rupture using the theory of interface formation.

11.1 Theory of interface formation.

The interface formation model consists of separating the equations of motion into those for the bulk fluid and those which apply on the free surface[2]. In the bulk fluid we have the usual Navier-Stokes equation along with the continuity equation

$$\frac{\partial \boldsymbol{u}}{\partial t} + (\boldsymbol{u} \cdot \nabla)\boldsymbol{u} = -\frac{1}{\rho}\nabla p + \nu \nabla^2 \boldsymbol{u}, \tag{11.1}$$

$$\nabla \cdot \mathbf{u} = \mathbf{0}. \tag{11.2}$$

[1] Although in fairness this was not probably the intention of the author.

[2] Since for an evolving liquid thread the interface is in a non-equilibrium state, in order to describe its evolution, it is necessary to develop models which take account of mass, momentum and energy fluxes in the interfacial layer and between this layer and the bulk phases (see Shikhmurzaev (1993) and (2005)).

where t is time, $\mathbf{u}$ is the velocity of the liquid, p is the pressure, ρ is the density of the liquid and ν is the kinematic viscosity. The above equations are complemented with the conventional boundary conditions for a gas-liquid interface, except that in this case, they are generalised to take account of variable surface tension and mass exchange between the bulk and the interface; these are the kinematic condition

$$\frac{\partial R}{\partial t} + \mathbf{w} \cdot \nabla R = 0, \tag{11.3}$$

which is applied at the free surface $R(\boldsymbol{r}, t) = 0$ having velocity $\boldsymbol{w}$. The tangential stress condition, which takes account of the variable surface tension σ (in this case the tensor $\mathbf{I} - \mathbf{nn}$ extracts the tangential component of $\mathbf{P}$) is given by

$$(\mathbf{I} - \mathbf{nn}) \cdot \mathbf{P} \cdot \mathbf{n} + \nabla\sigma = \mathbf{0}, \tag{11.4}$$

and finally the normal stress condition

$$p + \mathbf{n} \cdot \mathbf{P} \cdot \mathbf{n} = \sigma \nabla \cdot \mathbf{n}, \tag{11.5}$$

where $\mathbf{P} = -p\mathbf{I} + \mu[\nabla\mathbf{u} + (\nabla\mathbf{u})^T]$. In the standard model the free surface is treated as a mathematical surface (of zero thickness) with no property analogous to density in the bulk. However in the interface formation model the concept of surface density ϱ^s (which has a value ϱ^s_e at equilibrium) is used, which is really the density of the 'surface phase' of the fluid at the free surface. This allows us to construct conservation equations for the free surface so that we have the surface mass balance given by

$$\frac{\partial \varrho^s}{\partial t} + \nabla \cdot (\varrho^s \mathbf{w}) = -\left(\frac{\varrho^s - \varrho^s_e}{\tau}\right), \tag{11.6}$$

Liquid	Water	Glycerol 95%	Silicone Oil
μ (kg m^{-1}s^{-1})	1.5×10^{-3}	0.672	10^3
ρ (kg m^{-3})	1036	1248	10^3
σ_e (m s^{-2})	0.0697	0.0645	0.02
τ (s)	5.6×10^{-9}	8.3×10^{-6}	10^{-3}
ρ_e (kg m^{-3})	1.036×10^{-6}	1.248×10^{-6}	10^{-6}

Table 11.1: A table of parameters for fluids with different viscosities. In particular notice how the surface relaxation time τ is up to a million times greater for Silicone oil than for water. Taken from Shaw (2005) and Shikhmurzaev (2000).

which describes the mass flux along and into the free surface. Here the surface density ϱ^s is transported along the free surface with the velocity of the free surface $\mathbf{w}$. A consequence of this transport of surface density is the relaxation of the surface density towards its equilibrium value ϱ^s_e. This process of relaxation occurs with a characteristic time of τ which is known as the surface relaxation time. It is important to note that in the absence of motion ($\boldsymbol{w} = 0$), (11.6) implies that the free surface will 'relax' exponentially. Experimental investigations by Blake *et al.* (1999, 2002) (within the framework of this theory) have estimates of τ ranging from 10^{-9} to 10^{-7} seconds for most low to medium viscosity liquids such as water, and suggest that τ is proportional to μ, so that τ might be as high as 10^{-3} seconds for highly viscous liquids such as some silicone oils. Davis & Rideal (1963) estimated that the surface tension relaxation time for water is of the order of nanoseconds. These experimental observations are a confirmation of the findings of Shikhmurzaev (1997). Some estimates of liquid parameters like viscosity, equilibrium surface tension and the surface relaxation time are shown for water, glycerol (95% concentration) and Silicone oil in Table 11.1. We should note here that the right hand side of (11.6) is really an approximation to the mass flux between the bulk and free surface, which is valid if ϱ^s is close to its equilibrium value ϱ^s_e. In addition to the above mass balance of the surface density we must take account of this process in the boundary conditions of

the flow by prescribing

$$\varrho^s(\mathbf{u}-\mathbf{w})\cdot\mathbf{n}=\frac{\varrho^s-\varrho^s_e}{\tau}. \tag{11.7}$$

To relate the velocity gradients with the surface tension gradient we have[3]

$$(1+4\alpha\beta)\nabla\sigma=4\beta(\mathbf{I}-\mathbf{nn})\cdot(\mathbf{w}-\mathbf{u}), \tag{11.8}$$

where α and β are phenomenological constants. The equation of state relates the surface tension to the surface density[4] ϱ^s by

$$\sigma=\sigma(\rho^s)=\left(\frac{\sigma_e}{\varrho^s_e(\varrho^s_0-\varrho^s_e)}\right)[\varrho^s(\varrho^s_0-\varrho^s)], \tag{11.9}$$

where ϱ^s_0 is a constant corresponding to the value of the surface density that gives zero surface tension. The equilibrium surface tension and surface density of the free-surface are σ_e and ϱ^s_e respectively, where $\varrho^s_0>\varrho^s_e$. Therefore, $\sigma=\sigma_e$ when $\varrho^s=\varrho^s_e$, and $\sigma=0$ when $\varrho^s=\varrho^s_0$. Equation (11.9) is also chosen so that $\sigma=0$ when $\varrho^s=0$ (see Fig. 11.1). (Note that the equation of state (11.9) is quadratic in ϱ^s. This quadratic equation of state was introduced in Shikhmurzaev (2005), replacing a simpler linear equation of state in earlier papers.) Thus the surface tension σ will in general tend towards its equilibrium value σ_e, causing surface tension gradients and a Marangoni-like flow. If $\tau=0$ (so that the interface 'relaxes' instantaneously) in equations (11.3) - (11.9) then they become identical to the classical boundary conditions of viscous flow.

[3]Since we have a variable surface tension, we must have a tangential stress equation of the form

$$\text{tangential stress}+\nabla\sigma=0,$$

where the tangential stress can be written as a *constant*$\times(\mathbf{w}_{||}-\mathbf{u}_{||})$. In this case the subscripts represent tangential components and the constant is a function of the phenomenological coefficients α and β which describe how the interface responds to the surface tension gradient.

[4]This equation of state assumes that the process is barotropic (or isothermal) and states that the surface tension of the surface is coupled with the degree of rarefaction (or compression) within the interfacial layer.

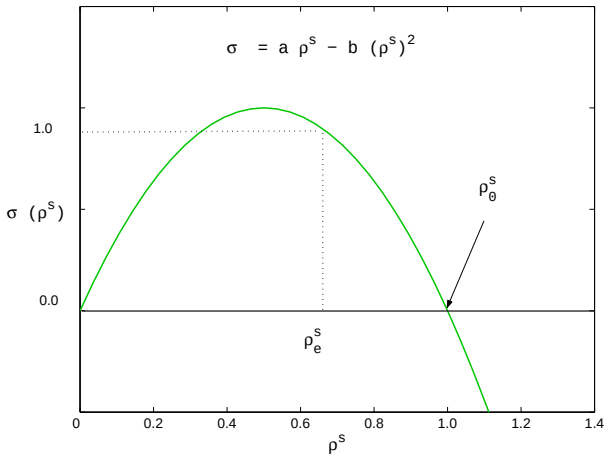

Figure 11.1: The dependence of the interfacial surface tension σ on the surface density ρ^s. As the rate of creation of 'fresh' free surface area increases (due to, for example, stretching of the interface) the surface density decreases and hence the surface tension is driven away from its equilibrium value σ_e.

The interface formation model is still controversial and is yet to be widely accepted. Indeed Eggers and Evans (2004) claim that the interface formation model is physically invalid, and especially the equation of state (11.9) which gives the surface tension in terms of a surface density (there is a reply to this in Shikhmurzaev and Blake (2004)). Also there is disagreement between these two groups over the mechanism which governs the surface tension relaxation time τ. In Eggers and Evans (2004) it is claimed that τ is of the order of 10^{-18} seconds, which they obtain from the observation that force is transmitted with the speed of light. In Shikhmurzaev and Blake (2004), it is claimed that the surface tension relaxation process instead scales with diffusion, giving the above estimates for τ of 10^{-9} seconds or greater.

Clearly more testing against experimental data is required until the model can be widely accepted (if accurate), or rejected (if inaccurate). Blake *et al.* (1999, 2002) provided experimental data in support of the interface formation model in the context of curtain coating, though their approach was criticised by Eggers & Evans (2004). Applications of the interface formation model to other flow situations offers some hope that

arguments for or against the interface formation model can be put to rest once and for all. Liquid jets on the microscopic scale present a promising way forward. It is hoped that they will provide a scenario quite different from curtain coating against which to consider this theory.

11.2 Microjets

We now consider a liquid jet emerging from a nozzle with a typical diameter a (which is of the order of micrometers or smaller). We use the equations from the previous section and non-dimensionalise velocities using the exit speed U of the jet upon leaving the orifice. For radial lengths we use the radius of the orifice a however for axial direction we shall use the (unknown) length of the jet s.

The equations are non-dimensionalised with respect to the scales for time, pressure, surface tension and surface density $s/U, \rho U^2, \sigma_e$ and ϱ_e^s respectively. The non-dimensionalised axi-symmetric polar coordinate system is described by (r, z), where r is the radial coordinate and z the axial coordinate. The z-axis points upstream and the origin of the coordinate system is taken to be at the centre of the orifice. The velocity of the liquid is $\mathbf{u} = u\mathbf{e_z} + v\mathbf{e_r}$, where $\mathbf{e_z}$ and $\mathbf{e_r}$ are the unit vectors in the z and r directions respectively. The free-surface is at $r = R(z,t)$ where t is the non-dimensional time. The surface velocity is $\mathbf{w} = u^s\mathbf{e_z} + v^s\mathbf{e_r}$. All quantities will be taken to be non-dimensional. If also we take the surface velocity as $\boldsymbol{w} = u^s\boldsymbol{e_z} + v^s\boldsymbol{e_r}$ using the slender jet expansions introduced by Eggers & Dupont (1994), we have

$$[u, u^s, p](r,z,t) = [u_1, u_1^s, p_1](z,t) + \varepsilon^2[u_2, u_2^s, p_2](r,z,t) + O(\varepsilon^4),$$

$$[v, v^s](r,z,t) = \varepsilon[v_1, v_1^s](z,t) + \varepsilon^3[v_2, v_2^s](r,z,t) + O(\varepsilon^5),$$

$$[R, \sigma, \varrho^s](r,z,t) = [R_1, \sigma_1, \varrho_1^s](z,t) + \varepsilon[R_2, \sigma_2, \varrho_2^s](r,z,t) + O(\varepsilon^2).$$

Then substituting into our equations we get

$$u_{1t} + u_1 u_{1z} = \frac{\sigma_{1z}}{We}\left(\frac{2}{R_1} - \kappa\right) - \frac{\sigma_1 \kappa_z}{We} + \frac{3u_{1zz}}{\widehat{\mathcal{R}e}} + \frac{6R_{1z}u_{1z}}{R_1 \widehat{\mathcal{R}e}}, \tag{11.10}$$

$$\kappa = \frac{1}{R_1}\left(1 + \varepsilon^2 R_{1z}^2\right)^{-1/2} - \varepsilon^2 R_{1zz}\left(1 + \varepsilon^2 R_{1z}^2\right)^{-3/2}, \tag{11.11}$$

$$R_{1t} + u_1 R_{1z} + \frac{1}{2} R_1 u_{1z} = \widehat{\mathcal{L}}\left(\varrho_1^s - 1\right), \tag{11.12}$$

$$\varrho_{1t}^s + \varrho_{1z}^s u_1^s + \varrho_1^s u_{1z}^s + \frac{\varrho_1^s v_1^s}{R_1} = \frac{1}{\widehat{\mathcal{Y}}}\left(1 - \varrho_1^s\right), \tag{11.13}$$

$$\sigma_1 = \varrho_1^s(1 + \lambda - \lambda \varrho_1^s), \tag{11.14}$$

and

$$u_1^s = u_1 + \widehat{\mathcal{A}}\sigma_{1z}, \qquad v_1^s = R_{1t} + u_1^s R_{1z}, \tag{11.15}$$

where the constants are given by

$$\widehat{\mathcal{R}e} = \frac{sU}{\nu}, \quad We = \frac{\rho U^2 a}{\sigma_e}, \quad \widehat{\mathcal{Y}} = \frac{\tau U}{s}, \quad \widehat{\mathcal{A}} = \frac{(1 + 4\alpha\beta)\sigma_e}{4\beta s U},$$
$$\varepsilon = \frac{a}{s} \quad \widehat{\mathcal{L}} = \frac{\varrho_e^s s}{\tau U \varrho^s a}, \quad \lambda = \frac{\varrho_e^s}{\varrho_0^s - \varrho_e^s} \tag{11.16}$$

11.2.1 Linear Analysis

In Decent (2006) two separate scalings for s were examined and here, we shall only examine the first of these. In the first case, s was taken to be equal to the (unknown) break-up length of the jet, with the assumption that $a/\left(\tau U\right) = O(1)$. In the second case, the axial length scale was taken to be $s = \tau U$, with the assumption that $a \ll \tau U$. In both these cases a small aspect ratio $\varepsilon = a/s \ll 1$ was used so as to enable the assumption of a slender jet. For the first case s was eliminated from the problem formulation, so that the results became independent of the unknown jet break-up length (so long as the break-up length was much greater than a). The classical constant surface tension formulation was obtained when $a \gg \tau U$.

Equations (11.10)-(11.15) have a steady state solution given by

$$u_1 = R_1 = u_1^s = \varrho^s = \sigma = 1, \qquad p = 1/We \quad \text{and} \quad v_1 = v_1^s = 0, \tag{11.17}$$

which corresponds to a uniform straight jet having constant surface tension along the jet. A temporal linear analysis can be considered about the steady state, such that

$$u_1 = 1 + \delta\widehat{u}(z,t)\exp\left(ik\overline{z} + \omega\overline{t}\right) + c.c. + O(\delta^2), \tag{11.18}$$

$$R_1 = 1 + \delta\widehat{R}(z,t)\exp\left(ik\overline{z} + \omega\overline{t}\right) + c.c. + O(\delta^2), \tag{11.19}$$

$$\sigma_1 = 1 + \delta\widehat{\sigma}(z,t)\exp\left(ik\overline{z} + \omega\overline{t}\right) + c.c. + O(\delta^2) \tag{11.20}$$

and

$$\varrho_1 = 1 + \delta\widehat{\varrho}(z,t)\exp\left(ik\overline{z} + \omega\overline{t}\right) + c.c. + O(\delta^2), \tag{11.21}$$

where δ is a small amplitude, k is the wavenumber of the travelling wave, ω is the growthrate and $c.c$ denotes complex conjugates. In addition we require the condition $0 < \delta \ll \varepsilon \ll 1$. Also we have small length and time scales given by $\overline{z} = z/\varepsilon$ and $\overline{t} = t/\varepsilon$. Substitution of these expansions into (11.10)-(11.15) and taking the limit $\varepsilon \to 0$ gives an eigenvalue relationship between the wavenumber k and the growthrate ω. Decent (2006) has examined the expression for ω to find the value of k which makes $Re(\omega)$ the largest, finding that for $\mathcal{Y} \to 0$, $\mathcal{R}e \to \infty$ and $Oh \to 0$ (the inviscid limit)

$$\begin{aligned} k^* &= \frac{1}{\sqrt{2}} + \mathcal{Y}\left(\frac{1-\lambda}{8\sqrt{We}}\right) \\ &+ \mathcal{Y}^2\frac{\sqrt{2}\,(1-\lambda)}{128We}\left(8\sqrt{2We}\mathcal{A}\,(1-\lambda) - 12\sqrt{2We}\mathcal{L} + 8We\mathcal{A}\mathcal{L} - 3\lambda - 1\right) + O(\mathcal{Y}^3). \end{aligned} \tag{11.22}$$

For $\mathcal{Y} \to 0$ and $We \to 0$, with $\mathcal{Y}/\sqrt{We} \to 0$,

$$k^* = \frac{1}{\sqrt{2}} + \mathcal{Y}\left(\frac{1-\lambda}{8\sqrt{We}}\right) + \mathcal{Y}^2\frac{\sqrt{2}\,(3\lambda+1)\,(\lambda-1)}{128We} + O\left(\frac{\mathcal{Y}^3}{We^{3/2}}\right), \tag{11.23}$$

where the non-dimensional constants have now been slightly rescaled (in order to eliminate s) and are given by

$$\mathcal{R}e = \frac{aU}{\nu},\ \ \mathcal{Y} = \frac{\tau U}{a},\ \ \mathcal{A} = \frac{(1+4\alpha\beta)\,\sigma_e}{4\beta aU},\ \ \mathcal{L} = \frac{\varrho_e^s}{\tau U\varrho^s}. \tag{11.24}$$

The eigenvalue relation was also solved computationally for O(1) values of the parameters in Decent (2006) and the result discussed.

11.2.2 Case 1: Periodically forced liquid jet.

In this case we shall simulate a disturbance at the orifice where the initial conditions are chosen so that we have a uniform velocity, surface density and radius along the jet.

We now rewrite our problem using the constants in (11.24) instead of (11.16) so as to remove s from all our non-dimensional constants except ε. We then have

$$u_{1t} + u_1 u_{1z} = \frac{\sigma_{1z}}{We}\left(\frac{2}{R_1} - \kappa\right) - \frac{\sigma_1 \kappa_z}{We} + \frac{3\varepsilon u_{1zz}}{\mathcal{R}e} + \frac{6\varepsilon R_{1z} u_{1z}}{R_1 \mathcal{R}e}, \tag{11.25}$$

$$\kappa = \frac{1}{R_1}\left(1 + \varepsilon^2 R_{1z}^2\right)^{-1/2} - \varepsilon^2 R_{1zz}\left(1 + \varepsilon^2 R_{1z}^2\right)^{-3/2}, \tag{11.26}$$

$$R_{1t} + u_1 R_{1z} + \frac{1}{2} R_1 u_{1z} = \frac{\mathcal{L}}{\varepsilon}\left(\varrho_1^s - 1\right), \tag{11.27}$$

$$\varrho_{1t}^s + \varrho_{1z}^s u_1^s + \varrho_1^s u_{1z}^s + \frac{\varrho_1^s v_1^s}{R_1} = \frac{1}{\varepsilon \mathcal{Y}}\left(1 - \varrho_1^s\right), \tag{11.28}$$

$$\sigma_1 = \varrho_1^s(1 + \lambda - \lambda \varrho_1^s), \tag{11.29}$$

and

$$u_1^s = u_1 + \varepsilon \mathcal{A} \sigma_{1z}, \qquad v_1^s = R_{1t} + u_1^s R_{1z}, \tag{11.30}$$

where $\mathcal{R}e$, $\mathcal{Y}$, $\mathcal{A}$, and $\mathcal{L}$ are given by (11.24).

We can attempt to solve the system of equations (11.25)-(11.30) numerically using the same method of finite differences which we used for spiralling jets in the previous chapter. We will again take a uniform spatial grid of size dz such that $z \in [0, \ell]$ where

$z = 0$ represents the nozzle and $z = \ell$ is the (numerical) length of the jet. As our initial condition we shall use the steady state given by (11.17) which corresponds to a uniform straight jet (this was also mentioned in Decent (2006)). Furthermore we impose the upstream boundary conditions at the nozzle

$$u(0,t) = 1 + \delta \sin(\kappa t) \quad \text{and} \quad R(0,t) \; = \varrho^s(0,t) \; = 1$$

where δ is some arbitrarily chosen amplitude of the initial velocity disturbance at the orifice and κ is a similarly chosen frequency of the disturbance. The discretized equations are then solved using the Richtmyer scheme until $R(z,t)$ reaches some required minimum when the program is halted. An example for certain parameter ranges using this method is shown in Fig. 11.2 where we have taken ε to be equal to 0.01.

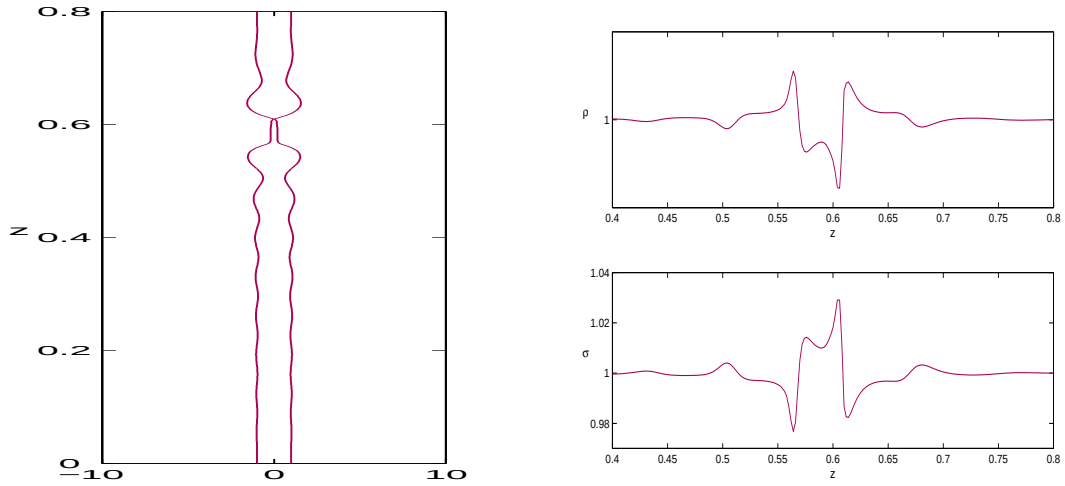

Figure 11.2: The profile of a liquid jet at 'breakup' when the theory of interface formation is used. The profiles of the surface density and surface tension are also shown. In this case the non-dimensional constants were taken as $\mathcal{R}e = 3000$, $We = 10$, $\delta = 0.01$, $\mathcal{Y} = 1$, $\mathcal{A} = 1$, $\mathcal{L} = 0.0001$ and $\kappa = 0.89$.

11.2.3 Case 2: Instability of a stationary column

In this case we shall take a stationary column of fluid and then examine its instability. We do a similar thing to the previous case and remove s from all our non-dimensional

constants appearing in (11.10)-(11.15) but in addition we consider a re-scaling of the equations so that we have the small length and time scales given by $\overline{z} = z/\varepsilon$ and $\overline{t} = t/\varepsilon$. The overall outcome is a set of equations with the non-dimensional constants independent of s and without ε;

$$u_{1\overline{t}} + u_1 u_{1\overline{z}} = \frac{\sigma_{1\overline{z}}}{We}\left(\frac{2}{R_1} - \kappa\right) - \frac{\sigma_1 \kappa_{\overline{z}}}{We} + \frac{3u_{1\overline{z}\overline{z}}}{\mathcal{R}e} + \frac{6R_{1\overline{z}}u_{1\overline{z}}}{R_1\mathcal{R}e}, \tag{11.31}$$

$$\kappa = \frac{1}{R_1}\left(1 + R_{1\overline{z}}^2\right)^{-1/2} - R_{1\overline{z}\overline{z}}\left(1 + R_{1\overline{z}}^2\right)^{-3/2}, \tag{11.32}$$

$$R_{1\overline{t}} + u_1 R_{1\overline{z}} + \frac{1}{2}R_1 u_{1\overline{z}} = \mathcal{L}\left(\varrho_1^s - 1\right), \tag{11.33}$$

$$\varrho_{1\overline{t}}^s + \varrho_{1\overline{z}}^s u_1^s + \varrho_1^s u_{1\overline{z}}^s + \frac{\varrho_1^s v_1^s}{R_1} = \frac{1}{\mathcal{Y}}\left(1 - \varrho_1^s\right), \tag{11.34}$$

$$\sigma_1 = \varrho_1^s(1 + \lambda - \lambda\varrho_1^s), \tag{11.35}$$

and

$$u_1^s = u_1 + \mathcal{A}\sigma_{1\overline{z}}, \qquad v_1^s = R_{1\overline{t}} + u_1^s R_{1\overline{z}}, \tag{11.36}$$

where again the non-dimensional constants $\mathcal{R}e$, $\mathcal{Y}$, $\mathcal{A}$, and $\mathcal{L}$ are given by (11.24).

We use a different numerical method to solve the above set of equations, namely we use a spatial domain $z = [0, L_p]$ where L_p is the length of one period of the jet (non-dimensionalised with respect to the jet radius). The spatial domain is uniform having n

grid points with the boundary conditions requiring periodicity so that

$$u(0,t) = u(L_p,t) \quad \text{and} \quad R(0,t) = R(L_p,t).$$

Unlike the previous method, the velocity cannot be determined in terms of an exit velocity. We therefore define U as $U^2 = \sigma_e/a\rho$ so that $We = 1$. This allows us to base our velocity scale on surface tension and inertia. In addition if we use the estimates from Blake *et al.* (2002) we have $\alpha = \mu/\delta l$ and $\beta = 1/\alpha$ where δl is the physical thickness of the free-surface interface, which is usually about 10^{-9} metres for most liquids. In this case we have the non-dimensional constants in (10.18) as

$$\mathcal{A} \approx \frac{5\sigma_e \delta l}{4\mu a U}, \quad \mathcal{L} \approx \frac{\lambda \delta l}{\tau U(\lambda+1)}. \tag{11.37}$$

where, for water, we have $\sigma_e = 0.073 Nm^{-1}$, $\rho = 10^3 kgm^{-3}$ and $\mu = 10^{-3} kgm^{-1}s^{-1}$. If we are to investigate the effects of large values of $\mathcal{Y}$ (as opposed to small values, which in the limit of $\mathcal{Y} \to 0$ reduce to the standard model) we will require fluids with very large viscosities and/or jets with very small radii. Fluids like Silicone Oil provide the best opportunity to explore the effects of interface formation phenomena in liquid jets, since such fluids can have viscosities up ten million times greater than water. Using the estimates for material parameters given in Table 11.1 for Silicone Oil we can estimate values for $\mathcal{Y}$ for different values of orifice radius a (see Table 11.2). We see that as the typical radius of the orifice decreases we have much larger values of the parameter $\mathcal{Y}$.

The equations are taken forward in time using a finite difference method (a variant of the two-step Lax-Wendroff method known as *McCormack's* method) on a uniform mesh. In our simulations we considered a periodic jet with the period chosen as 10 dimensionless length units. The radius was perturbed slightly to induce instability and

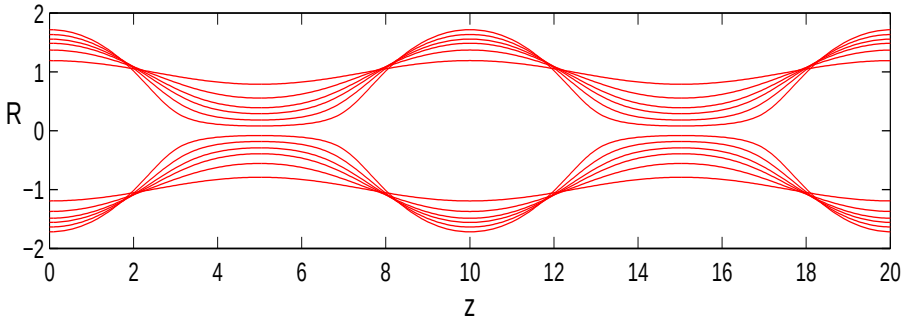

Figure 11.3: The profile of a liquid jet using the theory of interface formation for different non-dimensional times. The profile is calculated over two non-dimensional wavelengths for the parameters $\mathcal{R}e = 0.134$, $We = 1$, $\mathcal{Y}$=0.06, $\lambda = 2$, $\mathcal{A}$=1.69×10^{-6} and $\mathcal{L}$=1.1×10^{-4}.

the initial conditions were given by

$$R(\overline{z}, 0) = 1 + 0.05\cos(2\pi\overline{z}/10), \quad \varrho^s(\overline{z}, 0) = 1, \quad \text{for } \overline{z} \in [0, 10].$$

The initial velocities were taken to be zero.

11.3 Results and Discussion

In Case 1 we numerically solve (11.25)-(11.30) subject to having ε equal to 0.01 and then plot the radius, density and surface tension along the jet in Fig. 11.2 (we note that this method simulates a jet which has a periodic disturbance applied at the orifice). Pinch-off is assumed to take place once the radius has reached some minimum (chosen here as 5% of the unperturbed radius). The neck portion of the jet between droplets can be seen to experience a decrease in the surface density leading to an increase in the surface tension. The ends of the neck portion of the ligament between the droplets experiences an sharp fall in surface tension. In this case surface tension driven flow will act to bring fluid away from the ligament towards the ends where pinch-off takes place which is against the normal mechanism for pinch-off.

In Fig. 11.3 we consider Case 2 (i.e., Eqs. (11.31)-(11.36)) and evaluate the profile

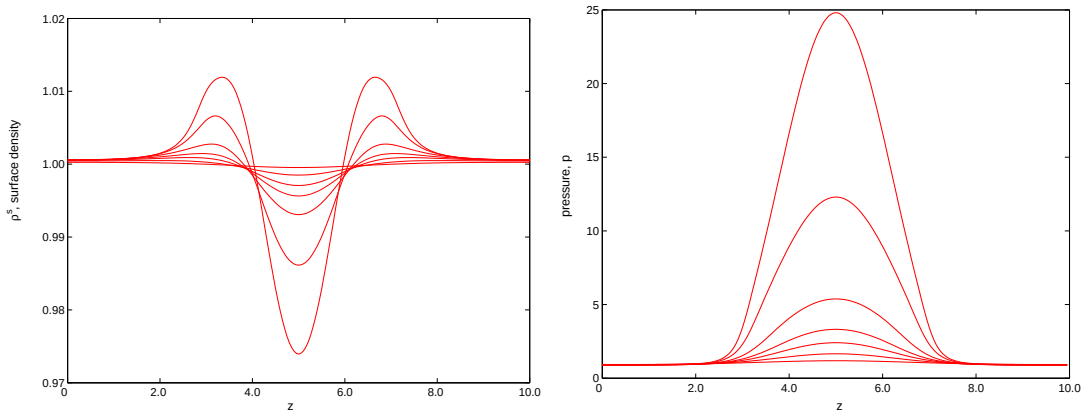

Figure 11.4: The surface density (left) and pressure (right) distribution (over one wavelength) along the jet for the non-dimensional times 102.5, 152.5, 172.5, 182.5, 192.5, 202.5 and 206.85. The surface density decreases where the liquid jet thins but increases on either side. The pressure increases with time.

a	$\mathcal{Y}$
$10^{-2}m$	4.47×10^{-3}
$10^{-4}m$	4.47
$10^{-5}m$	141.35
$10^{-6}m$	4470

Table 11.2: Estimates of the value of $\mathcal{Y}$ for Silicone oil for different jet radii a. The parameters used are those given in Table 11.1

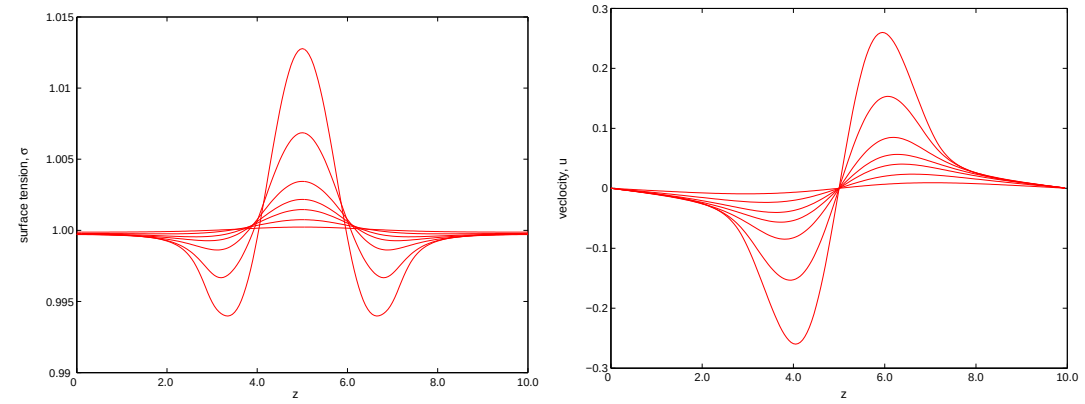

Figure 11.5: The surface tension (Right) and velocity (Left) distribution (over one wavelength) along the jet for the non-dimensional times 102.5, 152.5, 172.5, 182.5, 192.5, 202.5 and 206.85. The surface tension increases where the liquid jet thins but decreases on either side.

of a liquid jet over two non-dimensional wavelengths (here we take one wavelength to be equal to 10 jet radii). The parameters shown in Fig. 11.3 correspond to a glycerol 95% w/c jet of radius 100 μm. The jet radius is seen to decay to form a thin ligament between two droplets as shown. In Fig. 11.4 we show the corresponding surface density and pressure distribution along the jet for different times before breakup. Clearly the surface density decreases where the jet radius is smallest, however there is a small increase in surface density towards the ends of the ligaments joining the neck to the droplets. Furthermore, the pressure can be seen to increase rapidly at the position where the jet radius reaches a minimum. In Fig. 11.5 we plot the corresponding surface tension and axial velocity. It can be seen that the surface tension behaves in the opposite sense to the surface density, with a large increase in surface tension where the jet reaches a minimum and a decrease in surface tension (from equilibrium) on either side of this.

In Fig. 11.6 we show the profile of a 0.1μm water-glycerol liquid jet (with ten times the dynamic viscosity of water) at pinch-off. There is a noticeable difference between the standard model prediction and that produced using interface formation. When interface formation is included we see a more 'tear' drop shaped drop which is reminiscent of the breakup of highly viscous fluids. The pressure along the thread under the two models at the point of rupture is shown in Fig. 11.7 where it can be seen that the pressure using the interface formation is significantly lower along the thread, and particularly close to the point of rupture. This result is promising since for liquid threads in the nanometer range a more symmetrical profile at breakup is observed in molecular simulations (see Fig. 11.8). Such simulations do not agree with the results produced using the standard lubrication equations, whilst the stochastic lubrication equations which are formed by introducing a stochastic term into the evolution equations do a much better job.

The minimum radius and the corresponding pressure at this point for different times to breakup are shown in Fig. 11.9 and 11.10. Two outstanding features are readily ob-

servable, firstly, the time taken for the liquid thread to rupture is smaller and secondly the corresponding pressure at breakup is higher under the standard model as compared with the interface formation model. This is consistent with the qualitative description of the theory of interface formation and agrees with the findings of Shikhmuzaev (2005). we show that the pressure at the point of rupture of a liquid thread remains finite as $R \to 0$ when using the theory of interface formation in Appendix F.

In Fig. 11.11 we show a plot of the wavenumber $k = 2\pi/L_p$ against the non-dimensional time taken to breakup. The most unstable wavenumber k^*, at which the breakup time is the shortest, for the standard model is about $k^* \approx 0.32$ whilst using the interface formation model we have $k^* \approx 0.23$. This is in agreement with the findings of Decent (2006) where the most unstable wavenumber was seen to decrease as the parameter $\mathcal{Y}$ was increased (which can be viewed as the reduction in the initial jet radius and/or an increase in the relaxation time τ). The most unstable wavenumber calculated using the classical viscous theory for the parameters in Fig. 11.11 is $k^* = 0.197$. In Fig. 11.12 we show the time evolution of a 100nm water/glycerol jet over two wavelengths.

Figures 11.13 and 11.14 show photographs of two drops slowly being pulled apart by a syringe. The syringe has a typical diameter of 5mm and the high speed camera used in these experiments was capable of 4796 frames a second with an exposure time of 16μs. These pictures were taken by Jeremy Marston in the School of Chemical Engineering and in the cases shown (for water and Silicone oil respectively) they show the formation of microjets just before pinch-off. In the case of Silicone oil the thread formed before breakup is considerably longer and the appearance of a wavelike profile can be observed in frames before pinch-off take place and the thread snaps. Such pictures, crude as they are, provide a real chance that the effects of interface formation to the rupture of a liquid thread will soon be experimentally verified.

It is the view of this author that, whilst one dimensional nonlinear simulations can

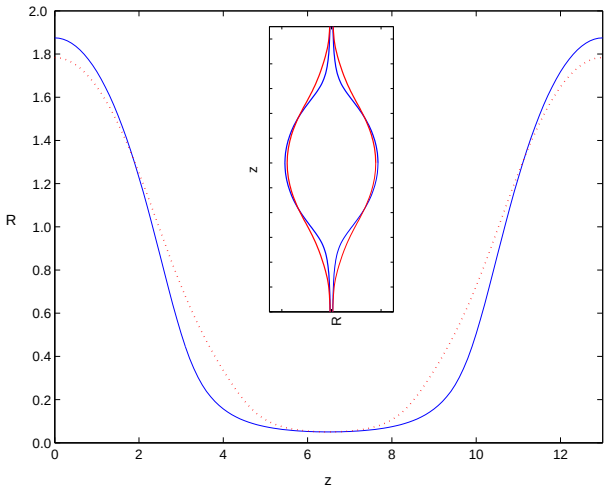

Figure 11.6: The profile at breakup of 0.1μm water-glycerol jet using the standard model and with the theory of interface formation. Here the parameters used are $\mathcal{R}e$=0.179, We=1.0, $\mathcal{A}$ = 2.2e-3, $\mathcal{L}$ = 5e-4, $L_p = 13$ and $\mathcal{Y} = 14.5$. The solid line (which appears as a blue line in colour) represents the profile calculated using the standard model. The inset shows the drop profile at breakup from which it can be seen that the interface formation model allows for a more 'tear drop' profile which is common in highly viscous jets.

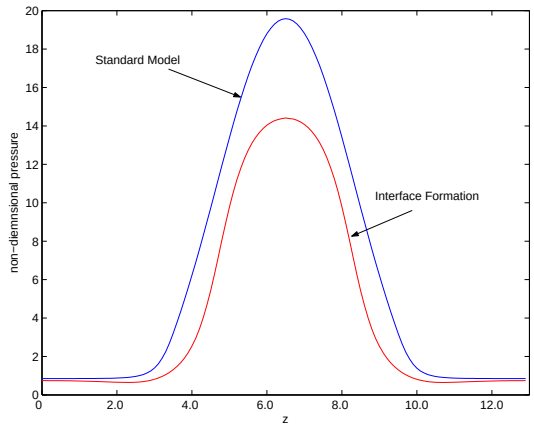

Figure 11.7: The pressure around the point of rupture for a liquid thread using the standard model and the theory of interface formation at the the time of pinch-off. Clearly the pressure along the thread, and particularly at the pinch-off point is significantly lower using the theory of interface formation. The variables used are the same as in Fig. 11.6.

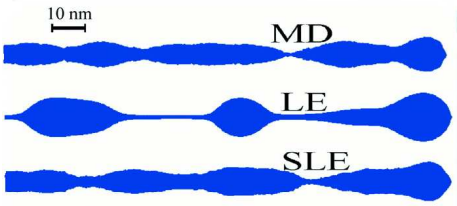

Figure 11.8: The shape of liquid jets using molecular simulation (MD), the standard lubrication equations (LE) and the stochastic lubrication equations (SLE). Clearly the use of a stochastic term in the lubrication equations does a better job of capturing the 'double-cone' shaped neck at pinch-off observed using molecular simulations. Picture taken from Moseler and Landman (2000).

give an indication of differences between the standard model and the interface formation model, it is necessary to move to two-dimensional or even three dimensional schemes in order to truly capture the intricate dynamics near rupture[5]. Since the effects of interface formation become very important as the jet radius shrinks (which inevitably leads to large pressures) it is perhaps unrealistic to expect an explicit scheme on a fixed grid to provide the necessary resolution to fully capture the last stages of breakup. In addition, in order to investigate extremely highly viscous fluids, the time step (for explicit schemes) must necessarily be very small. This leads to exceptionally long computing times. For these reasons a detailed numerical investigation into the dynamics of rupture incorporating the theory of interface formation will probably need to resort to implicit schemes (which have no such constraints upon the time step) along with adaptive meshes (to resolve regions of interest near the point of rupture).

It is hoped that future work will examine these models in further detail with more numerical results. At the time of writing this thesis Jeremy Marston is currently working with S. T. Thoroddsen at the National University of Singapore using a high speed camera capable of capturing a million frames a second (which is the only one of its kind in the world) to observe the dynamics of rupture for two drops which are slowly pulled apart.

[5]especially since by their very nature one dimensional models become ineffective close to pinch-off regions where radial effects become important and cause any 1D approximation to fail.

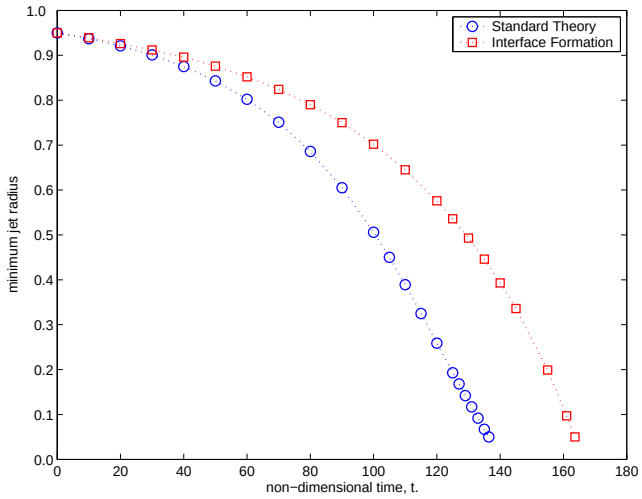

Figure 11.9: The evolution of the minimum radius for a liquid jet (water/glycerol) of initial radius 0.1μm having a dynamic viscosity ten times that of water. Here we have $\mathcal{R}e$ =0.179, We=1.0, $\mathcal{A}$ = 2.2e-3, $\mathcal{L}$ = 5e-4 and $\mathcal{Y}$ = 14.5. We see that the time to breakup is longer under the interface formation model and that differences between the standard model and the theory of interface formation become more noticeable as the jet radius shrinks.

If the outcome of such experiments suggests that interface formation is important in the last stages of pinch-off it is hoped that information regarding the parameter space where such effects become important will help in developing numerical simulations.

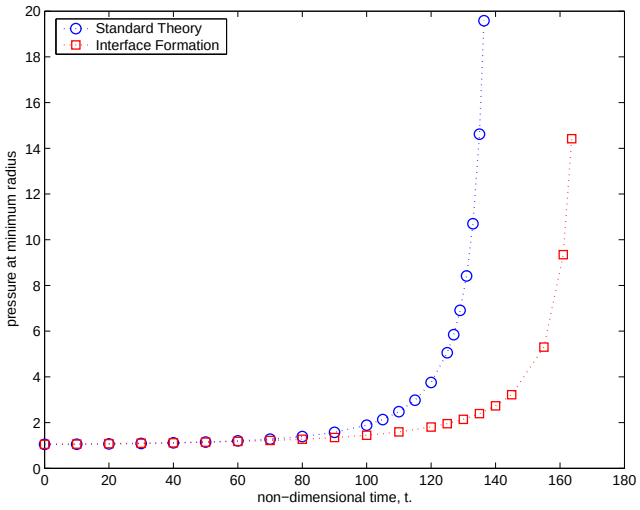

Figure 11.10: The evolution of the corresponding pressure at the minimum jet radius for a liquid jet (water/glycerol) of initial radius 0.1μm having a dynamic viscosity ten times that of water. Here we have $\mathcal{R}e$ =0.179, We=1.0, $\mathcal{A}$ = 2.2e-3, $\mathcal{L}$ = 5e-4 and $\mathcal{Y}$ = 14.5. We see that the pressure at the minimum radius (i.e., the breakup point) remain significantly smaller for the theory of interface formation than under the standard jet model. This offers the hope that with a scheme of greater accuracy it might be possible to show that the pressure remains finite (as opposed to reaching infinity under the standard model) as the jet radius shrinks to infinitesimal lengths.

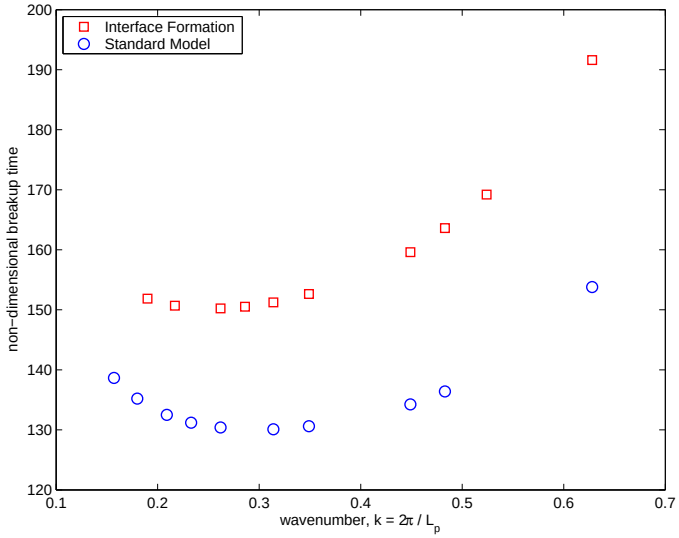

Figure 11.11: A plot of the non dimensional breakup times against wavenumber for the standard model and the present theory of interface formation. The most unstable wavenumber is the value of $k = k^*$ at which the breakup time is the smallest. It can be seen that for the standard model we have $k^*_{ST} \approx 0.32$ whilst for the theory of interface formation we have $k^*_{IF} \approx 0.23$. Here we have $\mathcal{R}e$=0.179, We=1, $\mathcal{A}$=0.0022, $\mathcal{L}$=0.0005 and $\mathcal{Y} = 14.5$.

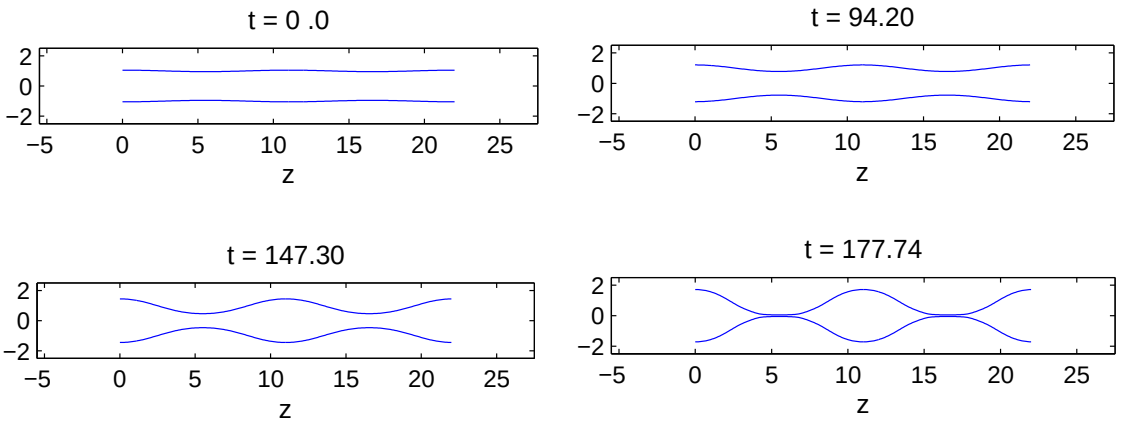

Figure 11.12: The profiles (over two wavelengths) at different non-dimensional times for a 100 nm water-glycerol jet using the theory of interface formation. Here the parameters used are $\mathcal{R}e$=0.179, We=1.0, λ = 2.0, $\mathcal{A}$ = 2.2e-3, $\mathcal{L}$ = 5e-4 and $\mathcal{Y}$ = 14.5. The vertical axes in each figure represent the non-dimensional radii of the thread.

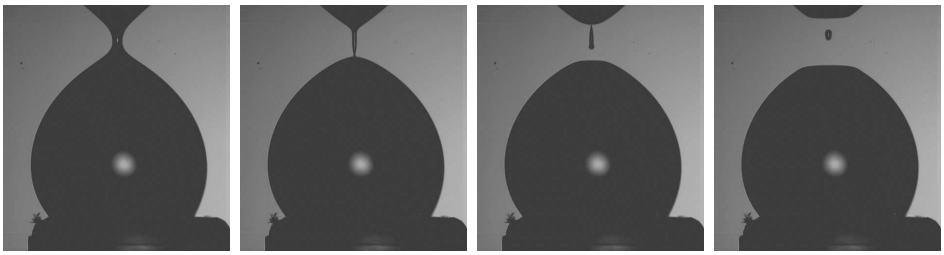

Figure 11.13: Microjet formation as two 'drops' are slowly pulled apart. In this case the working fluid is water and the time interval between pictures is approximately 218 μs. The drops are being pulled apart by using a syringe (having a diameter of 5mm) which can be seen in the bottom portion of the picture.

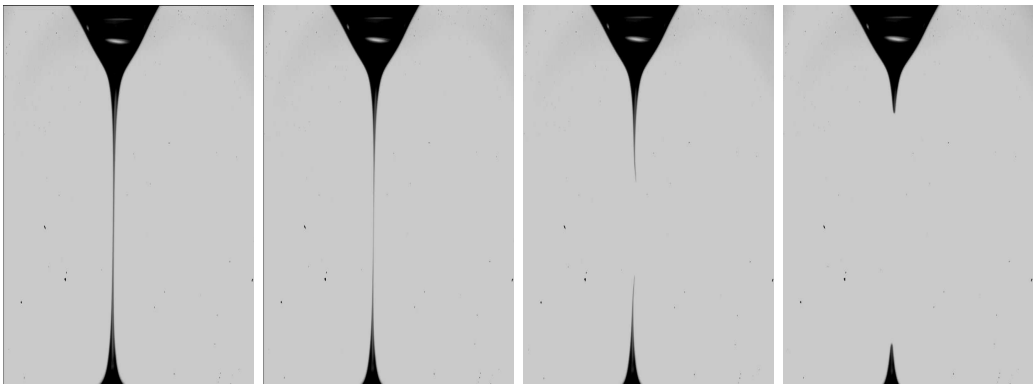

Figure 11.14: In this case we have a jet forming when two drops of silicone oil are pulled apart. Clearly the jet produced is much longer than in the case of water. In the penultimate picture the formation of a very fine thread of non-uniform thickness can be seen. In subsequent pictures the thread breaks and recoils towards the drop.

Chapter 12

Thermo-capillary effects in viscous liquid jets

In the preceding chapter we considered the evolution of a thread of fluid having a typical diameter in the micrometer and nanometer range. We incorporated the theory of interface formation into the standard slender jet equations (thereby introducing an expression for the surface density of the fluid) to investigate the effects of the surface relaxation on the growth and size of unstable waves along the free surface. The small but finite time required for the surface to 'relax' to its original state, which forms the crux of the theory of interface formation, is strongly dependent upon the viscosity of the fluid. As such, noticeable effects of interface formation on the breakup of liquid jets are highly dependent upon material properties of the fluid in addition to externally imposed conditions.

In this chapter our aim is to examine liquid jets having externally imposed thermal gradients along the free surface. This process of thermally modulating the free surface of a liquid jet is amongst the most recent and novel methods employed to control the rupture of a liquid jet. Whilst the technique is still in its infancy, it nevertheless has numerous applications to ink-jet printing (see Furlani (2006)) and micro-fabrication. The method is characterized by having a heating mechanism (usually MEMS based resistive

heating elements) located at the nozzle from which a liquid jet emerges. The heater is specially designed to allow for a controlled means of heating the surface of the liquid jet as it passes through the nozzle. Since surface tension is temperature dependent, downstream advection of thermal energy leads to surface tension gradients. The formation of tangential stresses, which occur as a consequence of variable surface tension, are balanced by inertia within the fluid. The presence of non-zero tangential stresses lead to the induction of Marangoni type flows, and cause flow of liquid towards regions with higher surface tension. In general it is found, that for most fluids, the surface tension decreases with increasing temperature (so that $d\sigma/dT < 0$), consequently hotter regions have a lower surface tension than cooler regions. Since Marangoni type flows are directed towards higher surface tension regions, there is a generation of flow from hotter regions to cooler regions. The ensuing flows within the jet cause a distortion of the free surface, leading to thinning of the jet in hot regions and swelling in cooler regions. In this way the induction of Marangoni flows can greatly affect the eventual breakup of a liquid jet and subsequent droplet formation[1].

Thermocapillary effects in liquid threads or sheets are still poorly understood but are now increasingly a topic of research interest. The first such works on the instability of non-isothermal jets, with temperature dependent surface tension, were those of Bauer (1984) and Xu and Davis (1985), both of which were linear stability investigations. Bauer (1984) considered a Stokes flow situation with an axially periodic temperature distribution to the liquid jet surface. He found that the breakup could be achieved through oscillatory temperature gradients along the jet. Xu and Davis (1985) considered a linear temperature distribution along the jet and using a lubrication type analysis concluded that capillary instabilities could be impeded, or even suppressed, by surface wave instabilities caused

[1]When temperature gradients act along the interface (i.e., parallel to it), fluid motion is always induced irrespective of the magnitude of the imposed temperature gradient. This is in sharp contrast to temperature gradients perpendicular to the free surface, where a critical or threshold, temperature is required to generate motion.

by surface tension gradients. Faidley and Panton (1990) were the first to control breakup of a liquid jet by using a fast responding heater at the nozzle to modulate the surface tension. They concluded that the Rayleigh mode was dominant and that thermal effects were unimportant to the growth of disturbances. However, Nahas and Panton (1991) showed that a CO_2 laser beam could be used, with appropriate laser intensity, to eliminate the primary surface disturbance, which suggested that the heating elements used by Faidley and Panton were unable to produce sufficient heating at the nozzle. Mashayek and Ashgriz (1994) investigated the breakup of a capillary jet subject to a spatially periodic ambient temperature. They also considered the application of an initial thermal disturbance to the surface of a liquid jet while the ambient temperature was kept spatially and temporally uniform. They found that a thermal disturbance could be used to induce a surface disturbance and that thermal disturbances dominate jet breakup if the ratio of surface to thermal disturbances is large. Furlani (2006) discusses how MEMS technology can be used to thermally modulate the free surface of a liquid jet and create picoliter-sized droplets with greater speed and versatility. Chwalek *et al.* (2002) have investigated the effects of heating at the nozzle in more detail. In particular they examined the effect of using an asymmetric resistive heating element encircling one half of the nozzle so that roughly half of the liquid jet is heated. They found that such a method could be used to deflect a microjet away from the nozzles axis of symmetry. For liquid sheets, Tilley & Bowen (2005) have shown that the time to rupture can be minimized by choosing the appropriate initial phase difference between velocity profile and temperature profile.

12.1 Formulation of Problem

We begin by considering a liquid jet emerging from an orifice as shown in Fig. 12.1. We consider the problem in cylindrical coordinates so that the initial direction of motion of the jet is taken to be the z-axis with the normal direction being the r-axis. We assume

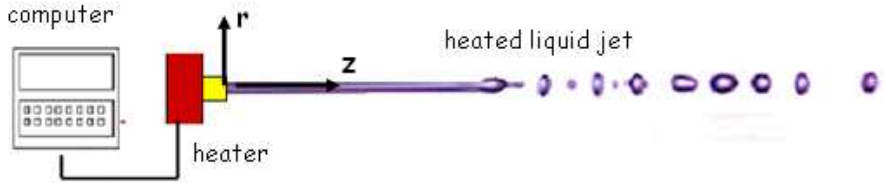

Figure 12.1: A diagram showing how thermal modulation can be used to control breakup and droplet formation in viscous liquid jets. Typically, resistive heating elements are placed around the orifice, so that the jet emerges into the ambient surrounding with a predetermined temperature distribution along the jet.

that the flow is axis-symmetric and that effects of the surrounding air can be ignored. The orifice is connected to a heater (which in turn is connected to a computer) so that the jet can be periodically heated (with a desired frequency) as it passes through the orifice. The equations governing the flow within the jet are given by

$$\boldsymbol{\nabla} \cdot \mathbf{u} = 0 \qquad \text{and} \qquad \rho \frac{D\mathbf{u}}{Dt} = -\nabla p + \nabla \cdot (\mu \mathbf{E}) = -\nabla p + \mu \nabla^2 \mathbf{u} + \nabla \mu \cdot \mathbf{E}, \tag{12.1}$$

where $\boldsymbol{u} = (u, v)$ is the velocity vector, ρ is the density of the liquid, t is time, p is the pressure, μ is the viscosity and $\mathbf{E} = \nabla \mathbf{u} + (\nabla \mathbf{u})^T$ is the deformation tensor. Since we wish to consider fluids with deformation rate dependent properties, we shall introduce here the non-Newtonian viscosity model we shall use, this is given by

$$\mu_a = \tilde{\mu}_0 (1 - \lambda)[1 + (h\dot{\gamma})^2]^{\frac{n-1}{2}} + \tilde{\mu}_0 \lambda, \tag{12.2}$$

which is commonly known as the Carreau model (see section 3.2.6 for more details and Bird *et al.* (2003) or Carreau *et al.* (1979)). In this case, μ_a is the shear rate dependent viscosity, $\dot{\gamma} = \sqrt{\boldsymbol{E} : \boldsymbol{E}/2}$ is the second invariant of the deformation tensor, $\tilde{\mu}_0$ is the zero-shear rate viscosity, h is a time constant, $\lambda \tilde{\mu}_0$ is the viscosity in the limit of infinite

shear and finally n is the flow index number[2] such that $0 \leqslant n \leqslant 1$. When $n = 1$ we have constant viscosity and therefore Newtonian behaviour.

The relationship between the temperature of a fluid and the surface tension of the free surface is expressed by

$$\sigma(T) = \sigma_a - \beta_p(T - T_a), \quad \text{where} \quad \beta_p = -\left(\frac{d\sigma}{dT}\right)_{T=T_a}, \tag{12.3}$$

where T is temperature and σ_a is the surface tension at the ambient temperature T_a (a more in depth analysis of variations in surface tension with temperature is given in Appendix E). The viscosity of the liquid is also affected by the change in temperature, and for most fluids can be described by the Arrhenius type relationship[3] (see also Chwalek *et al.* (2002))

$$\mu = \mu_a \exp(-\mu_p(T - T_a)), \quad \text{where} \quad \mu_p = -\left(\frac{d\mu}{dT}\right)_{T=T_a}, \tag{12.4}$$

where μ_a is the viscosity of the fluid at the ambient temperature (which is shear rate dependent) and is given by (12.2). We therefore have an expression for the viscosity in the form

$$\mu = \tilde{\mu}_0[(1-\lambda)(1 + (h\dot{\gamma})^2)^{\frac{n-1}{2}} + \lambda]\exp(-\mu_p(T - T_a)). \tag{12.5}$$

The parameter μ_p is a measure of how the viscosity changes with temperature. For certain melts like α-methyl styrene/silicone the viscosity is almost insensitive to changes in temperature when the temperature is varied between 100°C and 140°C but for changes

[2]We again use here n as the symbol for the flow index number, which replaces our earlier convention of using α. This is more in line with the traditional notation for the flow index number.

[3]This is perhaps the simplest type of relationship between the viscosity and temperature of a fluid. There are many polymers and melts which exhibit very exotic changes in viscosity with temperature. In particular there are some types of glasses which can exhibit a tenfold increase in viscosity for a 1% rise in temperature (see Dyre (2004)).

in temperature above this, between 140°C and 180°C the viscosity can drop by 90 %[4].

For non-Newtonian fluids the change in viscosity with temperature is unsurprisingly a lot more involved. In the present study we shall examine fluids which are Newtonian or fluids which are shear thinning but with flow index numbers close to unity. We therefore assume that any changes in viscosity with temperature can be approximately modelled using the above equation (in addition we assume that changes in temperature and shear rate affect the viscosity independently). A plot of the changing values of the surface tension and dynamic viscosity for an interface between air and water for different temperatures is shown in Fig. 12.2. This clearly demonstrates that both surface tension and viscosity decrease with increasing temperature (i.e., $\mu_p > 0$). In addition, we see the appropriateness of a linear relationship between surface tension and temperature and a exponential relationship between viscosity and temperature. A full explanation of why viscosity decreases with temperature is beyond the scope of this work (expressions for the viscosity of liquids and gases as a function of material parameters are given in Appendix E) but a brief discussion is presented in Batchelor (1963). We recapitulate here the main points. A liquid is usually composed of so called 'coherent' groups of molecules which resist deformation through the action of intermolecular forces. Shearing forces tend to break such coherent groups and viscosity can be thought of in terms of the resistance offered by such coherent groups. An increase in temperature leads to smaller coherent groups, which is a consequence of the increased agitation of individual molecules. As such there is less resistance to deformation and thus a reduction in the viscosity of the fluid. In general the density will also change with temperature but in this work we will ignore

[4]Wylie *et al.* (2007) use a hyperbolic tangent function to capture the rapid variation of viscosity μ_0 at low temperatures and viscosities at high temperatures $\mu_0 M$ such that

$$\mu(T) = \mu_0 \left[\frac{1+M}{2} - \frac{1-M}{2} \tanh\left(\frac{T - T_0 - T_a}{T_r} \right) \right]$$

where $M < 1$ is the viscosity contrast, T_a is the input temperature and T_r is the range of rapid variation in temperature.

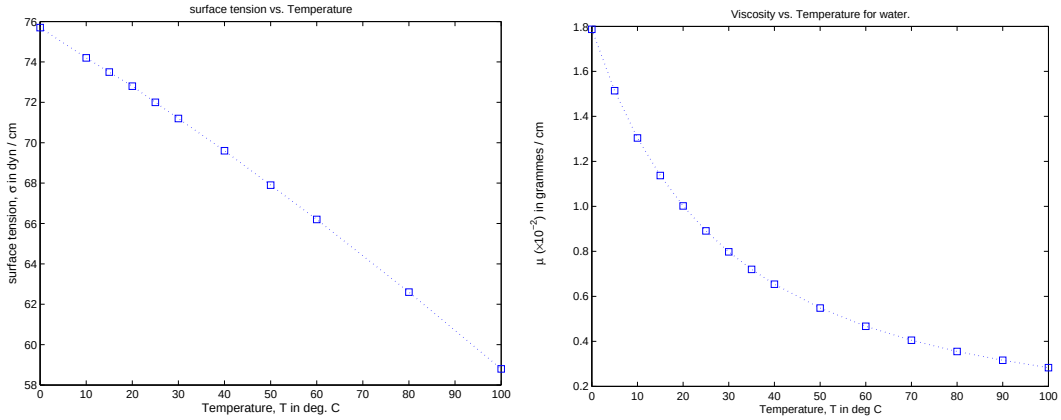

Figure 12.2: The surface tension σ (dyne/cm) and dynamic viscosity μ (gm/cm/s) at the interface between air and water for different temperatures. Clearly both the surface tension and viscosity decrease with increasing temperatures. Data taken from Batchelor (1967) p.596.

such changes (at any rate the changes will only enhance the reduction of viscosity and so can be incorporated into the change in dynamic viscosity). The conservation of energy equation [5] can be written as

$$\frac{\partial T}{\partial t} + \boldsymbol{u} \cdot \boldsymbol{\nabla} T = \kappa_T \boldsymbol{\nabla}^2 T, \tag{12.6}$$

where $\kappa_T = k/\rho c_p$ is the thermal diffusivity[6] of the fluid, k is the thermal conductivity and c_p is the specific heat capacity. The thermal diffusivity, for most liquids, rises with any increase in temperature although for water there is a small change in the opposite direction. A table containing the thermal diffusivity and thermal conductivities of some common fluids is shown in Table 12.1.

These equations are complemented by a number of boundary conditions. Since we are interested in symmetric disturbances we have the symmetry boundary conditions $u = v = \partial T/\partial r = 0$ at $r = 0$. At the free surface of the jet $r = R(z,t)$ we have that

[5] which is really an extension of the first law of thermodynamics, describing the difference in internal energies to the work done and heat added $\triangle U = Q + W$.

[6] Thermal diffusivity, usually denoted by the symbol α, has SI units of $m^2 s^{-1}$. Materials with high thermal diffusivity rapidly adjust their temperature to that of their surroundings.

	air	water	mercury	ethyl alcohol	olive oil	glycerine
κ_T (cm^2/s)	0.202	0.0014	0.042	0.00099	0.00092	0.00098
k (J/cm/s/deg C)	0.00025	0.0059	0.08	0.0018	0.0011	0.0029

Table 12.1: The thermal diffusivity and thermal conductivity of some common fluids at 15 °C and at standard pressure. Taken from Batchelor (1967)

tangential stresses are balanced by surface tension gradients, so that

$$\boldsymbol{n} \cdot \boldsymbol{\Pi} \cdot \boldsymbol{t} = \nabla\sigma \cdot \boldsymbol{t}, \tag{12.7}$$

where $\boldsymbol{n}$ and $\boldsymbol{t}$ are the normal and tangential vectors to the free surface given by

$$\boldsymbol{n} = (-R'/\xi, 1/\xi) \quad \text{and} \quad \boldsymbol{t} = (1/\xi, R'/\xi),$$

where $\xi = (1 + R')^{\frac{1}{2}}$ and R' is $\partial R/\partial z$. The stress tensor is given by $\boldsymbol{\Pi} = -p\mathbf{I} + \mu[\nabla\boldsymbol{u} + \nabla(\boldsymbol{u})^T]$. The normal stress within the fluid is balanced by the mean curvature times the surface tension (which is a variable here),

$$\boldsymbol{n} \cdot \boldsymbol{\Pi} \cdot \boldsymbol{n} = \sigma\kappa, \tag{12.8}$$

where κ is the mean curvature. The kinematic condition which requires a fluid particle on the free surface to remain there is expressed as

$$\frac{D}{Dt}(r - R(z,t)) = 0. \tag{12.9}$$

The normal heat flux across the interface is given by Newton's law of cooling so that

$$k\boldsymbol{\nabla}T \cdot \boldsymbol{n} = -H(T - T_a), \tag{12.10}$$

where k is the thermal conductivity[7] and H is the heat transfer coefficient[8]. If the free surface is assumed to be thermally insulated then the right hand side of the above equation is taken as zero.

We non-dimensionalize our variables based on the following scales,

$$\overline{z} = \frac{z}{L}, \quad \overline{r} = \frac{r}{a}, \quad \overline{u} = \frac{u}{U}, \quad \overline{v} = \frac{v}{U}, \quad \overline{t} = \frac{L}{U}, \quad \overline{p} = \rho U^2, \quad \overline{T} = \frac{T}{T_a}, \tag{12.11}$$

where a is the radius of the orifice, U is the exit speed of the jet, T_a is the temperature of the ambient surrounding into which the jet emerges and L is some axial length scale chosen so that (in keeping with the slender jet assumption) we have $\varepsilon = a/L << 1$. The viscosity is made dimensionless with the zero shear rate viscosity $\tilde{\eta}_0$ so that dimensionless expressions for μ and μ_a are given by

$$\mu = \mu_a e^{-\mu_p(T-1)} \quad \text{and} \quad \mu_a = (1-\lambda)(1+(h\dot{\gamma})^2)^{\frac{n-1}{2}} + \lambda.$$

Using these scalings the resulting non-dimensional set of equations, after dropping over-bars, are given by

$$\frac{\partial v}{\partial r} + \varepsilon \frac{\partial u}{\partial z} + \frac{v}{r} = 0, \tag{12.12}$$

$$\left(\varepsilon \frac{\partial u}{\partial t} + \varepsilon u \frac{\partial u}{\partial z} + v \frac{\partial u}{\partial r}\right) = -\varepsilon \frac{\partial p}{\partial z} + \frac{\mu_a e^{-\mu_p(T-1)}}{\varepsilon \mathcal{R}e}\left(\varepsilon^2 \frac{\partial^2 u}{\partial z^2} + \frac{1}{r}\frac{\partial}{\partial r}\left(r\frac{\partial u}{\partial r}\right)\right)$$
$$\frac{1}{\varepsilon \mathcal{R}e}\left(2\varepsilon^2 \frac{\partial \mu}{\partial z}\frac{\partial u}{\partial z} + \frac{\partial \mu}{\partial r}\left(\varepsilon \frac{\partial v}{\partial z} + \frac{\partial u}{\partial r}\right)\right), \tag{12.13}$$

[7]The thermal conductivity is a measure of a material's ability to conduct heat. It has SI units of kg m/s/K (also W m^{-1} K^{-1}), typically air is a poor conductor so $k_{air} \approx 0.025$ whilst $k_{silver} \approx 429$.

[8]The heat transfer coefficient H is a measure of the flow of heat between two materials. In general, as an approximation, it is defined by $Q = HA\triangle T$, where Q is the heat flow, A is some characteristic area and $\triangle T$ is the characteristic temperature difference (see Bird, Stewart and Lightfoot (2002) p.423 for more details)

$$\left(\varepsilon\frac{\partial v}{\partial t}+\varepsilon u\frac{\partial v}{\partial z}+v\frac{\partial v}{\partial r}\right)=-\frac{\partial p}{\partial r}+\frac{\mu_a e^{-\mu_p(T-1)}}{\varepsilon\mathcal{R}e}\left(\varepsilon^2\frac{\partial^2 v}{\partial z^2}+\left(\frac{1}{r}\frac{\partial v}{\partial r}-\frac{v}{r^2}+\frac{\partial^2 v}{\partial r^2}\right)\right)$$
$$\frac{1}{\varepsilon\mathcal{R}e}\left(2\frac{\partial\mu}{\partial r}\frac{\partial r}{\partial r}+\varepsilon\frac{\partial\mu}{\partial z}\left(\varepsilon\frac{\partial v}{\partial z}+\frac{\partial u}{\partial r}\right)\right), \quad (12.14)$$

$$\left(\varepsilon\frac{\partial T}{\partial t}+\varepsilon u\frac{\partial T}{\partial z}+v\frac{\partial T}{\partial r}\right)=\frac{1}{\varepsilon\mathcal{P}e}\left(\varepsilon^2\frac{\partial^2 T}{\partial z^2}+\left(\frac{1}{r}\frac{\partial T}{\partial r}+\frac{\partial^2 T}{\partial r^2}\right)\right), \quad (12.15)$$

with the tangential stress and normal stress conditions as

$$2\varepsilon\frac{\partial R}{\partial z}\left(\frac{\partial v}{\partial r}-\varepsilon\frac{\partial u}{\partial z}\right)+\left(1-\varepsilon^2\left(\frac{\partial R}{\partial z}\right)^2\right)\left(\frac{\partial u}{\partial r}+\varepsilon\frac{\partial v}{\partial z}\right)$$
$$=\varepsilon\frac{\mathcal{R}e}{We}\frac{e^{\mu_p(T-1)}}{\mu_a}\left(\varepsilon\frac{\partial\sigma}{\partial z}\left(1+\varepsilon^2\left(\frac{\partial R}{\partial z}\right)^2\right)^{-\frac{1}{2}}\right.$$
$$\left.+\varepsilon\frac{\partial R}{\partial z}\frac{\partial\sigma}{\partial r}\left(1+\varepsilon^2\left(\frac{\partial R}{\partial z}\right)^2\right)^{-\frac{1}{2}}\right), \quad (12.16)$$

and

$$\frac{2e^{-\mu_p(T-1)}}{\varepsilon\mathcal{R}e}\mu_a\left(\varepsilon^3\frac{\partial u}{\partial z}\left(\frac{\partial R}{\partial z}\right)^2+\frac{\partial v}{\partial r}-\left(\frac{\partial u}{\partial r}+\varepsilon\frac{\partial v}{\partial z}\right)\varepsilon\frac{\partial R}{\partial z}\right)$$
$$+(p_e-p)\left(1+\varepsilon^2\left(\frac{\partial R}{\partial z}\right)^2\right)=-\frac{\sigma\kappa}{We}, \quad (12.17)$$

where

$$\kappa=\frac{\left(1+\varepsilon^2\left(\frac{\partial R}{\partial x}\right)^2\right)^{-\frac{1}{2}}}{R}-\frac{\varepsilon^2\frac{\partial^2 R}{\partial x^2}}{\left(1+\varepsilon^2\left(\frac{\partial R}{\partial x}\right)^2\right)^{\frac{3}{2}}}, \quad (12.18)$$

and p_e is the external gas pressure which we can take to be zero.

The normal heat flux condition can be written as

$$\frac{\partial T}{\partial r}\left(\left(1+\varepsilon^2\left(\frac{\partial R}{\partial z}\right)^2\right)^{-\frac{1}{2}}-\varepsilon^2\frac{\partial T}{\partial z}\frac{\partial R}{\partial z}\left(1+\varepsilon^2\left(\frac{\partial R}{\partial z}\right)^2\right)^{-\frac{1}{2}}=-\varepsilon\mathcal{B}i(T-1), \quad (12.19)$$

along with the kinematic equation

$$v = \frac{\partial R}{\partial t} + u\frac{\partial R}{\partial z}. \tag{12.20}$$

The non-dimensional constants appearing in these equations are the *Reynolds* number, *Weber* Number, *Peclet*[9] and *Biot*[10] number which measure the relative importance of viscosity to inertia, surface tension to inertia, inertia to thermal diffusion and the ability to transfer heat to the surrounding respectively, these are given by

$$\mathcal{R}e = \frac{\rho U L}{\tilde{\mu}_0}, \quad We = \frac{\rho U^2 a}{\sigma_a}, \quad \mathcal{P}e = \frac{UL}{\kappa_T} \quad \text{and} \quad \mathcal{B}i = \frac{LH}{k}. \tag{12.21}$$

If we expand our variables using an asymptotic expansion, under the slender jet assumption, so the leading order axial velocity is independent of the radial direction r, we have

$$u = u_0(z,t) + (\varepsilon r)^2 u_2(z,r,t) + O((\varepsilon r)^3), \qquad v = (\varepsilon r)v_1(z,r,t) + O((\varepsilon r)^3),$$
$$p = p_0(z,r,t) + (\varepsilon r)^2 p_2(z,r,t) + O((\varepsilon r)^3), \quad T = T_0(z,t) + (\varepsilon r)^2 T_2(z,r,t) + O((\varepsilon r)^3),$$
$$\text{and} \quad R = R_0(z,t) + \varepsilon^2 R_2(z,t) + O(\varepsilon^3). \tag{12.22}$$

The continuity equation, at leading order gives $v_0 = -u_{0z}/2$. Similarly the shear rate, after using the expression for the leading order radial velocity v_0, gives at leading order $\dot{\gamma} = \sqrt{3}|u_{0z}|$, from which we have a leading order dimensionless expression for the apparent viscosity

$$\mu = [(1-\lambda)(1+3hu_{0z}^2)^{\frac{n-1}{2}} + \lambda]e^{-\mu_p(T_0-1)}.$$

[9] Jean-Claude-Eugene Peclet (1793-1857) was a French physicist at the Ecole Normale in Paris. He published a number of books but he is most famous for his *Traite de Chale et de Ses Applicationes aux Arts et aux Manufacture* (Paris 1879) which was distributed worldwide and translated into German.

[10] Jean Baptiste Biot (1774-1862) was a professor of physics at the College de France. He is famous, amongst other things, for the development of a method to test sugar concentration. He was awarded the Rumford Medal of the Royal Society in 1840 for his work on the polarization of light.

The momentum equation along the z-axis gives to leading order

$$\frac{\partial u_0}{\partial t} + u_0 \frac{\partial u_0}{\partial z} = -\left(p_0\right)_z + \frac{e^{-\mu_p(T_0-1)}}{\mathcal{R}e}\left(\mu_a \frac{\partial^2 u_0}{\partial z^2} + 4\mu_a u_2 + 2\frac{\partial \mu_a}{\partial z}\frac{\partial u_0}{\partial z} - 2\mu_p \mu_a \frac{\partial T_0}{\partial z}\frac{\partial u_0}{\partial z}\right), \tag{12.23}$$

whilst the momentum equation along the radial direction gives

$$\frac{\partial p_0}{\partial r} = 0, \tag{12.24}$$

which suggests that $p_0 = p_0(z,t)$, as expected for a slender jet. From the normal stress condition at leading order we get

$$p_0 = \frac{1}{We}\left(\frac{\sigma_0}{R_0}\right) - \frac{\mu_a e^{-\mu_p(T_0-1)}}{\mathcal{R}e} u_{0z}. \tag{12.25}$$

An expression for u_2 can be derived from the leading order equation for the tangential stress, which gives

$$u_2 = \frac{3}{2}u_{0z}\frac{R_{0z}}{R_0} + \frac{u_{0zz}}{4} + \left(\frac{\mathcal{R}e}{We}\right)\frac{e^{\mu_p(T_0-1)}}{\mu_a}\frac{\sigma_{0z}}{2R_0}. \tag{12.26}$$

Substitution of u_2 and p_0 into (12.23) give

$$\frac{\partial u_0}{\partial t} + u_0 \frac{\partial u_0}{\partial z} = -\frac{1}{We}\left(\frac{\sigma_0}{R_0}\right)_z + \frac{3e^{-\mu_p(T_0-1)}}{\mathcal{R}e}\left(\mu_a \frac{\partial^2 u_0}{\partial z^2} + 2\mu_a \frac{u_{0z}R_{0z}}{R_0} - \mu_p \mu_a \frac{\partial T_0}{\partial z}\frac{\partial u_0}{\partial z} + \frac{\partial \mu_a}{\partial z}u_{0z}\right) + \frac{2\sigma_{0z}}{R_0 We}. \tag{12.27}$$

The energy equation to leading order gives

$$\frac{\partial T_0}{\partial t} + u_0 \frac{\partial T_0}{\partial z} = \frac{1}{\mathcal{P}e}\left(\frac{\partial^2 T_0}{\partial z^2} + 4T_2\right), \tag{12.28}$$

where again T_2 can be obtained from the normal heat flux equation, so that

$$T_2 = \frac{1}{2R_0}\frac{\partial T_0}{\partial z}\frac{\partial R_0}{\partial z} - \frac{\overline{\mathcal{B}i}}{2R_0}(T_0 - 1), \tag{12.29}$$

where we have re-scaled the Biot number so that $\mathcal{B}i = \varepsilon\overline{\mathcal{B}i}$ with $\overline{Bi} = O(1)$. This rescaling effectively only considers the case where there is poor heat transfer to the surrounding (as is usually the case for most liquids when a small difference in temperature exist with the surrounding). The kinematic equation reduces to

$$\frac{\partial R_0}{\partial t} + u_0\frac{\partial R_0}{\partial z} + \frac{R_0}{2}\frac{\partial u_0}{\partial z} = 0. \tag{12.30}$$

Using the expression for u_2 and T_2 we get a set of leading order equations given by (after dropping the subscript zero)

$$\begin{aligned} u_t + uu_z = -\frac{1}{We}\left(\frac{\sigma}{R}\right)_z - \frac{2\beta_p T_z}{RWe} \\ + \frac{3e^{-\mu_p(T-1)}}{\mathcal{R}e}\cdot\frac{1}{R^2}\left[\frac{\partial}{\partial z}\left(\mu_a R^2\frac{\partial u}{\partial z}\right)\right] - \frac{3\mu_p\mu_a e^{-\mu_p(T-1)}}{\mathcal{R}e}T_z u_z, \end{aligned} \tag{12.31}$$

$$R_t = -\frac{R}{2}u_z - uR_z, \tag{12.32}$$

$$\text{and} \quad T_t + uT_z = \frac{1}{Pe}\frac{1}{R^2}\frac{\partial}{\partial z}\left(R^2\frac{\partial T}{\partial z}\right) - \frac{2\overline{\mathcal{B}i}}{R\mathcal{P}e}(T-1), \tag{12.33}$$

where $\sigma(T) = 1 - \beta_p(T-1)$.

When $\mu_p = 0$ (i.e., when the change in viscosity with temperature is ignored) and the fluid is Newtonian $n = 1$ we obtain the set of equations used by Furlani (2005).

12.2 Numerical Results

For reasons similar to those presented in section 5.1 we replace the leading order pressure term with the full curvature expression so that the axial momentum equation at leading

order is given by

$$u_t + uu_z = -\frac{1}{We}\left(\frac{\sigma}{R(1+\varepsilon^2 R_z^2)^{\frac{1}{2}}} - \frac{\varepsilon^2 \sigma R_{zz}}{(1+\varepsilon^2 R_z^2)^{\frac{3}{2}}}\right)_z - \frac{2\beta_p T_z}{RWe}$$
$$+\frac{3e^{-\mu_p(T-1)}}{\mathcal{R}e}\cdot\frac{1}{R^2}\left[\frac{\partial}{\partial z}\left(\mu_a R^2 \frac{\partial u}{\partial z}\right)\right] - \frac{3\mu_p\mu_a e^{-\mu_p(T-1)}}{\mathcal{R}e} T_z u_z. \tag{12.34}$$

Like in previous chapters we solve this system of equations (Eqs. 12.32 - 12.34) using a finite difference scheme, however, in this case the method of Lax-Wendroff does not work[11]. Instead we resort to McCormack's method, which whilst similar, is more stable, than Lax-Wendroff (see section 5.2 for more details). Although we have discussed McCormack's method in section 5.2 we now supplement that discussion and describe a more general form of this method which allows for solving nonlinear systems which need not be conservative in form. The method is based on a predictor-corrector format and can be used to solve the system

$$\frac{\partial u}{\partial t} + \frac{\partial F(u,x)}{\partial x} = G(u,x).$$

The predictor step is given by

$$u_i^p = u_i^n + \frac{\triangle t}{\triangle x}(F_{i+1}^n - F_i^n) + \triangle t G_i^n,$$

and the corrector step (which is calculated from the predictor step)

$$u_i^c = u_i^n + \frac{\triangle t}{\triangle x}(F_i^p - F_{i-1}^p) + \triangle t G_i^p,$$

[11]The problem terms appear to be the full expression for the mean curvature. When a variable surface tension is included, having its own evolution equation with initial conditions, the numerical instabilities at the nozzle grow along the jet. This was also the case when considering microjets using interface formation. This problem is not present in the surfactant covered rotating liquid jet problem, since in that case, there is no perturbation of the surfactant concentration (and hence the surface tension).

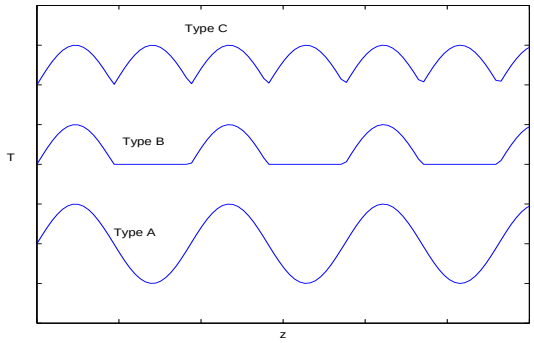

Figure 12.3: The different types of heating at the orifice. In particular Type B heating can be thought of a s pulsed heating.

where the superscript p refers to evaluating the functions F and G using u_i^p. The scheme is updated at each step using

$$u_i^{n+1} = \frac{1}{2}(u_i^p + u_i^c).$$

The boundary and initial conditions for the velocity and radius of the jet are given by

$$u(z,0) = R(z,0) = 1, \quad \text{and} \quad u(0,t) = 1 + \delta \sin(\kappa t/\varepsilon), \tag{12.35}$$

where δ and κ are the (velocity) disturbance amplitude and wavenumber. Since the jet is being periodically heated at the orifice, we have the initial condition for the temperature as

$$T(z,0) = 1 \quad \text{and} \quad T(0,t) = 1 + \delta_\theta \sin\left(\frac{\kappa_\theta t}{\varepsilon}\right), \tag{12.36}$$

where δ_θ and κ_θ are the magnitude of heating and frequency of heating respectively. In this case the initial temperature conditions reflect heating and cooling over one period (or alternatively an assumption that the fluid is initially at a temperature lower than the ambient ($T = 1 - \delta_\theta$) and emerges after being heated to the ambient temperature), we shall refer to this type of heating at the nozzle as 'Type $\mathcal{A}$'. We also consider other types of heating 'patterns' which correspond to heating over half cycles and pulsed heating,

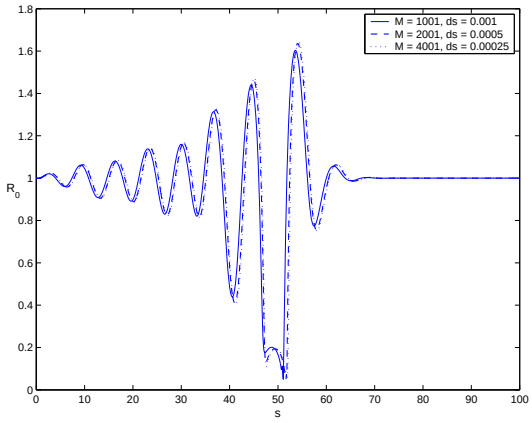

Figure 12.4: Accuracy check for various ds and various number of mesh points M. The other parameters are $We = 15.0$, $\mathcal{P}e = 500.0$, $\mu_p = 1.0$, $\beta_p = 0.8$, $\overline{\mathcal{B}i} = 0.5$, $\mathcal{R}e = 3000$, $\kappa = 0.89$, $\kappa_\theta = 0.2$, $\delta = 0.02$, $\delta_\theta = 0.1$, $dt = 5 \times 10^{-6}$ and the final time $t_f = 0.5232$.

these conditions at the nozzle are given by

$$T(0,t) = 1 + \frac{\delta_\theta}{2}\left(\sin\left(\frac{\kappa_\theta t}{\varepsilon}\right) + \left|\sin\left(\frac{\kappa_\theta t}{\varepsilon}\right)\right|\right) \quad \text{and} \quad T(0,t) = 1 + \delta_\theta \left|\sin\left(\frac{\kappa_\theta t}{\varepsilon}\right)\right|, \tag{12.37}$$

these two types of heating at the nozzle shall be referred to as 'Type $\mathcal{B}$' and 'Type $\mathcal{C}$' respectively (see Fig. 12.3). Throughout the rest of this work we use, unless otherwise stated, Type $\mathcal{B}$ heating at the orifice which is similar to pulsed heating at the orifice. Like in all preceding chapters we assume that breakup of the jet occurs when the minimum jet radius has reached five percent of the initial jet radius.

The accuracy of the numerical method is tested by changing the spatial grid size and/or time step (see Fig. 12.4).

In Fig. 12.5 we show the difference in breakup of a thermally heated Newtonian liquid jet when thermal diffusion is small ($\mathcal{P}e = 3000$). No heating at the orifice clearly delays the growth of disturbances and thus leads to shorter breakup lengths when compared to liquid jets which are thermally modulated at the orifice[12]. In Fig. 12.6 we show the radius

[12]The difference in breakup length for jets with and without heating were found to be different even when μ_p was varied.

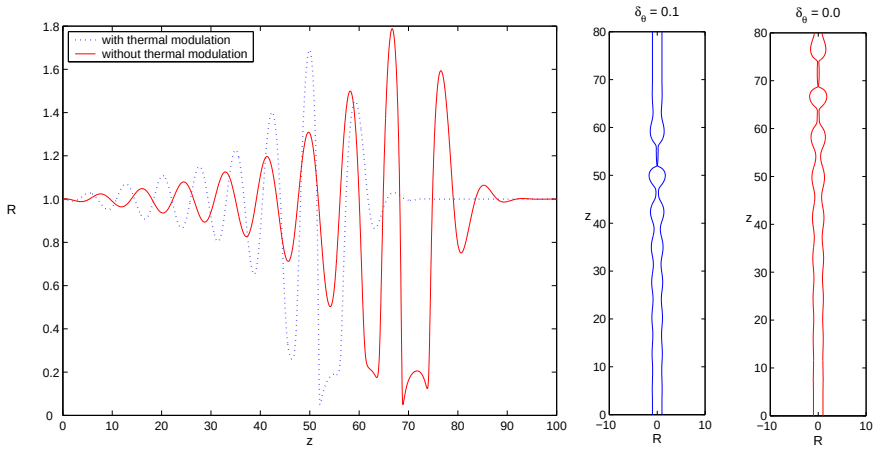

Figure 12.5: The difference between breakup dynamics for Newtonian liquid jets with thermal modulation (Type $\mathcal{A}$) and without thermal modulation. On the left we show the radius plotted against distance along the jet with the dashed line representing the numerical results with thermal modulation. On the right we show the profiles of jets at breakup with the parameters $\mathcal{R}e = 2750$, $We = 20.4$, $\mathcal{P}e = 3000$, $\overline{\mathcal{B}i} = 0.5$, $\delta = 0.02$, $\kappa = 0.74$, $\delta_\theta = 0.1$, $\kappa_\theta = 0.81$, $\mu_p = 0.0$ and $\beta_p = 0.6$.

and temperature along the jet for a thermally modulated jet with Type $\mathcal{B}$ heating for high ($\kappa_\theta = 0.76$) and low ($\kappa_\theta = 0.37$) frequency heating respectively. Clearly the breakup length is longer when the frequency of heating is smaller and we also notice that drop formation is clearly more pronounced when the frequency of heating is large (also note that satellite droplets are smaller in this case). We should note here that for low frequency heating the droplet produced appears to be an amalgamation of two droplets (i.e., a main droplet cannot be clearly identified). The size of main and satellite droplets produced by thermally heating jets when the (velocity) disturbance wavenumber (frequency) is varied is shown in Fig. 12.7. As expected, and in agreement with isothermal liquid jets, we see a reduction in size for both main and satellite droplets for increasing κ. For the parameter regimes considered for this figure, we found that droplets produced *without* heating at the orifice were almost identical in size except for very small wavenumbers κ, where jets without heating produced slightly smaller (the difference was less than 0.1 jet radii) sized droplets.

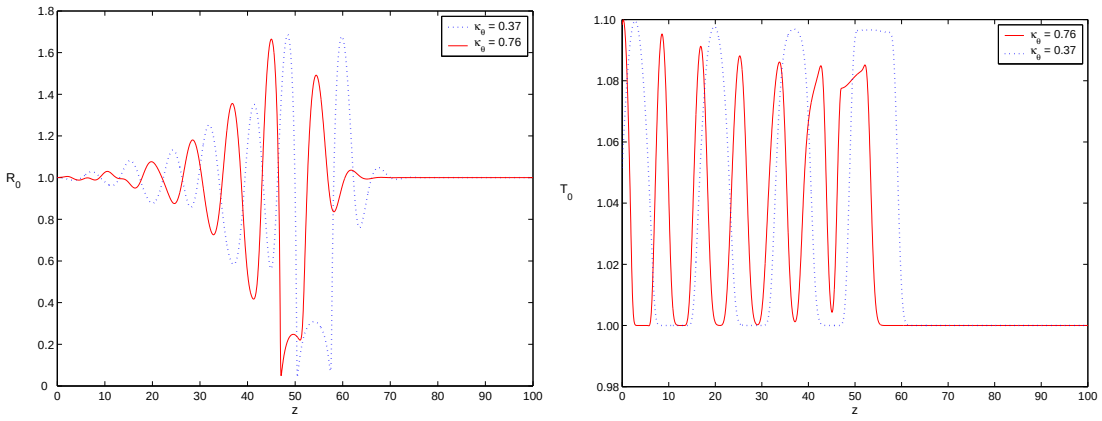

Figure 12.6: The radius and temperature profile along a thermally modulated shear thinning liquid jet for different κ_θ. The other parameters here are $\mathcal{R}e = 2850$, $We = 20.4$, $\mathcal{P}e = 10^4$, $\overline{\mathcal{B}i} = 0.5$, $\delta = 0.01$, $\kappa = 0.74$, $\delta_\theta = 0.1$, $\mu_p = 0.4$, $n = 0.8$, $\lambda = 0.2$, $h = 1$ and $\beta_p = 0.8$. It can be observed that decreasing κ_θ leads to longer jets and larger satellite droplets.

In Fig. 12.8 we plot the size of satellite droplets against the frequency of heating at the orifice. Satellite droplet sizes are found to decrease as the frequency of heating is increased with droplet sizes decreasing by almost a third when the frequency of heating is increased from $\kappa_\theta = 0.35$ to $\kappa_\theta = 0.8$. The profile near the locality of rupture for two different values of the heating frequency are shown in Fig. 12.9 and Fig. 12.10. These pictures are colour graphics showing the distribution of the temperature along the jet (the colourbar shows the variations of temperature) along with the profile at breakup. It can be observed that local minimums of the jet radius correspond to higher temperatures. This is in agreement with the predictions presented in the introduction to this chapter regarding Marangoni flows forcing liquid from hotter regions to cooler regions (thus leading to thinning in hotter regions). An interesting feature of Fig. 12.10 is that the local minimum (upstream of the drop) located at $z \approx 48$ is actually at the ambient temperature (shown as blue in colour) whilst the local upstream minimum immediately preceding it is at a higher temperature. This suggests that the evolution of the jet profile will continue in such a way so that the

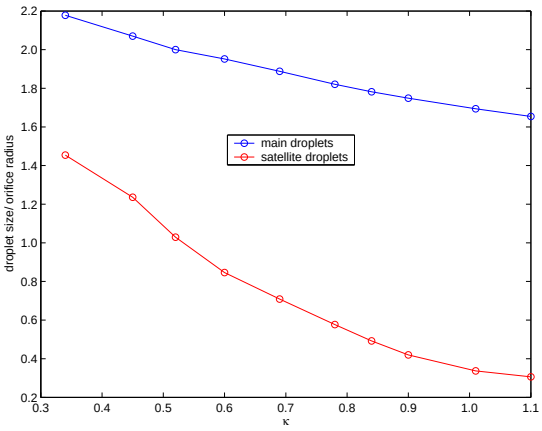

Figure 12.7: Droplet sizes for a thermally modulated liquid jet when the disturbance wavenumber κ is changed. The parameters here $\mathcal{R}e = 2600$, $We = 21.0$, $\mathcal{P}e = 10^4$, $\overline{\mathcal{B}i} = 0.5$, $\delta = 0.1$, $\delta_\theta = 0.1$, $\kappa_\theta = 0.5$, $\mu_p = 0.5$ and $\beta_p = 0.8$. The size of droplets without heating were approximately the same except for small κ where the difference in droplet sizes were less than 0.1.

two drops merge[13] into a single droplet (see left hand side of Fig. 12.10).

In Fig. 12.11 we show the change in breakup lengths as $\mu_p = -d\mu/dT$ is increased for a Newtonian and shear thinning liquid jet respectively. On account of the greater fall in viscosity with temperature, it can be observed that for both types of liquids, the breakup lengths decrease as μ_p is increased. It is important to note here that although we have considered values of μ_p which might normally be considered large, in practice such values would be typical for some melts and polymers within certain temperature ranges[14]. We select two different values of μ_p and plot the radius at breakup in Fig. 12.12 where we also show the effects on the viscosity along the jet.

In Fig. 12.13 and Fig. 12.14 we show colour graphics depicting the profile of thermally heated Newtonian liquid jets for changes in the Peclet number. For small Peclet numbers

[13]Note that using the present numerical simulations we cannot predict what happens after rupture (as is generally the case with other schemes). However, under the present theory we know that Marangoni flows facilitate pinch-off by displacing fluid away from hotter regions, so that we can *predict* that pinch-off will invariably take place in such 'hot' regions.

[14]Wylie *et al.* (2007) mention some such fluids. A value of $\mu_p = 12.0$ roughly equates to a drop in viscosity of 70% for a ten per cent increase in temperature. Irrespective of the value of μ_p a more noticeable change in breakup lengths would be expected for smaller values of $\mathcal{R}e$.

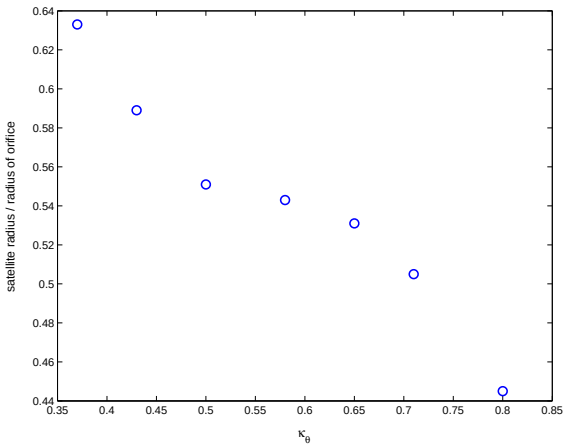

Figure 12.8: The size of satellite droplets against the frequency of heating κ_θ for a Newtonian fluid. Here the parameters are given by $\mathcal{R}e = 2850$, $We = 20.4$, $\mathcal{P}e = 10^4$, $\overline{\mathcal{B}i} = 0.5$, $\delta = 0.01$, $\kappa = 0.84$, $\delta_\theta = 0.1$, $\mu_p = 0.4$ and $\beta_p = 0.8$. It can be observed that satellite droplet sizes decrease with increased frequency of heating. The non-dimensional size of the satellite droplet when no heating is applied is 0.479.

we see very few 'hot' regions (shown as red in colour) and a more even distribution of thermal energy along the jet (which is to be anticipated since the inverse of the Peclet number, $1/\mathcal{P}e$, is a measure of the thermal diffusion of heat). Indeed this is true, even in regions close to where the jet profile is very small. This is in sharp contrast to the profile at high Peclet numbers where the jet consists of successive hot regions (shown as red in colour) and cold regions (shown as blue in colour). This can be explained by the relative difference in Peclet numbers (which is almost two orders higher in Fig. 12.14). For low Peclet numbers, thermal diffusion is high and is effective in 'smearing' out thermal gradients so that sharp contrasts in temperature are not observed. For high Peclet numbers, thermal diffusion is almost negligible so that thermal energy is simply convected along with the flow and is allowed to accumulate in certain regions.

In Fig. 12.15 and Fig. 12.16 we see the effects of changing the type of heating pattern employed at the orifice. In the case of pulsed heating (where we have a short interval of heating followed by no heating) we see the familiar 'hot-cold' regions (see Fig. 12.15). However, when we use heating type $\mathcal{B}$ we see relatively higher temperatures along

the jet (although again we see that thin portions of the jet correspond to the highest temperatures). Figures 12.17 and 12.18 show the profiles for Newtonian liquid jets using different (velocity) disturbance wavenumbers at the orifice. These figures demonstrate that rupture will not always occur in regions where the temperature is at its highest, and in particular we note that in Fig. 12.17 we have rupture occurring at approximately $z = 66$, yet this region is at the ambient temperature. Likewise in Fig. 12.18 we see that when $z \approx 19$ we have a swelled portion of the jet corresponding to the highest temperature along the jet. Thus it is important to note here, that rupture of a liquid thread occurs as a result of the interaction of capillary pressure *and/or* thermally induced Marangoni-flow. Also note that in Figs. 12.17 and 12.18 the initial velocity disturbance amplitude δ is of the same order as the magnitude of heating δ_θ. Unsurprising when δ is so large, capillarity may act independent of thermal effects, since in this case the jet ruptures on a much smaller time scale than it would when $\delta \approx 0.01$. To further elaborate this theme, we plot the breakup length of a periodically heated liquid jet for changes in the initial (velocity) disturbance amplitude δ in Fig. 12.19. It becomes apparent from this figure, that Marangoni flows (which are controlled by thermal gradients) dominate breakup as $\delta \to 0$ (this is evident by the increasing discrepancy in breakup lengths between thermally heated liquid jets and isothermal jets as $\delta \to 0$). Indeed in the limit $\delta = 0$, when our numerical method will predict infinite breakup lengths for isothermal jets (since in this case the equilibrium solution is taken forward indefinitely), we find that for a periodically heated jet breakup occurs at a finite value of 68.1. We therefore see that a purely thermal disturbance can destabilize the jet (through thermally induced tangential flow) and cause rupture. Moreover, the 'competition' or relative importance of surface disturbances and thermally generated Marangoni flows are characterized by the ratio δ/δ_θ. This result is in excellent agreement with the findings of Mashayek and Ashgriz (1994).

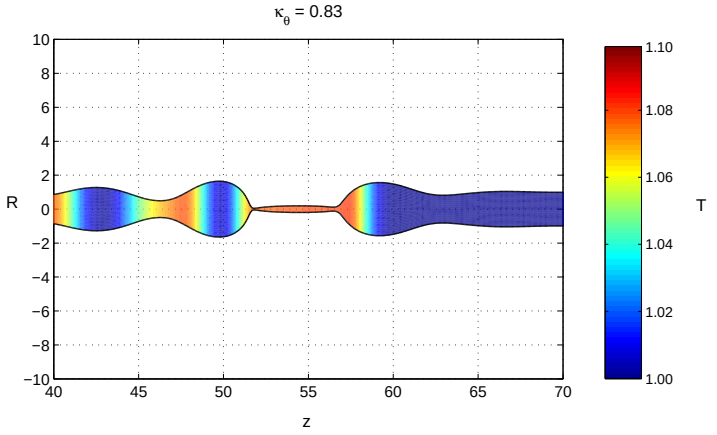

Figure 12.9: The profile for a thermally modulated Newtonian liquid jet near the point of rupture for high heating frequencies $\kappa_\theta = 0.83$. A colourbar is included for the temperature distribution. The other parameters here are $\mathcal{R}e = 2850$, $\mathcal{P}e = 10^4$, $We = 20.4$, $\overline{\mathcal{B}i} = 0.5$, $\delta = 0.01$, $\kappa = 0.74$, $\mu_p = 0.4$ and $\beta_p = 0.8$.

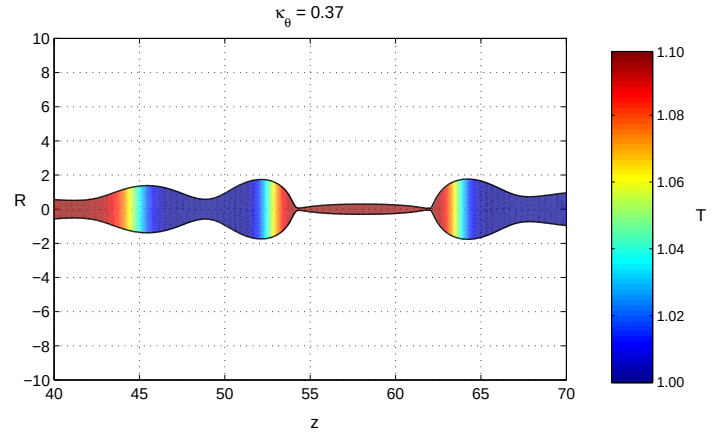

Figure 12.10: The profile for a thermally modulated Newtonian liquid jet near the point of rupture for low heating frequencies $\kappa_\theta = 0.37$. A colourbar is included for the temperature distribution. The other parameters here are $\mathcal{R}e = 2850$, $\mathcal{P}e = 10^4$, $We = 20.4$, $\overline{\mathcal{B}i} = 0.5$, $\delta = 0.01$, $\kappa = 0.74$, $\mu_p = 0.4$ and $\beta_p = 0.8$.

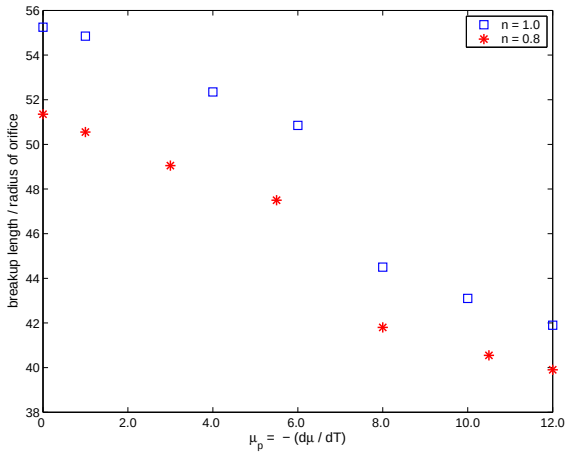

Figure 12.11: The breakup length of a Newtonian and shear thinning liquid jet plotted against $\mu_p = -\frac{d\mu}{dT}$. Clearly, as expected, the breakup length decreases as μ_p is increased (which corresponds to a more significant drop in viscosity). The other parameters here are $\mathcal{R}e = 2500$, $\mathcal{P}e = 500$, $We = 15.0$, $\overline{\mathcal{B}i} = 0.5$, $\delta = 0.02$, $\kappa = 0.89$, $\kappa_\theta = 0.2$ and $\beta_p = 0.8$. The shear thinning parameters are given by $\lambda = 0.2$ and $h = 1$.

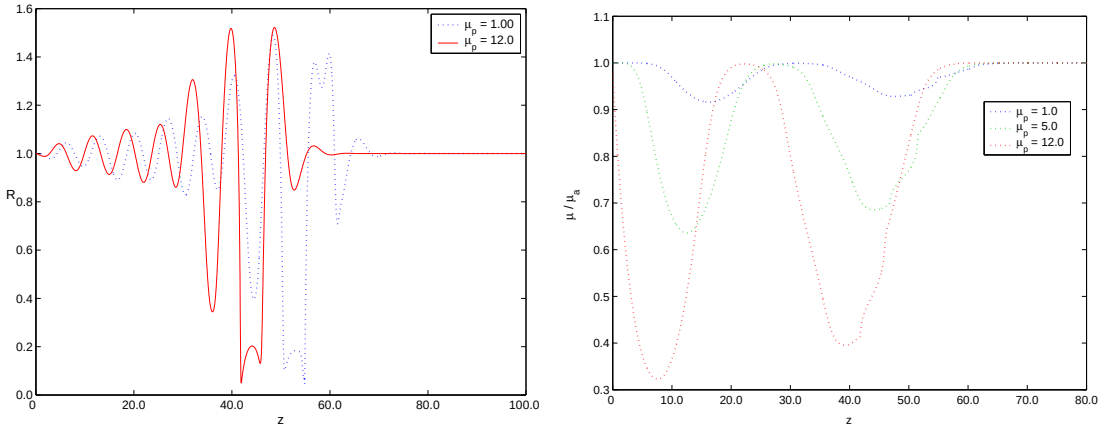

Figure 12.12: The radius and viscosity along a thermally modulated Newtonian liquid jet for different μ_p. The other parameters here are $\mathcal{R}e = 2500$, $\mathcal{P}e = 500$, $We = 15.0$, $\overline{\mathcal{B}i} = 0.5$, $\delta = 0.02$, $\kappa = 0.89$, $\kappa_\theta = 0.2$ and $\beta_p = 0.8$.

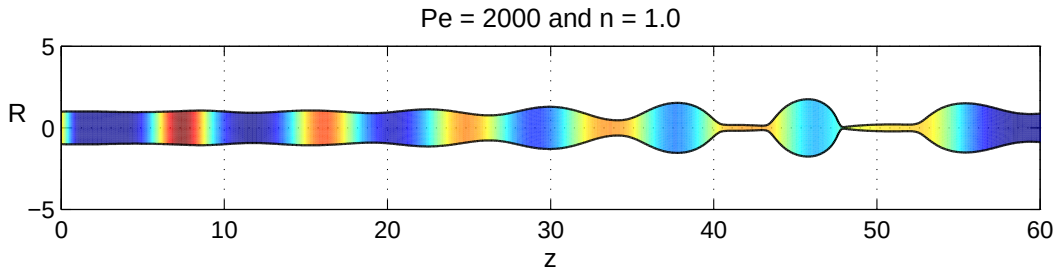

Figure 12.13: The profile of periodically heated Newtonian liquid jet at low Peclet numbers ($\mathcal{P}e = 2000$). The colours represent the temperature distribution which are defined by the colourbar in Fig. 12.10. Here we have $\delta_\theta = 0.1$, $\mathcal{R}e = 2850$, $We = 22.5$, $\overline{\mathcal{B}i} = 0.5$, $\delta = 0.025$, $\kappa = 0.84$, $\kappa_\theta = 0.72$, $\beta_p = 0.8$ and $\mu_p = 0$.

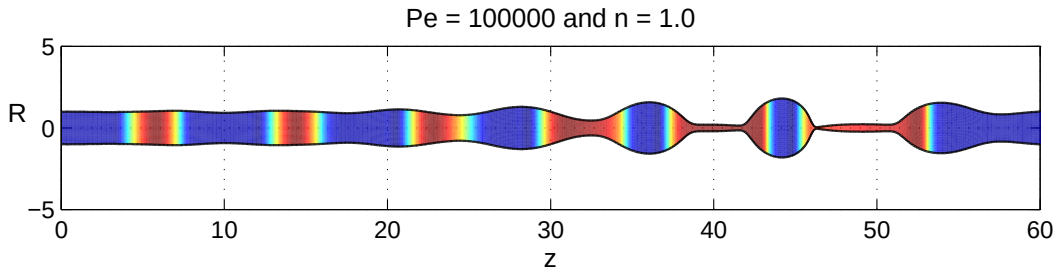

Figure 12.14: The profile of periodically heated Newtonian liquid jet at high Peclet numbers ($\mathcal{P}e = 10^5$). The colours represent the temperature distribution which are defined by the colourbar in Fig. 12.10. Here we have $\delta_\theta = 0.1$, $\mathcal{R}e = 2850$, $We = 22.5$, $\overline{\mathcal{B}i} = 0.5$, $\delta = 0.025$, $\kappa = 0.84$, $\kappa_\theta = 0.72$, $\beta_p = 0.8$ and $\mu_p = 0$.

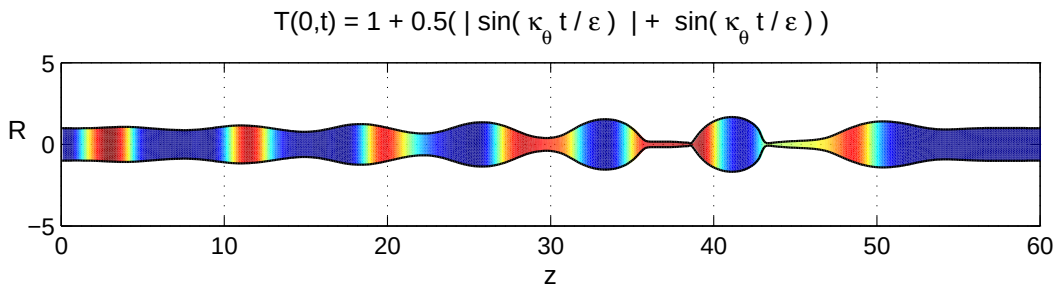

Figure 12.15: The profile of periodically heated shear thinning ($n = 0.8$) liquid jet with type $\mathcal{B}$ heating at the orifice. The colours represent the temperature distribution which are defined by the colourbar in Fig. 12.10. Here we have $\delta_\theta = 0.1$, $\mathcal{R}e = 2850$, $\mathcal{P}e = 10^4$, $We = 41.4$, $\overline{\mathcal{B}i} = 0.5$, $\delta = 0.05$, $\kappa = 0.84$, $\kappa_\theta = 0.72$ $\beta_p = 0.8$ and $\mu_p = 0.4$.

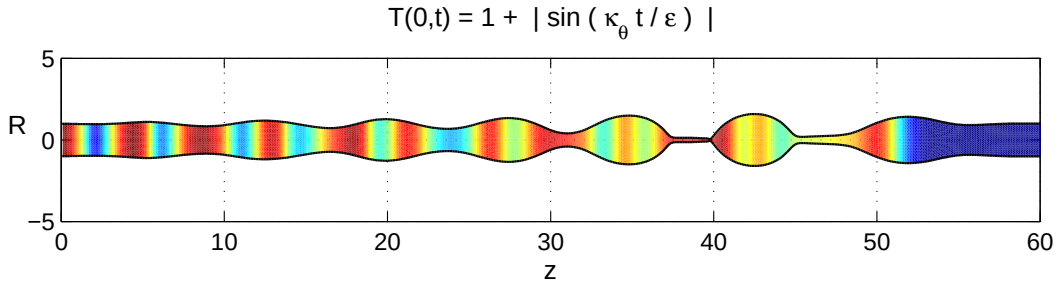

Figure 12.16: The profile of periodically heated shear thinning ($n = 0.8$) liquid jet with type $\mathcal{C}$ heating at the orifice. The colours represent the temperature distribution which are defined by the colourbar in Fig. 12.10. Here we have $\delta_\theta = 0.1$, $\mathcal{R}e = 2850$, $\mathcal{P}e = 10^4$, $We = 41.4$, $\overline{\mathcal{B}i} = 0.5$, $\delta = 0.05$, $\kappa = 0.84$, $\kappa_\theta = 0.72$ $\beta_p = 0.8$ and $\mu_p = 0.4$.

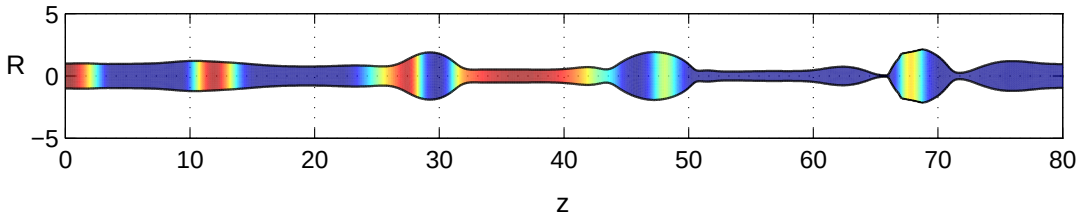

Figure 12.17: The profile of periodically heated Newtonian liquid jet with small (velocity) disturbance wavenumbers ($\kappa = 0.34$). The colours represent the temperature distribution which are defined by the colourbar in Fig. 12.10. The parameters here $\mathcal{R}e = 2600$, $We = 21.0$, $\mathcal{P}e = 10^4$, $\overline{\mathcal{B}i} = 0.5$, $\delta = 0.1$, $\delta_\theta = 0.1$, $\kappa_\theta = 0.5$, $\mu_p = 0.5$ and $\beta_p = 0.8$.

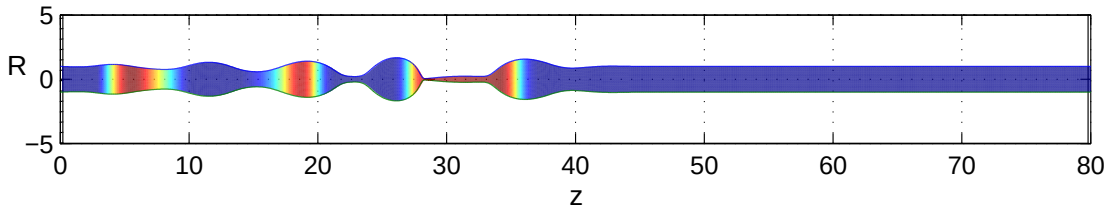

Figure 12.18: The profile of periodically heated Newtonian liquid jet with large (velocity) disturbance wavenumbers ($\kappa = 0.84$). The colours represent the temperature distribution which are defined by the colourbar in Fig. 12.10. The parameters here $\mathcal{R}e = 2600$, $We = 21.0$, $\mathcal{P}e = 10^4$, $\overline{\mathcal{B}i} = 0.5$, $\delta = 0.1$, $\delta_\theta = 0.1$, $\kappa_\theta = 0.5$, $\mu_p = 0.5$ and $\beta_p = 0.8$.

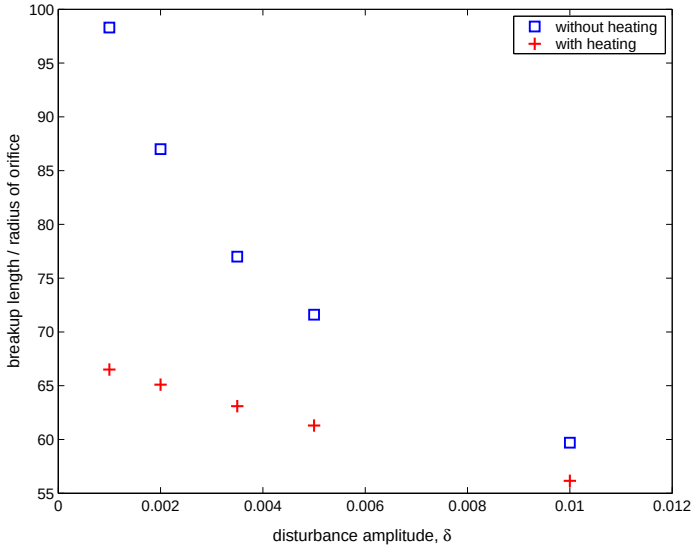

Figure 12.19: The breakup length of a Newtonian liquid jet for different initial (velocity) disturbance amplitudes in the case of periodic heating at the orifice ($\delta_\theta = 0.1$) and no heating at the orifice ($\delta_\theta = 0$). Clearly the difference in breakup lengths increases as $\delta \to 0$ and Marangoni flow dominates breakup. In the limit $\delta = 0$ the breakup length of a thermally heated liquid jet is 68.1. The parameters here $\mathcal{R}e = 4500$, $We = 18.0$, $\mathcal{P}e = 3500$, $\overline{\mathcal{B}i} = 0.5$, $\kappa_\theta = 0.26$, $\mu_p = 0.0$ and $\beta_p = 0.8$.

Chapter 13

Conclusions

The dynamics of breakup and droplet formation in a liquid jet under various complex situations has been investigated with a view to better understanding, and therefore controlling, interfacial disturbances which lead to rupture. A greater appreciation of such phenomena provides for the possibility of manipulating the resultant production of droplets, including satellite droplets. Particular attention was paid to problems with relevance to industry, including applications like industrial prilling where such control is vital in producing pellets with specific diameters and eliminating wastage through reducing satellite production. We summarize, in this chapter, the salient features gathered from our results. This discussion supplements those presented at the end of each chapter and is intended to give a concise description of some of the more important points noted therein.

A substantial portion of this thesis is devoted to gaining a mathematical understanding of the industrial prilling process. In addition, we hope that some of the topics discussed in preceding chapters, like the use of insoluble surfactants and insonifcation at the orifice, will provide a means to improve the process and create greater efficiency. As has already been mentioned, in such a process the rotation of the container from which the jet emerges produces curved jets which breakup due to centrifugal instabilities. Thus in this case, it is the rate of rotation which can be used to manipulate droplet sizes and breakup

lengths. Building upon previous works we have considered a theoretical stability analysis of a slender liquid jet emerging from an orifice placed on a rotating container. The liquid was modelled as an inelastic non-Newtonian fluid obeying a power law constitutive equation. In the analysis, the limit of high rotation speeds was considered, allowing us freedom to neglect the effects of gravity. Such parameter ranges have direct relevance to industrial prilling (see Wong *et al.* (2004)). The basic flow was computed using an asymptotic analysis which exploited the slenderness of the liquid jet (using an aspect ratio formed by the ratio of the orifice radius to tank radius). A temporal instability of the basic flow was investigated in the framework of linear stability theory and a dispersion relation between (local) wavenumber and growth rate were derived. A comparison with previous linear theories for Newtonian liquid jets was also made. It was found that at high rotation rates, longer jets with larger droplets were expected for shear thickening liquid jets when compared to shear thinning jets. In addition, the rotation of the container was shown to affect significantly the growth rates and most unstable modes of disturbances.

In Chapter 5 the one dimensional (reduced) set of equations for a spiralling liquid jet obeying a power law rheology (derived using the asymptotic analysis of the previous chapter) were solved numerically using a finite difference scheme based on the two-step Lax-Wendroff method. Apart from altering the rotation rates, surface tension and viscosity of the fluids under consideration the simulations allowed the manipulation of disturbances at the orifice. In particular, the initial amplitude of the disturbances could be changed as could the wavenumber (or equivalently the frequency) of disturbances at the orifice.

In particular, we noticed that a significant reduction in satellite droplet sizes could be obtained by increasing the shear thinning properties of the fluid. Decreasing the rotation rate was found to increase main droplet sizes for both shear thinning and shear thickening fluids.

Additionally, we found significant differences in the breakup of shear thinning and

shear thickening liquid jets near the final stages of breakup, as can be observed in Fig. 5.20. In almost all the numerical simulations carried out in this thesis we found that shear thickening jets always produce more droplets than shear thinning jets. Moreover droplets are larger and altogether the process of breakup resembles that of the breakup of a very viscous Newtonian liquid jet. We have seen that both break up lengths and satellite droplet sizes decrease as the shear thinning properties of the fluid are increased. Also the relative importance of rotation rates for shear thickening liquids as compared to shear thinning fluids have been investigated.

The process of breakup in power law liquid jets has highlighted the switching of breakup from downstream to upstream of droplets and vice versa. Even though such phenomena is observed for Newtonian jets, a clear explanation of the reasons behind this is still lacking.

We next extended this work so as to include the effects of surfactants. The introduction of such 'agents' on the free surface introduces an additional parameter with which to control the dynamics of breakup and thus can be used in unison with rotation to produce desired droplet features. Whilst the presence of surfactants will always delay breakup and lead to, in general, longer breakup lengths we have noticed a number of interesting features when surfactants are used in conjunction with variable rotation rates, these include

- The steady state trajectories of jets emerging from a rotating container tend to curve less and the radius along the jet decays more quickly when the importance of surfactants (characterized by the variable β) or initial concentration of surfactants is increased.

- Larger discrepancies between the breakup lengths of rotating liquid jets *with* and *without* surfactants are observed for high rotation rates in comparison to low rotation rates. This suggests that high rotation rates exaggerate the effects of surfactants on

the growth of disturbances.

- A significant increase in the difference in sizes between satellite droplets as the rotation rate is increased which, contrary to the effect on breakup lengths, suggests that increasing the rotation rate reduces the ability of surfactants to affect satellite droplet formation.

- Irrespective of the rotation rate, we found that in all cases the sizes of satellite droplets were smaller than their surfactant-free counterparts.

The inclusion of gravity (characterized by the non-dimensional Froude number $\mathcal{F}$) into the model for a rotating liquid jet allowed the opportunity of consolidating the work of previous chapters (although we did not consider non-Newtonian effects). The limit of small rotation rates ($\mathcal{R}b \to \infty$) so that we have a jet emerging from an orifice and falling under the influence of gravity was also considered. A linear stability analysis of these situations has revealed that the wavenumber of the most unstable mode along with the growth rate of this mode increases as the Froude number is decreased (i.e., the relative importance of gravity is increased). The use of surfactants in these cases is also shown to have a retarding effect on the growth of disturbances.

We included a short chapter devoted to an investigation on the insonification of rotating liquid jets, which can be achieved by, for example, using a loudspeaker at the orifice to generate a sound wave. We presented some simulations depicting the breakup of a shear thinning liquid jet undergoing insonification using a sound amplitude ten times greater than the 'natural' amplitude of disturbances. We found that

- Satellite droplets for rotating shear thinning liquid jets decrease as the frequency of the sound wave is increased.

- Shear thickening liquid jets generate larger droplets upstream of the breakup point as the frequency of the sound wave is increased.

In chapters nine and ten we investigated the effects of using a second fluid to generate a straight two-fluid or compound jet. Such jets have applications in their own right but can also be used to stabilize - or destabilize (depending on the type of application) the inner jet and thus provide the possibility of controlling some features of the breakup of the inner jet. The case of an inviscid-inviscid jet was considered using a linear stability analysis, this revealed

- Growth rates of disturbances increase as the interfacial surface tension is increased.
- The wavenumber of the most unstable mode also increases as the interfacial surface tension is increased and there exist certain critical values of the wavenumber (which depend upon the initial conditions, particularly the inner jet radius) above which disturbances no longer grow but oscillate.
- Increasing the wavenumber leads to smaller growth rates but larger wavenumbers at which disturbances are maximal.

A numerical investigation into the breakup of inviscid-inviscid compound liquid jets revealed a number of interesting features not seen previously, these included

- the formation of compound droplets with multiple cores, usually of different sizes when the interfacial surface tension ratio and wavenumber of disturbances were appropriately chosen.

The breakup of a viscous compound liquid jet when both the inner and outer fluids have a non-Newtonian rheology has been investigated numerically. The governing equations were reduced to a set of one dimensional equations with a single equation governing the velocity of both the inner and outer fluids. We found that

- The flow index number of the outer fluid dominates the dynamics of rupture and subsequent droplet formation.

We have also considered the breakup of liquid jets on the microscale by incorporating the effects of theory of the interface formation. Our numerical simulations support the linear results of Decent (2006) which suggest that for very viscous jets (or alternatively for jets with a very small radius)

- the breakup length can be significantly longer than predicted by the standard model.

In particular we examined the evolution of a liquid jet of initial radius 0.1μm having a viscosity ten times that of water. We investigated the most unstable wavenumbers associated with such microjets using the theory of interface formation and the classical slender jet formulation.

- We found that the theory of interface formation predicts slightly smaller value of the most unstable wavenumber compared with the classical theory. This result is in agreement with prediction of molecular dynamics simulations of Kwano (1998).

The limitations of the numerical method used were discussed and possible suggestions to improve the numerical method and explore more parameter ranges where the theory of interface formation might reveal more noticeable effects were made.

In chapter twelve we considered the breakup of a straight jet subject to thermal modulation at the orifice. In this case a number of points worth noting were

- The advection of thermal energy along the jet leads to Marangoni-type flows which work *with* capillary pressure and help thin the jet and lead to earlier breakup times and shorter breakup lengths.

- Different types of heating 'patterns' at the orifice were considered including pulsed heating. In general we found that the types of heating only affected the distribution of temperature along the jet, at least for large Peclet numbers anyway.

- There were substantial changes to satellite droplet sizes when the frequency of heating at the orifice is changed, in particular we found that satellite droplets decrease in size, by almost a third, when the frequency of heating κ_θ is varied between $0.35 < \kappa_\theta < 0.85$.

- For certain fluids, the dependence of viscosity on temperature can be significant. We considered a number of such cases and found as expected that jets with large values of μ_p tend to break earlier.

- A thermal disturbance at the orifice can induce rupture of a liquid jet in the absence of any initial (velocity) disturbance.

- The relative importance of surface disturbances to thermally generated Marangoni flows upon the dynamics of rupture is characterized by the ratio δ/δ_θ.

In summary a number of different techniques to manipulate the breakup and droplet formation in a liquid jet were considered. In all these cases we found that significant differences in breakup lengths and/or droplet sizes (including satellite droplets) can be achieved by altering fluid parameters and/or external conditions.

Chapter 14

Future Work

14.1 Slender liquid jets

The advent of new industrial applications, along with variations of existing ones, which take advantage of the rupture of a thread of liquid to generate droplets has created a need for greater understanding of the breakup of liquid jets in complex settings. Although this need has been met somewhat with a growth in research in modern times, there is still a great paucity in understanding the phenomena of rupture when the fluid thread is neither straight nor Newtonian. Inelastic non-Newtonian liquid jet breakup (along with the dynamics of pinch-off) have received considerably less attention than their Newtonian counterparts. This is despite the relative simplicity of the constitutive equation for fluids with shear rate-dependent material properties. As such there are numerous extensions to the work contained within this thesis. To begin with, only the simplest non-Newtonian liquid was considered for the spiralling liquid jet problem. Making use of the Carreau model to investigate shear thinning spiralling liquid jets would be a good extension especially for extremely small values of the flow index number. Another possible extension would be an investigation of the more intricate dynamics of pinch-off and drop formation along curved viscoelastic liquid jets. For the equivalent straight jet problem a number

of interesting features, like drop oscillations and drop merging (see Classen *et al.* (2005) and Li & Fontelos (2003)), have already been observed and are likely to be enhanced for rotating liquid jets. As with all liquid jet studies experimental studies provide the backdrop with which to compare linear and non-linear theories. In particular the role of exit effects and gravity have yet to be incorporated into the theories presented so far and it would be interesting to see if such factors play an important part in spiralling jet breakup (see also Appendix C).

The effects of the surrounding fluid on the disintegration on a thread of fluid is yet to be fully explored in the literature. Although some attempt at understanding the dynamics of a liquid jet emerging in a laminar flow has been made (see Cramer *et al.* (2002)), there is still a great shortage in such studies. Although there are some applications where a fluid may be injected into another fluid (say of an equal density or viscosity) it is much more common to find a liquid thread disintegrating in a fluid with a much smaller viscosity and density. Whilst in many cases the surrounding fluid is considered quiescent, in cases where the surrounding fluid is being externally driven to produce a cross-flow situation, the effect on the dynamics of pinch-off might be significant. At the time of writing this thesis there a no works dealing with the effect of the surrounding fluid on the breakup of a spiralling liquid jet. An obvious problem with considering a spiralling liquid jet emerging from a rotating container into an ambient fluid (which has a viscosity higher than air) is the ability to create a coherent jet without resorting to very high rotation rates. Nevertheless an analysis of curved jets (say falling under the influence of gravity) in another fluid would provide one extension to this thesis which would consolidate all the techniques which we have used to date. In addition when considering liquid microjets it is perhaps prudent to consider the effects of the surrounding medium, which are likely to have a greater effect on rupture, especially if the surrounding fluid is not quiescent but is in, say, laminar flow.

14.1.1 Thermal Modulation

The analysis presented on the effects of periodically heating a liquid jet could be extended by considering more complex patterns of heating at the nozzle. In particular, the ease with which a liquid jet may be heated (using MEMS device for example) at the nozzle, and especially heated with a predetermined geometry, means that an investigation of the instability of a straight liquid jet subject to non-axisymmetric disturbances could be investigated. It may be possible to consider the effects of heating the orifice in such a way so that only a portion of the emerging jet is heated. For example, if the heating mechanism has a 'ring' like structure, then heating can be applied at the orifice in such a way that, in cylindrical coordinates, only the portions $0 < \theta < \pi/2$ and $\pi < \theta < 3\pi/2$ are heated (which corresponds to heating the first and third quadrant of a circle). Clearly the resulting flow would be expected to have flow some θ-dependency. Thus, we could rewrite our system so as to include this θ dependence in all our variables. The resulting 2D set of equations would then need to be solved on the domain $0 < z < l_b$ and $0 < \theta < 2\pi$ both of which are fixed so the computations need not have adaptive meshes (which is a requirement when the radial dependence is included at leading order).

In order to fully investigate periodically heated non-Newtonian fluids it is necessary to develop a model for the change in viscosity with temperature for such fluids. Very little is available in the literature in this regards and thus is something which could form the basis of future work.

14.1.2 Dynamics near rupture

The phenomena of switching in the location of breakup for rotating liquid jets is something which is not yet fully understood. The complication arises when we have a rotating thread consisting of a drop which has thinning ligaments both upstream and downstream of the droplet. This has been observed both experimentally and numerically. In the simulations

we have presented we have noticed that only towards the very last stages of rupture can we tell whether breakup will occur behind the droplet or in front of it. It is probable that radial flow in the vicinity of rupture is responsible for the future evolution of the liquid thread near this point. It will therefore be interesting to explore this phenomenon using a two dimensional code which takes account of radial flow within the jet. This is the focus of current research within the School of Mathematics.

14.1.3 Compound liquid jets

A natural extension of the viscous compound liquid jet studies would be to introduce a radial dependence to the leading order velocity components within both fluids. This will allow the inner and outer fluids to have different velocities and will lead to a much more realistic model with which to make comparisons to experiments. In addition the inviscid-inviscid analysis could be extended to investigated curved compound liquid jets. In this case the effects of gravity on the formation of droplets with multiple cores would be interesting.

14.2 Two fluid flow in confined geometries.

In this section, with a view to presenting further ideas for possible future work, we shall briefly discuss two important methods of generating droplets; flow in T-shaped junctions and droplets formed in flow focusing.

14.2.1 Flow Focusing

The creation of small droplets with a selected range of diameters (usually much smaller than the diameter of the nozzle) is both highly desirable and economical in a number of practical applications. If a liquid jet is produced from a nozzle, syringe or orifice (or other similar device) the size of droplets produced will always be of the order of the typical diameter of the jet. This is problematic (and potentially much more expensive)

if droplets with a range of diameters are required. However, this issue can be partially resolved by exploiting satellite droplet formation (which although sometimes seen as a parasitic effect of breakup, can be utilized to produce very tiny droplets). Nevertheless to avoid inefficiency and wastage (which is important if the fluid is expensive or difficult to produce) a standard (and preferably less expensive fluid) can be used to 'focus' a liquid jet (see Fig. 14.1). This technique is known as *hydrodynamic focusing* and is very effective in producing droplets of desired sizes by varying the flow rate of the continuous and or dispersed phase.

In particular Xu & Nakajima (2004) used a combination of hydrodynamic focusing and microfluidic geometry to develop a microchannel droplet generation technique (see Fig. 14.1). The main ideas in this technique were to use two channels (containing the continuous phase) at an acute angle to the main channel (carrying the dispersed phase) so that the dispersed fluid was 'squeezed' by the continuous fluid upon leaving the junction. This led to the formation of a microthread, many times smaller than the main channel width, which eventually broke up into droplets due to surface tension. Xu & Nakajima (2004) showed that width of the dispersed phase d on exiting the T-junction could be controlled by changing the ratio of the flow rate of the dispersed phase F_d and the flow rate of the continuous phase F_c (i.e., changing $\Omega = F_d/F_c$). In particular they found that increasing Ω led to smaller values of the diameter of the microthread d on leaving the T-junction . This is to be expected since the continuous phase exerts a 'focusing' effect on the dispersed phase as the fluid leaves the T-junction orifice. The flow rate of the dispersed phase was also found to effect the narrowing of the microthread on leaving the junction as d decreased with increasing F_d.

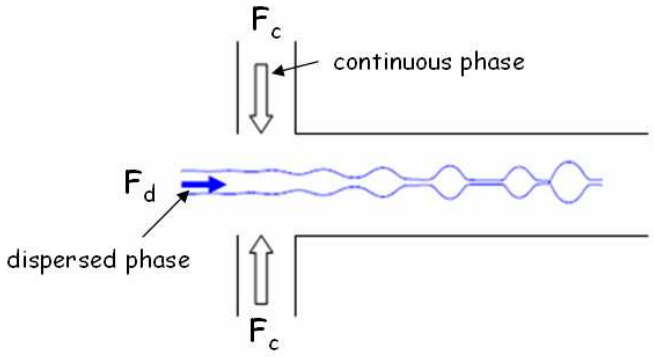

Figure 14.1: A diagram showing how 'flow focusing' can be used to manipulate the breakup of a liquid jet. In general the continuous phase is used to 'squeeze' the dispersed phase and create droplets.

14.2.2 T-Junctions

The flow of two immiscible fluids at a junction is ubiquitous in both nature (e.g flow through porous structures) and science (microfluidic applications). However despite the importance of such flows very little is still known about the underlying dynamics. The simplest way of examining such flows is to consider the dynamics of two immiscible liquids meeting at a T-junction (see Fig. 14.1 with only one tube for the continuous phase). In this case it has been found that modifications of the flow rates of the dispersed and continuous phases can result in droplet formation (see Garstecki *et al.* (2006) and Antencia & Beebe (2005)).

An interesting future direction for this thesis will be to examine in more detail the drop formation techniques in T-shaped junctions. At present there is no literature available (none which this author could find) which deals with a mathematical model of this process. In particular it would be nice if the drop formation in a tube (hanging pendant drop) technique which is widely found in the literature could in some way be combined with flow in a channel with a constriction (albeit a time dependent one). Any progress for this model will probably require a boundary integral method to solve for the evolving interface

between the dispersed and continuous phase.

A mathematical treatment of the different methods described above will also be an interesting project, especially since there is a clear similarity (where the two immiscible fluids meet) between the two methods.

Appendix A

Vector and Tensor Identities

In many industrial applications, like those considered in this thesis, it is convenient to use orthogonal coordinate systems. We list here some useful vector identities for orthogonal coordinates.

The divergence of a vector in an orthogonal curvilinear coordinate system. Let the structure functions for this coordinate system be h_u, h_v and h_w, then the divergence of a vector field $\boldsymbol{\zeta}(u, v, w)$ can be expressed as

$$\boldsymbol{\nabla} \cdot \boldsymbol{\xi}(u, v, w) = \frac{1}{h_u h_v h_w} \left(\frac{\partial}{\partial u}(h_v h_w \xi_u(u, v, w)) + \frac{\partial}{\partial v}(h_u h_w \xi_v(u, v, w)) + \frac{\partial}{\partial w}(h_u h_v \zeta_w(u, v, w)) \right). \tag{A.1}$$

The divergence of the second order stress tensor $\boldsymbol{\Pi} = \sigma_{ij}$ are more involved and are given by

$$(\nabla \cdot \boldsymbol{\Pi})_1 = \frac{1}{h_u h_v h_w} \left(\frac{\partial}{\partial u}(h_v h_w \sigma_{11}) + \frac{\partial}{\partial v}(h_w h_u \sigma_{21}) + \frac{\partial}{\partial w}(h_u h_v \sigma_{31}) \right) + \frac{\sigma_{21}}{h_u h_v} \frac{\partial h_u}{\partial v} + \frac{\sigma_{31}}{h_u h_w} \frac{\partial h_u}{\partial w} - \frac{\sigma_{22}}{h_u h_v} \frac{\partial h_v}{\partial u} - \frac{\sigma_{33}}{h_u h_w} \frac{\partial h_w}{\partial u}, \tag{A.2}$$

$$(\nabla \cdot \boldsymbol{\Pi})_2 = \frac{1}{h_u h_v h_w} \left(\frac{\partial}{\partial u}(h_v h_w \sigma_{12}) + \frac{\partial}{\partial v}(h_w h_u \sigma_{22}) + \frac{\partial}{\partial w}(h_u h_v \sigma_{32}) \right) + \frac{\sigma_{32}}{h_v h_w} \frac{\partial h_v}{\partial w} + \frac{\sigma_{12}}{h_v h_u} \frac{\partial h_v}{\partial u} - \frac{\sigma_{33}}{h_v h_w} \frac{\partial h_w}{\partial v} - \frac{\sigma_{11}}{h_v h_u} \frac{\partial h_u}{\partial v}, \tag{A.3}$$

and

$$(\nabla \cdot \mathbf{\Pi})_3 = \frac{1}{h_u h_v h_w}\left(\frac{\partial}{\partial u}(h_v h_w \sigma_{13}) + \frac{\partial}{\partial v}(h_w h_u \sigma_{23}) + \frac{\partial}{\partial w}(h_u h_v \sigma_{33})\right) + \frac{\sigma_{13}}{h_w h_u}\frac{\partial h_w}{\partial u} + \frac{\sigma_{23}}{h_w h_v}\frac{\partial h_w}{\partial v} - \frac{\sigma_{11}}{h_w h_u}\frac{\partial h_u}{\partial w} - \frac{\sigma_{22}}{h_w h_v}\frac{\partial h_v}{\partial w}. \tag{A.4}$$

The laplacian in orthogonal coordinates is given by

$$\nabla^2 = \frac{1}{h_u h_v h_w}\left(\frac{\partial}{\partial u}\left(\frac{h_v h_w}{h_u}\frac{\partial}{\partial u}\right) + \frac{\partial}{\partial v}\left(\frac{h_w h_u}{h_v}\frac{\partial}{\partial v}\right) + \frac{\partial}{\partial w}\left(\frac{h_u h_v}{h_w}\frac{\partial}{\partial w}\right)\right). \tag{A.5}$$

Appendix B
Dimensional Analysis in Jet Breakup Length.

Dimensional Analysis provides a powerful technique to determine an approximate relationship between the breakup length of a liquid jet and the variables used to describe the jet. Using the Buckingham Pi theorem, which states that

> The number of dimensionless groups used to describe a situation involving n variables is equal to $n-r$ where r is the rank of the dimensional matrix of the variables,

we can determine an expression for the breakup length of a liquid jet. We follow the analysis of Anno (1977) and first list the physical quantities involved in jet breakup with their dimensions (see Table B.1). Thus we assume that the breakup of a liquid jet depends solely upon the six variables tabulated in Table 1. However these variables, themselves, only depend upon three fundamental units: M (mass, S.I. units of kilograms), L (length, S.I. unit of meters) and T (time, S.I. unit of seconds) so that $r = 3$, and thus we expect $n - r = 3$ dimensionless groups used to describe jet breakup. In this case the problem can be written as in Anno (1977) so that we have

$$f(l_b, a, U, \rho, \mu, \sigma) = 0, \quad \text{and} \quad \phi(\pi_1, \pi_2, \pi_3) = 0,$$

where

$$\begin{aligned} \pi &= l_b^a a^b U^c \rho^d \mu^e \sigma^f = L^a L^b \left(\frac{L}{T}\right)^c \left(\frac{M}{L^3}\right)^d \left(\frac{M}{LT}\right)^e \left(\frac{M}{T^2}\right)^f \\ &= L^{a+b+c-3d-e} M^{d+e+f} T^{-c-e-2f}. \end{aligned} \tag{B.1}$$

We can choose three of the six constants (a-f) arbitrarily (although we must ensure that they are independent of the other three constants). As a first estimate we assume that one of the dimensionless groups contains l_b/a sot that $a = 1$ and $b = -1$. In addition eliminating surface tension from the problem $f = 0$ we have that $c = d = e = 0$ so that

$$\pi_1 = l_b^1 a^{-1} U^0 \rho^0 \mu^0 \sigma^0. \tag{B.2}$$

Variable	Symbol	Dimensions
Jet breakup length	l_b	L
Jet radius	a	L
Typical jet velocity	U	L/T
Liquid density	ρ	M/L^3
Liquid viscosity	μ	M/LT
Surface tension	σ	M/T^2

Table B.1: A list of variables used to describe the breakup of a liquid jet with their dimensions.

For the dimensionless group π_1 we do not have viscosity appearing, and in order to rectify this we now choose $e = 1$. Since π_1 contains l_b we can choose $a = 0$ and again we also choose $f = 0$ (no surface tension). We then must have $b = c = d = -1$. This leads to another dimensionless group, namely

$$\pi_2 = l_b^0 a^{-1} U^{-1} \rho^{-1} \mu^1 \sigma^0 = \frac{\mu}{\rho a U} = \frac{1}{\mathcal{R}e}, \tag{B.3}$$

where $\mathcal{R}e$ is the familiar Reynolds number. For the last dimensionless group we include surface tension so that $f = 1$, we again take $a = 0$ and now choose $e = 0$. We then have $b = d = -1$ and $c = -2$ so that

$$\pi_3 = l_b^0 a^{-1} U^{-2} \rho^{-1} \mu^0 \sigma^1 = \frac{\sigma}{\rho a U^2} = \frac{1}{We}, \tag{B.4}$$

where We is the Weber number. Thus we have

$$\phi \left[\left(\frac{l_b}{a} \right), \mathcal{R}e, We \right] = 0, \tag{B.5}$$

whence the simplest functional relationship for the breakup of a liquid jet can be expressed as

$$\left(\frac{l_b}{a} \right) = k \mathcal{R}e^{\alpha} We^{\beta}, \tag{B.6}$$

where α and β are constants to be determined experimentally. For low velocity jets Weber (1931) formulated the expression

$$l_b = a\sqrt{We} \ln \left(\frac{a}{2\delta} \right) \left[1 + \frac{3\sqrt{We}}{\mathcal{R}e} \right], \tag{B.7}$$

where δ is the amplitude of the initial perturbation.

Appendix C
Exit Conditions and Relaxation of Velocity.

When a liquid jet emerges from a nozzle or orifice placed at the end of a tube (as shown in Fig. C.1) the velocity profile changes from a Poiseuille profile to that of plug flow. This is a result of the change in shear stress which has a finite value along the nozzle (right up to $z = 0$) and then changes to zero (due to the assumption that the effects of the surrounding fluid are negligible) after $z = 0$. We will demonstrate the relaxation of the velocity profile by considering a simple momentum balance. We will follow closely the analysis of Middleman (1995) but here we generalize the foregoing analysis to include the effects of shear thinning and shear thickening.

Let us assume that the velocity profile for a power law fluid in a tube (see Spurk (1997) p.199), can be expressed as

$$u_z = U_0 \frac{3\alpha + 1}{\alpha + 1} \left(1 - \left(\frac{r}{R_0} \right)^{1+\frac{1}{\alpha}} \right), \tag{C.1}$$

where α is the flow index number, R_0 is the radius of the tube and U_0 is some average velocity[1]. We assume that this expression for the profile is valid right up to the tube exit $z = 0$.

Far downstream of the tube, it is reasonable to expect that the velocity profile is that of plug flow (with velocity U_∞ and radius R_∞), since in this region there is no longer any shear stress on the free surface of the jet. Thus we expect

$$u_z = U_\infty. \tag{C.2}$$

[1]In general the average velocity will also depend upon the flow index number so that

$$U_0 = \frac{\alpha}{3\alpha + 1} (\tau_w / m)^{1/\alpha} R,$$

where τ_w is the shear stress at the tube wall and m is the flow consistency number. However this dependency does not affect the resulting analysis.

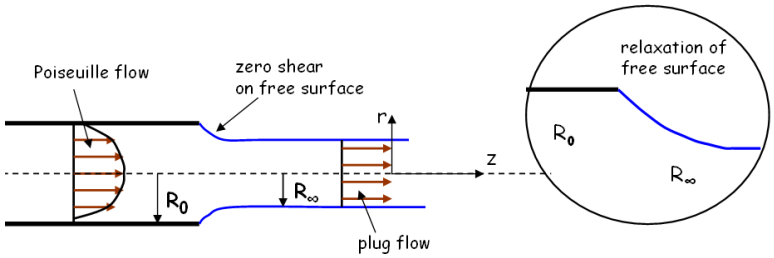

Figure C.1: The relaxation of the jet profile after emerging from a tube.

We now consider the conservation of mass and axial momentum. If the fluid is assumed to be incompressible we have

$$R_\infty^2 U_\infty = R_0^2 U_0 \tag{C.3}$$

from conservation of mass. The conservation of momentum is more involved (see Middleman (1995)), however since here we wish to simply give an idea of how the flow index number of the fluid can affect the relaxation of the liquid jet upon leaving the tube we follow Middleman and simply equate the momentum fluxes at the tube exit with the momentum flux some distance away from the tube exit when the velocity distribution have sufficiently relaxed to that of plug flow. This leads to

$$\int_0^{R_0} \left(\frac{3\alpha+1}{\alpha+1}\right)^2 \rho U_0^2 \left(1-\left(\frac{r}{R_0}\right)^{1+\frac{1}{\alpha}}\right)^2 r dr = \int_0^{R_\infty} \rho U_\infty^2 r dr, \tag{C.4}$$

so that

$$\left(\frac{3\alpha+1}{\alpha+1}\right)^2 \rho U_0^2 \left(\frac{r^2}{2} - \frac{2R_0^\alpha}{R_0^{\alpha+1}} \cdot \frac{\alpha R_0^{3+\frac{1}{\alpha}}}{3\alpha+1} + \frac{R_0^\alpha}{R_0^{2\alpha+2}} \frac{\alpha R_0^{4+\frac{2}{\alpha}}}{2(2\alpha+1)}\right)_0^{R_0} = \frac{\rho}{2} U_\infty^2 R_\infty^2. \tag{C.5}$$

After simplifying we get the identity

$$\frac{3\alpha+1}{2\alpha+1} R_0^2 U_0^2 = R_\infty^2 U_\infty^2, \tag{C.6}$$

which after using (8) we have

$$\xi = \frac{R_\infty}{R_0} = \sqrt{\frac{2\alpha+1}{3\alpha+1}}. \tag{C.7}$$

Thus ξ is a measure of the contraction of the liquid jet upon leaving the orifice. For Newtonian liquids, where $\alpha = 1$, we have that $\xi = \sqrt{3}/2 = 0.866$, a result first derived by Harmon (1955) and agreeing with the experimental results of Middleman & Gavis (1961) at relatively large Reynolds numbers, $\mathcal{R}e \sim 100$. For general power law liquids where

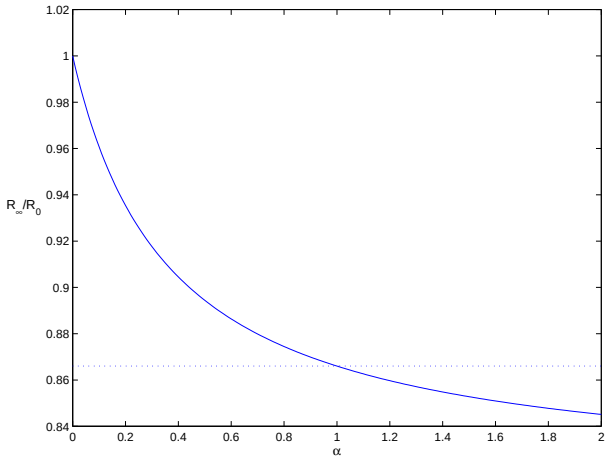

Figure C.2: The contraction of a liquid jet after emerging from a tube. It can be seen that as the flow index number α increases the jet contracts more.

$0 < \alpha < 2$ we have different values of ξ as shown in Fig. C.2. We see that as the flow index number α is increased we have a greater contraction of the jet downstream of the orifice. In addition for highly shear thinning liquid jets, where α is very small, we have almost no contraction of the jet.

At low Reynolds number, such that $\mathcal{R}e \sim 10$, experimental results (Middleman and Gavis (1961)) show that $\xi \sim 1.1$ which does not correlate with the simplistic theory presented above. Two reasons stand out in explaining why, firstly at low Reynolds numbers surface tension cannot be ignored and secondly the surface in reality will attempt to 'relax' before the tube exit $z = 0$ due to upstream diffusion of vorticity from the tube exit (see Middleman (1995) for more details). Indeed Middleman (1995) suggest rewriting the momentum balance equation above so that we have, for Newtonian fluids,

$$\int_0^{R_0} \left(\rho u_z^2(z=0) + p_0 - 2\mu \left(\frac{\partial u_z}{\partial z} \right) \right) r dr - \int_0^{R_\infty} (\rho U_\infty^2 + p_\infty) r dr = 2\pi\sigma(R_0 - R_\infty), \quad \text{(C.8)}$$

where σ is the surface tension and $p_0 = \sigma/R_0$ and $p_\infty = \sigma/R_\infty$ respectively.

C.1 Exit velocity from a tank

The velocity of an inviscid fluid emerging from a hole placed on the side of a cylindrical drum can be calculated using *Torricelli's* equation. To do this we first use Bernoulli's equation[2] without the time derivative, which can be written as (see also Bird *et al.* (2003))

$$\frac{1}{2}(u_2^2 - u_1^2) + \int_{p_1}^{p_2} \frac{1}{\rho} dp + g(h_2 - h_1) = 0. \quad \text{(C.9)}$$

[2]Note that here we have integrated along a streamline to get this result. In addition we have assumed that the gravitational force can be written in conservative form.

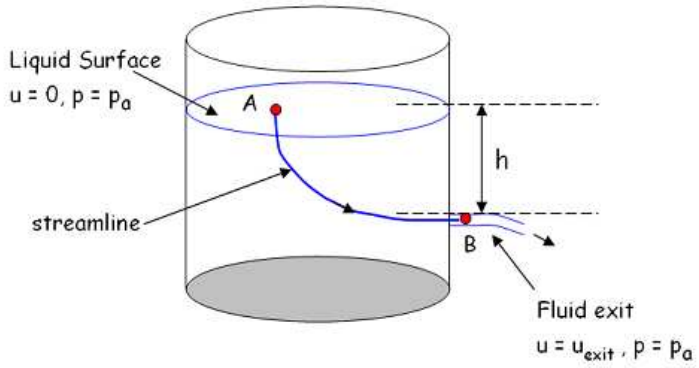

Figure C.3: Fluid emerging from a partially filled cylinder which has an uncovered top. Particles 'A' and 'B' are on the same streamline.

In Fig. C.3 we see that particles 'A' and 'B' lie along the same streamline and that both these particles are at the atmospheric pressure p_a so that in the above equation the second term is identically equal to zero. Substituting the velocities and noting that $h_2 - h_1 = h$ we have that

$$v_{exit} = \sqrt{2gh}, \tag{C.10}$$

which is known as Torricelli's equation. It is important to note that this equation is only valid for flows which are incompressible and under the assumption that the height of the fluid surface is changing very slowly with time.

Appendix D
Unsteady Centreline Analysis.

We now consider an unsteady trajectory so that we allow the leading order components of X and Z to be time dependent. Our analysis will follow closely that presented by Părău *et al.* (2007). A fuller and more detailed analysis of the unsteady trajectory is given in Partridge (2006). When X and Z are time dependent the kinematic condition necessitates that the radial and azimuthal velocity components have leading order terms of the form

$$v = v_0(s,\phi,t) + \varepsilon n v_1 + \cdots, \qquad w = w_0(s,\phi,t) + \varepsilon n w_1 + \cdots$$

where all other variables are given in section 4.1. If we denote $E = X_t Z_s - X_s Z_t$ we have from the kinematic condition and conservation of mass equation

$$v_0 = E\cos\phi \qquad \text{and} \qquad w_0 = -E\sin\phi$$

The second tangential stress condition gives

$$v_{1\phi} = w_{1\phi} = 0.$$

The continuity and first tangential stress condition give

$$v_1 = -\frac{u_{0s}}{2} - \frac{SE}{2}, \qquad u_1 = (u_0 S - E_s)\cos\phi,$$

and

$$u_2 = \frac{3}{2}(u_{0s} + SE)\frac{R_{0s}}{R_0} + \frac{u_{0ss} + (SE)_s}{4}.$$

We see that these terms are identical to those presented earlier when the centreline is steady, i.e., $E = 0$. By choosing $w_1 = 0$ and requiring that R_1 be periodic in ϕ we have a new solvability condition from the leading order pressure term

$$\begin{aligned} E_t + u_0(X_{st}Z_s - Z_{st}X_s) + u_0 E_s - \frac{E}{2}(u_{0s} + SE) + \frac{3}{\mathcal{R}e}ES^2 \\ u_0^2 S - \frac{2}{\mathcal{R}b}u_0 + \frac{(X+1)Z_s - ZX_s}{\mathcal{R}b^2} - \frac{3}{\mathcal{R}e}u_{0s}S - \frac{S}{WeR_0}. \end{aligned} \tag{D.1}$$

The leading order Navier Stokes equation in the axial direction becomes

$$u_{0t} - E(X_{st}Z_s - Z_{st}X_s) + u_0u_{0s} + 2u_0ES - EE_s$$
$$= -\frac{1}{We}\left(\frac{1}{R_0}\right)_s + \frac{2}{\mathcal{R}b}E + \frac{(X+1)X_s + ZZ_s}{\mathcal{R}b^2} + \frac{3}{\mathcal{R}e}\frac{(R_0^2(u_{0s} + SE))_s}{R_0^2}. \tag{D.2}$$

Finally the kinematic condition, at leading order can be written as (see Părău *et al.* (2007)

$$R_{0t} + (u_0 - X_tX_s - Z_tZ_s)_s\frac{R_0}{2} + R_{0s}(u_0 - X_tX_s - Z_tZ_s) = 0. \tag{D.3}$$

The Eqs. (D.1)-(D.3) are solved along with the arc length condition for X, Z, R_0 and u_0. If small perturbations to the steady centreline of Chapter 4 of the form $X(s,t) = X_0(s) + \widehat{X}(s,t)$ and $Z(s,t) = Z_0(s) + \widehat{Z}(s,t)$ are considered which are linearized in $\widehat{X}$ and $\widehat{Z}$. Then it can be shown that $\widehat{X}$ and $\widehat{Z}$ always remain small, unless mode 4 breakup occurs (see Părău *et al.* (2007)).

Appendix E
Temperature dependence of viscosity and surface tension in fluids.

E.1 Viscosity in fluids.

Understanding how changes in temperature affect the dynamic viscosity and surface tension of a fluid requires an understanding of the molecular interactions within fluids. Whilst such a molecular theory for gases is well developed, for fluids it is very poorly understood due to the lack of any rigorous kinetic theory of transport properties in fluids.

In this section we present a few equations describing the viscosity of a fluid to its material properties (see also Bird *et al.* (2003)). Our aim here will be, within the scope of this work, to give a brief outline of how changes in temperature affect the viscosity and surface tension of a fluid. For a more detailed analysis the reader is referred to Bird *et al.* (2003) and most textbooks on thermodynamics.

In general the molecules within a fluid can be imagined to be tightly packed into coherent structures so that the motion of individual molecules are restricted to vibrations within a 'cage' like mesh formed by nearest neighbours. Thus, in order for a molecule to move from one position within a cage to another it must navigate its way through an energy barrier (formed by the potential between molecules). By using such energy considerations in light of the theory developed by Henry Eyring[1] one may arrive at the following relation

$$\mu \approx \frac{\tilde{N}h}{\tilde{V}} \exp(3.8T_b/T) \tag{E.1}$$

where h is Planck's constant (6.626×10^{-34} J $\cdot$ s), $\tilde{V}$ is the volume of a mole of liquid, $\tilde{N}$ is the Avogadro number (6.022×10^{23} molecules/g-mol, T_b is the temperature of vaporization and T is temperature. Hence this supports the empirically derived formula for the change in viscosity with temperature (Arrhenius type law) given by $\mu = A \exp(B/t)$ where A and

[1] Henry Eyring (1901-1981) is famous for his development of theories to describe transport properties in liquids.

B are constants and agrees with the experimental findings that viscosity decreases with temperature.

In gases, using the kinetic theory of gases, it is possible to derive the expression

$$\mu = \frac{2}{3\pi^{\frac{3}{2}}} \frac{\sqrt{m\kappa T}}{d^2}, \tag{E.2}$$

where m is the mass of molecules, κ is the Boltzmann constant (1.381×10^{-23} J/K), d is the molecular diameter and T is again the temperature. Thus for gases, unlike liquids, increasing the temperature leads to *higher* viscosities. However, experimental evidence suggests that at low temperatures the viscosity varies more rapidly than $\sqrt{T}$.

E.2 Surface tension in fluids.

We have already come across a definition of surface tension as an inward pull or internal pressure experienced by molecules *on* the free surface to molecules *within* the bulk (see introduction to Chapter 6). This occurs due to the disparity in potential energies between molecules on the free surface and in the bulk. By considering the energy per molecule in a liquid, the surface tension of a liquid can be written as (see Palmer (1976))

$$\sigma = \frac{1}{4} N n \triangle \varepsilon, \tag{E.3}$$

where N is the number of molecules per unit area, n is the number of molecules and $\triangle\varepsilon$ is the energy required to totally overcome the interactive force of its nearest neighbour (this is effectively the energy required to take the particle to infinity).

Statistical thermodynamics can be used to show that the mean thermal energy of a molecule at an absolute temperature T is given by

$$E_t = \kappa T, \tag{E.4}$$

where κ is the Boltzmann constant.

If we let $\triangle\varepsilon_0$ be the potential energy of a molecule at the equilibrium distance r_0[2]from its neighbour (see Batchelor (1967) for more details about equilibrium distances) and use the assumption that the interaction energy between a pair of molecules in a liquid is approximately equal to the mean thermal energy of a molecule at the critical temperature T_c (see Palmer (1976)) we have that

$$\triangle\varepsilon \approx \triangle\varepsilon_0 - \kappa T = \kappa(T - T_c). \tag{E.5}$$

[2]The equilibrium separation distance is approximately $r_0 \approx 3 - 4 \times 10^{-10} m$ and by using the mass of a molecule and the corresponding density of the substance it is possible to work out the average spacing between molecules. For most gases at normal temperatures the average spacing between molecules and their neighbours is approximately $10r_0$ whilst for most liquids it is of the order r_0.

We can estimate N by considering molecules to be cubes having the diameter of a molecule a_m. In one mole of any substance we have $\tilde{N}$ molecules so that for a liquid with molar mass M the average volume per molecule is given by

$$a_m^3 = M/\rho\tilde{N}, \tag{E.6}$$

where $\tilde{N}$ is Avogadros constant and ρ is the density at a *particular* temperature. It therefore follows that

$$N \approx 1/a_m^2 = (\tilde{N}\rho/M)^{\frac{2}{3}} \tag{E.7}$$

whence it follows that

$$\sigma \approx (n/4)(\tilde{N}\rho/M)^{\frac{2}{3}}\kappa(T_c - T). \tag{E.8}$$

Equation (E.8) therefore predicts that the surface tension will decrease with increasing temperature, a result which can be experimentally verified.

Appendix F
Rupture of liquid threads without singularities

In this section our aim is to provide a short insight into the dynamics of rupture in liquid threads using the theory of interface formation as presented by Shikhmurzaev (2005). Our main objective is to demonstrate how the theory of interface formation predicts a reduction in the surface tension in the vicinity of rupture, thus counteracting the 'blow up' of the mean curvature (and therefore pressure) inherent in the standard theory of breakup and pinch-off in liquid jets. The analysis here supplements the work presented in Chapter 11 and is designed to examine the local dynamics associated with pinch-off as opposed to the global dynamics of breakup and droplet formation.

Shikhmurzaev (2005) was the first to incorporate the theory of interface formation into the classical slender jet model. The mathematical formulation is essentially the same as found in Decent (2006) (which is therefore also similar to the analysis of chapter eleven). However there are some notable differences between the two works, in particular certain simplifying assumptions about the the interaction between the interface and the bulk were made in Shikhmurzaev (2005), these simplifying assumptions were removed by Decent (2006). In Shikhmurzaev (2005) the mass exchange between the bulk and the interface was neglected and the surface velocity of the interface was assumed to be equal to the bulk velocity. In addition the full curvature expression for the pressure was not included (which is an ad-hoc inclusion at any-rate and although it does not capture equilibrium shapes near rupture it is sufficient for the present work). The variables were made dimensionless to 'natural' length and time scales so that the resulting leading order equations were given by (see also Shikhmurzaev (2005) and Eqs. (11.31) - (11.36))

$$\frac{\partial u}{\partial t} + u\frac{\partial u}{\partial z} = \frac{1}{R^2}\frac{\partial}{\partial z}(R\sigma) + \frac{3}{R^2}\frac{\partial}{\partial z}\left(R^2\frac{\partial u}{\partial z}\right), \tag{F.1}$$

$$\frac{\partial R}{\partial t} + u\frac{\partial R}{\partial z} + \frac{R}{2}\frac{\partial u}{\partial z} = 0, \tag{F.2}$$

and

$$\frac{\partial \varrho^s}{\partial t} + u\frac{\partial \varrho^s}{\partial z} + \frac{\varrho^s}{2}\frac{\partial u}{\partial z} = 0, \tag{F.3}$$

where the variables have their usual meanings from chapter eleven.
The surface equation of state has the form

$$\sigma = a\varrho^s - b(\varrho^s)^2. \tag{F.4}$$

This set of equations describes the final stages of the evolution of the interface of a liquid thread before rupture[1]. Here we wish to illustrate the physical mechanisms which are relevant in the last stages before breakup and so it is sufficient to consider the evolution of a liquid cylinder subject to an initial symmetric disturbance given by (see Shikhmurzaev (2005))

$$R(z,0) = 1 - A\exp(-Bz^2), \tag{F.5}$$

with initial distributions

$$\varrho^s(z,0) = \varrho^s_e, \qquad u(z,0) = 0, \tag{F.6}$$

and with boundary conditions on the velocity u as

$$u(0,t) = 0, \quad \frac{\partial u}{\partial z} \to 0, \quad \text{as} \quad z \to \infty. \tag{F.7}$$

In Shikhmurzaev (2005), (F.1) - (F.7) were solved using an implicit method with the equilibrium surface density chosen so that $\rho^s_e = 0.6$ (which is consistent with the experiments of Blake and Shikhmurzaev (2002)), and with the constants $A = 0.1$ and $B = 10$. In this section we modify our earlier explicit code (see chapter eleven) to solve the above set of equations with boundary and initial conditions using similar values for the constants. The results for the surface density, surface tension and radius are shown in Figs. F.1-F.3.

A qualitative picture of the thinning process of a liquid thread is given in Shikhmuzaev (2005) which we recapitulate here. As the capillary pressure drives fluid away from the vicinity of the pinch-off point, the rate of stretching of the cylindrical column (which is proportional to the rate at which 'fresh' free surface area is created) increases. This necessitates that the surface density decrease (due to the high rate of creation of surface area!) as in Fig. F.1. The time scale of the whole process is too small for the interfacial properties to relax to their equilibrium values (i.e., Eq. (F.3) has zero right hand side as opposed to (11.34)) and so the equation of state (F.6) predicts that the surface tension increases slightly from its equilibrium value (see Fig. F.2, and in particular $t = 5.0$). A consequence of the increase in the surface tension is a higher capillary pressure (due to the Laplace-Young equation) which helps drive more fluid out of the neck region (see Fig. F.3). However, and most importantly for the whole process under consideration, the gradient is surface tension causes Marangoni flows which in effect *inhibit* the capillary pressure from displacing fluid away from neck regions. Further reductions in the fluid radius (see Fig. F.3) lead to greater stretching of the free surface and so to a decreasing of the surface density which in turn drags the surface tension down (see the equation of

[1]In particular this set of equations are applicable at very small time scales just before rupture. At these time scales the surface relaxation mechanism is unable to bring surface properties back to their equilibrium values.

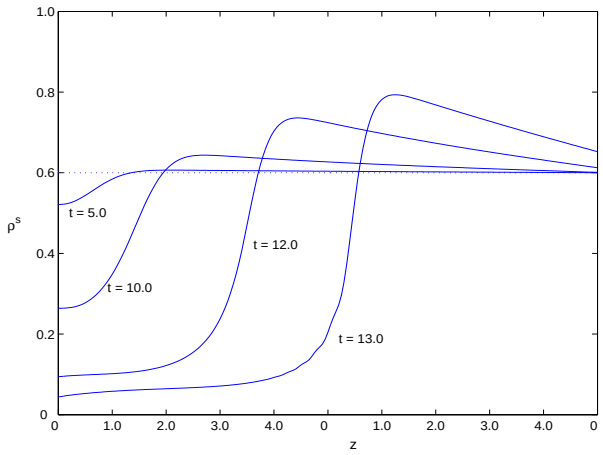

Figure F.1: Profiles of the surface density ρ^s for different times for a liquid thread towards the last stages of rupture. The dotted line represents the equilibrium profile at $t = 0$.

state (F.6) and Fig. F.2). Thus as the fluid radius of the neck decreases (leading to larger mean curvatures) so too does the surface tension, and so by the Laplace-Young equation ($p \sim \sigma(1/R)$) the pressure remains *finite* rather than blowing up to infinity as would occur when using the classical constant surface tension formulation.

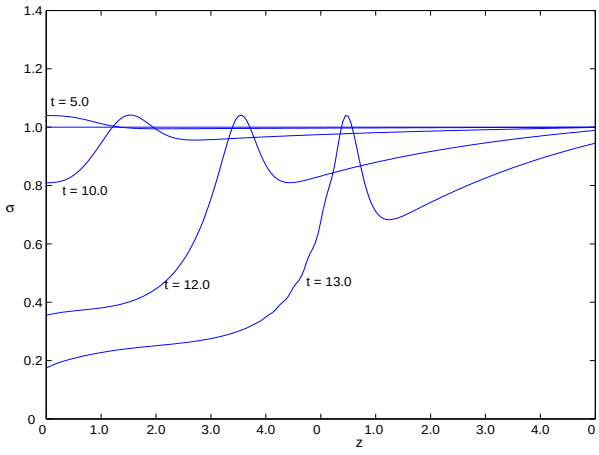

Figure F.2: Profiles of the surface tension σ at different times for a liquid thread towards the last stages of rupture. At equilibrium the surface tension has a uniform value $\sigma = 1.0$.

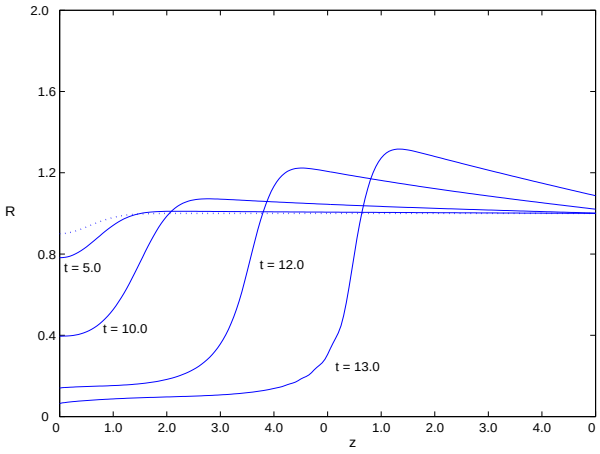

Figure F.3: Profiles of the thread radius R at different times for a liquid thread towards the last stages of rupture. The dotted line represents the equilibrium profile at $t = 0$.

Appendix G
Numerical Scheme: An Example

In this chapter we wish to elaborate upon the numerical scheme employed to determine the profile of a liquid jet at 'breakup'. Recall from (5.6) and (5.7) that for a rotating non-Newtonian liquid jet, we wish to solve the following coupled set of equations

$$A_t = [F(u,A)]_s, \tag{G.1}$$
$$u_t = [G(u,A)]_s + H(u,A), \tag{G.2}$$

where

$$F(u,A) = Au \tag{G.3}$$
$$G(u,A,u_s,A_s) = -\frac{u^2}{2} - \frac{4}{We}\frac{(2A+(\varepsilon A)_s - \varepsilon^2 A_{ss})}{(4A+\varepsilon^2 A_s^2)^{\frac{3}{2}}} \tag{G.4}$$
$$H(u_s,A) = \frac{3}{\mathcal{R}e}\frac{1}{A}\left[|\sqrt{3}u_s|^{\alpha-1}u_s A\right]_s + \frac{1}{\mathcal{R}b^2}((X+1)X_s + ZZ_s). \tag{G.5}$$

We choose equally spaced points along both the t and s axes, namely

$$s_j = s_0 + j \times ds \quad (j = 1, 2..J) \quad \text{and} \quad t_n = t_0 + n \times dt \quad (n = 1, 2..N),$$

where $s = s_0$ is the location of the nozzle and $s = s_J$ is the numerical 'end' of the jet. Here t_0 is the initial time. We use our steady state solutions for u and A (calculated using a Runge-Kutta method) to determine u_j^0 and A_j^0 for $j = 0, 1, 2...J$. Similarly we can determine both X and Z from our steady state solution (and since the centreline is assumed to remain steady in the rotating frame we can use these values of X and Z for all successive time steps). Thereafter we use the two-step Lax-Wendroff scheme (which is an explicit finite difference scheme) to carry forward this solution one time step dt at a time. We continue to do this until there exists a value of $A_j < 0.0025$.

To employ the method of Lax-Wendroff we first discretize the expressions for F, G and H. In order to do this we write the spatial derivatives as

$$u_s = \frac{u_{j+1}^n - u_{j-1}^n}{2ds}, \tag{G.6}$$

and

$$u_{ss} = \frac{ui^n_{j+1} - 2 * u^n_j + u^n_{j-1}}{(ds)^2}, \tag{G.7}$$

where similar expressions apply for A.
We thus see that in order to determine a finite difference equation form for F, G and H we require 'imaginary' values for both u and A corresponding to u_{-1}, u_{J+1}, A_{J+1} and A_{-1}. This is easily achieved by using extrapolation methods so that

$$u^n_{J+1} = 2 * u^n_J - u^n_{J-1} \quad \text{and} \quad A^n_{J+1} = 2 * A^n_J - A^n_{J-1},$$

and

$$u^n_{-1} = 3 * u^n_1 - 3 * u^n_2 + u^n_3 \quad \text{and} \quad A^n_{-1} = 3 * A^n_1 - 3 * A^n_2 + A^n_3.$$

We now determine so called 'intermediate' values (this is the first step of the two-step Lax-Wendroff method, see Hirsch (1988)) for u and A (see page 79 for further details). We thus have

$$u^{n+\frac{1}{2}}_{j+\frac{1}{2}} = \frac{1}{2}(u^n_{j+1} + u^n_j) + \frac{dt}{2ds}(G^n_{j+1} - G^n_j) + \frac{dt}{2ds}H^n_j, \qquad j = 0, 1, 2...J \tag{G.8}$$

$$A^{n+\frac{1}{2}}_{j+\frac{1}{2}} = \frac{1}{2}(A^n_{j+1} + A^n_j) + \frac{dt}{2ds}(F^n_{j+1} - F^n_j), \qquad j = 0, 1, 2...J \tag{G.9}$$

Using these 'intermediate' values for u and A we determine 'intermediate' fluxes $\tilde{F}(u^{n+\frac{1}{2}}_{j+\frac{1}{2}}, A^{n+\frac{1}{2}}_{j+\frac{1}{2}})$, $\tilde{G}(u^{n+\frac{1}{2}}_{j+\frac{1}{2}}, A^{n+\frac{1}{2}}_{j+\frac{1}{2}})$ and $\tilde{H}(u^{n+\frac{1}{2}}_{j+\frac{1}{2}}, A^{n+\frac{1}{2}}_{j+\frac{1}{2}})$. We then find u and A (this constitutes the second step of the two-step Lax-Wendroff method) such that

$$u^{n+1}_j = u^n_j + \frac{dt}{ds}(\tilde{G}^{n+\frac{1}{2}}_{j+\frac{1}{2}} - \tilde{G}^{n+\frac{1}{2}}_{j-\frac{1}{2}}) + \tilde{H}^{n+\frac{1}{2}}_{j+\frac{1}{2}}, \qquad j = 0, 1, 2...J \tag{G.10}$$

$$A^{n+1}_j = A^n_j + \frac{dt}{ds}(\tilde{F}^{n+\frac{1}{2}}_{j+\frac{1}{2}} - \tilde{F}^{n+\frac{1}{2}}_{j-\frac{1}{2}}) \qquad j = 0, 1, 2...J \tag{G.11}$$

This system is complemented by boundary conditions at both the nozzle (s=s_0). At the nozzle we have the condition

$$u^n_0 = 1 + \delta\cos(\kappa(n\Delta t)/\varepsilon) \qquad \text{and} \qquad A^n_0 = 1 \quad \text{for } n = 0, 1, 2...$$

We allow this procedure to continue until such a time that a value of A along the jet has reached 0.0025 or less. Once this has occurred (say at $n = N$) we stop the scheme and record the values of u^N_j and A^N_j for $j = 0, 1, ..J$.
We demonstrate the result of one such run of the numerical scheme for a shear thinning liquid jet ($\alpha = 0.6$) for which we take the numerical length of the jet $L = 1.1$. We choose $J = 2200$ which necessitates that $ds = 0.0050$. We also choose $dt = 2e - 6$. The other parameters chosen for this case are $\kappa = 0.85$, $\delta = 0.01$, $\mathcal{R}e = 3000$, $We = 10.0$ and $\mathcal{R}b = 2.0$. The program continues to run until 360049 time steps have been completed

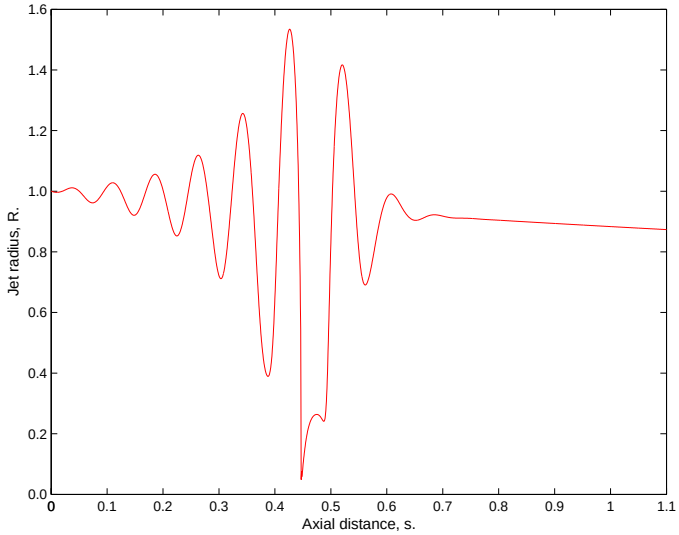

Figure G.1: The radius of a liquid jet at 'breakup'. Breakup occurs when the jet radius is $R = 0.05$ and for this particular case breakup is seen to occur when $s = 0.447$. The breakup time is $t = 0.4825$.

whence the profile for the jet radius $R = A^{\frac{1}{2}}$ is shown in Fig. G.1.

Appendix H
Instability of Non-Newtonian rotating jets with surfactants

In this section we present a short paper on the instability of non-Newtonian liquid jets with surfactants. This work is currently being finalised and will soon be submitted to the Journal of Physics D.

Abstract

The industrial prilling process provides a quick and reliable technique for the production of small spherical pellets and beads. In such a process, the rotation of a liquid jet is utilized to control drop sizes and breakup lengths. In general larger droplets are observed as the rotation rate is decreased. The addition of surfactants to the free surface of a rotating liquid jet provides a possibility of further manipulating breakup lengths and droplet sizes and allows for the possibility of reducing unwanted satellite droplets . In this paper, we build upon the work of Uddin *et al.* [141], and investigate the instability of a rotating liquid jet (having a power law rheology) with a layer of surfactants along its free surface. Using a long wavelength approximation we reduce the governing equations into a set of one dimensional equations. We use an asymptotic theory to find steady solutions and then carry out a linear instability analysis on these solutions.

H.1 Introduction

The manufacture of small spherical pellets can be achieved through the industrial prilling process. In such a process a specially perforated large cylindrical drum is made to rotate about its axis. Molten liquid is pumped into the drum, and long curved jets are produced from the holes in the surface of the drum which break up due to centrifugal and capillary instabilities. Break up leads to the production of droplets, which subsequently solidify, and form pellets. This process is widely used in industry for the manufacture of fertilizers, magnesium and aluminium pellets (see Andersen & Yttri [2] and Ornek *et al.* [101]).

Previous studies to investigate the prilling process for Newtonian liquids have been investigated by Wallwork *et al.* [149, 148] and Decent *et al.* [36]. Nonlinear effects have also been considered by Părău *et al.* [104, 105] and Wong *et al* [153]. The linear instability of rotating power law jets were investigated by Uddin *et al.* [141]. Experimental studies

to model the prilling process for Newtonian jets were performed by Wong *et al.* [153] with a similar investigation for power law jets by Hawkins *et al.* [69].

Previous studies on the effect of surfactants along straight liquid threads or bridges have been carried out by Whitaker [151], who considered the instability of a liquid thread encased in an inviscid environment and Hansen *et al.* [65] who investigated the linear instability of a liquid thread (containing soluble surfactants) with a viscous surrounding fluid. They found, as expected, that surfactants slow the growth of disturbances and that as the importance of surfactant activity increases that the dominant, or most unstable, wavenumber decreases. Timmermans and Lister [139] have considered nonlinear approximations to the governing equations of a surfactant laden thread in an inviscid surrounding. They formulated a one-dimensional nonlinear model to investigate instability of the thread to changes in surface tension gradients. Using a scaling argument they showed that surfactants are swept away from pinching regions and thus have little effect on any dynamics in those regions. Extension of these situations involving coaxial jets have been considered by Kwak and Pozrikidis [84] and Blyth and Pozrikidis [17] and a fully non linear one dimensional approximation to the governing equations for liquid bridges has been performed by Abravaneswaran and Basaran [1]. The effects of surfactants on the deformation of droplets has also been extensively studied (see Stone & Leal [134]). The stability of two-layer channel flow and flow down an inclined plane with insoluble surfactants has been investigated by Blyth & Pozrikidis [15, 16]. A review of the surfactant transport equation for an elongating thread and a stretched interface is provided by Blyth & Pozrikidis [14]. The effects of surfactants on the instability of a curved liquid jet obeying a power law rheology is lacking in the literature and it is our aim in this paper to explore this further.

H.2 Problem Formulation

We assume that a large cylindrical container having radius s_0 is made to rotate with angular velocity Ω along its axis of symmetry. A small orifice is placed at the side of the container having radius a which is considered small in relation to the radius of the container. The orifice is designed in such a way so that the emerging liquid jet is coated with a thin layer of surfactant along its free surface.

We examine the problem by considering a coordinate system (x, y, z) which rotates with the container, having an origin at the axis of the container and with the position of the centre of the orifice at $(s_0, 0, 0)$. The effects of gravity on the jet can be neglected if the centripetal acceleration of the jet $s_0\Omega^2$ is much greater than the acceleration due to gravity g, as is the case with industrial prilling. Then the jet moves solely in the $x - z$-plane and thus we can describe the centreline of the jet by coordinates $(X(s,t), 0, Z(s,t))$, where s is the arclength along the centreline of the jet, measured from the orifice, and t is time.

The rotation of the container causes the jet to curve on leaving the orifice and any analysis of the jet in the rotating (x, y, z) coordinate system becomes cumbersome. We therefore introduce a coordinate system previously used by Wallwork [148] which is similar to the approach adopted by Ribe [118] and Entov & Yarin [52], where we have one

coordinate lying along the centreline of the jet corresponding to the arc length s of the jet, with the remaining coordinates as the plane polar coordinates n, ϕ (radial and azimuthal) in any cross section of the jet. The associated unit vectors are represented by $\mathbf{e_s}$, $\mathbf{e_n}$ and $\mathbf{e}_\phi$ respectively and their derivation is explained further in [148].

To describe the flow we use the velocity vector $\boldsymbol{u} = u\boldsymbol{e_s} + v\boldsymbol{e_n} + w\boldsymbol{e_\phi}$ to arrive at the familiar equations of motion (including the continuity equation) given by

$$\nabla \cdot \boldsymbol{u} = 0, \tag{H.1}$$

$$\boldsymbol{u}_t + \boldsymbol{u} \cdot \nabla \boldsymbol{u} = -\frac{1}{\rho}\nabla p + \frac{1}{\rho}\nabla \cdot (\eta[\nabla \boldsymbol{u} + \nabla \boldsymbol{u}^T]) - 2\boldsymbol{\omega} \times \boldsymbol{u} - \boldsymbol{\omega} \times (\boldsymbol{\omega} \times \boldsymbol{r}), \tag{H.2}$$

where ρ and p are the density and pressure, t is time and η is the apparent viscosity such that

$$\eta = m\left(\frac{\boldsymbol{\gamma} : \boldsymbol{\gamma}}{2}\right)^{\frac{\alpha-1}{2}}, \tag{H.3}$$

where m is the flow consistency number, α is a dimensionless number referred to as the flow index number and $\boldsymbol{\gamma} = \nabla \boldsymbol{u} + (\nabla \boldsymbol{u})^T$ is the rate of strain tensor. Fluids with α less than or greater than unity are termed shear thinning and shear thickening respectively. The angular velocity vector of the container is given by $\boldsymbol{\omega} = (0, \omega, 0)$.

The concentration of surfactant along the free surface of the jet is governed by (see Blyth and Pozrikidis [14])

$$\Gamma_t + \boldsymbol{\nabla}_s \cdot (\Gamma \boldsymbol{u}_s) + \Gamma(\boldsymbol{\nabla}_s \cdot \mathbf{n})(\boldsymbol{u} \cdot \mathbf{n}) = S(\Gamma, B_s) + D_s \boldsymbol{\nabla}_s^2 \Gamma \tag{H.4}$$

where $\boldsymbol{\nabla}_s = (\mathbf{I} - \mathbf{nn}) \cdot \boldsymbol{\nabla}$ is the surface gradient operator, D_s is the surface diffusivity of surfactant and $\boldsymbol{\nabla}_s \cdot \mathbf{n} = \kappa$ where κ is the mean curvature of the free surface. S is the surfactant source term which takes into account absorption from the free surface and is a function of the surfactant concentration on the surface Γ and surfactant concentration in the bulk B_s. In this paper we consider insoluble surfactants (so S is taken as zero) and assume that the diffusivity of surfactant is small and negligible (i.e., $D_s = 0$). Under these assumptions, and after using the properties of the surface gradient operator, we have

$$\Gamma_t + \boldsymbol{u} \cdot \boldsymbol{\nabla}\Gamma - \Gamma \mathbf{n} \cdot ((\mathbf{n} \cdot \boldsymbol{\nabla})\boldsymbol{u}) = 0. \tag{H.5}$$

The boundary conditions which apply on the free surface of the jet are identical to those found in [141] except here the presence of a variable surface tension (which is a consequence of the addition of surfactants) leads to nonzero tangential stresses. Thus we have the normal stress condition can be written as $\mathbf{n} \cdot \boldsymbol{\Pi} \cdot \mathbf{n} = \sigma\kappa$ where $\boldsymbol{\Pi}$ is the total stress tensor given by $p\mathbf{I} + \boldsymbol{\tau}$, $\boldsymbol{n}$ is the normal vector given by $\nabla(n - R(s,t,\phi))/|\nabla(n - R(s,t,\phi))|$ and κ is the mean curvature such that $\kappa = \nabla \cdot \boldsymbol{n}$. The tangential stress conditions are given by $\boldsymbol{t}_i \cdot \boldsymbol{\Pi} \cdot \boldsymbol{n} = \boldsymbol{t}_i \cdot \nabla\sigma$ for $i = 1$ and $i = 2$ where $\boldsymbol{t}_i$ are the two tangent vectors to the normal at the free surface. The kinematic condition is given by $\frac{D}{Dt}(R(s,t,\phi) - n) = 0$, for $n = R(s, \phi, t)$.

the equation of state relating the surfactant concentration Γ to the surface tension of

the liquid-gas interface is given by the nonlinear Szyskowsky equation

$$\sigma = \tilde{\sigma} + \Gamma_\infty R_g T \log\left(\frac{\Gamma_\infty - \Gamma}{\Gamma_\infty}\right) \tag{H.6}$$

where σ_∞ is the surface tension of the liquid in the absence ($\Gamma = 0$) of any surfactant, Γ_∞ is the maximum packing concentration of surfactant, R_g is the universal gas constant and T is the temperature.

We make our equations dimensionless using the transformations

$$\{\overline{u}, \overline{v}, \overline{w}\} = \frac{1}{U}\{u, v, w\}, \quad \{\overline{s}, \overline{X}, \overline{Z}, \overline{t}, \varepsilon\} = \frac{1}{s_0}\{s, X, Z, U, a\},$$
$$\overline{p} = \frac{p}{\rho U^2}, \quad \{\overline{n}, \overline{R}\} = \frac{1}{a}\{n, R\}, \quad \overline{\Gamma} = \frac{\Gamma}{\Gamma_\infty}, \quad \text{and} \quad \overline{\sigma} = \frac{\sigma}{\sigma_e}$$

where U is the exit speed of the jet in the rotating frame, ε is the aspect ratio of the jet, and u, v and w are the tangential, radial and azimuthal velocity components relative to the centreline of the jet respectively.

We exploit the fact that the radius of the orifice is small when compared to the radius of the cylinder by expanding u, v, w, p in Taylor series in εn (see Eggers [49] and Hohman *et al.* [73]), and R, X, Z in asymptotic series in ε. We assume that the leading order axial component of the velocity is independent of ϕ and that the centreline of the jet is unaffected by small perturbations. Thus we have

$$\begin{aligned}
u &= u_0(s,t) + (\varepsilon n)u_1(s,\phi,t) + (\varepsilon n)^2 u_2(s,\phi,t) + \cdots \\
v &= (\varepsilon n)v_1(s,\phi,t) + (\varepsilon n)^2 v_2(s,n,\phi,t) + \cdots \\
w &= (\varepsilon n)^2 w_2(s,\phi,t) + \cdots \\
p &= p_0(s,n,\phi,t) + (\varepsilon n)p_1(s,\phi,t) + \cdots \\
R &= R_0(s,t) + \varepsilon R_1(s,\phi,t) + \cdots
\end{aligned}$$

$$X = X_0(s) + \varepsilon X_1(s,t) + \cdots \qquad Z = Z_0(s) + \varepsilon Z_1(s,t) + \cdots \tag{H.7}$$

In addition we have the following expansions for the surfactant concentration Γ and variable surface tension σ as

$$\begin{aligned}
\Gamma &= \Gamma_0(s) + \varepsilon^2 \Gamma_1(s) + O(\varepsilon^4), \\
\sigma &= \sigma_0(s) + \varepsilon^2 \sigma_1(s) + O(\varepsilon^4).
\end{aligned} \tag{H.8}$$

Both these quantities are assumed to vary on the frees surface of the jet and only along the jet.

For completeness we have, in the above expansion for the leading order pressure term p_0 assumed a dependence upon n. We shall eventually go on to see that the following analysis will suggest that p_0 is independent of n.

From the continuity equation we obtain

$$O(\varepsilon n) \quad : \quad u_{0s} + 2v_1 = 0 \tag{H.9}$$
$$O(\varepsilon n)^2 \quad : \quad u_{1s} + 3v_2 + w_{2\phi} + 3v_1 \cos\phi S = 0. \tag{H.10}$$

From the second tangential stress condition we get

$$O(\varepsilon) \quad : \quad {R_0}^3 v_{1\phi} = 0 \tag{H.11}$$
$$O(\varepsilon^2) \quad : \quad 3{R_0}^2 R_1 v_{1\phi} + {R_0}^4 (w_2 + v_{2\phi}) = 0. \tag{H.12}$$

Thus (H.9) implies that $v_1 = -u_{0s}/2$ and from (H.12) we have

$$w_2 + v_{2\phi} = 0. \tag{H.13}$$

From the first tangential stress condition at leading order we have

$$u_1 = u_0 S \cos\phi, \tag{H.14}$$

where $S = (X_{0s} Z_{0ss} - X_{0ss} Z_{0s})$. After differentiating (H.13) with respect to ϕ (and noting that v_2 is periodic in ϕ) we obtain

$$w_{2\phi} = -v_{2\phi\phi}. \tag{H.15}$$

Therefore,

$$v_{2\phi\phi} - 3v_2 = u_{1s} + 3v_1 S \cos\phi, \tag{H.16}$$

and using the expressions for u_1 and v_1 we see that

$$v_{2\phi\phi} - 3v_2 = \left(u_0 S_s - \frac{u_{0s}}{2} S \right) \cos\phi. \tag{H.17}$$

Periodic solutions for v_2 and w_2 are

$$v_2 = \frac{1}{4} \left(\frac{u_{0s}}{2} S - u_0 S_s \right) \cos\phi, \tag{H.18}$$

$$w_2 = \frac{1}{4} \left(\frac{u_{0s}}{2} S - u_0 S_s \right) \sin\phi \tag{H.19}$$

The apparent viscosity can be expressed as

$$\eta = m |\sqrt{3} u_{0s}|^{\alpha - 1} \left(1 + (\varepsilon n) \frac{(\alpha - 1)}{u_{0s}} \left(u_0 S_s - \frac{u_{0s}}{2} S \right) \cos\phi + O((\varepsilon n)^2) \right). \tag{H.20}$$

The first tangential stress condition at next order ($O(\varepsilon^2)$) gives

$$u_2 = \frac{3}{2} u_{0s} \frac{R_{0s}}{R_0} + \frac{u_{0ss}}{4} + |\sqrt{3} u_{0s}|^{1-\alpha} \left(\frac{\mathcal{R}e_\alpha}{We} \right) \frac{\sigma_{0s}}{2R_0}. \tag{H.21}$$

From the second Navier-Stokes equation, we have at leading order $p_{0n} = 0$. Thus $p_0 = p_0(s, \phi, t)$, i.e., p_0 is independent of n. At order ε we get

$$p_1 = \left({u_0}^2 S - \frac{2}{\mathcal{R}b} u_0 + \frac{(X+1)Z_s - ZX_s}{\mathcal{R}b^2} \right) \cos\phi - \frac{|\sqrt{3}u_{0s}|^{\alpha-1}}{\mathcal{R}e_\alpha} \left(\frac{6-\alpha}{2} u_{0s} S + \alpha u_0 S_s \right) \cos\phi \tag{H.22}$$

For simplicity of notation we will relabel X_0 and Z_0 with X and Z respectively.

The Navier-Stokes equation in the azimuthal direction gives at leading order $p_{0\phi} = 0$ which is automatically satisfied. At order ε we get the above equation for p_1. From the normal stress condition we obtain at leading order and order ε

$$p_0 = -\frac{|\sqrt{3}u_{0s}|^{\alpha-1}u_{0s}}{\mathcal{R}e_\alpha} + \frac{1}{R_0 We}, \qquad p_1 = \frac{1}{R_0 We}\left(-\frac{R_{1\phi\phi} + R_1}{{R_0}^2} + S\cos\phi \right) + \frac{4|\sqrt{3}u_{0s}|^{\alpha-1}}{\mathcal{R}e_\alpha} v_2.$$

If we now substitute the expression for p_1 from (H.22) into the above equation, and note that R is periodic in ϕ, we get

$$\begin{aligned}(X_s Z_{ss} - X_{ss} Z_s) \left(\frac{(7-\alpha)|\sqrt{3}u_{0s}|^{\alpha-1}u_{0s}}{2\mathcal{R}e_\alpha} + \frac{1}{R_0 We} - u_0^2 \right) + \frac{2}{\mathcal{R}b} u_0 \\ = \frac{(X+1)Z_s - ZX_s}{\mathcal{R}b^2} + \frac{(\alpha-1)|\sqrt{3}u_{0s}|^{\alpha-1}}{\mathcal{R}e_\alpha} u_0 (X_s Z_{sss} - X_{sss} Z_s).\end{aligned} \tag{H.23}$$

This equation is valid only if the leading order terms in the expansion of X and Z are independent of t. If we had retained leading order translational velocity terms v_0 and w_0 in our expansions for v and w, and had $X_{0t} \neq 0$ and $Z_{0t} \neq 0$, then the right hand side of (4.32) would contain some additional unsteady terms in $E = Z_s X_t - Z_t X_s$. However $E \approx 0$ has already been found in Părău *et al.* [105] to be a very accurate approximation between the orifice and the break up point of the jet. In particular Părău *et al.* [104] considered an expansion of the form $X(s,t) = X_0(s) + \widehat{X}(s,t)$ and $Z(s,t) = Z_0(s) + \widehat{Z}(s,t)$ and then solved the linearized version of the resulting equations. Perturbations of the steady centreline were found to be within a maximum deviation of order 10^{-2} and thus are relatively small when compared to $O(1)$ values of $X_0(s)$ and $Z_0(s)$ (effectively making the trajectory steady). This is backed up by the experimental observations of Wong *et al.* [153], which show that the centreline of the jet is steady (in the rotating frame), giving $X_t \approx 0$, $Z_t \approx 0$ and $E \approx 0$ for experimental observations.

The Navier-Stokes equation in the axial direction at order ε is

$$u_{0t} + u_0 u_{0s} = -p_{0s} + \frac{(X+1)X_s + ZZ_s}{\mathcal{R}b^2} + \frac{|\sqrt{3}u_{0s}|^{\alpha-1}}{\mathcal{R}e}(u_{0ss} + 4u_2 + u_{2\phi\phi}), \tag{H.24}$$

which after using the expressions for u_2 and p_0 becomes

$$u_{0t} + uu_{0s} = -\frac{1}{We}\left(\frac{\sigma_0}{R_0}\right)_s + \frac{(X_0+1)X_{0s} + Z_0 Z_{0s}}{\mathcal{R}b^2} + \frac{3|\sqrt{3}u_{0s}|^{\alpha-1}}{\mathcal{R}e_\alpha}\cdot\left(\alpha u_{0ss} + 2u_{0s}\frac{R_{0s}}{R}\right) + \frac{2\sigma_{0s}}{WeR_0}. \quad \text{(H.25)}$$

From the kinematic condition, we obtain at order ε

$$R_{0t} + \frac{u_{0s}}{2}R_0 + u_0 R_{0s} = 0. \quad \text{(H.26)}$$

The arclength equation at leading order gives

$$X_s^2 + Z_s^2 = 1. \quad \text{(H.27)}$$

And finally the last equation to be found is the convection-diffusion equation which at leading order is

$$\Gamma_{0t} + u_0\Gamma_{0s} + \frac{u_{0s}}{2}\Gamma = 0 \quad \text{(H.28)}$$

We see that we have now five equations (H.23), (H.25), (H.26), (H.27) and (H.28) for the five unknowns u_0, R_0, Γ_0, X and Z. The dimensionless equation of state relating the surfactant concentration Γ to the surface tension of the liquid-gas interface is given by the nonlinear Szyskowsky equation

$$\sigma = 1 + \beta\log(1-\Gamma), \quad \text{(H.29)}$$

where the parameter $\beta = \Gamma_\infty R_g T/\tilde{\sigma}$ determines how 'effective' or important surfactants are.

H.3 Steady-state solutions

We search for steady state solutions by considering all the variables to be functions of s. In this case have

$$uu_{0s} = -\frac{1}{We}\left(\frac{\sigma_0}{R_0}\right)_s + \frac{(X_0+1)X_{0s} + Z_0 Z_{0s}}{\mathcal{R}b^2} + \frac{3|\sqrt{3}u_{0s}|^{\alpha-1}}{\mathcal{R}e_\alpha}\left(\alpha u_{0ss} + 2u_{0s}\frac{R_{0s}}{R}\right) + \frac{2\sigma_{0s}}{WeR_0}, \quad \text{(H.30)}$$

$$(X_s Z_{ss} - X_{ss}Z_s)\left(\frac{(7-\alpha)|\sqrt{3}u_{0s}|^{\alpha-1}u_{0s}}{2\mathcal{R}e_\alpha} + \frac{1}{R_0 We} - u_0^2\right) + \frac{2}{\mathcal{R}b}u_0 = \frac{(X+1)Z_s - ZX_s}{\mathcal{R}b^2} + \frac{(\alpha-1)|\sqrt{3}u_{0s}|^{\alpha-1}}{\mathcal{R}e_\alpha}u_0(X_s Z_{sss} - X_{sss}Z_s), \quad \text{(H.31)}$$

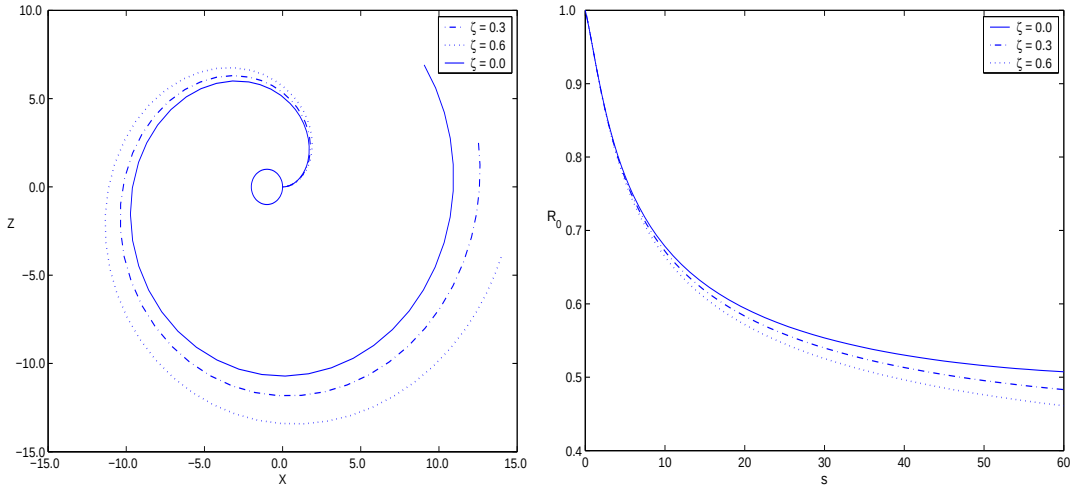

Figure H.1: The effect of changing the initial surfactant concentration ζ on the steady centreline and radius of a rotating liquid jet obtained using a Runge-Kutta method. Here we have $\mathcal{R}b = 3.2$, $We = 5.4$ and $\beta = 0.5$. Clearly a greater initial surfactant concentration leads to the jet curving less and radius decaying more quickly.

$$\frac{u_{0s}}{2}R_0 + u_0 R_{0s} = 0. \tag{H.32}$$

and

$$u_0 \Gamma_{0s} + \frac{u_{0s}}{2}\Gamma = 0. \tag{H.33}$$

From (H.32) and (H.33) we observe that $R_0^2 u_0$ and $\Gamma_0^2 u_0$ are constant, and by using $R_0(0) = 1$, $\Gamma_0(0) = \zeta$ and $u_0(0) = 1$, we have $R_0^2 u_0 = 1$ and $\Gamma_0^2 u_0 = \zeta^2$ so that we can substitute R_0 and u_0 in the previous equations, which now become

$$u_0 u_{0s} = -\frac{(1 + \beta \log(1 - \zeta u_0^{-\frac{1}{2}}))}{We}\frac{u_{0s}}{2\sqrt{u_0}} + \frac{\beta\zeta}{2u_0 We}\frac{u_{0s}}{(1 - \zeta u_0^{-\frac{1}{2}})} + \frac{(X+1)X_s + ZZ_s}{\mathcal{R}b^2} + \frac{3|\sqrt{3}u_{0s}|^{\alpha-1}}{\mathcal{R}e_\alpha}\left(\alpha u_{0ss} - \frac{u_{0s}^2}{u_0}\right), \tag{H.34}$$

$$(X_s Z_{ss} - X_{ss} Z_s)\left(u_0^2 - \frac{(7-\alpha)|\sqrt{3}u_{0s}|^{\alpha-1}u_{0s}}{2\mathcal{R}e_\alpha} - \frac{1}{We}(1 + \beta\log(1 - \zeta u_0^{-\frac{1}{2}}))\sqrt{u_0}\right) = \frac{2u_0}{\mathcal{R}b} - \frac{(X+1)Z_s - ZX_s}{\mathcal{R}b^2} + + \frac{(\alpha-1)|\sqrt{3}u_{0s}|^{\alpha-1}}{\mathcal{R}e_\alpha}u_0(X_s Z_{sss} - X_{sss}Z_s), \tag{H.35}$$

and finally

$$X_s^2 + Z_s^2 = 1. \tag{H.36}$$

The unknowns in (G.34)-(G.36) are X, Z and u_0. The solution to this set of equations without surfactants was found to be almost identical (see Părău *et al* [104]) to the solutions of (G.34)-(G.36) in the inviscid limit (i.e., as $Re \to \infty$). In addition, it can be shown that

viscosity has a negligible influence on the steady state solutions for X, Z and u_0 except in the case of highly viscous fluids (see Uddin *et al.* [141]). We therefore solve (G.34)-(G.36) in the inviscid limit.

H.4 Temporal Instability

In this section we consider the linear stability of disturbances about our leading order steady state solution obtained in the previous section. In this linear analysis it is sufficient to consider a linearized version of the surface tension equation of state. By expanding (G.29) in a Taylor series about the initial surfactant concentration ζ we have

$$\begin{aligned}\sigma &= (1+\beta\log(1-\zeta)) + \sigma'(\zeta)(\Gamma-\zeta) \\ &= (1+\beta\log(1-\zeta)) - \frac{\beta}{(1-\zeta)}(\Gamma-\zeta) \\ &= \sigma_e - E\Gamma \end{aligned} \tag{H.37}$$

where $\sigma_e = (1+\beta\log(1-\zeta)) + \frac{\beta\zeta}{(1-\zeta)}$ is the surface tension of the undisturbed liquid jet corresponding to a uniform surfactant concentration ζ and $E = \beta/(1-\zeta)$ is the Gibbs elasticity.

If the centreline of the rotating jet is assumed to curve over a lengthscale of $s = O(1)$ and perturbations along the jet are of order a (which is comparable to ε when $s = O(1)$) then travelling wave modes of the form $\exp(ik\overline{s} + \lambda\overline{t})$ must be considered, where $\overline{s} = s/\varepsilon$ and $\overline{t} = t/\varepsilon$, in order to have $k = k(s) = O(1)$ and $\lambda = \lambda(s) = O(1)$. We begin by expressing our disturbances about our steady state (obtained from the previous section) as

$$(u, R, \Gamma) = (u_0, R_0, \Gamma_0) + \delta(\widehat{u}, \widehat{R}, \widehat{\Gamma})\exp(ik\overline{s} + \lambda\overline{t}), \tag{H.38}$$

where δ is some dimensionless small constant. In this case the barred symbols denote steady state solutions and k is a real wavenumber with λ being complex, so that $\lambda = \lambda_r + i\lambda_i$ where λ_r is the growth rate of disturbances and λ_i is the wavenumber of disturbances along the jet. In order to prevent instability to wavemodes with zero wavelength we replace the leading order pressure term in (G.30) with the full curvature expression. We thus have

$$\begin{aligned}u_{0t} + uu_{0s} = -\frac{1}{We}\left(\sigma_0\left(\frac{1}{R(1+R_{0s}^2)^{\frac{1}{2}}} - \frac{\varepsilon^2 R_{0ss}}{(1+R_{0s}^2)^{\frac{3}{2}}}\right)\right)_s + \frac{(X+1)X_s + ZZ_s}{\mathcal{R}b^2} \\ + \frac{3|\sqrt{3}u_{0s}|^{\alpha-1}}{\mathcal{R}e_\alpha}\left(u_{0ss} + 2u_{0s}\frac{R_{0s}}{R}\right) + \frac{2\sigma_{0s}}{WeR_0}.\end{aligned} \tag{H.39}$$

We substitute (H.38) into our governing equations (G.26), (G.28) and (H.39), and drop overbars from our variables. We get at leading order the eigenvalue relation

$$\left(\frac{3\Lambda}{\overline{\mathcal{R}e}}k^2+(\lambda+iku_0)\right)(\lambda+iku_0)^2-\frac{k^2\sigma R_0}{2We}\left(\frac{1}{R^2}-k^2\right)(\lambda+iku_0) \\ +\frac{Ek^2\Gamma_0}{2R_0We}(\lambda+iku_0)=0, \tag{H.40}$$

where $\Lambda=|u_{0s}|^{\alpha-1}$ and we have rescaled the Reynolds number (and based it on the orifice radius a) so that $\overline{\mathcal{R}e}=\varepsilon\mathcal{R}e$ to bring in viscous terms and obtain a distinguished limit. By choosing $\lambda_i=-ku_0$ so that disturbances are convected along the jet we find that

$$\lambda_r^2+\frac{3\Lambda}{\overline{\mathcal{R}e}}k^2\lambda_r-\frac{k^2}{2We}\left(\sigma R_0\left(\frac{1}{R^2}-k^2\right)-\frac{E\Gamma_0}{R_0}\right), \tag{H.41}$$

which has solution

$$\lambda_r=-\frac{3\Lambda}{\overline{\mathcal{R}e}}k^2+\frac{k}{2}\sqrt{\left(\frac{3\Lambda k}{\overline{\mathcal{R}e}}\right)^2+\frac{2}{We}\left(\frac{1}{R_0^2}-k^2\right)\sigma R_0-\frac{2E\Gamma_0}{RWe}}. \tag{H.42}$$

Differentiating the above equation to find the wavenumber (using a suitable maths package like MAPLE for example) for which λ_r is a maximum (which we shall henceforth refer to as k^*) we find

$$k^*=\frac{1}{(2R_0^3)^{\frac{1}{4}}}\left(\frac{(\sigma-\Gamma_0E)}{\sigma\sqrt{2R_0}+3Oh\Lambda\sqrt{\sigma}}\right)^{\frac{1}{2}}, \tag{H.43}$$

where $\mathcal{O}h=\sqrt{We}/\overline{\mathcal{R}e}$ is the Ohnesorge number. When there is no surfactant present (i.e., $\Gamma_0=0$) we have $\sigma=1$ and the above expression reduces to the most unstable wavnenumber of a viscous power law liquid jet (see Uddin *et al.* [141])

$$k^*=\frac{1}{(2R_0^3)^{\frac{1}{4}}}\frac{1}{\sqrt{3Oh\Lambda+\sqrt{2R_0}}}. \tag{H.44}$$

List of References

[1] Abravaneswaran, B., and Basaran, O., A., 1999, 'Effects of insoluble surfactants on the nonlinear deformation and breakup of stretching liquid bridges,' Phys. of Fluids, **11**, 15, 997-1015.

[2] Andersen, K. G. and Yttri, G., 1997. Porso vert, Universitets for laget Oslo.

[3] Antencia. J. and Beebe, D., J., 2005, "Controlled microfluidic interfaces," Nature, **437**, September.

[4] Anno, J. N., 1977, *The mechanics of liquid jets,* Lexington Books.

[5] Ashgriz, A. and Mashayek, F., 1995, "Temporal analysis of capillary jet breakup," J. Fluid Mech., **291**, 163-190.

[6] Balmforth, N. J., Craster, R. V., and Toniolo, C., 2003, " Interfacial instability in non-Newtonian fluid layers," Phys. of Fluids, **15**, 11, 3370-3384.

[7] Bauer, H. F., 1984, 'Feee liquid surface response induced by fluctuation of thermal Marangoni convection,' AIAA J, **22**, 421-428.

[8] Becker, E., Hiller, W., J., and Kowalewski, T., A., 1991, "Experimental and theoretical investigations of large amplitude oscillation of liquid droplets," J. Fluid Mech., **231**, 189

[9] Berezin, M. P., Hutter, K., and Spodavara, 1998, " Stability analysis of gravity driven shear flows with free surface for power law fluids," Archives of Applied Mathematics, **68**, 169-178.

[10] Bird, R., B. and Armstrong, A., 1987, "*Dynamics of polymeric liquids: Vol 1, Fluid Mechanics,*" Wiley, New York.

[11] Bird, R., B., Stewart, W. E. and Lightfoot, E., W., 2002 "*Transport phenomena,*" John Wiley, New York, 2nd Edition.

[12] Blake, T.D., Bracke, M. & Shikhmurzaev, Y.D., 1999, "Experimental evidence of nonlocal hydrodynamic influence on the dynamic contact angle," Phys. Fluids 11 (8), 1995-2007.

[13] Blake, T.D. & Shikhmurzaev, Y.D., 2002, "Dynamic wetting by liquids of different viscosity,"J. Colloid Interface Sci. 253, 196-202.

[14] Blyth, M., G., and Pozrikidis, C., 2004a, "Evolution Equations for the surface concentration of an insoluble surfactant; applications to the stability of an elongating thread and a stretched interface," Theoret. Comput. Fluid Dynamics, **17**, 147-164.

[15] Blyth, M., G., and Pozrikidis, C., 2004b, "The stability of two-layer channel flow with surfactants," J. Fluid Mech., **505**, 59-86.

[16] Blyth, M., G., and Pozrikidis, C., 2004c, "The effect of surfactant on the stability of film flow down an inclined plane," J. Fluid Mech., **521**, 241-250.

[17] Blyth, M., G., Luo, H. and Pozrikidis, 2006, "Stability of axisymmetric coreannular flow in the presence of an insoluble surfactant," J. Fluid Mech., **548**, 207-235.

[18] Bousfield, D., W. and Denn, M, M., 1987, "Jet breakup enhanced by initial breakup," Chem. Eng. Comm., **53**, 61.

[19] Bousfield, D., W., Stockel, I., H. and Nanivadekar, C., K., 1990, "The breakup of liquid jets with large velocity modulations," J. Fluid Mech., **218**, 601.

[20] Brenner, M., P., Eggers, J., Joseph, K., Nagel., S., R., and Shi, X., D., 1997, "Breakdown of scaling in droplet fission at high Reynolds number" Phys. Fluids, **9**, 1573-1590.

[21] Carreau, P., J., Kee, D., D., and Daroux, M., 1979, 'An analysis of the viscous behaviour of polymeric solutions, ' Can. J. Chem. Eng., **57**, 135-140.

[22] Chaudhary, K., C., and Redekopp, L., G., 1980a, "The nonlinear capillary instability of aliquid jet: Part 1. Theory," J. Fluid Mech., **96**, 257.

[23] Chaudhary, K., C., and Maxworthy, T., 1980b, "The nonlinear capillary instability of aliquid jet: Part 2. Experiments on jet behaviour before droplet formation," J. Fluid Mech., **96**, 275.

[24] Chaudhary, K., C., and Maxworthy, T., 1980c, "The nonlinear capillary instability of aliquid jet: Part 2. Experiments on satellite formation and control," J. Fluid Mech., **96**, 287.

[25] Chwalek, J., M., Trauernicht., D., P., Delametter, C., N., Sharma., R., Jeanmaire, D., L., Anagnotopoulos, C., N., Hawkins., G., A, Abravaneswaran, B., Panditaratne, J., C., and Basaran., O. A., 2002, 'A new method for deflecting liquid microjets,' Phys. of Fluids, **14**, 6, L37-40.

[26] Clasen, C.,, Eggers, J., Fontelos, M., A., Li, J. and McKinley, G., H. "The beads-on-string structure of viscoelastic threads" , J. Fluid Mech., accepted (2005)

[27] Coronado-Matutti, O., Souza-Mendes, P. R., and Carvallo, M. S., 2004, " Instability of pseudoplastic liquid in couette flow between concentric cylinders," Journal of Fluids Engineering, **3**, 126, 386-390.

[28] Cramer, C., Beruter, B., Fischer, P. and Windhab, E., J., 2002, "Liquid jet stability in a laminar flow field," Chem. Eng. Technol., 25, 5, 499-506.

[29] Crane, L. S., Birch, S. and McCormack, P., O., 1964, "The effect of mechanical vibration on the breakup of a cylindrical water jet in air," Brit. J. Appl. Phys., **15** 743.

[30] Craster, R. V., Matar, O. V. and Papageorgiou, D. T., 2005, "Pinchoff and satellite formation in compound viscous threads," J. Fluid Mech., **533**, 95-124.

[31] Craster, R. V., Matar, O. V. and Papageorgiou, D. T., 2003, "Pinch-off of compound threads with sharp viscosity contrasts," Phys. of Fluids, **15**, 11, 3409-3428.

[32] Cummings, L. J. and Howell, P. D., 1999, "On the evolution of axisymmetric fibres with surface tension, inertia and gravity," J. Fluid Mech., **389**, 361-389.

[33] Davies, J.T. & Rideal, E.K., 1963, *Interfacial Phenomena*, second edition. Academic Press, ISBN 0-12-206056-3

[34] Day, R. F., Hinch, E., J. and Lister,, J., R., 1998, "Self similar pinchoff of an inviscid fluid," Phys. Rev. Letts. **80**, 4, 704.

[35] Decent, S. P., King, A. C. and Wallwork, I. M., 2002, "Free jets spun from a prilling tower," Journal of Engineering Mathematics, **42**, 265-282.

[36] Decent, S. P., 2006, "On the instability of microjets," Continuum Mechanics and Thermodynamics, **17**, 7, 525-543.

[37] Decent, S. P., King, A. C., Simmons, M. H.,Părău, E. I., Wong, D. C. Y., Wallwork, I. M., Gurney, C., and Uddin, J., 2007, "The trajectory and stability of a spiralling liquid jet: Part II. Viscous Theory," submitted to Appl. Math. Modelling.

[38] Decent, S. P., King, A., C., Wallwork, I., M., Gurney, C., J., and Uddin, J., 2007*a*, "Viscous jets curved by gravity," in preparation

[39] DeGennes, P., Brochard-Wyart, M. and Quere, D., 2002. Perles, Gouttes, bulles, perles et ondes.

[40] Dias, F. and Vanden-Broeck, J. M., 1990, "Flows emerging from a nozzle and falling under gravity," J. Fluid Mech., **213**, 465-477.

[41] DuChateau, P., and Zachmann, D., 1989, *Applied Partial Differential Equations*, Harper & Row Publishers, New York.

[42] Del Gaudio, P., and Colombo, P., 2005, "Mechanisms of formation and disintegration of alginate beads obtained by prilling," International Journal of Pharmaceutics,1-9.

[43] Donelley, R., J., and Glaberson, W., 19666, 'Experiments on the capillary of a liquid jet,' Proc. R. Soc. London, Ser. A, **290**.

[44] Doshi, P. Suryo, R., Yidirim, O., E., McKinley, G. H., and Basarn O., A, 2003, "Scaling in pinch-off of generalized Newtonian fluids," J. Non-Newtonian Fluid Mech, 1-27.

[45] Dumas, H., Tardy, M., Rochat, M., H., Tayot, J., L., 1992, " Prilling process apllied to collagen solutions," Drug Dev. Ind. Pharm, **18**, 1395-1409.

[46] Dyre., J., C., 2004, 'Heirs of liquid treasures,' Nature Materials, **3**, 749-750.

[47] Eggers, J., 1993, "Universal pinching of 3D axisymmetric free-surface flow," Phys. Rev. Lett. **71**, 22, 3458-3460.

[48] Eggers, J. and Dupont, T., F., 1994, "Drop formation in a one dimensional approximation of the Navier-Stokes equation," J. Fluid Mech., **262**, 205-221.

[49] Eggers, J., 1997, "Nonlinear dynamics and breakup of free surface flows," Rev. Mod. Physics, **69**, (3), 865-929.

[50] Eggers, J. & Evans, R., 2004, "Comment on 'Dynamic wetting by liquids of different viscosity' by T.D. Blake and Y.D. Shikhmurzaev," J. Coll. Int. Sci. 280, 537-538.

[51] Eggleton, C., D., Pawar, Y., P., and Stebe, K., J., 1999, 'Insoluble surfactants on a drop in an extensional flow; a generalization of the stagnated surface limit to deform interfaces,' J. Fluid Mech. **385**, 79-99.

[52] Entov, V. M., and Yarin A. L., 1984, "The dynamics of thin liquid jets in air," J. Fluid Mech. **140**, 91-113.

[53] Faidley, R., W., and Panton, R., L., 1990, ' Measure ment of liquid jet instability induced by surface tension variations, ' Expl. Thermal Fluid Sci. **3**, 383-387.

[54] Fletcher, D., A., Polanker, D., V., Huie, P., Miller, J., Mannor, M., F., and Blumenkranz, M., S., 2002, "Intravascular drug delivery with pulsed liquid microjets," **120**, 1206-1208.

[55] Fontelos, M., A., and Li, J., 2004, "On the evolution and rupture of filaments in Giesekus and FENE models," J. Non-Newtonian Fluid Mech., **118**, 1-16.

[56] Furlani, E., P., 2005, 'Thermal modulation and instability of viscous microjets,' Nanotech., **1**, 668-671.

[57] Gabbanelli, S., Drazer, G. and Koplik, J., 2005, "Lattice Boltzmann method for non-Newtonian (power law) fluids," Physical Review E, **72**.

[58] Garcia, F., J. and Castellanos, A, 1994, " One dimensional models for slender axisymetric viscous liquid jets," Phys. Fluids, **6**, 8, 2676-2689.

[59] Garstecki, P., Fuerstman, M., J., Stone, H. A. an d Whitesides,. G, M., 2006, "Formation of droplets and bubbles in a microfluidic T-junctionscaling and mechanism of break-up," Lab on Chip, **6**, 437-446.

[60] Goedde, E. F, and Yuen, M. C., 1970, "Experiments on liquid jet instability," J. Fluid Mech., **40**, 495-511.

[61] Goldin, M., Yerushalmi, H., Pfeffer, R. and Shinnar, R., 1969, "Breakup of a laminar capillary jet of a viscoelastic fluid," J. Fluid Mech., **38**, 4, 689-711.

[62] Gottlieb, D., and Turkel, E., 1978, "Boundary conditions for multistep finite difference methods for time-dependent equations," Journal Computational Physics, **26**, 181-196.

[63] Griffin, M., D., and Anderson, J., D., 1977, " On the application of boundary conditions to time dependent computations for quasi one dimensional flows, "Computers and Fluids, **5**, 127-137.

[64] Haenlein, A., 1931, Forsch. Geb. Ingenieurwes. **2**, 139.

[65] Hansen, S., Peters, G., W., M. and Meijer, H., E., H., 1999, "The effect of surfactant on the stability of a fluid filament embedded in a viscous fluid," J. Fluid Mech., **382**, 331-349.

[66] Hardas, N., Danviriyakul, S., Foley, J., L., Nawar, W., W., and Chinachoti, P., 2000, Accelerated stability studies of microencapsulated anhydrous milk fat, Lebensm.-Wiss. Technol., **33**, 506-513.

[67] Harkins, W. D. and Brown, F., E., 1919, "The determination of surface tension (free surface energy), and the weight of falling drops," J. Am. Chem. Soc. **41**, 499.

[68] Harmon, D., B., 1955, 'Drop sizes from low speed jets," J. Franklin Inst. **259**, 519.

[69] Hawkins, V., L., Simmons, M.. J., H., Brisbane, C., J., Uddin, J., and Decent, S. P., 2007, 'Break-up of Spiralling Non-Newtonian Liquid Jets,' 6th International Conference on Multiphase Flow, Leipzig, Germany.

[70] Hertz, C., H., and Hermanrud, B., 1983, "A liquid compound jet," J. Fluid Mech., **131**, 271-287.

[71] Hirsch, C., 1988a, *Numerical computation of internal and external flows; volume 1, fundamentals of numerical discretization*, John Wiley & Sons.

[72] Hirsch, C., 1988b, *Numerical computation of internal and external flows; volume 2, computational methods for inviscid and viscous flows*, John Wiley & Sons.

[73] Hohman, M., M., Shin, M., Rutledge, G. and Brenner, M., P., 2001, "Electrospinning and electrically forced jets. I. Applications," Phys. Fluids, **13**, 8, 2221-2236.

[74] Hwang, C., Chen, J., Wang, J., and Lin,. J, 1994, "Linear stability of power law liquid film flows down an inclined plane," J. Phys D: Appl. Phys. **27**, 2297-2301.

[75] Israelachvili, J., 1995. *Intermolecular and surface forces*, 2nd edition, Academic Press.

[76] Joseph, D., D., Nelson,., J., Renardy., M. and Renardy., Y., 1991, " Two-dimensional cusped interfaces," J. Fluid Mech., **223**, 383.

[77] Jung, T., Kamm, W ., Breitenbach, A., Kaiserling, E., Xiao, J., X., and Kissel, T., 2000, Biodegradable nanoparticles for oral delivery of peptides: Is there a role for polymers to affect mucosal uptake? Eur. J. Pharm. Biopharm., **50**, 147-160.

[78] Kalaaji, A., Lopez, B., Attane, P., and Soucemarianadin, A., 2003, "Breakup length of forced liquid jets," Phys. of Fluids, **9**, 15, 2469-2479.

[79] Keller, J., B and Miksis, M., J., 1983, "Surface tension driven flows," SIAM J. Appl. Math, **43**, 268-277.

[80] Keller, J. B., Rubinow, S. I., and Tu, Y. O., 1973, "Spatial instability of a jet," Phys. Fluids, **16** 2052-55.

[81] Kitamura, Y., and Takahashi, T., 1982, "Breakup of jets in power law in power law non-Newtonian liquid systems," Can. Engng, **60**, 732-737.

[82] Koplik, J. and Banavar, J., R., 1993, "Molecular dynamics of interface rupture," Phys. Fluids A **5** 521.

[83] Kowalewski, T., A., 1996, "On the separation of droplets from a liquid jet," Fluid Dyn. Res., **17**, 121-145.

[84] Kwak, S., and Pozrikidis, C., 2001, Effect of surfactants on the instability of a liquid thread or annular layer. Part I: Quiescent fluids, Int. J. Multiphase Flow, **27**.

[85] Kwano, S., 1998, "Molecular dynamics of rupture phenomena in a liquid thread," Phys. Rev. E, **58** ,4, 4468-4472,

[86] Lee, H., C., 1974, "Drop formation in a liquid jet," IBM J. Res. Dev. **18** 364.

[87] Liao, Y-C., L., Franses, E. I., and Basaran, O., A., 2006, 'Deformation and breakup of a stretching liquid bridge covered with an insoluble surfactant monolayer,' Phys. Fluids, **18**, 022101-21.

[88] Li, J., and Fontelos, M., A., 2003, "Drop dynamics on the beads-on-string structure for viscoelastic jets: A numerical study," Phys. Fluids, **15**, 4, 922-936.

[89] Lin, S. P., 2003, *Breakup of Liquid Sheets and Jets*, Cambridge University Press, United Kingdom.

[90] Lister, J., R. and Stone, H., A., 1998, "Capilary Breakup of a Viscous Thread Surrounded by Another Viscous Thread," Phys. Fluids, **10**, (11), p.2758

[91] Loscertales, I., G., Barrero, A., Guerrero, I., Cortijo, R., Marquez, M. and Ganan-Calvo, A., M., 2002, "Micro/Nano Encapsulation via Electrified Coaxial Liquid Jets," Science **295**, 1695

[92] Maguire, L., M., Zhang, H. and Shamlou, P., A., 2003, "Preparation of small unilamellar vesicles (SUV) and biophysical characterization of their complexes with poly-L-lysine condensed plasmid DNA," Biotechnol. Appl. Biochem, **37**, p.73-81

[93] Mashayek, F., and Ashgriz, N., 1994, 'Nonlinear instability of liquid jets with thermocapillary,' J. Fluid Mech., **283**, 97-123.

[94] Middleman, S., 1995, *Modeling Axisymmetric flows; dynamics of films, jets and drops*, Academic Press.

[95] Middleman, S., 1965, 'Stability of a viscoelastic jet,' Chem. Eng. Sci. **20**, 1037-1040.

[96] Middleman, S., and Gavis., J., 1961, 'Expansion and contraction of capillary jets of Newtonian liquids,' Phys. Fluids, **4**, 355.

[97] Morrison, F. A., 2001, "*Understanding Rheology,*" Oxfor University Press

[98] Mortanto, W., Baish, S., M., Costner, E., A., Prausnitz, M., R. and Smith, M. K., 2005, "Fluid dynamics in conically shaped microneedles," AIChE Journal, **51**, 6.

[99] Moseler, M. and Landman, U., 2000, "Formation, stability and breakup of nanojets," Science, **289**, 1165.

[100] Nahas, N., M., and Panton, R., L., 1991, Control of surface tension flows -Instability of a liquid jet. Trans. ASME, J. Fluids Eng. **112**, 296-301.

[101] Ornek, D., Gurkan, T. and Oztin, C., 2000, "Prilling of Aluminium Sulphate," Journal of Chemical Technology & Biotechnology, **75**, 8, 689-694.

[102] Palmer, S., J., 1976, 'The effect of temperature on surface tension,' Phys. Educ., **11**, 119-120.

[103] Papageorgiou, D., T., 1995, "On the breakup of viscous liquid threads," Phys. Fluids, **7**, 1529.

[104] Părău, E. I., Decent, S. P., Simmons, M. J. H., Wong, D. C. Y. and King, A. C., 2007, "Nonlinear viscous liquid jets from a rotating orifice," J. of Eng. Maths., **57**, 159-179.

[105] Părău, E. I., Decent, S. P., King, A. C., Simmons, M. J. H., Wong, D. C. Y., 2006, "Nonlinear travelling waves on a spiralling liquid jet," Wave Motion, **43**, 599-613.

[106] Partridge, L., 2006, 'An experimental and theoretical investigation into the break-up of curved liquid jets in the prilling process,' PhD Thesis, University of Birmignham.

[107] Peregrine, D., H., Shoker, G., and Symon, A., 1990, "The bifurcation of liquid bridges," J. Fluid Mech., **212**, 25.

[108] Perrin, B., 2004,"Improving Insecticides through Encapsulation," Pesticide Outlook.

[109] Pimbley, W., T., and Lee., H., C., 1977, 'Satellite droplet formation in a liquid jet,' IBM J. Res. Dev. **21**, 21-25.

[110] Plateau, J., 1873, "Statique Experimentale et Theoretique des Liquides Soumis aux Seules Forces Moleculaires," Gauthier Villars, Paris, **II**, 319.

[111] Pozrikidis, C., 1997, '*Introduction to Theoretical and Computational Fluid Dynamics*,' Oxford University Press.

[112] Prausnitz, M., R., 2001, "Analysis: Overcoming skin's barrier; The search for effective and user friendly drug delivery," **3**, 2, 233-236.

[113] Press, W., H., Teukolsky, S., A., Vetterling, W., T., and Flannery, B., P. 2001, *Numerical Recipes in Fortran 77: The art of scientific computing*, Cambridge University Press.

[114] Ramos, J., I., 1998, 'Annular liquid jets and other axisymmetric free-surface flows at high Reynolds numbers,' Applied Mathematical Modelling, **22**, p.423-452.

[115] Ramos, J., I., 1999, 'Asymptotic analysis of compound liquid jets at low Reynolds numbers,' Applied Mathematics and Computation, **100**, p.223-240.

[116] Rayleigh, W., S., 1878, "On the instability of jets," Proc. Lond. Math. Soc **10**, 4.

[117] Rayleigh, W., S., 1899, "Investigations in cappillarity," Phil. Mag., **48**, 321.

[118] Ribe, N., M., 2004, "Coiling of visocus jets," Proc. R. Soc. Lond. A, **460**, 3223-3239.

[119] Richtmyer, R., D. and Morton, K., W., 1967, *Difference Methods for Initial Value Problems*, 2nd eds, New York, John Wiley and Sons.

[120] Rowlinson, J. S. and Widom, B., 1982, *Molecular theory of capillarity*, Dover.

[121] Rutland, D., F. and Jameson, G., J., J., 1970, "Theoretical prediction of the sizes of drops formed in the breakup of capillary jets," Chemical Engineering Science, **25**,1689-1698.

[122] Sakai, T., and Hoshino, N., 1980, "Production of uniform droplets by longitudal vibration of audio frequency," J. Chemical Eng. Japan, **13**, 4, 263-268.

[123] Sanz, A., and Meseguer, J., 1985, One-dimensional analysis of the compound jet, J. Fluid Mech. **159**, 55-68.

[124] Savart, F., 1833, Annal, Chim. **53** 337.

[125] Shaw, A., J., 2005, Coalescence of two volumes, PhD thesis. Univeristy of Birmingham.

[126] Shi., X., D., Brenner, M., P., and Nagel, S., 1994, ' A cascade of structure in a drop falling from a faucet,' Science, **265**, 219.

[127] Shikhmurzaev, Y. D., 1993, "The moving contact line on a smooth solid surface," Int. J. Multi-phase Flow **19**, 589-610.

[128] Shikhmurzaev, Y.D., 1997, "Spreading of drops on solid surfaces in a quasi-static regime," Phys. Fluids **9**, 266.

[129] Shikhmurzaev, Y.D. & Blake, T.D., 2004, "Response to the comment on [J. Colloid Interface Sci. 253 (2002) 196] by J. Eggers and R. Evans," J. Coll. Int. Sci. 280, 539-541.

[130] Shikhmurzaev, Y.D., 2005, "Capillary breakup of liquid threads: a singularity-free solution," IMA J. Appl. Math. 70, 880-907.

[131] Spurk,, J., H., 1997, *Fluid Mechanics*, Springer-Verlag.

[132] Squires, T., M., and Quake, S., R., 2005, "Microfluidics: Fluid physics at the nanoliter scale," Rev. Mod. Phys, 7:3, 977-1026.

[133] Srignano, W., A. and Mehring, C., 2000, Review of the theory of distortion and disintegration of liquid streams, Progress in Energy and Combustion Science, **26**, 609-655.

[134] Stone, H., A., and Leal, L., G., 1990, 'The effect of surfactant on drop formation and breakup,' J. Fluid Mech., **220**, 161-186.

[135] Suryo, R., Doshi, P., and Basaran, O., A., 2006, 'Nonlinear dynamics and breakup of liquid jets,' Phys. of Fluids., **18**, 8, 082107-31.

[136] Tate, T., 1864, "On the magnitude of drop of liquid formed under different circumstances," Phil. Mag. **27** , 176.

[137] Teng, H., C.M.Kinoshita, and S.M. Masutani, 1995, Prediction of Droplet Size from the Breakup of Cylindrical Liquid Jets, International Journal of Multiphase Flow, 21, No. 1, 129- 136.

[138] Tilley, B., S., and Bowen, M., 2005, 'Thermocapillary control of rupture in thin viscous fluid sheets,' J. Fluid Mech. **541**, 399-408.

[139] Timmermans, M-L, E., and Lister, J. R., 2002, 'The effect of surfactant on the stability of a liquid thread,' J. Fluid Mech. **459**, p289-306.

[140] Tuck, E. O., 1976, "The shape of free jets of water under gravity," J. Fluid Mech., **76**, 625-640.

[141] Uddin, J., Decent, S., P., and Simmons, M., H., 2006, "The instability of shear thinning and shear thickening liquid jets: linear theory," ASME J. of Fluids Eng., **128**, 968-975.

[142] Uddin, J., Decent, S., P., and Simmons, M., H., 2007a, "Breakup and Droplet formation in rotating non-Newtonian liquid jets," submitted to Int. J. Eng. Sci.

[143] Uddin, J., Decent, S., P., and Simmons, M., H., 2007b, "The instability of rotating liquid jets with surfactants," submitted to Fluid Dyn. Res.

[144] Uddin, J., Decent, S., P., and Simmons, M., H., 2007c, "The instability of non-Newtonian rotating liquid jets with surfactants," submitted to J. Phys. A.

[145] Uddin, J., Decent, S., P., and Simmons, M., H., 2007d, "Pinch-off in compound non-Newtonian liquid threads," in preparation for submission to Applied Mathematical Modelling.

[146] Uddin, J., Decent, S., P., and Simmons, M., H., 2007e, "Periodically heating a non-Newtonian liquid jet," in preparation for submission to IOP J. Phys. D.

[147] Vanden-Broeck, J. M. and Keller, J. B., 1982, "Jet rising and falling under gravity,' J. Fluid Mech., **124**, 335-345.

[148] Wallwork, I. M., 2002a, "The trajectory and stability of a spiralling liquid jet," Ph.D. Thesis, University of Birmingham, Birmingham.

[149] Wallwork, I. M., Decent, S. P., King, A. C. and Schulkes, R. M. S., 2002b,"The trajectory and stability of a spiralling liquid jet. Part 1, Inviscid Theory," J. Fluid Mech., **459**, 43-65.

[150] Weber, C., 1931, 'Zum Zerfall eines Flussigkeitsstrahles.' Z. Angew. Math. Mech, **11**, 136-154.

[151] Whitaker, S., 1976, 'Studies of drop-weight method for surfactant solutions III,' J. Colloid Interface Sci., **51**, 231-248.

[152] Wilson, H., J. and Rallison, J., M., 1997, "Short wave instability of co-extruded elastic liquids with matched viscosities," J. Non-Newtonian Fluid Mech. **72**, 237-251.

[153] Wong, D. C. Y., Simmons, M. J. H., Decent, S. P., Parau, E. I. and King, A. C. , 2004, "Break-up dynamics and drop sizes distributions created from spiralling liquid jets," International Journal of Multiphase Flow, **30**, 5, 499-520.

[154] Wylie, J. J., Huang, H., and Miura, R., M., 2007, 'Thermal instability in drawing viscous threads, ' J. Fluid Mech., **570**, 1-16.

[155] Xu, J. J., and Davis, S. H., 1984, 'Instability of capillary jets with thermocapillarity,' J. Fluid Mech., **161**, 1-26.

[156] Xu, Q. and Nakajima, M., 2004, "The generation of highly monodisperse dropletsb through the breakup of hydrodynamically focused microthread in a microfluidic device," App. Phys. Letts, **85**, 17.

[157] Yarin, A., L., 1993, "*Free liquid jets and films: hydrodynamics and rheology,*" Longman

[158] Yildirim, O. E. and Basaran, O. A., 2001, "Deformation and breakup of stretching bridges of Newtonian and shear-thinning liquids: comparison of one and two-dimensioanl models," Chem. Eng. Sci. , **56**, 211-233.

[159] Yosi, H. *et al.*, 2001, Inn. Food Sci. Em. Technol., **2**, 55.

[160] Yuen, M., C., 1968, "Non-linear capillary instability of a liquid jet," J. Fluid Mech., **33**, 151-163.